Water contents and lithium isotope compositions of the Mesozoic-Cenozoic lithospheric mantle of eastern North China Craton: constraints from peridotite xenoliths

Pei Li

Water contents and lithium isotope compositions of the Mesozoic-Cenozoic lithospheric mantle of eastern North China Craton: constraints from peridotite xenoliths

Thesis by **Pei LI**

IN PARTIAL FULFILLMENT OF THE REQUIREMENTS FOR THE DEGREE OF

DOCTOR OF PHILOSOPHY AT

USTC, University of Science and Technology of China,
School of Earth and Space Sciences

and

UL, Université de Lorraine,
Ecole doctorale RP2E, Spécialité Géosciences

August, 2012

Defended November 22 2012 at USTC.

Committee Members

XU Yigang	GIG/CAS, Guangzhou	Chairman
ZHANG Hongfu	IGG/CAS, Bejing	reviewer for INPL
INGRIN Jannick	Université Lille 1, Lille	reviewer for INPL
DALLAI Luigi	CNR-Ist., Pisa	reviewer for INPL
ZHENG Yongfei	USTC, Hefei	
CHEN Fukun	USTC, Hefei	
ZHENG Jianping	CUG, Wuhan	
XIA Qunke	USTC, Hefei	PhD Director
DELOULE Etienne	CRPG-CNRS, Nancy	PhD Director

Acknowledgements

First and foremost, I wish to thank Dr. Qunke Xia and Dr. Etienne Deloule, my thesis advisors, at whose suggestions this work was done, for encouragement and guidance throughout the course of the research. They are also thanked for their always care on my living at Hefei and Nancy during the past seven years.

I would like to thank Denis Mangin, Michel Champenois, Claire Rollion-Bard, and Marc Chaussidon for their generous help and patient teaching on measurements by ion microprobe at CRPG, thank Rucheng Wang and Wenlan for their assistances on EMPA at Nanjing University and thank Yilin Xiao and Zhenhui Hou for the LA-ICP-MS measurements at USTC. I appreciate Xiaozhi Yang and Yantao Hao, and they help me a lot with measurements during FTIR experiments when I joined the lab as a freshman; I enjoy and benefit from discussing with them and Jia Liu over scientific issues.

I thank the professors, who have contributed greatly to my geological education at the university: Yongfei Zheng, Shuguang Li, Jiangfeng Chen, Xiachen Zhi, Daogong Chen, Zhi Xie and Ji'an Hong.

Thanks also go to many friends at Nancy for providing the assistances and friendship. Lu Zhang and Junbo Duan double as a teacher to help in French; XianQing Mao is very kind and always invites me to join their activities to color my life. Many other people who have not been mentioned above but contribute to my thesis, and thanks are due to all of them.

Last but not least, I would like to thank my devoted parents for raising and educating me. I love them so much, and I would not have made it this far without them.

Abstract

A systematic Fourier transform infrared spectrometer (FTIR) and ion microprobe (SIMS) investigation of the major mineral phases (olivine, orthorpyroxene and clinopyroxene) in peridotite xenoliths from seven localities across the eastern North China Craton (Penglai, Qixia, Changle, Hebi, Daxizhang, Qingdao and Junan), was undertaken to clarify the compositions and concentrations of the structural H-species (known as H_2O or water) within these nominally anhydrous minerals (NAMs), the possible spatial and temporal variations of water contents in the lithospheric mantle and controlling factors, and to place constraints on the melt-rock interactions in the lithospheric mantle by studies of the lithium isotopic systematics in mantle peridotite.

Nominally anhydrous minerals, such as cpx and opx in peridotite xenoliths, generally contain some amounts of structural OH, known as water, with their contents (ppm H_2O by wt %) varying from 27 to 746 ppm for cpx and 8 to 346 ppm for opx in all studied xenoliths. The homogeneous H_2O distribution within grains and the equilibrium partitioning of H_2O between cpx and opx both demonstrate that the measured H_2O contents of pyroxenes can be representative of the pre-eruptive state. The ol are almost anhydrous, generally considered as a consequence of H loss during decompression ascent.

A significant contrast in water content is observed in peridotite xenoliths hosted by the Mesozoic and Cenozoic basalts, hinting at a temporal evolution of water content in the lithospheric mantle beneath the eastern NCC. The H_2O contents in cpx and opx of the Cenozoic samples (Penglai, Qixia, Changle, and Hebi) are from 27 to 223 ppm and from 8 to 94 ppm, respectively. By contrast, the H_2O contents in cpx and opx of the Mesozoic samples (Qingdao and Junan) are from 466 to746 ppm and from 187 to 346 ppm, respectively. In addition, the water contents of Daxizhuang xenoliths display the Cenozoic affinity, varying from 103 to 311 ppm in cpx and from 30 to 141 ppm in opx.

The low water contents of the Cenozoic peridotite xenoliths, generally lower than their counterparts worldwide and the N-MORB source, probably reflect the unique nature of the relatively ancient lithospheric mantle that has survived the late Mesozoic to early Cenozoic lithospheric thinning event. The reheating from upwelling asthenospheric flow, accompanying that thinning, would devolatilize the overlying lithospheric mantle, resulting in the water depletion. By contrast, the inferred high water signature of the late Mesozoic lithospheric mantle is likely to represent the intermediate between the Cenozoic depletion and the early Cretaceous enrichment in water content. The late Mesozoic paleo-Pacific subduction is assumed to have caused that water enrichment, and the resulting high water content, in turn, would weaken the lithosphere and initiate the thinning. The devolatilization, facilitated by thinning of the hydrated and weak lithospheric mantle pieces at bottom, is one possible way by which the lithospheric mantle strengthens itself to survive in the convecting mantle.

The in-situ Li contents vary from 1.5 to 10.6 ppm in ol, from 0.2 to 62.2 ppm in opx and from 1.6 to 59.7 ppm in cpx for the Cenozoic peridotites (Penglai, Qixia and Hebi). These extreme Li inter-mineral and intra-mineral disequilibria, combined with the numerical simulations, demonstrate a strong and transient Li enrichment event that occurred at the mantle source short prior to the volcanic transports. This recent melt-rock interaction that produced the extreme Li enrichment was too transient to be recorded by other elemental or isotopic systems, and the mantle metasomatism defined by LREE enrichments in cpx from Penglai and Hebi was not the one that caused the Li enrichment. The inferred Li content of up to 600 ppm would call on differentiated carbonatitic melts to interact with the peridotites.

The peridotite samples from Penglai, Qixia and Hebi share more or less the similar Li and Li isotopic signatures that suggest two superimposed Li enrichment events: a limited Li enrichment (< 5 ppm) and large δ^7Li depletion (-20~-10‰) of the domains of these xenoliths, followed by a recent and transient infiltration of high Li and δ^7Li (up to +20‰) melts/fluids. The inferred low δ^7Li melts call upon anomalies

melting in the mantle source that contains Li isotopic anomalous, so does the inferred high δ^7Li melts.

From the line of Li isotopic evidences, we conclude that there are recycled components, both Li isotopically heavy and light, in the mantle beneath the eastern North China, and they are most likely derived from the subduction-modified mantle and highly dehydrated slab, respectively, due to the western subduction of the paleo-Pacific plate since late Mesozoic.

The decoupling of high water content from Li enrichment, i.e. high Li contents and low Li contents in Cenozoic samples; and low Li contents and high water contents in late Mesozoic samples, may hint at an incorporation mechanism by which Li partitions into mineral is compensated by H^+ leaving mineral (defined by the substitution). The Li-rich melt-peridotite interactions may contribute much or add to the low water signature of the Cenozoic lithospheric mantle beneath the eastern NCC.

.

Key words: North China Craton, lithospheric mantle, peridotite xenolith, water content, lithium isotopes, FTIR, ion microprobe, recycled components

Table of contents

1 Introduction

1.1 Background and motivation

The lithosphere is the rigid outer layer of the Earth, with the thickness ranging from a few tens of kilometers beneath rift zones to > ~250 km beneath some Archean cratons. This veneer, although trivial volumetrically, is not only the paradise for life development on the Earth, but also holds the key to understanding many phenomenon and geologic processes in the deep Earth, ranging from the earthquakes, volcanism or the formation of economic ore deposits, with their implications on human ordinary life, to the continental growth, the mantle heterogeneity and the likes that seem distant from our daily life but matter much to basic scientific issues. The lithosphere is the cornerstone for the sake of well reading the Earth's history, in that it is only accessible region of the solid earth that can deliver us abundant and diversified natural samples of different depths and different ages, with which we can look back the earth history, or even look forward.

The lithosphere, more strictly, is defined as one of the two thermal boundary layers in planet Earth. It can be distinguished from the underlying convecting mantle by different types of cooling (Parsons and Sclater, 1977). Within this upper thermal boundary layer heat is transferred primarily by conduction, allowing the temperatures at Earth's surface to lie below the mantle adiabat defined by the potential temperature of the convecting mantle, which lost heat by buoyant upwellings. The lithosphere consists of crust and mantle portions that are separated by the Moho, a chemical discontinuity upon which the rock are differentiated from basaltic to granitic in composition, and beneath which peridotite dominates. The oceanic and the continental lithospheres have distinct crustal compositions: primary and basaltic, and evolved and roughly tonalitic, respectively. Between the mantle portions are there also differences, which determines the destinies of the overlying crust. On moving away from the ocean ridge where the new oceanic lithosphere is born, oceanic crust and its thin underlying layer of melt-depleted mantle cool themselves by conduction of heat into the oceans, and become mechanically coupled together to form what is known as lithosphere during the enduring cooling. As the plate ages, the oceanic

lithosphere mantle cools further, and thickens by the accretion of the convecting mantle directly at its base. Then, the oceanic lithosphere as a whole is growing compositionally similar to the underlying asthenosphere from which it was derived as the thickening continues. At the same time the lithosphere is also becoming progressively more denser, and eventually at a point it exceeds the underlying mantle in density and becomes gravitationally unstable, then descends back into the convecting mantle at subduction zones, the process is known as plate subduction, which make the Earth unique among the terrestrial planets. The oceanic lithosphere is short-lived, with a life of less than 200 Ma, so it fails as the "life raft". And fortunately, life on the Earth is endowed with another alternative, the continental lithosphere.

Unlike the oceanic lithospheric mantle, which contributes to the destruction of the overlying crust, the continental counterpart appears to help in the long-term survival of continental crust, and to serve as a "life preserver" (Carlson et al., 2005). Due to the melt extraction during its formation, much of the continental lithospheric mantle is relatively less dense and much thicker than its oceanic counterpart. Its thickness mainly depends on the compositional difference between it and underlying convecting mantle, as well as on the geothermal gradient. The continental lithosphere, although often much thicker than the oceanic counterpart, is typically weaker. It can be inferred from the observations that the oceanic lithosphere usually lacks the internal deformations which abound within its continental counterpart (Hawkesworth et al., 1999). Although continental lithosphere appears to be long-lived, many may have already been destroyed and recycled, leaving no trace of their prior existences. Geochemical studies of ocean island basalts using radiogenic isotopes as tracers have identified isotopic end members that have been interpreted to represent pods of recycled ancient continental crust in the convecting mantle (Hofmann 1997). Among the continental lithospheric mantle, these beneath Archean cratons have the coldest, deepest, and strongest roots. These cratons, coupling with their roots as a whole can float on the convecting mantle over billion years, and still remain intact.

Cratons are the cores of continents that formed primarily in the Archean and have for the most part remained stable since formations (Lee et al., 2011). The high degree of melt depletion, documented by the low contents of moderately incompatible trace elements and some major element indicators such as high Mg# in olivine in cratonic peridotite, has long been assumed to hold the key to the longevity of cratonic

lithosphere (Griffin et al., 1999). It is not only responsible for producing the chemical buoyancy (Boyd and McAllister, 1976; Lee et al., 2003), leaving the mantle residuum with less Fe and Al, the latter of which is the requirement to make the dense mineral garnet. Also it has to be held accountable for sweeping away most of the incompatible trace elements from mantle, adding to the cold geotherms in lithospheric mantle (Karato, 1986; Pollack, 1986) and boosting the resistance to the convection from the underlying asthenosphere. That is because among those elements are the radioactive elements, such as potassium, uranium, and thorium, which determine the heat-producing capacity of the lithospheric mantle, and moreover the element "water" or hydrogen, more precisely, the removal of which can significantly enhance the viscosity of mantle rock by a factor of hundred times compared with that of water-saturated mantle (Hirth and Kohlstedt, 1996; Shapiro et al., 1999a; Dixon et al., 2004).

However, many peridotite xenoliths from the cratons or the post-archean continents frequently show evidences for a multistage history involves depletion in a basalt component followed by enrichment in incompatible trace elements, especially LILE, at some later time (Menzies and Hawkesworth, 1987; Menzies, 1990). Although in some cases the highly enrichment in LILE reflects infiltration of xenoliths by the host magma, at least some cases that enrichment unambiguously indicates the metasomatsim is ancient. It is not surprising that the lithospheric mantle have been infiltrated by metasomatic melt or fluid, given that it has been floating above the convecting mantle for billion years. To what extents that metasomatism occurred in the lithospheric mantle matters. Because the localized metasomatism just insignificantly affects the average composition and strength of the lithosphere and contributes little to the destruction of lithosphere. If the metasomatism happens on a large scale, the consequence could be more dramatic, leading the lithosphere mantle into instability. Rudnick et al. (1998) noted that the average K_2O content (0.15%) measured in cratonic peridotite xenoliths is too high to produce less curved geotherms that match those recorded by the thermobarometry of xenoliths, and conclude that the average cratonic lithosphere has not been metasomatised too much, as was once assumed, and the enrichment signature is a local phenomenon due to the biased samples representing the general lithospheric mantle.

Longevity of cratonic lithosphere, however, is not forever, as was once assumed. The craton can be reactivated, and its coupling root can also be removed and replaced.

North China Craton, one of the oldest Archean cratons, and with crust record as old as 3.8 Ga, remains a valuable showcase for understanding the evolution of the cratonic lithosphere and its destruction. Although the mechanism and geodynamic reason responsible for lithospheric thinning of the NCC have been extensively debated (Menzies et al., 2007, and the reference therein), there is growing consensus that the prerequisite of such destruction is weakening of the lithosphere mantle (Niu et al., 2005; Wu et al., 2008). It is tempting to consider the mantle metasomatism, a reverse process to form a lithosphere, a likely candidate in well doing that job. The metasomatic agent can bring H_2O and LILE-rich melts from underlying convecting mantle, or even more flux if linked to the subduction zone environment, to lower the solidus and viscosity of mantle rock, and also to make it denser and less refractory by interactions.

The finding that hydrogen, although the most abundant element in the universe and also everywhere on surface of planet Earth when bonded with oxygen to appear as liquid water can enter trace abundances into crystal lattices of mantle olivine and pyroxene, known as Nominally Anhydrous Minerals (NAMs), has tremendous geodynamic implications (Bell and Rossman, 1992a; Hirth and Kohlstedt, 1996). It is shaping the old ideas over the way by which the earth and atmosphere have been evolving. Knowledge of the amount of water, or hydrogen species, inside the earth at present, and in the past, is a critical issue for understanding the petrological, geochemical, geophysical and dynamical processes of the Earth, as well as for constraining the segregation, accretion and evolution model of the planet and the whole cycle of hydrogen in its interior. This relies heavily on the well-known fact that water, even in trace amounts, can exert a strong influence on many chemical and physical properties of its host silicate minerals/rocks, including mechanical and rheological strength (e.g. Griggs, 1967; Kronenberg et al., 1986; Hirth and Kohlstedt, 1996), rate of ionic diffusion (Goldsmith, 1987; Elphick et al., 1988), melting behavior (Kushiro, 1972; Arndt et al., 1998) and electrical conductivity (Karato, 1990); and, if extracted from minerals, it contributes to the formation of ore deposits and hydrous fluids, and even to the triggering of deep-seated earthquakes (Meade and Jeanloz, 1991). After pioneering works lead by Griggs and Blacic (1965) and Martin and Donnay (1972), and the early speculations of Fyfe (1970)-later reviewed by Ackermann et al. (1983)-who stated that OH-bearing anhydrous minerals might be a significant reservoir for water in the Earth's mantle, it has been gradually and widely

accepted that NAMs can commonly contain few to several thousand ppm of water (H_2O by weight) in their lattice, predominated by OH and/or less molecular H_2O, and are the main hydrogen reservoir in the deep earth, especially in the upper mantle (Bell and Rossman, 1992a; Ingrin and Skogby, 2000; Bolfan-Casanova, 2005). Such water may play crucial but diversified roles on many properties and processes in the earth (e.g. Williams and Hemley, 2001; Keppler and Smyth, 2006). The upper mantle is mainly made of olivine and pyroxene, so these nominally anhydrous minerals in principle can also incorporate some water/hydroxyl in them. A thorough investigation about water in peridotite xenoliths coupled with other geophysics/geochemistry information is therefore necessary for a better understanding of the entire Earth system. Fourier transform infrared (FTIR) absorption spectroscopy is a highly sensitive, site-specific, high resolution, and non-destructive in situ method for studying structural OH and H_2O molecular in mineral. It can give detailed structural information of OH in the crystal lattice, and provide quantitative determination of that structural OH, although depending on the experimentally-calibrated absorption coefficients for given phases. (Rossman, 1996).

The addition of water or fluids from the flat subducting slab (Farallon Plate) to rehydrate the overlying lithospheric mantle has proven the main cause of the lithospheric mantle thinning, 50~100 km loss, beneath the Colorado Plateau since the Menozoic (Li et al., 2008 and Lee et al., 2011). For the same reason, this mechanism may have taken place in the case of the thinning beneath the NCC. The North China Craton has been surrounded and influenced by a series of subduction since the Phanerozoic, including the southern subduction of the ancient Asian ocean beneath its northern margin at the Paleozoic, and northern collision of the Yangzi block on its southern margin, forming the Dabie-Sulu Orogen, at the early Mesozoic, and most importantly the western subduction of the Pacific plate beneath the east Asia since later Mesozoic. It is tempting to expect that the upper mantle beneath the North China or the Big Mantle Wedge (Zhao et al., 2007) is water enriched. Then, the released water may migrate up to affect the overlying lithospheric mantle.

If the subduction has provided fluids to rehydrate the lithospheric mantle beneath the NCC, we can expect contaminations of recycled materials in the upper mantle. However, there is no compelling geochemical evidence from Cenozoic basalts confirming that claim, probably due to the dilution of the recycled components over a long distance from subduction zone. Here, we introduce a more sensitive stable

isotopic system, lithium isotopes, to trace the mantle metasomatism linked to the potential recycled material in the upper mantle.

The stable isotopes have been employed to trace the crustal components in the mantle and study melt/fluid-rock interactions at surface and in deep lithospheric mantle (Tomascak et al., 2002; Brooker et al., 2004; Elliott et al., 2004, 2006). Lithium isotope system is still relatively youthful field but has its own charm to attract increasing attentions. The significant relative mass difference (16%) between its two stable isotopes theoretically promises a large Li isotope fractionation at low temperature. Li is a highly fluid-mobile element (Brenant al., 1998; Chan et al., 1999, 2002), causing Li migration during water/rock interactions at the surface conditions, such as the Li leaching from the upper continental crust by weathering, and at the depth where the metamorphic dehydration processes occur. In addition, as a moderately incompatible element (Ryan and Langmuir, 1987, Brenan et al., 1998, Seitz and Woodland, 2000), Li tends to partition preferentially into melt phases during magmatic processes such as partial melting and crystallization, resulting in the enrichment of Li in the crust relative to the mantle. These factors contribute to Li elemental and isotopical fractionation between different layers of the earth. The Li content of primitive mantle is estimated between 1.0~1.8ppm (McDonough and Sun, 1995; Magna et al., 2006), and the isotopic composition vary narrowly between +2~+6‰ with an average value of +4‰ (Chan et al., 1992; Tomascak et al. 2008). By contrast, the average Li content and Li isotopic composition of the upper continental crust is about 35±11ppm and 0±2‰ respectively (Teng et al., 2004), and those of the upper altered oceanic crust is greater 12 ppm than and +8‰ respectively (Chan et al., 1992, 2002), depending on the extent of alteration. The more altered the oceanic crust is, the more and heavier the Li is taken by alteration minerals. So Li isotopes system has been suggested a more sensitive and potential tracer for recognizing recycling of surface-modified materials into the mantle (Tomascak et al., 2002; Brooker et al., 2004; Elliott et al., 2004, 2006). However, as more Li isotopic data from mantle peridotites were released, its reliability as a diagnostic tracer is increasingly questioned, arguing that the anomalous Li isotopic ratios recorded in xenoliths may be a consequence of the Li diffusion-induced fractionation at high temperature rather than of contaminations by recycled components isotopically fractionated at low temperature. It is well established that Li isotopes have different diffusion rates, with ^{7}Li running 3% much faster than ^{6}Li in silicate mineral and melt (Richard et al.,

2003). Moreover, the Li diffusion rate differs also exists among individual mineral phase, with the higher Li diffusion rate in pyroxene than in olivine (Rudnick and Ionov, 2007; Parkinson et al., 2007). These Li diffusive differences are responsible for isotopically zoned mineral grains and/or inter-mineral isotope disequilibria observed in mantle xenoliths. This kinetic isotope fractionation can also occur at a large scale (Lundstrom et al., 2005, Teng et al., 2006). Teng et al., (2006) found that the change in δ^7Li of up to 20‰ at distances varying from 1 to 30 m from the contact. Given the cause by diffusive isotopic fractionation is widespread, the anomalous Li isotopic signatures are necessarily interpreted with caution when linked to recycled components. Here, in my thesis, Li contents and isotopic compositions were measured in situ and by profile on the mineral grains using ion microprobe, promising solid interpretations over melt-rock interactions.

Mantle xenoliths, fragments of the deep lithosphere, are scraped from the wall-rock surrounding the volcanic conduits and then transported quickly to the surface by the lavas, such as alkaline and kimberlitic magma. Since the magmas rise from thier source to the surface in a very short time (just few days or even few hours), followed by quick cooling when exposing to the air, the xenoliths are thus believed to represent almost “quenched” products and their source information could be kept roughly. These xenoliths provide snapshots of the lithosphere of different depths beneath particular regions at the time of their eruption. In a word, the deep-suited mantle xenoliths are most effective objects for researching the lithospheric mantle itself.

In this thesis, 53 mantle peridotite xenoliths were collected across most of the mantle xenolith outcrops in eastern NCC, ranging from the most eastern dominances in Shandong province (including six localities: Penglai, Qixia, Qingdao, Daxizhang, Changle, and Junan) where the lithospheric mantle have suffered the most thinning and it is generally believed that all the archean roots have been removed, to Hebi of Henan province, near the Trans-North China Orogen, where the subcontinental mantle have been relatively less modified and there are solid signs favoring relics of the ancient mantle. Among these xenoliths those from Junan, Qingdao and Daxizhuang were captured by Mesozoic alkali basalt, and the rest in Cenozoic basalt.

The aims of this thesis are first to obtain the water contents in lithospheric mantle by studies of mantle peridotite xenoliths, contributing to the geophysical database for water in the deep lithosphere worldwide, further to clarify the water distribution, i.e. the possible spatial and temporal variations of water, in the lithospheric mantle, and

hint at a possible link to the lithospheric thinning beneath the eastern NCC. Second, the aims are to provide a new view to examine the melt/fluid-rock interaction in the lithospheric mantle in term of lithium isotopes, placing constraints on the origin of the mantle metasomatic agents.

1.2 Thesis outline

The thesis has been organized in eight chapters, including this introduction; the rest of the chapters were written as separated manuscripts.

Chapter 2 gives a brief introduction to the geological background of the North China Craton, our studied regions and Dabie-Sulu UHP, and the issue concerning the thinning of lithospheric mantle beneath the NCC. Then a summary of the previous works by others is given for Penglai, Qixia, Changle, Hebi, Daxizhuang, Junan and Qingdao localities where our samples were collected. At last, the descriptions of our representative peridotites are presented in term of rock-types, rock texture, modal mineralogy and mineral texture.

Chapter 3 offers a description of all analytical methods applied during this thesis, including electrical microprobe (EMP) for major elements, LA-ICP-MS for trace elements, FTIR for hydrogen species and contents, and SIMS for Li content and Li isotopic ratios.

Chapter 4 compiles all the experimental data, including major elements for all mineral phases, water contents for pyroxene, trace elements for cpx and Li contents and isotopic ratios for all mineral phases in all peridotite xenoliths. These data are cornerstone for the detailed discussion in the following chapters.

Chapter 5 discusses the mantle depletion by partial melting, and mantle enrichment by mantle metasomatism. The mantle depletion process is viewed from chemical compositions and some geochemical indicators of mineral phases, and is then roughly modeled using HREEs. The enrichment process is identified by enrichment of the incompatible trace elements but Li, and further subdivided by their patterns and distributions of rare earth elements into mantle metasomatism of different natures.

Chapter 6 discusses the water contents and the contrasts between the Cenozoic lithospheric mantle and the Mesozoic lithospheric mantle beneath the NCC, and attempts to unveil this temporal variation.

Chapter 7 details the Li and Li isotopic systematics of the peridotites and related melt-rock interaction in the lithospheric mantle, and place constraints on the origin of the mantle metasomatic agents.

Chapter 8 includes a summary of the results and the final conclusions of these studies.

2 Geological background and previous works

The continental regions on the Earth consist of several Precambrian cratons and Phanerozoic orogenic belts between them (Fig. 2-1). These cratons, with either Archean or Precambrian basements, represent the cores of continents that have not been deformed for at least 1 Ga, in strong contrast to the active orogenic belts (Lee et al., 2011).

The North China Craton (NCC) is relatively small among those cratons with Archean basements worldwide. From a view of a smaller scale, The NCC is one of the main tectonic unites in the eastern China, which comprises other three tectonic unites: from north to south, the eastern Central Asian Orogenic Belt, the Dabie-Sulu ultrahigh-pressure (UHP) metamorphic belt, and the South China Craton (Fig. 2-2). These units were amalgamated during the Phanerozoic. Inside the NCC, it can be subdivided into three parts: the eastern NCC, the western NCC and the central NCC between them (Zhao et al., 2000, 2001). These tectonic units in the eastern China are detailed below.

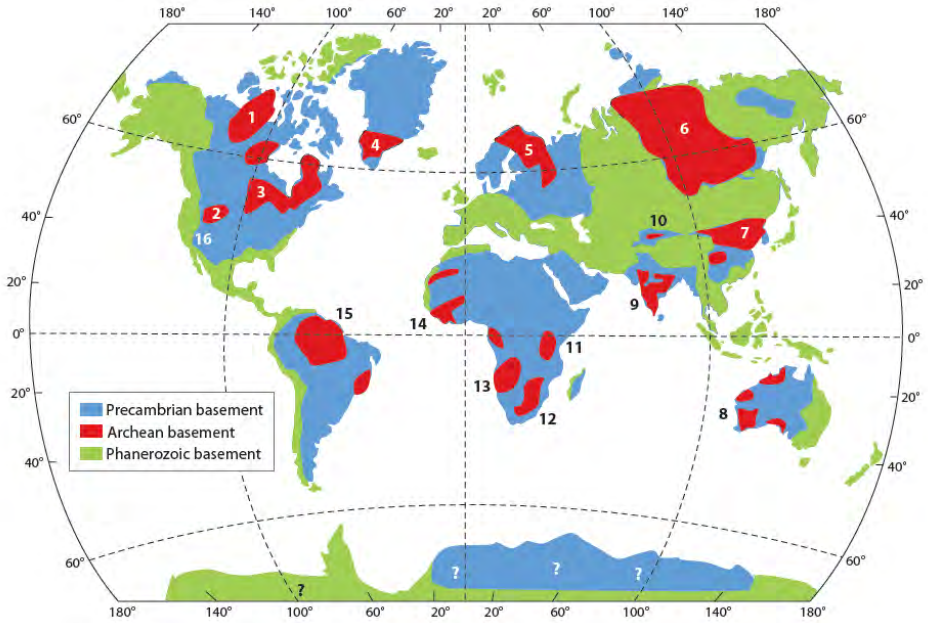

Figure 2-1. Map of Precambrian (>540 Mya) and Phanerozoic (<540 Mya) crustal basement. Archean cratons are shown in red. Cratons are labeled as follows: 1, Slave; 2, Wyoming; 3, Superior; 4, Greenland; 5, Fennoscandian; 6, Siberian; 7, North China; 8, west Australian; 9, Indian; 10, Tarim; 11, Tanzanian; 12, South African (Kaapvaal); 13, Congo; 14, west African; 15, Amazonia; 16, Colorado Plateau. (from Cin-Ty A. Lee, (2011))

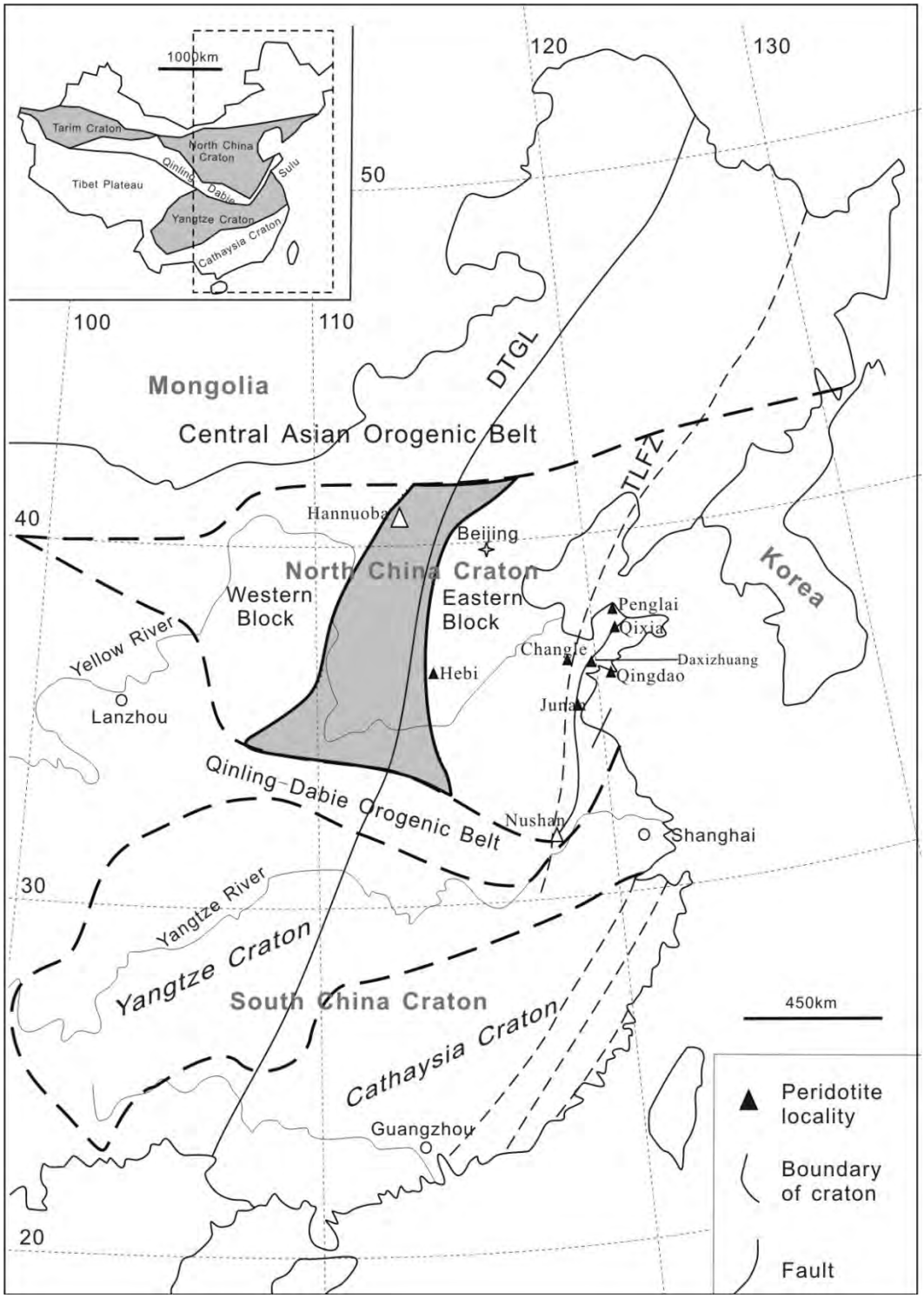

Figure 2-2. Simplified tectonic units of eastern China and localities of peridotite xenoliths in this study.

2.1 The North China Craton

The North China Craton (NCC) is the Chinese part of the Sino-Korean Craton (SKC), and is also can be seen as the North China Block (NCB) in the literature. It is

one of the most ancient cratons on the Earth, composed of early Archean and Proterozoic basements with the oldest recorded crustal ages >3.8 Ga (e.g. Liu et al., 1992), and is also the largest craton in China, covering an area >1,700,000 km. It is bounded by the Central China orogeny (including the Qinling–Dabie Shan–Sulu belts) to the SW, and the Inner Monglia–Daxinganling orogenic belt (the Chinese part of the Central Asian Orogenic Belt) on the north (Figure2-1 and 2-2). The western boundary is more complex, where the Qilian Shan and Western Ordos thrust belts obscure any original continuity between the NCC and the Tarim Block. The location of the southeastern margin of the craton is currently under dispute (Oh and Kusky et al., 2007), with uncertain correlations between the North and South China Cratons and different parts of the Korean Peninsula. The Yanshan belt is an intracontinental orogen that strikes east–west through the northern part of the craton (Davis et al., 1994; Bai and Dai 1998).

There are two major large-scale geological and geophysical linear zones cutting across NCC (Fig. 2-2). To the west, the craton is cut by the Daxing'anling-Taihangshan Gravity Lineament (DTGL); to the east, the craton is traversed by the Tan-Lu Fault Zone (TLFZ). Based on the lithological assemblage, tectonic evolution and P-T-t paths of metamorphic rocks, the North China Craton can be divided into the Western and Eastern Blocks, separated by the Central Orogenic Belt, the assembly of the two blocks during the Proterozoic cratonization (Zhao et al., 2000; 2001). The Western Block is composed of late Archean to early Proterozoic metasedimentary belts that unconformably overlie the Archean basement; the latter consists mainly of granulite facies gneiss and charnockite with small amounts of mafic granulites and amphibolites. The basement of the Central Orogenic Belt consists of late Archean amphibolites and granulites, and 2.5 Ga granite-greenstone terrains with overlying 2.4-2.2 Ga bimodal volcanic rocks in the southern region and thick carbonate and terrigenous sedimentary rocks interleaved with thin basalt flows in the central region. The Eastern Block is composed of late Archean orthogneisses intruded by 2.5 Ga syntectonic granitoids. The collision between the Western and Eastern blocks 1.8-2.0 Ga ago may have led to the formation of the Central Orogenic Belt and the final amalgamation of the North China Craton.

In detail, The NCC includes several micro-blocks and these micro-blocks amalgamated to form a craton or cratons at or before 2.5 Ga (Geng 1998; Kusky et al., 2001, 2004, 2006; Kusky and Li, 2003; Zhai 2004; Zhao et al., 2000, 2001), although

others have suggested that the main amalgamation of the blocks did not occur until 1.8 Ga (Zhao et al., 2001, 2006; Liu, S.W., et al., 2004, 2006; Guo et al., 2005; Kroner et al., 2005a, b, 2006). Exposed rock types and their distribution in these micro-blocks vary considerably from block to block. All rocks .2.5 Ga in the blocks, without exception, underwent the 2.5 Ga metamorphism, and were intruded by 2.5–2.45 Ga granitic sills and related bodies. Nd_{TDM} models show that the main crustal formation ages in the NCC are between 2.9 and 2.7 Ga (Chen and Jahn, 1998; Wu et al., 2003a, b). Emplacement of mafic dyke swarms at 2.5–2.45 Ga has also been recognized throughout the NCC (Liu, 1989; Li, J.H. et al., 1996; Li, T. S. 1999).

The NCC, however, did not survive the way by which most of its counterparts worldwide did, such as the Kaapvaal Craton (South Africa), the Slave craton (North Canada) and the Siberian Craton. It experienced widespread tectonothermal reactivation since the Phanerozoic (Menzies et al., 1993; Xu, X.S. et al., 1998, 2004; Menzies et al., 2007 and the references therein). Its reactivation was well recorded by lines of evidences. First, the growing activities of magmatism in the NCC is the most straight evidence, beginning from the Ordovician with the intrusions of kimberlitic magmas through the thickest part of the craton, and culminating in the late Mesozoic-Cenozoic with voluminous intrusive and volcanic rocks of varying compositions, ranging from mafic to dominantly felsic (Menzies et al., 2007 and the references therein). Some even argued that the reactivation could begin as early as Proterozoic ages, on the ground that the dominance of Proterozoic Re-Os model ages over the Archean ones within the mantle peridotite suites may imply that significant changes occurred to the NCC, with the archean roots replaced by the younger material during the Proterozoic (Gao et al., 2002; Wu et al., 2003b). Second, the NCC also experienced development of extensive sedimentary basins (most of the eastern portion of the craton is covered by Quaternary sediments) and presently has higher heat flow (60 mW/m^2: Hu et al., 2000) compared to other Archean and Proterozoic cratons (Nyblade et al., 1990; Jaupart and Mareschal).

These changes in both thermal state and chemical composition of the lithospheric mantle were best recorded and constrained by mantle xenoliths of rocks and mineral concentrates. Xenoliths carried in Ordovician kimberlitic magmags are deep-seated garnet-facies peridotites. These xenoliths, together with the appearance of diamonds in the kimberlites and the P-T equilibrium conditions preserved in the inclusions/mineral concentrates of these diamonds, indicate a “shield” geotherm for

the Palaeozoic lithosphere, characterized by low heat flow of 40 mW/m^2, and thick lithospheric keel (~ 200 km). By contrast, xenoliths hosted in late Cretaceous and Cenozoic basalts are dominated by fertile spinel-facies peridotites, which represent a shallower and hotter lithospheric mantle from the thermobarometry, in good agreement with an average present-day surface mean heat flow of 80 mW/ m^2 and thin lithosphere of 60-80 km from the geophysical observations. And it was also a compositionally heterogeneous lithospheric mantle (Fan and Hooper, 1989; Xu et al., 1995; Xu, X.S. et al., 1998; Zheng et al., 1998, 2001, 2006; Fan et al., 2000; Rudnick et al., 2004; Reisberg et al., 2005; Ying et al., 2006). Collectively, these lines unambiguously demonstrate that more than 100 km of the Archean root was removed or strongly modified during late Mesozoic-early Cenozoic time beneath the NCC, at least the Eastern part (Menzies et al., 1993; Griffin et al., 1998; Xu, 2001, 2007; Zheng et al., 2001, 2006; Gao et al., 2002, 2004, 2008; Zhang et al., 2002, 2005, 2008, 2009a; Wu et al., 2006). The mechanism and tectonic driving force responsible for the NCC lithospheric thinning have been intensely debated during the last decade (Menzies et al., 2007 and references therein).

2.2 Lithospheric thinning and the destruction of the NCC

The lithospheric thinning in eastern China was observed as early as 1990s, and described in different works. (Fan and Menzies, 1992; Menzies et al., 1993; Griffin et al., 1998; Menzies and Xu, 1998; Menzies et al., 2007), but was first formally identified as a scientific issue by Menzies et al. (1993). It did not catch too much attention until recently (mostly, the past decade) when it was linked to the destruction of the craton. Although there is no intrinsic connection between the two, the relation is indeed obvious in many ways. It also remains unclear, however, over the cause, extents, mechanism and timing, as well as tectonic controlling factors, for this geodynamical process.

The scale for the lithospheric thinning involves both its horizontal and vertical distribution, which indicates how wide and how thick the lithosphere has been removed, respectively. There is at present a general consensus that the NCC has experienced significant lithospheric thinning, especially its eastern domain. Recent studies show that, not only the NCC, but also the north-east and south-east China are

characterized by rather thin lithosphere relative to other ancient cratons on the Earth (Zou, 2001; Xu et al., 2002; Wu et al., 2003a). Based on these work, it seems that the entire eastern China, to the east of the DTGL, has experienced lithospheric thinning. This can be further supported by the thermal structure (Fig. 2-3a: He et al., 2001) and seismic tomography (Fig. 2-3b: Priestley et al., 2006) of the upper mantle beneath the eastern China. The issue over the vertical thinning involves the removal of either only the lithospheric mantle or both part of the lower crust and the underlying lithospheric mantle, which is still much debated until recently (Menzies et al., 1993; Griffin et al., 1998; Menzies and Xu, 1998; Zheng, 1999; Xu, 2001; Wu et al., 2003a, b; Gao et al., 2004; Xu and Bodinier, 2004; Menzies et al., 2007).

How the lithospheric keel below eastern China had been lost has been the subject of hot debate during the past 20 years, among which previous studies were largely focused on the eastern NCC, where the lithospheric thinning is most obvious. Several mechanisms or models have been proposed to explain this thinning below the NCC, which can be grouped into two end-members: the "top-down" rapid delamination models versus "bottom-up" protracted thermomechanical-chemical erosion models.

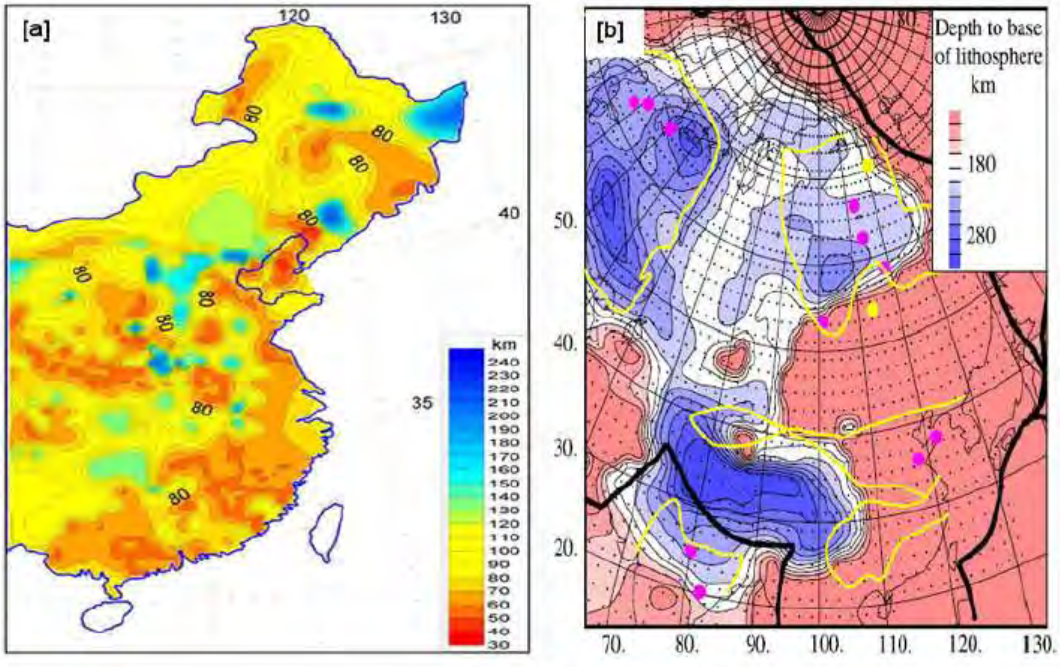

Figure 2-3. Thermal structural (a) and tomography structure (b) of the upper mantle beneath the eastern China. (after He et al., 2001 and Priestley et al., 2006, respectively)

The Delamination model predicts a short period (less than 10 Ma) (Yang et al., 2003; Gao et al., 2004). Yang et al. (2003) suggested that lithospheric delamination took place primarily in the early Cretaceous, based on the evidence for widespread

crustal melting during 130-110 Ma which would require thinning of the lithosphere. By contrast, Gao et al. (2004) argued for Jurassic delamination of the lower crust, based on their discovery that Jurassic andesites, dacites and adakites from Xinglonggou (north NCC) have chemical signatures consistent with their derivation as partial melts of eclogites that interacted with mantle peridotite; in this case, they proposed that the lithospheric thinning had reached such a stage by the late Jurassic that lower crustal rocks could be delaminated, converted to eclogites, incorporated into the convecting mantle and melted. The latter model, however, is difficult to reconcile with the fact that Mesozoic mafic and felsic magmatism peaked in the early Cretaceous (Yang et al., 2003; Xu et al., 2004; Wu et al., 2005) rather than the Jurassic; furthermore, rapid delamination is clearly at odds with the protracted Mesozoic magmatism (~100 Ma) in the NCC (Xu et al., 2004), and it is not easy to reconcile the linear thinning along the whole east China.

The thermomechanical-chemical erosion models, by contrast, hints at a protracted process, possibly up to 100 Ma (e.g. Griffin et al., 1998; Xu, 2001). In this scenario, lithospheric thinning proceeded by heat transport into the lithosphere and small-scale asthenospheric convection induced by extension. Once lithospheric mantle was thermally converted to asthenosphere, it can convectively mix with, and eventually be replaced by, the underlying asthenosphere (Davis, 1994). A recent hypothesis suggests that the lithospheric thinning has been initiated by hydration weakening, for which the water required may come from dehydration of the subducted Paleo-Pacific lithosphere that remained horizontally stagnant within the transition zone beneath eastern China (Niu, 2005). The westward thrust of the Pacific plate into the transition zone underneath east China has been recently observed by high-resolution seismic tomography (Huang and Zhao, 2006). Furthermore, the subduction may even lead to the gravity anomaly in eastern China and the formation of the DTGL in the early Cretaceous (e.g. Niu, 2005; Xu, 2007). This subduction-related mechanism is also supported by evidence from mineral compositions of mantle peridotites with different formation ages (Zheng et al., 2006). For the past two decades, the time-scale of such destruction has been debated, including its beginning, peak-period and ending. This, however, relies fundamentally on the well understanding of how the lithosphere keel has been removed. A short time interval of only 10 to 20 Ma, or even less, for delamination-induced thinning (Yang et al., 2003; Gao et al., 2004) is in strong contrast to that of over 100 Ma for erosion-induced thinning (Griffin et al., 1998; Xu,

2001; Xu et al., 2004). Some relevant geological, geochemical and geophysical data on a 200 Ma time scale for the NCC are summarized by Menzies et al. (2007), so that these events can be cross-correlated. The presence of mantle derived plutonic rocks around 180-190 Ma is believed to mark the reactivation of the cratonic lithosphere, the early Cretaceous is widely agreed to mark a key.

In addition, many other thinning models or mechanisms have been proposed, and are intermediate between the above two end member models. The differences in chemical composition and orgnization of the lithospheric mantle beneath the eastern North China Craton prior to and after its thinning according to different models are illuminated in Fig. 2-4

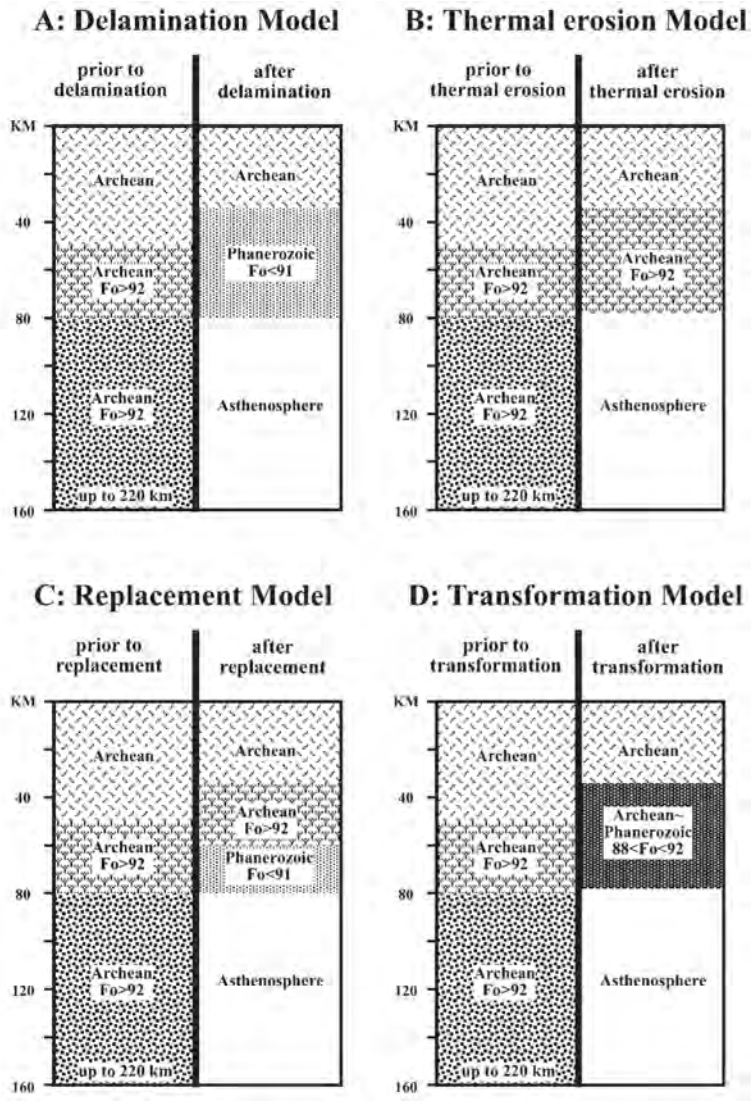

Figure 2-4. Schematic diagram of the lithosphere beneath the eastern North China Craton prior to and after its thinning according to different models (From Zhang et al, 20009).

2.3 The Dabie-Sulu UHP Belt

The Dabie-Sulu UHP belt, the eastern part of the Central China orogeny, lies between the North China Craton and South China Craton, extending from east to west for ca. 2000 km in the central-eastern China (Fig. 2-2). It is separated into two terrains by about 500 km of left-lateral strike-slip displacement along the TLFZ. At the east, the Sulu terrain is segmented into a number of blocks by several NE-SW trending faults that sub-parallel to the TLFZ. At the west, the Dabie terrain is the major segment, separated into a series of continuous zones by several EW-trending faults of large scales. The formation of the Dabie-Sulu UHP belt mainly in the Triassic was caused by collision between the North China and Yangtze Cratons with peak metamorphism at ~ 245 Ma (Hacker et al., 1998), followed by a series of closing of ocean basins. The basement of the Dabie-Sulu UHP terranes is metamorphic and igneous, such as schists, greenstones, gneisses, and rare quartzites, marbles, granulites, and eclogites, intruded by granitoids. The occurrence of eclogites first suggests that pressures of metamorphism were high. Discovery of coesite, diamond, and extreme ^{18}O-depletion, as well as exsolution of cpx, rutile and apatite, in eclogites (e.g. Okay et al., 1989; Wang et al., 1989; Xu, S.T. et al., 1992; Yui et al., 1995; Ye et al., 2000) demonstrates the subduction of the continental crust to mantle depths of about 200 km and the subsequent quick exhumation (see also a review by Zheng, Y.F. et al., 2003). The chronological evolution in terms of the subduction and exhumation of the Dabie-Sulu UHP Belt can be simplified as the following: the peak metamorphism are at ~ 240-245 Ma, with differential exhumation processes to crustal levels in different areas, e.g. eclogites-facies recrystallization at ~ 230 Ma in central Dabie and granulitization at ~ 220 Ma in north Dabie, prior to amphibolite- facies retrogression at ~ 200 Ma (Zheng, Y.F. et al., 2003; and references therein).

2.4 Localities and samples

The deep xenoliths, from the lower crust and lithospheric mantle, can serve as time capsules for unveiling temporal evolutions of the lithosphere directly. Fortunately, the mantle xenoliths are widely distributed in the north China, south China, and eastern China of our interest in this study (Fig. 2-2). Our research area is

the eastern part of the NCC, where the signs of the lithospheric thinning are most obvious. Mantle peridotite xenoliths in this thesis were collected across most of the mantle xenolith outcrops in Eastern NCC, ranging from the eastern domains in Shandong province (including six localities: Penglai, Qixia, Qingdao, Daxizhuang, Changle, and Junan) where the lithospheric mantle have suffered most the thinning and it is generally believed that all the archean roots have been all removed, to Hebi of Henan province, near the Trans-North China Orogen, where the subcontinental mantle have been relatively less modified and there are solid proofs for the ancient remainders (Zheng et al., 2001, 2006). Among these xenoliths those from Junan, Qingdao and Daxizhuang were exhumed by Mesozoic alkali basalts, and the others in Cenozoic basalts. Unfortunately, there is no mantle xenoliths hosted by the volcanic rocks that predated the late Cretaceous.

Six of the seven localities in this thesis are concentrated in Shangdong province, where three stages of igneous rocks from the Paleozoic, Mesozoic, and Cenozoic that contain mantle xenoliths can be identified. The Mengyin kimberlites, emplaced during the Paleozoic at ~470 Ma (Zhang and Yang, 2007; Yang, 2009), contain abundant harzburgite xenoliths (Chi and Lu, 1996; Gao et al., 2002; Zheng et al., 2007; Zhang et al., 2008). Among the Mesozoic rocks, the Tietonggou diorite in Laiwu (~125 Ma) contains harzburgite and dunite xenoliths, some of which yield the Archean Os model ages; Qindao diorite (Xu,et al., 2008; Gao et al., 2008). During the Cenozoic, alkaline volcanic activities were pervasive in more localities, including Changle-Linqu, Yishui, Penglai, Qixia and Wudi fields. Most of these localities are close to or within the Tan-Lu Fault (Fig. 2-2).

Tan-Lu Fault is a long-lived N-NE trending wrench fault that originated from the collision between the NCC and the Yangtze craton in the Triassic. It has taken a great role in shaping the tectonic frames of Shangdong region, cutting the province from north to south into two distinct structural units: the eastern jiaodong unite and the western Luxi unite. The tectonics of the Jiaodong unit is more complex than that of the Luxi unite due to the occurrence of the Sulu ultrahigh pressure metamorphic belt. The Jiaodong can further be subdivided into the Jiaobei block, one part of the NCC, and the Jiaonan orogen, within the region of Sulu UHP Belt, the eastern part of Qinling-Dabie-Sulu orogenic belt. Between these two parts is the Wulian–Mishan Fault (Zhai et al. 2000). The Sulu UHP belt has been truncated by the Tan-Lu sinistral fault offset by about 500 km to the north (Xu, J.W. et al., 1987). Compared with the

consensus that the suture of the collision can be well defined by the Dabie UHP belt to the west of Tan-Lu zone, that suture to the east of the fault was much debated. This belt was traditionally regarded as the suture to the east, the same as that to the west (Okay et al., 1992; Yin et al., 1993), but growing evidences favor a crustal-detachment model proposed by Li (1994) based on the interpretation of linear aeromagnetic anomalies, surface geological observations, and deep seismic profiles, in which the upper crust of the Yangtze Craton was detached from its lower crust and thrust over the NCC for more than 400 km, whereas the lower part of the lithosphere was subducted under the NCC along a subsurface suture running east of Nanjing. This means that the deep lithosphere, including the lower crust and its underlying mantle part, beneath the Sulu UHP belt should still belong to that of the NCC. Chung (1999) inferred the same plate boundary between the NCC and SCC based on the studies of the trace element and isotope characteristics of Cenozoic basalts in Shandong Province around the Tan-Lu fault and Subei Basin.

2.4.1 Qixia

Qixia volcano area is located at the eastern of Shandong province (Fig. 2-2). The presence of 2800 Ma TTG and granitic gneiss basement in the Qixia area confirms that this region is a part of the NCC (Zhai et al., 2000; Wu, J.S. et al., 1998), not the structurally uncertain unit which was once confused by the debate that where did the North China–Yangtze boundary cut through Shandong peninsula (Zhang, K.J. 2000; Faure et al., 2001). Two episodes of volcanism occurring in Miocene to Pliocene time (18.1 to 4.3 Ma) and Pliocene time (6.4 to 5.9 Ma) were identified in Qixia areas. The host lavas (alkali olivine basalts, basanites, nephelinites) carry abundant deep-seated xenoliths including dominant spinel lherzolite, dunite, clinopyroxenite (Zheng et al., 1998), Fe-rich olivine websterites (Fan et al., 2000) and megacryst suites that include augite, anorthoclase, phlogopite, ilmenite, and garnet. Equilibration temperatures of 850 to 1020℃ (Zheng et al., 1998) and 840 to 980℃ (Rudnick et al., 2004) both suggest entrainments of these lherzolites from depths shallower than 45 km, implying that the lithosphere is relatively thin there (Zheng 1998). Based on major element systematics, the variable extents of 0% to 25% removal of a batch melt at low pressure (<3 GPa) from a primitive mantle were obtained for peridotite xenoliths

(Rudnick et al., 2004; Gao et al., 2002). Re-Os measurements in Qixia peridotite xenoliths show that the $^{187}Os/^{188}Os$ varies within a rather narrow range of 0.1241–0.1299, overlapping that of Primitive Upper Mantle (PUM), and generally TRD and TMA ages are relatively young (0–700 Ma), with one exception with significantly older ages (TRD and TMA of 1300 and 1600 Ma, respectively). The samples define very poor correlations on a Re–Os isochron plot, resulting probably from (1) recent melt extraction, so the Os isotopic composition has not had time to evolve to match Re/Os ratio, or (2) derivation of the xenoliths from a source with heterogeneous $^{187}Os/^{188}Os$. Although it is not possible to well constrain the timing of formation of the lithosphere due to the lack of an isochron or good correlations between $^{187}Os/^{188}Os$ and indicators of fertility, it should be younger than ~1000 Ma (Gao et al., 2002). Gao (2002) further claimed that the "new" generation of lithosphere that followed the removal of the old root could postdate the eruption of the kimberlitic magmatism in Ordovician, and are most likely to associate with the Mesozoic collision of the Yangtze and NCC on the ground the geological lines of evidences.

The lack of correlation between equilibration temperature (hence derivation depth) and bulk composition indicated chronologically unstratified beneath the NCC (Gao et al., 2002). This was also confirmed by the lack of relation between equilibration temperature and major elements compositions on the same area (Rudnick, 2004). Thus, variations in degree of partial melting are not easily related to a simple lithospheric column generated during a single upwelling event, where shallower residues are predicted to be more refractory than deeper.

In this thesis, eight fresh xenoliths, all spinel-facies lherzolites of small sizes (1~4 cm) with coarse-grained or fine-grained texture, were collected from the same area in Qixia than previous work (Zheng et al., 1998; Gao et al., 2002). The xenoliths were captured in olivine nephelinites dated at ~6 Ma by K-Ar method (Jin, 1985). No hydrous minerals have been found, and the modal proportions of mineral phases are presented Table 2-1. The GPS position of the outcrop is N37º12'15.5'', E120º43'23.8''.

The xenoliths are coarse-grained in texture, and usually show a large orthopyroxene porphyroblast adjacent to clinopyroxene and olivine (Fig. 2-4A-B).

Table 2-1. Modal mineral proportions for Qixia peridotite xenoliths

Sample	Rock-Type	Olivine	Opx	Cpx	Spinel
QX-01	Sp-Lher	68	23	6	3
QX-04	Sp-Lher	60	25	12	3
QX-14	Sp-Lher	70	20	8	2
QX-15	Sp-Lher	63	27	8	2
QX-18	Sp-Lher	67	23	9	2
QX-49	Sp-Lher	63	24	11	2
QX-50	Sp-Lher	70	20	9	1
QX-51	Sp-Lher	61	20	18	1

2.4.2 Penglai

Penglai volcano of Shandong province is located ~ just 50 km northern of Qixia. It seems that both regions are controlled by the same episodes of volcanism (E et al., 1987). The Penglai volcanoes, erupted during the Neogene at 5.7~4.2 Ma (Liu, 1999).

Chu et al. (2009) studied the Os isotopes of peridotite xenoliths in Penglai, and showed that like peridotite xenoliths from other Cenozoic basalts in the eastern North China Craton (Gao et al., 2002), the Penglai xenoliths have Os model ages that range back to the Mesoproterozoic, with a distribution of Os isotopic compositions identical to that seen in modern abyssal peridotites. This similarity between Cenozoic lithosphere and abyssal peridotites implies that this lithosphere formed during the Mesozoic or Cenozoic and that it is unlikely that the present lithospheric mantle beneath the eastern NCC was a modified Archean lithospheric mantle. The cpx separates have high initial ε_{Nd} (+5~+24 with average of +10) and ε_{Hf} (+7~+75 with average of +25) and low $^{87}Sr/^{86}Sr$ ratio (~0.7030), consistent with their derivation from convecting upper mantle during the Mesozoic or Cenozoic.

In this thesis, the ten collected samples are all spinel lherzolites occurring in alkali basalts dated at about 8 Ma by K-Ar method (Liu et al., 1990). The GPS position of the outcrop is N37º46’42.2’’, E120º44’46.4’’.

The most xenoliths range in size between 3 and 10 cm. These peridotite xenoliths are fresh, generally coarse-grained (1~3mm) and equigranular, with some displaying porphyroclastic textures. No hydrous minerals have been found in them. The modal mineralogy of xenoliths was given in Table 2-2.

Table 2-2. Modal mineral proportions for Penglai peridotite xenoliths

Sample	Rock-Type	Olivine	Opx	Cpx	Spinel
PL-01	Sp-Lher	62	27	9	2
PL-10	Sp-Lher	72	20	6	2
PL-17	Sp-Lher	72	19	7	2
PL-19	Sp-Lher	67	18	12	3
PL-31	Sp-Lher	71	16	11	2
PL-32	Sp-Lher	76	13	10	1
PL-36	Sp-Lher	65	22	10	3
PL-42	Sp-Lher	75	16	8	1
PL-44	Sp-Lher	72	15	11	2
PL-46	Sp-Lher	78	14	9	1

2.4.3 Changle

Changle volcano of Shandong province is within the Tan-Lu fault zone. It is one of the volcanoes in the Changle-Linqu volcanic field next to the Shanwang volcano and Beiyan volcano (Zheng et al., 1998; Xiao et al., 2010). There are hundreds of such Cenozoic volcanoes in the Changle-Linqu volcanic field and basalts in this area directly overlie the Early Tertiary coal-bearing lacustrine sedimentary rocks of the Wutu Formation (Wang et al., 2003). Two major episodes of volcanism can be identified: Niushan episode (~14.5 Ma) and Yaoshan episode (~4.3 Ma). The basalts are mainly alkali olivine basalts, with olivine nephelinites and basanites in minor. Abundant and varied deep-seated xenoliths are contained in these host basalts.

The xenoliths typically range from 5 to 10 cm across. Five on six collected coarse-grained samples are spinel lherzolites, and the last is a spinel harzburgite (Fig.). The GPS position of the outcrop is N36º37’11.5’’, E118º51’59.3’’.

These xenoliths are mainly characterized by tabular equigranular and porphyroclastic texture (Fig. 2-4C-D). All samples are anhydrous peridotites. The modal mineralogy of xenoliths is given in Table 2-3.

Table 2-3. Modal mineral proportions for Changle peridotite xenoliths

Sample	Rock-Type	Olivine	Opx	Cpx	Spinel
CL-01	Sp-Lher	61	25	11	3
CL-22	Sp-Lher	68	22	9	1
CL-31	Sp-Lher	72	16	9	3
CL-32	Sp-Lher	73	16	10	1
CL-35	Sp-Harz	74	22	2	2
CL-38	Sp-Lher	72	15	11	2

2.4.4 Hebi

Hebi volcano of Henan province erupted ~4Ma ago (K-Ar age; Liu et al., 1990). Olivine nephelinites contain abundant small mantle xenoliths (1-5 cm in diameter) and garnet and pyroxene megacrysts. While Hebi xenoliths are highly refractory harzburgite and Cpx-poor lherzolite with high Mg# of olivines, minor transitional and fertile samples with relatively low Mg# of olivines also exist. The high-Mg group has been interpreted as shallow relics of the Archean cratonic mantle, and the low-Mg group as newly accreted lithosphere (Zheng et al., 2001). Further, the in-situ sulfide Re-Os isotope analysis of harzburgite xenoliths (Zheng et al., 2001, 2006), lent strength to the claim that Hebi is, so far, the only locality in the NCC with solid evidences for relicts of the Archean mantle.

In this thesis, the nine xenoliths are spinel harzburgite except two, HB64 and HB12, which is spinel lherzolite and dunite, respectively. The GPS position of the outcrop is N35º47’10.1’’, E114º12’34.7’’.

The Hebi xenoliths most show coarse textures (Fig. 2-4E-G). Modal mineralogy is given in Table 2-4. Ol and opx are large (>2mm) with straight boundaries, and while cpx and spl are irregular and smaller (1–3 mm). Cpx are rare in xenolith and are always in direct contact with large ol.

Table 2-4. Modal mineral proportions for Hebi peridotite xenoliths

Sample	Rock-Type	Olivine	Opx	Cpx	Spinel
HB-02	Sp-Harz	82	16	<0.5	1
HB-06	Sp-Harz	83	16	0	1
HB-07	Sp-Harz	79	20	0	1
HB-10	Sp-Harz	73	26	0	1
HB-12	Sp-Harz	80	18	0	2
HB-16	Sp-Harz	84	15	0	1
HB-17	Sp-Harz	78	21	0	1
HB-64	Sp-Harz	82	10	7	1

2.4.5 Qingdao

The Qingdao region, ~200km southern of Qixa, is within the Sulu orogen. There are two episodes of magmatism. In early Cretaceous (135~115 Ma) (Zhao, G.T. et al., 1998), mafic magmatism widely occurred and produced abundant mafic dikes (Yang et al. 2004; Liu et al. 2006) or bimodal volcanic rocks (Fan et al. 2001). These mafic

dikes and volcanic rocks are generally interpreted as derived from the lithospheric mantle, thus they record Late Mesozoic enrichment processes of the lithospheric mantle in terms of geochemical and isotopic compositions (Fan et al. 2001; Yang et al. 2004; Liu et al. 2006).

Late Cretaceous mafic magmatism also occurred as dikes or lava flows in the Qingdao region (Zhao, G.T. et al. 2001; Yan et al. 2003). The basaltic lava flow from the Wangshi Group of the Jiaodong region was interpreted to as resulting from the uprising asthenosphere (Yan et al. 2003). The basaltic flooding in the Wangshi Group was an important magmatism during the Late Cretaceous in the Jiaodong region, which has been dated in ca74 Ma (Yan et al. 2003).

The Late Cretaceous mafic dikes display their geochemical features completely different from those of the Early Cretaceous mafic dikes (Zhao, G.T. et al. 2001). They are enriched in large ion lithophile element (LILE) and light rare earth elements (LREE) without high field strength element (HFSE) depletion. These temporal geochemical variations reflect changes of the magma sources beneath the Qingdao region, shifting from the lithosphere to the asthenosphere.

The Pishikou mafic dike is representative of the mafic dikes in the Qingdao region. It tends NW and cuts the alkali granite of the Laoshan granite bodies. The dike is about 5–6 m wide and extends several thousand meters. Pishikou (multiple) mafic dikes are composed of the southern dike and the northern dike. The Pishikou mafic dike from the Qingdao region of Shandong Province was emplaced at 86–78 Ma. The mafic dike has geochemical features significantly different from those of the Early Cretaceous mafic dikes and basalts. Its trace element and isotopic compositions resemble those of the Japan Sea back-arc basin basalts, suggesting that the mafic dike was derived from an asthenosphere source, but contaminated by materials from the subducted Pacific slab. This discovery illustrates that the subducted Pacific slab had material contribution to the Late Cretaceous magmatism in the eastern North China craton. This material contribution obviously started since the Late Cretaceous Cretaceous (Zhang, J. et al., 2008, 2009).

The Pishikou mafic dike also contains abundant xenoliths of mantle peridotites such as spinel lherzolite and harzburgite and lower crust granulites as well as mantle xenocrysts. These xenoliths are all spinel-facies and can be subdivided into two groups: high-Mg and low-Mg types based on their distinct textural and mineralogical features. High-Mg peridotites with inequigranular textures, have high Mg# (up to

92.2) in olivines, and high Cr# (up to 55) in spinels. Cpx in the high-Mg# peridotites are characterized by LREE-enriched pattern and evolved Sr-Nd isotopic compositions. These characteristics of high-Mg peridotites sharply contrast with those of low-Mg peridotites that mimic the 'new' lithosphere derived from the convecting mantle. Because they are featured by low Mg# (< 90) in olivines and low Cr# (< 12) in spinels, and the Cpx from low-Mg# peridotites have low REE abundances (ΣREE = 12 ppm), LREE-depleted REE patterns ((La/Yb)N < 1), and depleted Sr-Nd isotopic features. Based on these observations and further reasoning, Zhang, J. et al., (2008, 2009) claimed that while high Mg# group represents fragments of the Archaean and/or Proterozoic lithospheric mantle that modified by carbonatitic and silicate melts to some extents prior to or during Mesozoic time, the low-Mg# group represent samples from newly accreted, cooled asthenospheric mantle.

Zhang et al., (2009b) reported the Li isotopes composition of these two types of peridotite xenoliths, combined with their Sr-Nd isotopes evidences, further securing their claim that while the high-Mg# harzburgites represent the refertilized Archean lithospheric mantle by melt/rock interaction, the low-Mg# lherzolites roughly represent the newly accreted lithospheric mantle.

In this thesis, just two small peridotite xenoliths (Table 2-5), preserved in that Pishikou mafic dike, were collected. The GPS position of the outcrop is N37º12'15.5'', E120º43'23.8''.

The xenoliths show granulobalstic textures with straight to smooth grain boundaries (Fig. 2-4H-I). Ol and opx are relatively large (<1.5mm), and cpx is usually less than 1 mm, showing a triple junctions with ol and opx.

Table 2- 5. Modal mineral proportions for Qingdao peridotite xenoliths

Sample	Rock-Type	Olivine	Opx	Cpx	Spinel
QDPS-16	Lherzolite	64	20	12	1
QDPS-24	Lherzolite	70	19	10	1

2.4.6 Daxizhuang

Daxizhuang country of City Jiaozhou is within Jiaolai basin, southwest of Shandong province. The Jiaolai Basin is located in the north of the Wulian-Yantai fault which is generally considered as the boundary between the NCC and the Sulu orogen. The crystalline basement of the Jiaolai Basin consisting of the Neo-Archaean

Jiaodong Group and the Palaeo-Proterozoic Jinshan Group is overlain by the Meso-Proterozoic Fenzishan Group and the Neo-Proterozoic Penglai Group. The Mesozoic and Cenozoic fault basins filled with clastic deposits and volcanic rocks are developed upon old rocks in this region. Cretaceous volcanic rocks were widely distributed in the Basin. The lower part of the volcanic sequence is the Qingshan Group consisting of intermediate to alkali K-rich lava and pyroclastic rock as well as rhyolitic lava and pyroclastic rock. The upper part is the Wangshi Group composed of basalts at the bottom and clastic deposits at the top. The Jiaozhou Formation is conformably lying on the Hongtuya Formation (the lower part of the Wangshi Group) in the Jiaolai Basin. The upper part of the Jiaozhou Formation is Cenozoic in age. The basalt containing mantle xenolith and megacryst is located in Daxizhuang Village (our study area), 2 km northeast of Jiaozhou City and covers an area of only 0.1 km2. By stratigraphic correlation, the basalt from Daxizhuang belongs to the Late Cretaceous Hongtuya Formation, and aged 73.5 Ma by further ^{40}Ar-^{39}Ar technique (Yan et al., 2003).

The Daxizhuang basalt, belonging to Wangshi group basalt, is a high-Ti alkaline basalt. On the hand specimen, the basalt is dark in color with porphyritic texture and massive structure, and consists of 8% ~15% phenocryst of olivine and a matrix made up of plagioclase and pyroxene. Geochemically, it is characterized by enrichments of LILEs and LREEs with no obvious fractionation. It also has Sr-Nd isotope compositons characteristic of the convecting mantle. Yan et al., (2005) proposed that the parental magma was a mixture of melts derived from the convecting mantle and the ‘newly’ accreted lithosphere.

The Daxizhuang basalt also contains mantle xenoliths and megacryst of most interested to us, because the Mesozoic basalts rarely cropped out in eastern China, merely appearing on the northeast margin of the NCC, compared with the dominance of felsic intrusions. Unfortunately, these basalt hardly contain any deep-suited xenoliths, with one exception in Fangcheng where the early Cretaceous (125 Ma) alkali basalt contain pyroxenenite and xenocystal including olvine and pyroxene. The xenoliths, ranging from 3 to 10 cm in size, are dominantly spine-spcies lherzolites having granular structure.

The xenoliths were collected from the Daxizhuang basalt, and among them nine peridotite xenoliths were chosen and presented in this thesis. They are all spinel lherzolites, ranging from 2 to 10 cm in diameter. Modal mineral abundances by

volume are 56-77% for olivine, 16-30% for opx, 6-19% for cpx and 1-2% for spinel (Table 2-6). Mineral grains are relatively large (> 1 mm), and olivine, opx and cpx can reach ~ 1 cm in size.

Most of olivine grains exhibit deformed texture and kink belt. The minor interstitial spinel is brown in color and often occurs as holly-leaf shape. Some cpx grains show narrow spongy rims (Fig. 2-4J-K).

Table 2-6. Modal mineral proportions for Daxizhuang peridotite xenoliths

Sample	Rock-Type	Olivine	Opx	Cpx	Spinel
DXZ-01	Sp-Lher	56	24	18	2
DXZ-02	Sp-Lher	74	17	8	1
DXZ-04	Sp-Lher	77	16	7	1
DXZ-14	Sp-Lher	72	17	10	1
DXZ-17	Sp-Lher	65	27	7	1
DXZ-27	Sp-Lher	55	29	14	2
DXZ-36	Sp-Lher	59	30	10	1
DXZ-39	Sp-Lher	64	20	15	1
DXZ-42	Sp-Lher	69	23	6	2

2.4.7 Junan

Junan volcano, occurring as breccia dike, is 20 km north of Junan County, Shandong province, and is located in the Sulu orogenic belt like the other two mantle xenoliths-bearing Mesozoic basalts. The NWW-trending dike intruded Late Mesozoic porphyritic syenite and extended up to 200 m with average width of 10 m. Whole rock K–Ar age determination on the matrix of the basaltic rocks shows that these rocks formed at Late Cretaceous (ca.67 Ma). A variety of mantle and lower crustal xenoliths and megacrysts have been found in these basaltic rocks. They are dominantly spinel or spinel-free peridotites and subordinate pyroxenites (websterites and orthopyroxenites), felsic granulites and augite xenocrysts (Ying et al., 2006, 2010).

In detail, two types of granulite xenoliths, including two-pyroxene granulite and the Garnet-bearing granulite, were found and identified. Upon comprehensive study of these crustal xenoliths, Ying et al. (2010) made the following claims: (1) The Junan granulite xenoliths are fragments of the Precambrian lower crust of the NCC, whose protolith was the assimilation–fractional crystallization product of an Archean mafic magma (2.3 Ga) that have experienced granulite-facies metamorphism during the Late

Paleoproterozoic; (2) There is consistent petrological and seismic Moho depth, and there is no underplating induced crust–mantle transition zone is absent beneath the Junan region; and (3) The lower crust extended to depth around 35 km in Late Cretaceous, compared with 40–50 km depth in Early Jurassic, implying the lower crust of NCC was significantly thinned during Late Mesozoic.

The peridotitic xenoliths are all lherzolites, no dunite and harzburgite have been found in these basaltic rocks. The peridotite xenoliths are all spinel lherzolites that can be subdivided into two types according the Mg# of their olivines: the very rare high Mg# (Fo=92.0) group and the dominantly low Mg# group (Fo<90). Upon the detailed studies of these peridotites, Ying et al. (2006) concluded that the low-Mg# group represents the fragments of the newly accreted lithosphere, whereas the high-Mg# peridotite represent a sample from the old refractory residues of the Archean/Proterozoic lithosphere.

In our collections, all ten xenoliths are rounded spinel-lherzolites from 2 to 6 cm in size with various degrees of alteration. The modal mineralogy of these xenoliths is highly variable, ranging from 53 to 79% for olivine, from 5 to 25% for opx, from 8 to 25% for cpx and between 1 and 2 for spinel (Table 2-7). The lherzolites display equilibrated texture with triple junctions and curved grain boundaries (Fig. 2-4L).

Table 2-7. Modal mineral proportions for Junan peridotite xenoliths

Sample	Rock-Type	Olivine	Opx	Cpx	Spinel
JN-03	Sp-Lher	53	28	17	2
JN-11	Sp-Lher	74	6	19	1
JN-24	Sp-Lher	73	12	15	2
JN-26	Sp-Lher	65	10	23	2
JN-35	Sp-Lher	71	16	11	2
JN-43	Sp-Lher	77	8	14	1
JN-44	Sp-Lher	65	23	9	3
JN-47	Sp-Lher	64	10	25	1
JN-53	Sp-Lher	79	12	8	1
JN-65	Sp-Lher	75	14	10	1

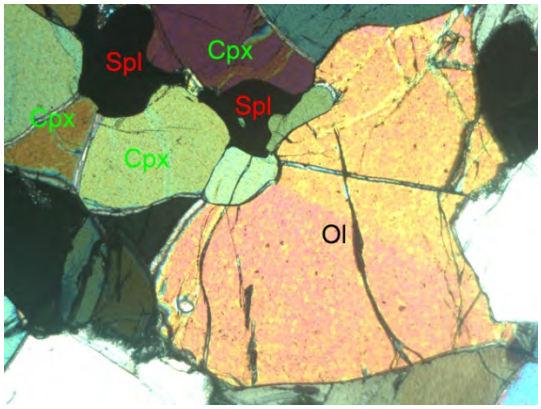
Spl
Cpx
Cpx
Spl
Cpx
Ol

A

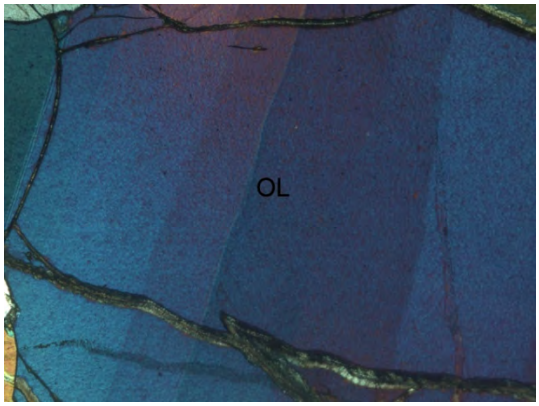
OL

B

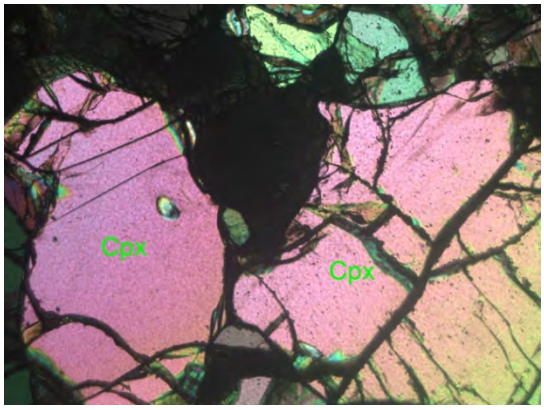
Cpx
Cpx

C

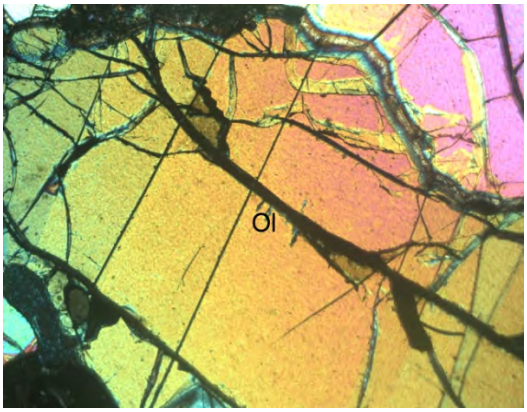
Ol

D

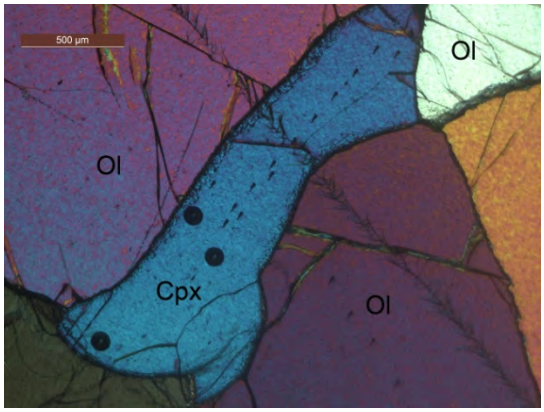
500 µm
Ol
Ol
Cpx
Ol

E

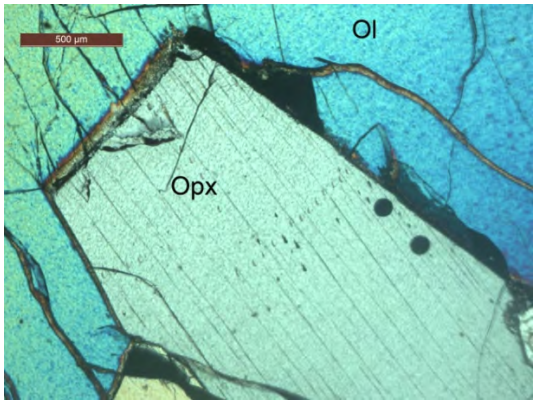
500 µm
Ol
Opx

F

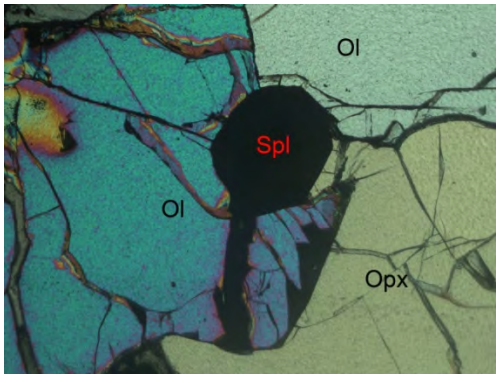
Ol
Spl
Ol
Opx

G

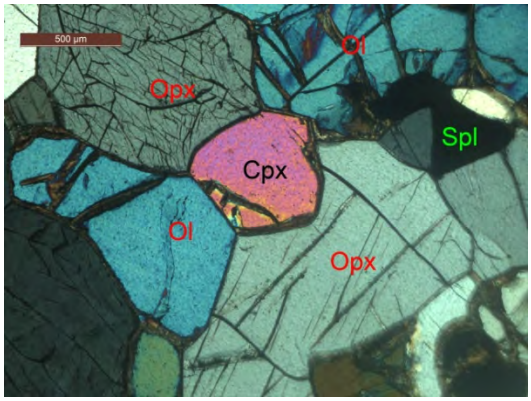

H

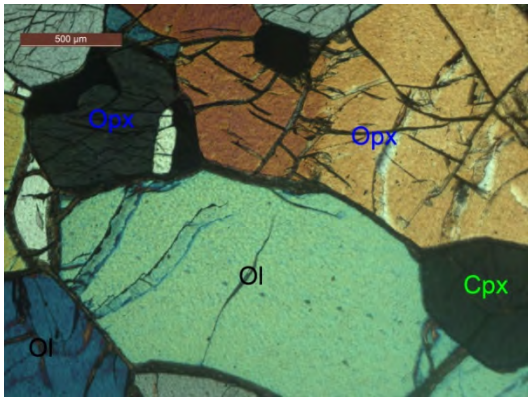

I

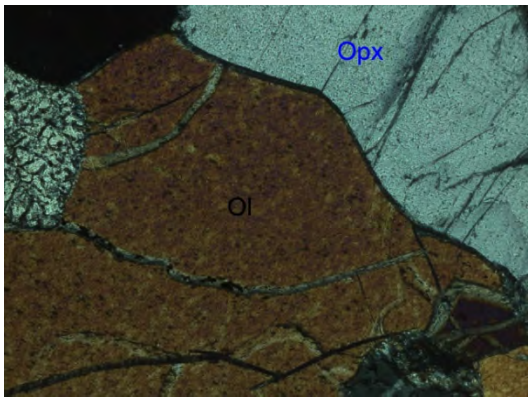

J

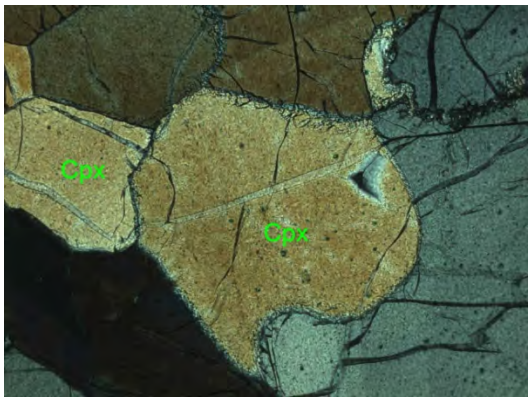

K

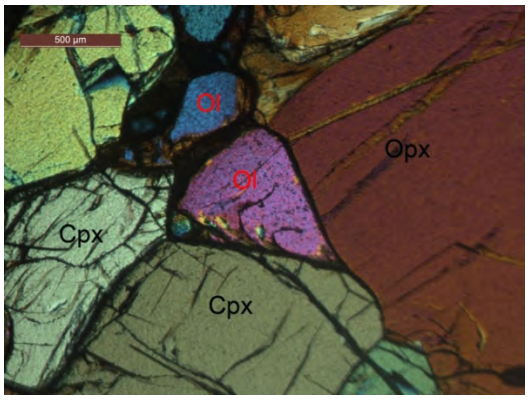

L

Figure 2-4. Photomicrographs of representative textures of the studied peridotite xenoliths: **A** and **B,** textures of QX01 in crossed light, and kink band of olivine in **B**; **C** and **D**, textures of CL35 in crossed light; **E**, **F** and **G**, textures of HB01 in crossed light. Narrow spongy rims of cpx and opx in **E** and **F**; **H** and **I**, textures of QDPS16 in crossed ligh; **G** and **K**, textures of DXZ04 in crossed and plane light, respectively. the spongy rim of cpx in **K**; **L,** textures of JN53 in crossed light.

3 Analytical methods

3.1 Electron microprobe (EMP)

Major element compositions of main mineral phases in mantle peridotite xenoliths, i.e., olivine, pyroxene and spinel, were determined by a JEOL JXA-8100 superprobe at Nanjing University, China. Operating conditions were as follows: 15 kV accelerating voltage, 10 nA beam current and <5 μm beam diameter. Natural minerals and synthetic oxides were used as standards, and a program based on the ZAF procedure was used for data correction. Multi-point measurements were carried out from the core to the rim region of each mineral grain, and 3-4 grains of each mineral were measured in every sample.

Supplementary analyses were conducted for another three samples from Hebi on a Cameca SX100 EMP at University Henri Poincare, Nancy, France. The experimental conditions were similar to that at Nanjing University: 15 kV accelerating voltage,10 nA beam current, <5 mm beam size, natural minerals and synthetic oxides as standards. The methods, however, used for raw data correction, were different: it is a program based on PAP procedure (Pouchou and Pichoir, 1985) for the Cameca 100 EMP, and on ZAF procedure (in reference to the three factors of matrix effects: atomic number (Z), absorption (A) and fluorescence (F)) for the JEOL JXA-8100 EMP.

It is noted that here all the sample for EMP analysis are mounted on the form of thin section with the thickness of ~0.03mm, and subsequent SIMS analyses for Li were conduct on the same mineral grains with the same thin section mounts.

3.2 LA-ICP-MS

Trace element compositions of Cpx and a few Opx were carried out at LA-ICP-

MS laboratory of University of Science and Technology of China. FTIR thin sections (double polished mineral grains with thickness ~0.2mm) were broken, and cloudy and crack-free minerals grains were selected to mount in epoxy pellet, and then polished, washed and dried. Mineral grains were ablated in situ with a Coherent company GeoLas pro ArF laser system, with a beam wavelength of 193nm at 10 Hz repetition rate and 10 J/cm^2 energy per plus. The ablation crater diameters are 60 μm, or 90 μm when the grains it big enough. The sample aerosol was carried to ICPMS by high purity Helium with flow rate of 0.3 l/min. A typical analysis consists of 80-100 replicates within 80-100s. PerkinElmer DRCII ICPMS was used to analysis the aerosol samples with the RF power 1350w and nebulized gas flow rate 0.7L/min. Sample analysis results processed with LaTEcalc software. The signal intensities (counts per ppm) for each element were calibrated against the NIST 610 silicate glass and the ^{44}Ca content of samples was used as an internal standard. Typical analytical precision ranges from 2% to 5%.

3.3 Fourier transform infrared spectroscopy (FTIR)

This trace “water” in these stoichiometrically anhydrous minerals have posed a challenge to the accurate determinations due to their low concentrations, usually ranging between few tens ppm to hundreds ppm. Although there are several methods to obtain contents of water, the FTIR proves the most sensitive and convenient method for detecting water in NAMs. In addition, it does not only probe the concentration, but also the structure of hydrous species in a mineral. But it also has its

own disadvantages as many other methods. The FTIR is not intrinsically quantitative but requires calibration by independent analytical methods, such as SIMS, Thermogravimetric analysis (TGA), Nuclear magnetic resonance (NMR) and the likes. This shortcoming, however, does not prevent FTIR from being the most popular method to qualify the trace "hydrogen" in minerals.

3.3.1 Water content in NAMs measured by FTIR

Double-polished thin sections with a thickness of about 0.2 mm were prepared for the FTIR investigation (resin was used during the polishing treatment). The cleaning procedure of the sections prior to measurements included 10 to 20 hours dissolution in ethanol or acetone to remove the residual epoxy, followed by heating in an oven at ~ 100 °C for 3 to 10 hours to remove the surface absorbed water. Infrared spectra were obtained at wavelengths from 650 to 6000 cm-1 using a Nicolet 5700 FTIR spectrometer (Fig. 3-1), coupled with a Continuμm microscope at the School of Earth and Space Sciences, University of Science and Technology of China (USTC) in Hefei. The principal advantages of such treatment are that: First, it is easy to observe the sample spot and to check the quality optically before the measurements; second, the liquid-N2 cooled detector placed over the microscope is optimized for a focused beam; Third, the focused IR beam yields higher intensities than a measurement in the sample chamber of the spectrometer. The samples were measured by unpolarized radiation with an IR light source, KBr beam-splitter and liquid-nitrogen cooled MCT-A detector. A total of 128 or 256 scans were counted for each spectrum at a 4 cm-1 or 8 cm-1 resolution. Optically clean, inclusion- and crack-free areas, usually centered in the core region of each grain, were selected for the measurements with apertures of 30×30 or 50×50 μm, depending critically on the size and quality of the mineral grains. Large and fresh grains were selected for the H-profile analysis.

Quantitatively accurate measurement for the content of hydrogen species in anisotropic minerals requires the preparation of oriented single crystals along (1) three crystallographic axes, (2) three random, but orthogonal sections of a crystal, or (3) two orthogonal sections oriented parallel to each of the two axes of the indicatrix ellipsoid and the using of polarized IR radiation (Libowitzky and Rossman, 1996). Such preparations of the samples, however, are always time consuming and difficult in many petrological situations, and sometimes it even seems impossible. In this case,

we instead measure a statistically significant number of individual grains, at least 20, for each mineral in the same sample using the unpolarized light, and their average absorbance is used to derive the water content. The unpolarized measurement of random mineral grains proves an accurate measurement of hydrogen-species in anisotropic minerals, secured by the theory developed by Sambridge et al. (2008) and the following supports from experiment work on natural minerals by Kovács (2008). The basic theory of light propagation in crystal and those developed by Sambridge will be detailed in the following section 3.3.2.1.

The unpolarized measurements were performed on a statistically significant number of individual grains for each mineral in the same sample. Assuming that crystal orientation is randomly distributed between individual grains, (as evidenced by the variability in our FTIR results) so an average value was used. Water contents were calculated by the modified form of Beer-Lambert Law: $\Delta=I\times c\times t$. where Δ is the integral absorption area (cm^{-1}) of absorption bands, I is the integral specific absorption coefficient ($ppm^{-1}\bullet cm^{-2}$), c are the contents of hydrogen species (ppm H_2O), t is the thickness of the section (cm). In this thesis, the integral region was set mostly in the range of 3000 to 3750 cm^{-1}, although it could be down to ca. 2800 cm^{-1} for some opx spectra. The mineral specific calibration coefficient used in the calculation is 7.09 $ppm^{-1}.cm^{-2}$ for cpx, 14.84 $ppm^{-1}.cm^{-2}$ for opx from Bell et al. (1995). The thickness was measured using a digital micrometer and reported as the average of 20-40 measurements covering the whole thin section. Baseline corrections for the obtained IR spectra were conduct with a linear fit method provided by OMNIC software.

The uncertainties in the obtained results derive from: (1) Unpolarized light. This was once considered the main uncertainty during the analysis but it is now estimated to be mostly less than 5% according to the theory developed by Sambridge et al. (2008). (2) Baseline correction. Some strongly rising, non-linear baselines may be an intrinsic part of the spectrum in the OH region. These baselines commonly arise from Fe^{2+} and may arise from silicate overtones in thick samples. A major, subjective source of uncertainty in IR measurements of OH in minerals remains the choice of baseline. Error introduced by different baseline corrections, e.g. spline-fit, polynomial-fit or slightly changing the points during the fitting is usually < 5%. (3) Variation of thin sections thickness. This was less than 5% centered on the average value for each sample. (4) Absorption coefficients. There are slight differences

between absorption coefficients in cpx and opx in our samples and those used to determine the mineral specific absorption coefficients (Bell et al., 1995), due to their different compositions and densities. These variations are estimated to be generally < 10%. On the whole, the total uncertainty, summing each single error, is estimated < 30%. Detailed FTIR profile analyses performed at the USTC lab show that the two augite megacrysts hosted by Nushan Cenozoic basanites are homogeneous in term of water content. These two megacrysts then serve as standards to monitor potential instrument shift during analysis. During the analytical period of the NCC samples, the maximum difference for two augites is less than 4% for the integrated areas within OH absorption bands (Fig. 3-2). The megacrysts were also analyzed at the lab of the LMTG. The maximum difference of peak height and integrated area within OH absorption area between the USTC lab and the LMTG lab (Toulouse, France) is <3% during cross-check analysis.

Figure 3-1. Picture of the Nicolet 5700 FTIR spectrometer coupled with a microscope located at USTC

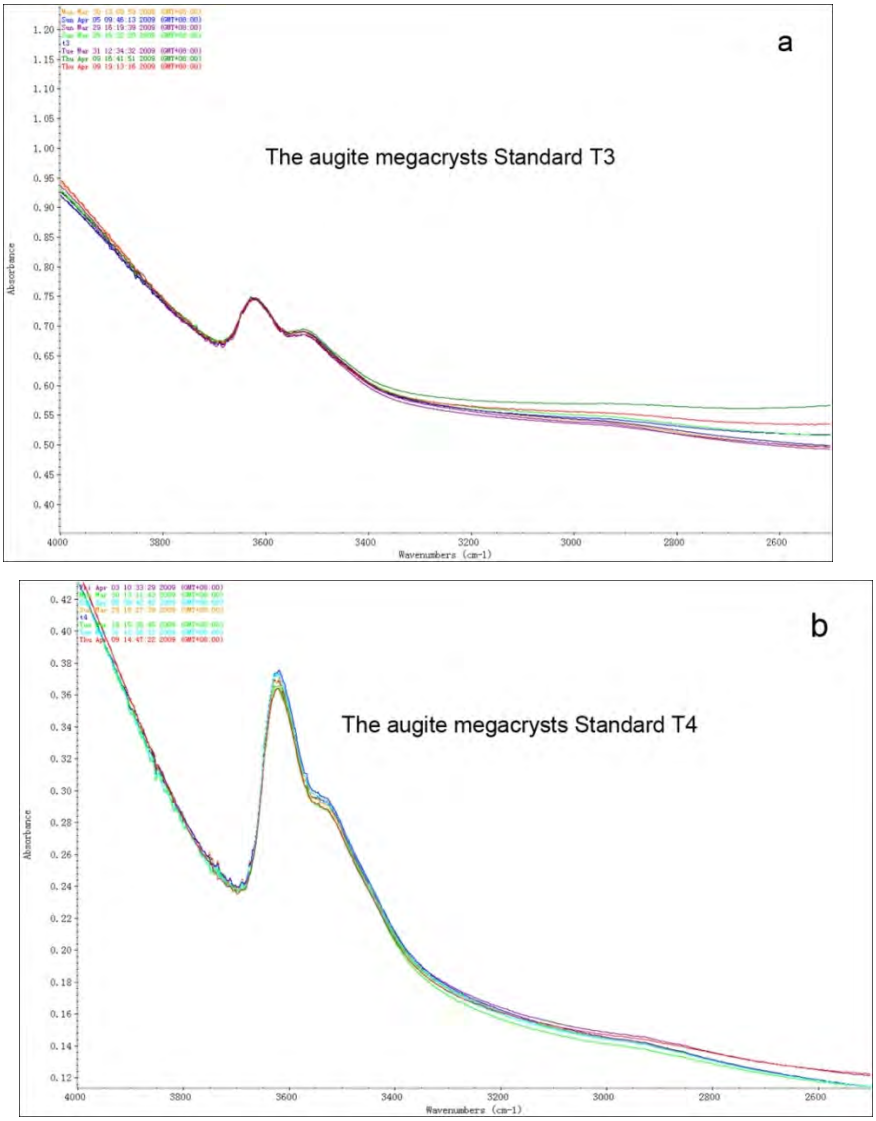

Figure 3-2. The instrument shift during analysis monitored by two augite megacrysts standard T3 in **a** and T4 in **b**. The difference in shift of the integral areas over the absorption bands is less 4% in **a**, and less 3% in **b**.

3.3.2 The theoretical background for quantitative analysis

3.3.2.1 The common quantitative methods by FTIR

It has long been claimed that, in general, only polarized light that parallels to the principal optical axes can be used to recover the total absorbance for quantitative analysis of OH defects in anisotropic crystals, and the Beer-Lambert law on which we rely to calculate the concentration of the absorber (here is O-H of interest) is valid only for isotropic crystals and for the absorbance measured along the principal optical

directions in anisotropic crystals. The use of unpolarized light, apparently, cannot theoretically yield quantitative data (Libowitzky and Rossman 1996; Bell et al. 2003, 2004).

Those claims are based on the following theories and observations. According to the classic optical indicatrix theory which is well known to us as the cornerstone for describing the optical properties of crystals and allowing calculation of refractive indices for light propagating through anisotropic media, the incident light, whatever polarized or not, will first splits up into two linearly polarized light waves at surface when entering an anisotropic crystal without following the optical axis by accident. Then the two split light continue to propagate through the crystal and at last combine again when leaving the crystal. For simplifying question, assuming a linearly polarized light enters an anisotropic crystal (except following the optical axis direction again), it will split into two perpendicularly polarized waves, and intensities of which can be given by the following formulas

$$I_{max} = I_0 \bullet \cos^2\phi, \quad I_{min} = I_0 \bullet \sin^2\phi \qquad (1)$$

The formulas can be also rewritten in term of transmittance, then:

$$T(\phi) = T_{max} \bullet \cos^2\phi + T_{min} \bullet \sin^2\phi \qquad (2)$$

Here, ‘max’ and ‘min’ represent respective maximum and minimum value of absorbance along the ‘principal directions’ that parallel to the axis of the elliptic indicatrix section. And this elliptic indicatrix section is defined by the intersection of the plane perpendicular to the incident light with the indicatrix ellipsoid. This implies that in most cases we cannot align the **E**-vector within a crystal parallel to the absorber thanks to the birefringence of crystal optics, and then the measured absorbance, either using polarized or unpolarized incident light, is combination of the absorbance of two split waves. These claims are consistent with the experiment work.

Stern et al. (1982) prepared the calcite crystal sections that were well oriented and polished, and acquired the spectra with linearly polarized light at different rotation angles. This is what we know as angular absorbance method. The angular absorbance figures in that experiment can be fitted by the following formula:

$$A(\phi) = -\log(T_{max} \bullet \cos^2\phi + T_{min} \bullet \sin^2\phi) \qquad (3)$$

It is easily found that equation (2) and (3) are actually the same, just with different forms of expression. So it is also easy to unveil the relation between the unpolarized and polarized spectra, assisted by the following two equations:

(4)

] (5)

$$A(\phi) = A_{min}\sin^2 \phi + A_{max}\cos^2 \phi \quad (6)$$

Apparently, the integral equation (2) has no numerical solution, and equation (4) can be derived on the assumption that the value of T is close to 1, implying that the absorbance is very small and close to 0. The condition is easily can be met in practice by making the section thin enough (~0.2mm in our analysis for determining OH).

At last, Libowitzky (1996) advanced two ways by which accurate measurement of the concentration of the absorber in anisotropic crystals can be obtained using polarized light. (1) On three random, but orthogonal sections of a crystal, or (2) preferably on two orthogonal sections oriented parallel to each of two axes if the indicatrix ellipsoid.

Such preparations of the samples are always time consuming and difficult in many petrological situations, and sometimes it even seems impossible. For example, the paucity of suitable grains in high-pressure experimental run products and some mantle xenoliths has prevented quantification of OH by these conventional infrared techniques. In an attempt to overcome these problems, Asimow et al. (2006) invented a method using polarized IR-spectroscopy on randomly oriented crystals, but information on the orientation of the analyzed grains is still needed. Furthermore, the quality of the polarizer also affects the measured polarized absorbance, which may introduce systematic errors if a different instrument is used from that on which the calibration was obtained (Libowitkzy and Rossman 1996). Clearly, the most general and straightforward approach to determine OH contents in minerals would be to use unpolarized IR spectroscopy on randomly oriented grains. Such an approach has been dismissed in the past because it was argued that unpolarized absorbance is not linearly proportional to the thickness (Libowitzky and Rossman 1996). Moreover, no self-consistent absorbance theory was available to relate unpolarized measurements to calibrations obtained from polarized spectra, nor to describe quantitatively the dependence of unpolarized absorbance on orientation. So the theoretical support for guiding unpolarized measurements is urgently needed.

Maxwell's electromagnetic (EM) theory of light is the most basic theory about light. Optical indicatrix theory, used for calculation of refractive indices for light

propagating through anisotropic media, is derived from that theory. It is used to analyze measurements of absorbance of electromagnetic radiation in anisotropic minerals, including the important applications of infrared (IR) spectroscopy in quantifying water content of minerals like olivine and pyroxenes. Theoretically, optical indicatrix theory is valid only for non-absorbing anisotropic crystals. But the solution of Maxwell's equations for light propagation in media, like the above case of OH absorbing in olivine and pyroxene crystals, where both refractive index and absorption vary anisotropically, has been largely neglected by modern researchers. Instead they have relied upon empirical evidence to determine relationships between different parameters, such as the angular dependence of absorbance, or transmittance on crystallographic orientation of polarized light in biaxial minerals. Consequently, there has been debate on the appropriate form of this relationship with several alternatives suggested (see Libowitzky and Rossman 1996).

Sambridge et al. (2008) re-examine the early work on theory of light propagation through returning to the fundamental theory based on solutions to Maxwell's equations, and delivered a new theory about the light propagation in anisotropic weak-absorbing crystals. This theory predicts the distribution of transmittance and absorbance as a function of direction and polarization angle of incident light. It confirms that a previously deduced empirical expression, like the equations above, is a good approximation to the full theory under a wide range of conditions. The theory also shows that principal polarized absorbances correspond to the eigenvalues of an absorbance ellipsoid, not a simple indicatrix ellipsoid that was once usually assumed. The final result can be expressed as follow:

$$A_{\mathrm{unpol}}(\phi,\psi) = \tfrac{1}{2}[A_a(\cos^2\phi\cos^2\psi + \sin^2\psi)+A_b(\cos^2\phi\sin^2\psi+\cos^2\psi)+A_c\sin^2\phi] \quad (7)$$

Where A_{unpol} (ϕ,ψ) represents the absorbances of unpolarized incident light with such direction in an anisotropic crystal, and A_a, A_b, and A_c are the principal polarized absorbances .

Clearly, integration of this equation over all incident angles will lead to a simple relation between total measured unpolarized absorbance and the three principal polarized absorbances. It can be concluded that the average value of measured unpolarized absorbances will be roughly equated with that of three principal polarized absorbances if there are enough unpolarized measurements.

3.3.2.2 The new theoretical background for unpolarized analysis

Light propagation in non-absorbing anisotropic crystals

Let's begin with the case of light propagation in non-absorbing crystals with anisotropic refractive index, before dealing with the more general case. In short, Maxwell's equations tell us that the optical properties of a medium are determined by the relation between the displacement vector **D** and the electric vector **E** of the propagating electromagnetic wave. An anisotropic medium corresponds to the case where three components of **D** and **E** are linearly related through

$$\mathbf{D} = [\varepsilon]\,\mathbf{E}$$

where [ε] is the dielectric tensor. Since **D** and **E** are 3 component vectors [ε] is in general a 3 × 3 matrix (second-rank tensor) and Equation 1 represents a 3 × 3 system of equations. The general theory leads to the conclusion that given any direction of the wave normal two waves can be propagated with their vibrations linearly polarized along the principal axes of the elliptic section on the index ellipsoid. The plane perpendicular to an arbitrary incident light direction cuts the index ellipsoid and creates a cross-sectional ellipse. The principal axes of that ellipse define the electric

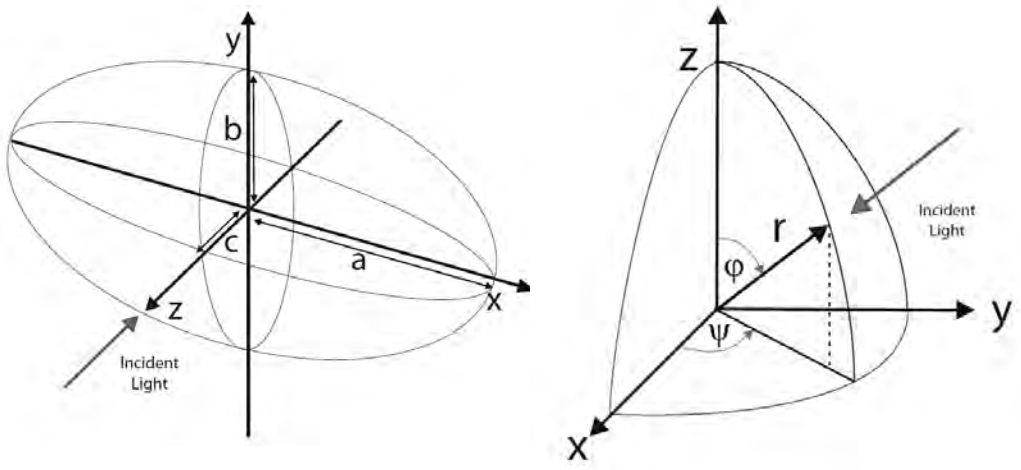

vector directions of the two propaga sible in the crystal (Fig. general each wave propagates along different paths in crystal, a phenomenon known as birefringence.

Figure 3-3. (a) Perspective view of an indicatrix ellipsoid with incident light propagating toward the center along the **z**-axis. Here the semi axes of the ellipsoid are *a*, *b*, and *c*, in the **x**, **y**, and **z** directions, respectively. (**b**) Radius of an ellipsoid, *r*, at an arbitrary point on its surface defined by the angles φ and ψ. Here φ is the angle between the radial and the *z* axis, and ψ is the angle between the x-axis and the projection of *r* on the *x-y* plane. These are the

standard spherical polar angles.

Light propagation in absorbing anisotropic crystals

The theory of light propagation in absorbing anisotropic media is described in detail by Pancharatnam (1955) and extended by RR and Born and Wolf (1980). The above summary of light propagation in non-absorbing anisotropic media provides the setting for an extension to absorbing media. Compared with the case of non-absorbing anisotropic crystals, the absorption coefficient *k,* combined with the parameter z of traveling distance (eg., the thickness of crystal), is needed to describe light propagation in an absorbing medium.

Moreover, unlike the non-absorbing case where incident light splits up into two linearly polarized light waves that propagate through an anisotropic crystal, Pancharatnam (1955) showed that when the principal axes of the index and absorption ellipsoids do not coincide, then the solution to Maxwell's equations permits two elliptically polarized waves to propagate without distortion through the crystal (Fig. 3-4). It is noted that linear polarization is a special case of the most general form of elliptical polarization with the eccentricity of the ellipse tending to zero. In general, any type of incident light in any direction will be split entering the crystal. Each will propagate through the crystal with its own refractive indices and absorption coefficients. At the exit surface the two beams will combine. It is the intensity of the combined (output) light beam and how it depends on the polarization angle of incident linearly polarized light are our most concern and interest.

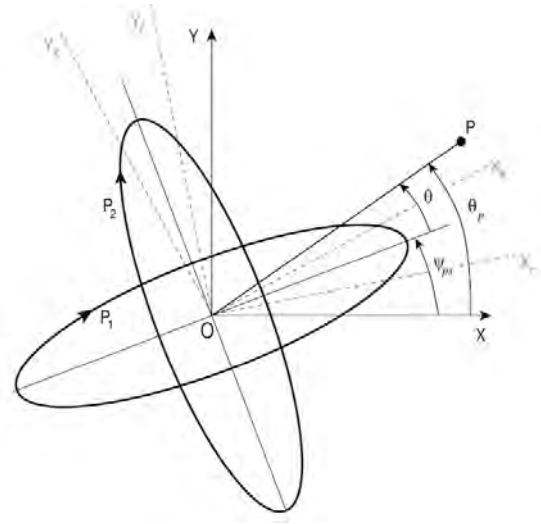

Figure 3-4 Shows the paths traced out by the E-vector of two elliptically polarized waves, P1 and P2. Only these two waves can propagate undistorted through a birefringent absorbing crystal. Incident light will be split into these components before traversing the crystal. While *OX* and *OY* are arbitrary reference axes, *OXr-OYr and OXk* and *OYk* are the principal axes of the index ellipse and the absorbance ellipse, respectively. The elliptical polarizations are defined by two angles (φps,ψps). The first is the eccentricity of the ellipse (it is not shown here but on the Poincaré sphere), and the second is the angle between the semi-major axis and the x-axis. P represents incident linearly polarized light with angle θps.

Before the more general equation can be derived, many intermedit processes are

ommited for volume concerns here. To whom it may interest, you are strongly recommended to view the original paper by Malcolm Sambridge (2008) in which the Poincaré sphere (Fig. 3-4) was introduced to represent the geometry of any type of polarized light (elliptical, circular, or linear), and further to calculate the transmission of the incident light after passing through the crystal.

(9)

Where and I is the intensity of incident light beam before entering and after leaving a absorbing crystal, respectivey; and are the absorption coefficients of the two spilt waves in crystal, and z is the distance through which the waves propagate; while is the phase difference between the two split waves, , a phase delay between the faster and slower waves, depends on the light derection and the cross sections of the index and absorption ellipsoids; measures the polarization of the incident light (Fig. 3-3). And at last, is eccentricity of the ellipse formed by rotation of the E-vevtor.

Clearly, the general equation shows how the total transmission of incident light varies with the incident polarization angle for an arbitrary direction of light through a birefringent absorbing crystal. But this formula is still too complex for the general public to be applied, and a possible simplified version is needed. And the equation indeed can be simplified when is zero on the following considerations and reasoning. In crystals with orthorhombic or higher order symmetry, the principal axes of index and absorption are aligned, indicating that the two split waves is linearly polarized (i.e.,) through travelling in a crystal. Moreover, it is shown by RR (section 4) that even in the most general case of biaxial crystals for most directions of incident light the properties of the transmitted beam can be determined by considering them as orthogonal linearly polarized waves. Specifically if the incident light is exactly along the optic axis then we have linearly polarized waves along the principal axes of absorbance, and if the incident light is appreciably inclined to both we have linear polarization along the principal axes of refraction in the cross sectional plane. These considerations each suggest the simplification $\phi ps = 0$, so that Equation (9) becomes

(10)

And this can be rewritten in the other form that is more familiar to us.

, where (11)

This expression is commonly cited in the literature (i.e., Equation (2)) as an empirically determined relation between transmittance and polarization angle when the incident light direction is along a principal direction of the index ellipsoid (e.g., Libowitzky and Rossman 1996). The theoretical development here provides a proof of the relationship for arbitrary incident light direction in crystals with orthorhombic symmetry or higher, which is also appropriate for most directions in monoclinic or triclinic crystals. It should be emphasized that all equations and derivations presented or not above are based on the assumption of weak absorption. The demand is easily met when transparent and thin petrographic sections are well prepared. To continue developing the equation (11), we can get the equation (3) and its approximation (4) that were mentioned before.

$$A() = -\log(T_{max}\cos^2 + T_{min}\sin^2) \qquad (3)$$

$$A() = A_{min}\sin^2 + A_{max}\cos^2 \qquad (4)$$

Further, Equation (4) can be described by 3D absorbance ellipsoid as Equation (7)
Then we integrate it, and obtain:

(12)

In words, the sum of the principal absorbances of the sample is as three times as the average of many measured unpolarized absorbances. This is also where does γ, the orientation factor in Beer-Lambert Law, originally come from.

In addition, integration of Equation (7) can hint at some implications for guiding our accurate unpolarized analyses in practice. If values of polarized absorbances along three principal axis is following the order of , the values of unpolarized measurements can only vary gently between , the minimum and , the maximum, but not so dramatically as those of polarized absorbances along principal axis (from to). The unpolarized absorbance is just the average of the extreme polarized absorbances defined by the inclined ellipse.

The implications from the basic theory

In the case of quantitative measurements of OH in NAMs (i.e., olivine and pyroxene) in our own analyses, the unpolarized spectra of pyroxene show that the

integrated absorbance gently varies with the random orientations of grains by no more than five times, consistent with the work done to Pakstani olivine by Kovács (2008). Both observations have confirmed the above theory that the unpolarized measurement serves to conceal extremity of polarized measurement.

But in some case where some mineral grains have abnormal absorption bands with high unpolarized absorbance (much more than five times) compared with the rest of others. Now more cautions are needed to deal with those grains. We need to re-examine the clarity of the grains to exclude any "clouds" or fissures on the beam area, because it cannot be explained by anisotropic absorption caused by special orientation of crystal given the averaging of unpolarized light. These dirty may contain some fluid inclusions and secondary hydrous minerals, both of which contribute much to the O-H absorption. If the shapes and positions of absorption bands is as usual, there is maybe another possibility that the abnormally high absorbance is likely reflect the heterogeneity of water contents among individual grains rather than the introduction of "exotic" water components, and that heterogeneity is in part cause by water loss in different mineral grains. It need more work to figure out which cause works.

3.4 Secondary ion mass spectrometry (SIMS)

The in situ measurements of Li contents and Li isotopic compositions by Cameca 1270 on the mantle olivine and pyroxene grains were performed at the CRPG, Nancy (Fig. 3-5). All these measurements were conducted on the same thin sections that were once used for EMPA. The procedure for preparing the samples: the removal of thin carbon film from the sections used for EMPA with diamond paste was followed by cleaning with ultrasonic washing of 20 min for three times. Then it was put into

the oven under 45 degrees for one hour. At last it was coasted with gold film and loaded in the mount for analysis.

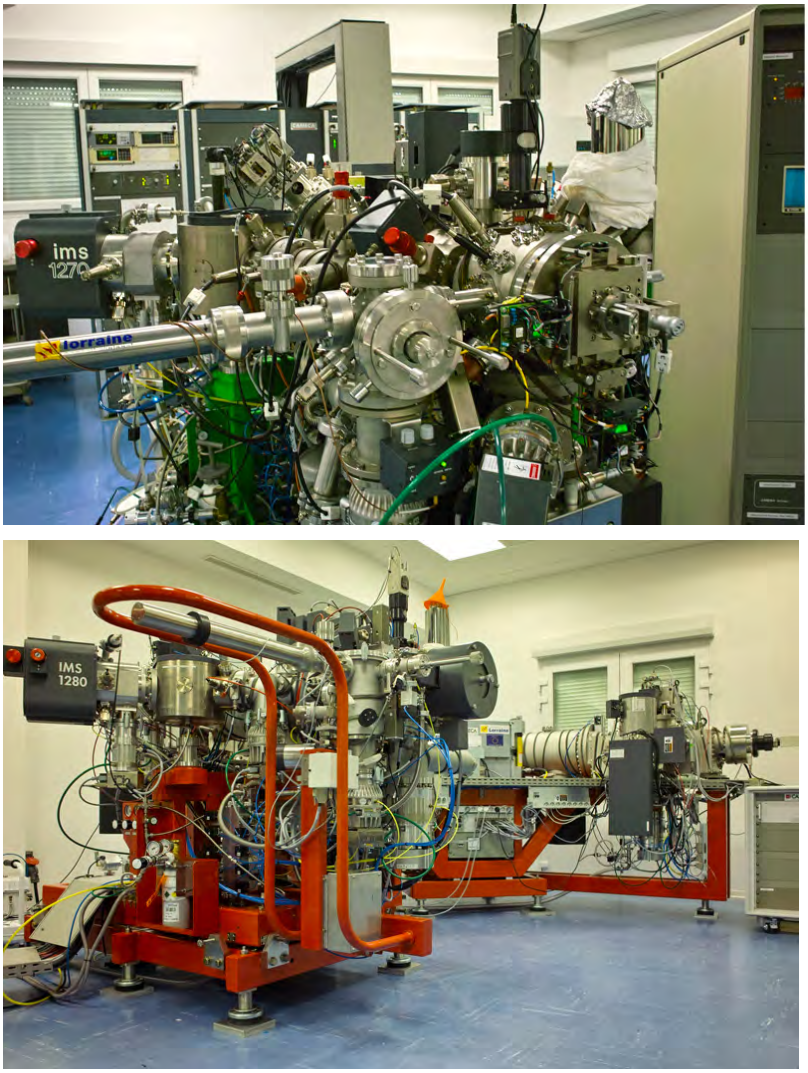

Figure 3-5. Pictures for the Cameca IMS 1270 (above) and the new-arriving 1280HR2 (below), both located at CRPG, Nancy.

3.4.1 Rationale and instrumentation

During ion probe analysis, the sample surface is bombarded with a beam of focused high-energy ions. The impact of each ion displaces atoms in the sample, creating a "collision cascade" which causes surface atoms that receive more than their binding energy to be ejected, or sputtered. While many of the matrix atoms are sputtered as neutral particles, some are ejected as ions which can be accelerated by an electrostatic field for mass spectrometric analysis. In its simplest form the ion microprobe (Fig. 3-6) consists of a source of primary (bombarding) ions, an ion optical column that generates a finely focused primary ion beam, an extraction system which transfers the secondary ions from the surface of the sample to the entrance slit

of the mass spectrometer and the mass spectrometer itself. Depending on the polarity of the secondary ion accelerating voltage, either positive or negative ions can be extracted. Not only are ions of individual elements produced, but also ionized molecular combinations of elements present in the matrix. These “molecular” ions can consist of two, three or more atoms, forming clusters that survive long enough to travel from source to detector. There is a high probability that in chemically complex minerals, the intensity measured at any given mass will include a contribution from molecular, as well as elemental, ions. However, there are often small differences in mass, owing to the “mass defect” of the atoms concerned, which can be used to separate atomic from molecular ions. The frequent necessity of separating elemental from molecular species on this basis dictates that secondary ion mass spectrometers used for geological research should have high mass resolution and they are almost exclusively of the magnetic sector type.

High mass resolution is achieved with a ‘double focusing’ mass spectrometer, which combines an electrostatic filter with a magnet sector. The secondary ions are dispersed according to their velocity in the electrostatic sector and then focused according to their velocity in the electrostatic sector and then focused according to their momentum by the magnetic sector (in some instruments the magnet precedes the electrostatic sector). The mass resolving power is increased by decreasing the width of the entrance and exit slits and by restricting the transmission of the higher energy component of the secondary ion beam. However, there is a simultaneous decrease in the transmission of ions through the mass spectrometer.

For ion microprobes with small magnets, secondary ion transmission diminishes rapidly when the mass resolution exceeds 1000, in contrast with the largest instruments where no intensity loss until the mass resolution exceeds 5000. There are a number of ways by which the transmission of the mass spectrometer may be increased. If its physical size is increased, the slit width of a given mass resolution will be greater, allowing more secondary ions to enter. Increasing the extraction voltage reduces the initial angular spread of the secondary ions sputtered from the sample surface; the energy spread is then a smaller proportion of the total ion energy. This leads to greater transmission for the same mass resolution, but there are practical limits on the size of the extraction voltage which can be applied.

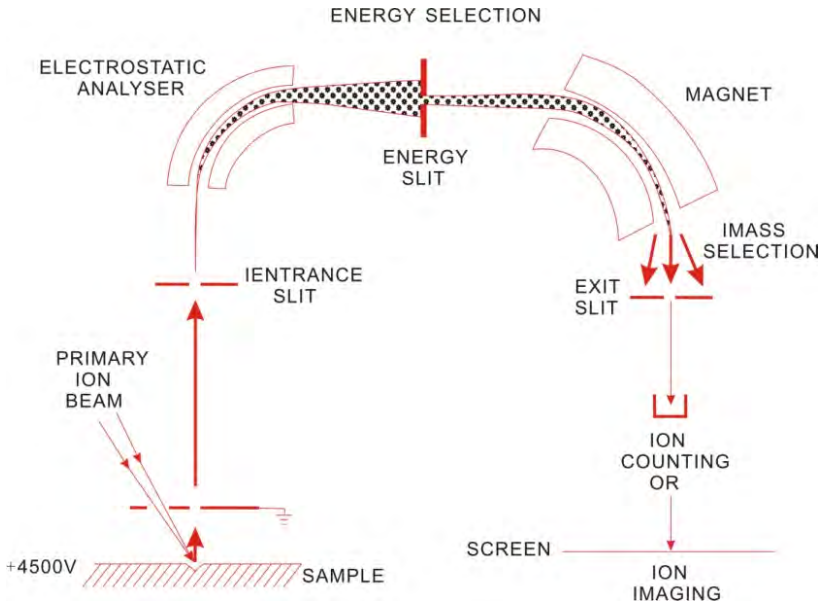

Figure 3-6. Diagrammatic representation of ion micropobe

3.4.2 The analytical Setting for measurements

Lithium concentrations and isotopic compositions of major mineral phases in peridotite xenoliths were measured on gold-coated thin sections using Cameca IMS 1270 ion microprobe at Nancy, following the procedure developed by Chaussidon and Robert (Chaussidon et al., 1998). A 13 kV, 8-10 nA O- primary beam was focused on an area of 10-25 mm in diameter on the sample surface. Positive secondary ions accelerated through 10 kV were analyzed at a mass resolution of ~ 1200 with an energy offset of 80 ± 20 eV for content determination, and at high mass resolution of ~ 2192 without energy offset for isotopic determination. Secondary ions were counted with an electron multiplier in pulse counting mode. The lithium contents and isotopic compositions were determined in different sessions and using different settings so that they do not correspond to the same sputtered spots. But they are close enough to be treated as the same area. For each mineral grains, two (for small grains) to a few tens (for relatively large grains) of points between the rim and the core were analyzed for abundances and isotopic ratios, for which depth profiles were constructed respectively.

For Li-content analyses, counting times were 4 s for ^{6}Li; 8 s for ^{7}Li; 2 s for ^{29}Si and 2 s for ^{30}Si over 20 cycles (the counting for ^{6}Li and ^{29}Si were introduced for the sake of stabilizing the pulse of magnet). The measured ^{7}Li/^{30}Si ratios were corrected for the relative useful yields of Li and Si determined on five standards from Zabargad

peridotites, Red sea (olivine BZ29, opx BZ226 and cpx BZCG and BZ226, Decitre et al. 2002) in the same analytical session. These standard minerals show the similar chemical compositions to our target samples. The relative analytical precision, including counting statistics and reproducibility, ranges from ~ 1 to 5%. In order to obtain Li-isotopic data, 24-30 cycles were accumulated with counting time of 2s for mass on 6.5 (background monitor), 20 s for ^{6}Li and 5 s for ^{7}Li. The ion intensities on ^{7}Li peak range from 10000 to 600000 cps, depending on the sample Li content and the intensity of the primary beam. Olivine BZ29, cpx BZ226 and BZCG, and opx BZ226 (Decitre et al. 2002) were used as standards for the calibration of the raw data. The yielded results are given in the traditional δ-notation ($\delta = (R_1/R_2\text{-}1) \times 1000$, where R_1 and R_2 are the ^{7}Li/^{6}Li ratios in the sample and standard, respectively) in per mil unit relative to L-SVEC (^{7}Li/^{6}Li$_{LSVEC}$ = 12.0191; Flesch et al., 1973). The instrumental mass fractionation is defined as Δi ($=\delta^{7}Li_{measure} - \delta^{7}Li_{ture}$). The value of Δi may change between different sessions, owing to variations in the ion probe set up and electron multiplier aging (Deloule et al., 1991). The measured δ^{7}Li values of standard samples during two separated analytical durations are presented in Fig. 3-7. Our SIMS data are reliable, supported by the comparison with those obtained by other method. For Hebi samples, our δ^{7}Li range for olivines were roughly consistent with the previous data reported by Tang et al. (2010) using MC-ICP-MS for mineral separates, whereas these for the pyroxenes diverged strongly due to the extreme isotopic heterogeneities that have been concealed by the averages.

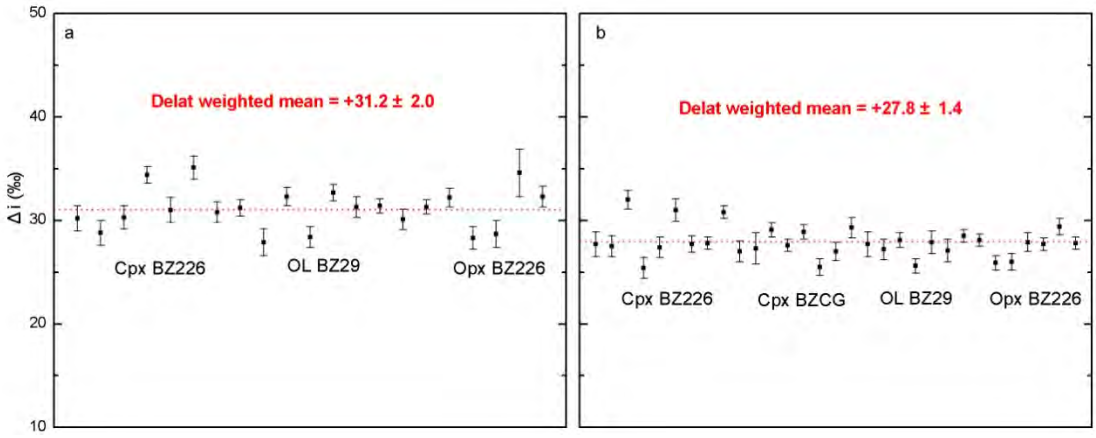

Figure 3-7. Standard Li isotopic variation and fractionation during the analyses with 2σ error bars. a-b, representatives of the standard data collected in two continuous periods that were separated by reloading a new primary ion source (Duoplasmatron).

4 Results

This chapter compiles all the experimental data involved in this thesis, including EMP for major elements concentrations of mineral phases in peridotite, LA-ICP-MS for trace elements concentrations of cpx, FTIR for water contents, and SIMS for Li contents and isotopic ratios in the peridotite xenoliths. These data are detailed separately below.

4.1 EMP results

4.1.1 Major elements concentrations

Given that the relatively small size xenoliths that may bias the modal mineralogy and thus the bulk composition, and the probable presence of the pockets of host basalts near the rims or introduction of the secondary minerals during post-volcanism, major elements of the minerals, instead of the bulk rock, in xenoliths were determined. The mineral chemical data for xenoliths are viewed as a more reliable indication of rock composition than the whole rock data.

The EMP measurements show no inter- and intra-grain heterogeneities for individual minerals in each peridotite samples based on multi-analyses at core and rim. And thus minerals in these xenoliths are homogenous and the average compositions are given in Table 4-1 for the olivines in the peridotite xenolith from all the localities in this thesis, in Table 4-2 for the othopyroxenes, in Table 4-3 for the clinopyroxenes, and Table 4-4 for the spinels. Our results are consistent with the previous reported data for samples from these localities (e.g., Fan and Hooper, 1989; Zheng et al., 1998, 2001, 2007; Rudnick et al., 2004; Ying et al., 2006; Yan et al., 2003, 2005; Zhang et al., 2009a, Chu et al., 2009; Xiao et al., 2010).

The EMP data demonstrate that almost all the studied xenoliths in this thesis are truly mantle peridotites, which are fragments of the lithospheric mantle rather than cumulates that are the crystallization products of the mafic basalts. Olivine is the main mineral phase in peridotite xenoliths and is a major host for magnesium, iron, and nickel. The Mg# in olivine, described as $100*Mg/(Mg+Fe_{tot})$ (all expressed in mole

fraction), is a good indicator sensitive to the extent of melt depletion in bulk rock, and sometime is more reliable than the Mg# of bulk peridotite, which is more susceptible to modifications by secondary metasomatised processes in the mantle and percolating melt in its ascent to surface, or weathering on the surface. The Mg# values range from 89.43 to 91.31 in Penglai, 90.58 to 91.44 in Qixia, 86.70 to 90.41 in Changle, 91.87 to 92.70 in Hebi, 89.99 to 90.94 in Qingdao, 87.91 to 91.40 in Daxizhuang, and 88.48 to 89.79 in Junan xenoliths. The Mg# values in samples have a total range of 87.91 to 92.70, with the lowest value in the xenoliths from Daxizhuang, and the highest values in those from Hebi. Samples in each locality usually show a narrow olivine Mg# range. Only the xenoliths from Daxizhuang display a large spectrum, according to which the xenoliths can be subdivided into two groups: the low Mg# group (87.91~88.94) and the high Mg# group (90.31~91.40). The high Mg# group has not yet been identified by previous studies on this area (e.g. Yan et al., 2003, 2005) in which all the peridotite xenoliths are highly fertile with Mg# in olivine of less than 89. The Mg# values of olivines in all the xenolith but those from the Cenozoic Hebi fall into a range of 88 to 92, typical for off-craton spinel-peridotite xenoliths (Boyd, 1997). In contrast, the high Mg# of Hebi olivines in xenoliths, all refractory harzburgites or dunites, have the characteristics of on-craton mantle xenoliths that typically exceed 92 with an average of 92.8 in Mg# of olivines (Bernstein et al., 2007).

NiO contents in olivines in all the xenoliths range broadly from 0.06 to 0.30 wt%. In details, NiO contents in olivines vary from 0.22 to 0.30 wt% in Penglai, 0.16 to 0.27 wt% in Qixia, 0.24 to 0.28 wt% in Changle, 0.24 to 0.30 wt% in Hebi, 0.23 to 0.24 wt% in Qingdao, 0.14 to 0.19 wt% in Daxizhuang, and 0.13 to 0.19 wt% in Junan xenoliths. The olivines from Daxizhuang and Junan have slightly less NiO contents than those from the rest of localities. Although the Hebi xenoliths are more refractory than all the others, suggested by their high Mg# in olivines, they cannot be evidently distinguished from the others in term of NiO content, which, to some extents, is also another measure of depletion of bulk rock on the ground that Ni is a compatible element during partial melting and the olivine is main host for Ni in peridotite. The potential correlation between NiO contents and Mg# in olivines lacks among samples in each locality.

Orthopyroxene, also named opx for short, is a main mineral phase only secondary to olivine in peridotite. The Mg# of opx is similar or slightly greater than that of

olivine when they are in equilibrium, due to a relative Fe-Mg partition coefficient of close to unity that is independent of P and T (Seckendorff et al., 1993). The Mg# values in opx, as those in coexisting olivines, have a broad range of 88.98 to 93.31, with also the lowest value in DXZ27 and the highest value in HB10. All the opx slightly exceed their coexisting olivines in Mg#. The CaO content of opx varies depending on the temperature of equilibration of the sample as well as its bulk composition. This is what the Ca-in-opx geothermometer of Brey and Kohler (1990) is based on. Among all the xenoliths these opx from Daxizhuang show the highest CaO contents of 0.93 to 1.47 wt %, with a restricted range of 1.0 to 1.3 wt% than those from both Junan and Qingdao samples that share the similar fertility (Mg# in ol) to Daxizhuang samples, ranging from 0.67 to 0.94, let alone the opx from the rest of localities. In the plot of end-member composition, all studied opx are limited to a narrow area that belongs to the mantle opx (Fig. 4-1).

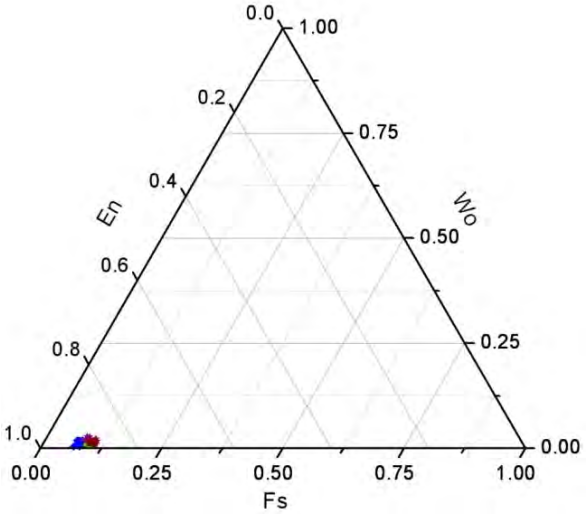

Fig. 4-1 End-member compositions of opx from the studied peridotites in the NCC

Clinopyroxene (cpx), although low in abundance, is a major repository for sodium, calcium, chromium, and titanium. The Mg# of cpx, too, like opx, is slightly higher than that of coexisting olivine, due to a K_d of greater than 1. The Mg# values range from 90.44 to 92.94 in Penglai, 91.53 to 93.99 in Qixia, 91.16 to 91.76 in Changle, 92.39 to 93.92 in Hebi, 91.26 to 91.59 in Qingdao, 88.33 to 92.31 in Daxizhuang, and 89.05 to 90.45 in Junan xenoliths. The variation of Mg# values in cpx is on the same pace with coexisting olivine and opx. And in one place the peridotite that has the highest Mg# value in olivine or opx is always that with the highest Mg# value in cpx. But it is also note that the Mg# values in cpx, in many

cases, are much higher than those in coexisting olivine or opx, predicted by the equilibration partitioning of Mg-Fe. The main reason is probably the high proportion of Fe^{3+} in the total Fe. In the end-member composition plot (Fig. 4-2), all cpx except one from HB (blue mark) belong to diopside (Cr-diopside), which is characteristic of mantle pyroxene.

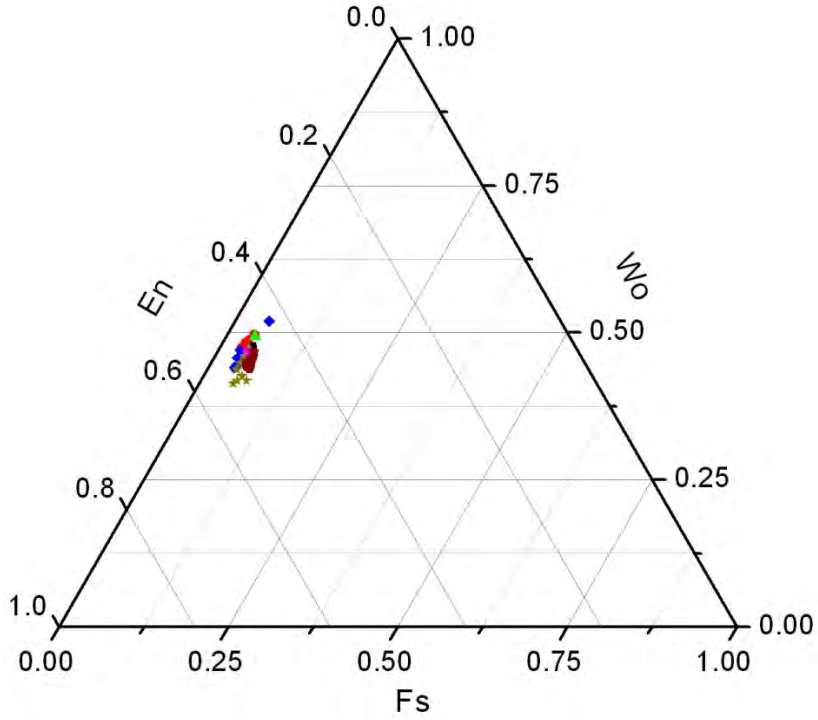

Figure 4-2. End-member compositions of cpx from peridotites in the NCC

The Ca content of cpx is strongly T-dependent and is between 40 and 50 mol % wollastonite component ($Ca_2Si_2O_6$, it does not exist in nature).

The cpx in Penglai xenoliths have a narrow CaO content range of 20.13 to 20.94 wt%, but one higher value of 22.09 wt% for sample PL46, which has the highest Mg# values among the Penglai samples. These in Junan xenoliths also share the same narrow range, but with slightly low values ranging from 19.13 to 20.04 wt%. The cpx from the rest of places have relatively variable Cao contents. The CaO contents vary from 22.28 to 23.60 wt% in Qixia, 19.12 to 21.40 wt% in Changle, 20.46 to 23.22 wt% in Hebi, 20.95 to 22.05 wt% in Qingdao, and 17.71 to 22.11 wt% in Daxizhuang. It is noted that the samples with the lowest CaO contents are also those with lowest Mg# values in olivine and pyroxene. The low CaO contents may be related with the metasomatism.

The Al_2O_3 content in cpx, like the CaO content, depends on the Temperature, but also the bulk composition of rock. The depletion of melt can lower the Al_2O_3 content

of bulk rock and to some extents that of the pyroxene. The Al_2O_3 contents in cpx here range from 1.81 to 7.91 wt%, with the low contents in those relatively refractory samples, such Hebi (1.81~4.25 wt%) and Qixia (2.11~6.72 wt%), and the high contents in those fertile samples (7~8 wt%) from Junan and Daxizhuang. The Cpx in Penglai contains 3.30 ~ 7.51 wt% Al_2O_3, with a narrower range of 6.28 to 6.95 wt%. The most fertile sample PL44 and refractory sample PL46 have the highest value of 7.51 wt% and the lowest value of 3.30 wt%, respectively, indicating the role of bulk composition. Up to 1.5 wt% Cr_2O_3 is observed in our xenolith cpx. It is generally believed that the molar Cr/Al in cpx is nearly identical to that of its bulk peridotite and correlates positively with the extent of melt depletion.

Spinel, the only stable aluminous phase at moderate pressure (30~80 km at mantle), as opposed to the feldspar at low pressure (<30km) and the garnet at high pressure (>80km), is made up of Al_2O_3, Cr_2O_3, FeO and MgO. The Cr#, defined as Cr/(Cr+Al), reflects both the degree of depletion of the bulk rock and also the T and P of equilibration. Spinel crystallized from depleted peridotites or at high P in the garnet-facies have high Cr#, whereas spinel from less depleted peridotites or at lower T and P in the spinel-facies have low Cr# (Roeder et al., 1994). The Cr# values of spinel and the Mg# values of olivines in peridotite xenoliths show a positive correlation, pointing to a partial melting process. The Cr# values range from 3.3 to 42.14 in Penglai, from 24.1 to 42.9 in Qixia, from 17.8 to 64.0 in Hebi, from 9.8 to 25.6 in Changle, from 9.8 to 41.4 in Daxizhuang and from 8.1 to 10.9 in Junan.

Table 4-1. Major Element Concentrations of ol in the Peridotite xenoliths of this study

Locality	Sample	SiO2	TiO2	Al2O3	Cr2O3	FeO	MnO	MgO	CaO	Na2O	K2O	NiO	TOTAL	Mg#
Penglai	PL-01	41.08	0.02	0.02	0.00	9.87	0.15	49.19	0.02	0.00	0.00	0.28	100.64	89.89
	PL-10	41.14	0.01	0.01	0.02	9.52	0.15	48.90	0.04	0.01	0.00	0.27	100.08	90.16
	PL-17	41.13	0.01	0.01	0.01	9.75	0.17	48.66	0.03	0.01	0.00	0.27	100.05	89.89
	PL-19	41.26	0.01	0.03	0.01	9.89	0.14	48.89	0.03	0.01	0.00	0.29	100.55	89.81
	PL-31	41.07	0.00	0.02	0.01	9.91	0.16	49.56	0.03	0.01	0.01	0.20	100.98	89.95
	PL-32	41.08	0.00	0.01	0.00	9.90	0.18	48.46	0.03	0.00	0.01	0.26	99.94	89.72
	PL-36	41.07	0.01	0.01	0.00	9.86	0.10	49.01	0.02	0.01	0.00	0.22	100.32	89.86
	PL-42	41.09	0.02	0.01	0.01	9.47	0.14	49.50	0.04	0.01	0.01	0.28	100.60	90.31
	PL-44	40.86	0.01	0.00	0.01	10.27	0.17	48.77	0.04	0.00	0.00	0.30	100.42	89.43
	PL-46	41.14	0.00	0.01	0.02	8.56	0.12	50.43	0.03	0.00	0.01	0.29	100.61	91.31
Qixia	QX-01	41.24	0.01	0.00	0.00	8.59	0.13	50.00	0.02	0.00	0.00	0.24	100.23	91.21
	QX-04	41.14	0.00	0.01	0.00	8.66	0.19	49.35	0.00	0.02	0.00	0.27	99.64	91.04
	QX-14	41.34	0.00	0.00	0.02	9.05	0.13	48.83	0.01	0.00	0.00	0.23	99.62	90.58
	QX-15	40.69	0.01	0.01	0.01	8.72	0.13	50.32	0.02	0.01	0.01	0.16	100.09	91.14
	QX-18	41.25	0.00	0.01	0.00	8.42	0.10	49.06	0.03	0.01	0.00	0.23	99.11	91.22
	QX-49	41.32	0.00	0.02	0.00	8.87	0.19	48.40	0.00	0.01	0.00	0.20	99.01	90.68
	QX-50	41.36	0.00	0.01	0.02	8.52	0.14	49.47	0.02	0.00	0.00	0.24	99.77	91.19
	QX-51	41.18	0.00	0.00	0.01	8.29	0.14	49.64	0.01	0.00	0.01	0.22	99.50	91.44
Changle	CL-22	41.29	0.00	0.03	0.03	10.89	0.17	47.78	0.04	0.00	0.01	0.24	100.46	88.67
	CL-31	41.00	0.00	0.02	0.00	9.87	0.18	48.51	0.03	0.02	0.00	0.28	99.91	89.75
	CL-32	40.85	0.00	0.00	0.03	10.33	0.17	48.41	0.01	0.00	0.01	0.24	100.04	89.31
	CL-35	41.07	0.02	0.02	0.03	9.33	0.12	49.31	0.05	0.01	0.00	0.25	100.20	90.41
	CL-38	41.11	0.03	0.01	0.04	9.99	0.17	49.22	0.02	0.00	0.00	0.25	100.84	89.78
Hebi	HB-01	41.57	0.01	0.01	0.02	7.81	0.11	49.81	0.07	0.01	0.00	0.26	99.68	91.91
	HB-02	41.41	0.01	0.01	0.01	7.91	0.13	50.13	0.04	0.01	0.00	0.25	99.92	91.87
	HB-06	41.76	0.02	0.01	0.00	7.33	0.11	50.20	0.06	0.00	0.00	0.26	99.78	92.43
	HB-07	41.52	0.01	0.01	0.01	7.82	0.12	50.29	0.02	0.01	0.00	0.26	100.07	91.98
	HB-10	41.50	0.00	0.01	0.02	7.17	0.09	51.03	0.01	0.00	0.00	0.27	100.12	92.70
	HB-12	41.62	0.00	0.03	0.04	7.16	0.14	50.74	0.07	0.00	0.00	0.29	100.09	92.67
	HB-13	41.28	0.00	0.02	0.03	7.70	0.13	50.11	0.08	0.00	0.00	0.30	99.66	92.07
	HB-17	41.63	0.00	0.02	0.02	7.21	0.11	50.24	0.07	0.02	0.00	0.24	99.58	92.55
	HB-64	41.69	0.00	0.01	0.02	7.27	0.16	51.16	0.08	0.02	0.02	0.22	100.64	92.46
Qingdao	QDPS-16	40.89	0.01	0.02	0.02	9.58	0.15	48.29	0.09	0.02	0.01	0.23	99.29	89.99
	QDPS-24	41.20	0.00	0.02	0.04	8.69	0.14	48.92	0.08	0.00	0.00	0.23	99.31	90.94
Daxizhang	DXZ-01	39.93	0.02	0.04	0.04	10.82	0.16	48.80	0.11	0.03	0.01	0.16	100.11	88.94
	DXZ-02	40.61	0.01	0.03	0.05	8.71	0.11	50.21	0.13	0.02	0.01	0.15	100.03	91.14
	DXZ-04	40.77	0.00	0.01	0.02	8.60	0.16	50.40	0.11	0.02	0.00	0.14	100.23	91.27
	DXZ-14	39.91	0.00	0.02	0.03	11.02	0.16	48.34	0.09	0.02	0.00	0.17	99.75	88.66
	DXZ-17	40.56	0.00	0.02	0.04	8.46	0.10	50.41	0.09	0.01	0.00	0.16	99.86	91.40
	DXZ-27	40.10	0.00	0.01	0.04	11.69	0.17	47.71	0.09	0.02	0.00	0.14	99.96	87.91
	DXZ-36	40.14	0.01	0.03	0.04	10.95	0.15	48.51	0.07	0.01	0.01	0.15	100.08	88.76
	DXZ-39	40.54	0.01	0.00	0.00	9.15	0.14	49.88	0.09	0.00	0.01	0.19	100.01	90.67
	DXZ-42	40.48	0.01	0.02	0.04	9.50	0.14	49.66	0.15	0.02	0.00	0.16	100.19	90.31
Junan	JN-03	40.22	0.01	0.02	0.02	10.72	0.14	48.27	0.07	0.02	0.01	0.16	99.66	88.93
	JN-08	40.34	0.00	0.03	0.03	10.65	0.15	48.61	0.09	0.01	0.02	0.16	100.09	89.06
	JN-11	40.38	0.01	0.01	0.02	10.65	0.15	48.35	0.05	0.02	0.00	0.13	99.78	89.00
	JN-24	40.46	0.01	0.02	0.01	10.29	0.16	48.93	0.08	0.01	0.00	0.17	100.14	89.45
	JN-26	39.99	0.00	0.01	0.04	11.36	0.18	48.97	0.05	0.02	0.00	0.14	100.76	88.48
	JN-35	40.29	0.00	0.03	0.01	10.21	0.12	48.83	0.06	0.02	0.00	0.16	99.73	89.50
	JN-43	40.06	0.01	0.03	0.00	10.53	0.13	49.14	0.09	0.02	0.01	0.17	100.18	89.27
	JN-44	40.02	0.00	0.03	0.01	10.86	0.15	48.65	0.09	0.04	0.01	0.17	100.01	88.88
	JN-46	40.03	0.00	0.01	0.03	10.54	0.16	49.15	0.07	0.02	0.01	0.17	100.18	89.27
	JN-47	39.99	0.00	0.02	0.01	10.80	0.14	48.32	0.08	0.02	0.02	0.16	99.56	88.86
	JN-53	39.89	0.00	0.02	0.00	10.00	0.17	49.34	0.06	0.02	0.01	0.19	99.71	89.79
	JN-54	40.38	0.00	0.04	0.01	10.35	0.14	49.07	0.07	0.01	0.00	0.15	100.22	89.42
	JN-59	40.39	0.01	0.04	0.01	10.66	0.01	48.81	0.07	0.02	0.01	0.15	100.18	89.09
	JN-65	40.01	0.02	0.01	0.00	10.70	0.15	48.50	0.08	0.02	0.00	0.15	99.65	88.99

Table 4-2. Major Element Concentrations of opx in Peridotite xenoliths of this study

Locality	Sample	SiO2	TiO2	Al2O3	Cr2O3	FeO	MnO	MgO	CaO	Na2O	K2O	NiO	TOTAL	Mg#
Penglai	PL-01	55.25	0.08	4.29	0.20	6.40	0.16	33.23	0.51	0.08	0.01	0.04	100.24	90.26
	PL-10	55.53	0.11	4.34	0.20	5.86	0.14	33.22	0.54	0.08	0.00	0.05	100.06	85.02
	PL-17	55.82	0.11	4.16	0.17	6.24	0.14	32.90	0.46	0.07	0.01	0.07	100.16	84.05
	PL-19	55.69	0.09	4.04	0.21	6.21	0.13	33.19	0.50	0.07	0.00	0.07	100.21	84.25
	PL-31	55.63	0.12	4.44	0.31	6.23	0.15	33.55	0.62	0.09	0.01	-	101.17	84.33
	PL-32	55.63	0.11	3.75	0.25	6.61	0.16	33.25	0.57	0.06	0.01	0.05	100.45	83.42
	PL-36	55.28	0.07	4.18	0.13	6.35	0.12	33.17	0.46	0.07	0.00	0.05	99.89	90.30
	PL-42	54.94	0.11	4.61	0.19	6.01	0.17	33.30	0.56	0.07	0.00	0.09	100.04	84.71
	PL-44	55.35	0.11	4.46	0.14	6.37	0.15	33.22	0.49	0.08	0.00	0.06	100.43	90.28
	PL-46	56.42	0.03	2.36	0.33	5.46	0.15	34.25	0.59	0.03	0.01	0.07	99.69	91.80
Qixia	QX-01	56.91	0.03	2.44	0.27	5.61	0.13	34.08	0.59	0.02	0.01	0.07	100.15	91.55
	QX-04	56.34	0.05	3.01	0.21	5.66	0.11	33.54	0.50	0.01	0.00	0.03	99.45	91.35
	QX-14	55.83	0.10	3.87	0.16	6.25	0.17	33.24	0.52	0.05	0.01	0.07	100.24	90.47
	QX-15	56.74	0.01	1.25	0.35	5.82	0.19	34.82	0.79	0.05	0.00	0.02	100.04	91.42
	QX-18	56.63	0.01	2.52	0.22	5.69	0.14	33.50	0.57	0.01	0.01	0.06	99.35	91.30
	QX-49	55.84	0.08	3.65	0.25	6.13	0.18	33.04	0.43	0.03	0.01	0.01	99.65	90.58
	QX-50	56.70	0.03	2.16	0.27	5.72	0.15	34.17	0.60	0.00	0.00	0.04	99.83	91.42
	QX-51	55.62	0.09	3.70	0.17	6.23	0.13	33.19	0.42	0.01	0.01	0.05	99.62	90.47
Changle	CL-01	55.53	0.06	3.97	0.23	5.74	0.15	32.82	0.62	0.10	0.01	0.06	99.29	91.06
	CL-22	54.94	0.12	4.29	0.24	6.74	0.15	31.52	0.75	0.08	0.01	0.06	98.89	89.29
	CL-31	55.42	0.05	3.92	0.25	6.19	0.15	32.49	0.70	0.09	0.01	0.06	99.34	90.34
	CL-32	56.08	0.07	3.82	0.17	6.23	0.16	32.75	0.54	0.04	0.00	0.07	99.90	90.37
	CL-35	56.00	0.02	3.92	0.20	5.79	0.15	32.80	0.57	0.13	0.00	0.01	99.57	90.99
	CL-38	55.60	0.09	3.55	0.21	6.41	0.19	33.17	0.47	0.02	0.01	0.04	99.74	90.22
Hebi	HB-01	56.52	0.01	2.18	0.52	5.09	0.12	33.30	0.92	0.05	0.00	0.07	98.81	92.10
	HB-02	58.44	0.00	0.88	0.23	4.82	0.12	34.48	0.52	0.02	0.00	0.07	99.56	92.73
	HB-06	56.15	0.02	3.27	0.79	4.53	0.09	33.41	0.91	0.05	0.01	0.06	99.32	92.93
	HB-07	56.05	0.06	3.19	0.14	5.26	0.08	34.25	0.26	0.00	0.01	0.07	99.37	92.07
	HB-10	58.61	0.00	0.66	0.25	4.53	0.12	35.41	0.21	0.00	0.00	0.06	99.86	93.31
	HB-17	56.36	0.05	3.31	0.45	4.70	0.11	33.48	0.92	0.08	0.01	0.07	99.54	92.70
	HB-64	56.61	0.02	3.36	0.77	4.59	0.10	35.11	0.94	0.12	0.00	-	101.62	93.17
Qingdao	QDPS-16	54.77	0.09	5.10	0.46	5.87	0.16	31.79	0.96	0.04	0.00	0.08	99.32	90.62
	QDPS-24	55.18	0.07	4.25	0.53	5.84	0.14	32.74	0.82	0.03	0.01	0.12	99.73	90.90
Daxizhang	DXZ-01	53.18	0.21	6.21	0.43	6.83	0.15	32.07	1.16	0.18	0.01	0.04	100.46	89.33
	DXZ-02	54.24	0.00	4.25	0.83	5.54	0.14	33.40	1.47	0.05	0.00	0.04	99.95	91.49
	DXZ-04	54.59	0.06	4.09	0.67	5.56	0.15	33.83	1.10	0.08	0.00	0.04	100.17	91.55
	DXZ-14	54.51	0.05	3.35	0.67	6.91	0.15	33.03	1.08	0.13	0.00	0.05	99.92	89.50
	DXZ-17	55.10	0.04	3.11	0.72	5.38	0.14	34.54	1.05	0.04	0.00	0.03	100.15	91.97
	DXZ-27	53.88	0.09	4.45	0.49	7.22	0.16	32.72	0.93	0.15	0.00	0.02	100.12	88.98
	DXZ-36	54.39	0.06	4.33	0.46	6.85	0.14	33.20	0.90	0.14	0.01	0.05	100.54	89.62
	DXZ-39	54.43	0.02	4.02	0.65	5.62	0.13	33.63	1.07	0.01	0.00	0.04	99.60	91.43
	DXZ-42	53.90	0.06	4.39	0.87	5.89	0.13	33.02	1.40	0.06	0.01	0.04	99.75	90.91
Junan	JN-03	53.84	0.13	5.16	0.34	6.79	0.16	32.97	0.89	0.18	0.00	0.04	100.50	89.64
	JN-08	54.03	0.15	5.00	0.31	6.67	0.15	33.09	0.81	0.15	0.00	0.05	100.42	89.84
	JN-11	54.05	0.12	4.33	0.23	6.79	0.18	33.40	0.60	0.09	0.01	0.04	99.84	89.77
	JN-24	54.26	0.14	4.98	0.37	6.33	0.14	32.91	0.87	0.15	0.01	0.04	100.19	90.26
	JN-26	53.98	0.11	4.19	0.22	7.12	0.18	32.94	0.60	0.10	0.01	0.07	99.52	89.19
	JN-35	53.99	0.10	4.80	0.35	6.48	0.15	33.28	0.71	0.16	0.02	0.05	100.11	90.16
	JN-43	53.71	0.14	5.17	0.33	6.82	0.13	32.77	0.94	0.16	0.00	0.04	100.19	89.55
	JN-44	53.78	0.16	5.15	0.27	6.82	0.14	32.90	0.83	0.14	0.00	0.04	100.24	89.59
	JN-46	53.85	0.13	4.74	0.26	6.71	0.16	33.02	0.73	0.13	0.00	0.03	99.76	89.76
	JN-47	53.60	0.15	5.11	0.31	6.85	0.15	33.19	0.77	0.17	0.01	0.05	100.35	89.63
	JN-53	53.71	0.11	4.73	0.34	6.32	0.15	33.60	0.67	0.16	0.01	0.04	99.84	90.45
	JN-54	54.29	0.11	4.67	0.35	6.49	0.19	33.08	0.71	0.13	0.01	0.02	100.07	90.09
	JN-59	54.02	0.14	4.88	0.28	6.81	0.00	33.19	0.71	0.14	0.01	0.05	100.22	89.68
	JN-65	53.93	0.15	5.13	0.31	6.70	0.16	32.93	0.85	0.14	0.01	0.05	100.37	89.75

Table 4-3. Major Element Concentrations of Cpx in the Peridotite xenoliths of this study

Locality	Sample	SiO2	TiO2	Al2O3	Cr2O3	FeO	MnO	MgO	CaO	Na2O	K2O	NiO	TOTAL	Mg#
Penglai	PL-01	52.13	0.47	6.84	0.49	2.72	0.08	14.83	20.54	1.84	0.00	0.03	99.98	90.67
	PL-10	52.20	0.44	6.28	0.44	2.58	0.11	15.36	20.90	1.55	0.01	0.03	99.88	91.39
	PL-17	52.39	0.47	6.66	0.44	2.66	0.08	14.91	20.64	1.80	0.00	0.03	100.09	90.90
	PL-19	52.00	0.52	6.95	0.58	2.62	0.10	14.71	20.58	1.86	0.01	0.02	99.94	90.92
	PL-31	52.54	0.48	6.33	0.72	2.61	0.05	15.72	21.02	1.58	0.00		101.05	91.49
	PL-32	52.19	0.47	5.66	0.55	2.81	0.08	15.38	20.94	1.50	0.01	0.03	99.61	90.71
	PL-36	52.14	0.47	6.86	0.48	2.65	0.09	14.80	20.30	1.81	0.01	0.03	99.65	90.89
	PL-42	52.00	0.46	6.38	0.42	2.48	0.07	15.39	20.78	1.44	0.00	0.03	99.47	91.71
	PL-44	52.05	0.62	7.51	0.42	2.75	0.08	14.60	20.13	1.99	0.00	0.03	100.18	90.44
	PL-46	53.48	0.05	3.30	0.76	2.26	0.08	16.66	22.09	1.14	0.01	0.03	99.87	92.94
Qixia	QX-01	53.18	0.04	2.72	0.47	2.18	0.07	17.33	23.59	0.12	0.01	0.00	99.72	93.41
	QX-04	54.51	0.14	4.04	0.57	2.12	0.11	15.62	22.32	0.72	0.00	0.01	100.15	92.94
	QX-14	52.40	0.49	6.72	0.40	2.30	0.10	14.21	21.23	1.41	0.00	0.02	99.27	91.68
	QX-15	53.16	0.02	2.18	0.91	2.00	0.08	17.55	23.49	0.55	0.01	0.02	99.99	93.99
	QX-18	53.10	0.05	2.65	0.47	2.20	0.10	16.94	23.44	0.23	0.00	0.04	99.23	93.23
	QX-49	52.76	0.41	5.14	0.57	2.27	0.08	15.13	22.60	0.93	0.00	0.01	99.89	92.25
	QX-50	53.75	0.03	2.11	0.73	2.03	0.08	16.90	23.52	0.19	0.01	0.06	99.41	93.69
	QX-51	52.02	0.48	5.43	0.50	2.47	0.06	14.99	22.28	0.95	0.00	0.00	99.18	91.53
Changle	CL-01	53.58	0.18	4.99	0.63	2.74	0.10	15.87	21.08	0.89	0.00	0.03	100.08	91.16
	CL-22	52.09	0.61	6.40	0.48	2.45	0.08	14.78	19.97	1.15	0.00	0.02	98.00	91.50
	CL-31	53.21	0.29	5.72	0.44	2.58	0.08	15.28	19.63	2.00	0.00	0.00	99.23	91.35
	CL-32	52.39	0.49	6.34	0.40	2.39	0.08	14.45	21.40	1.25	0.01	0.05	99.26	91.51
	CL-35	53.26	0.31	6.50	0.44	2.34	0.11	14.40	19.12	2.68	0.00	0.00	99.17	91.64
	CL-38	52.45	0.42	5.92	0.57	2.30	0.06	14.34	21.20	1.16	0.00	0.02	98.43	91.76
Hebi	HB-01	53.71	0.03	3.32	1.41	2.08	0.05	16.78	21.00	0.66	0.00	0.04	99.11	93.50
	HB-02	55.25	0.02	1.81	0.36	1.97	0.05	17.06	22.39	0.37	0.00	0.04	99.34	93.92
	HB-13	47.24	5.26	5.53	0.73	2.87	0.05	13.81	23.22	0.65	0.01	0.03	99.40	89.57
	HB-17	53.64	0.12	4.19	0.84	2.42	0.10	16.46	20.29	0.95	0.00	0.05	99.06	92.39
	HB-64	53.60	0.14	4.25	1.38	2.28	0.09	17.40	20.46	1.34	0.01		100.95	93.15
Qingdao	QDPS-16	52.03	0.22	5.76	0.72	2.74	0.08	16.06	20.95	0.59	0.00	0.01	99.17	91.26
	QDPS-24	52.78	0.14	4.72	0.84	2.69	0.09	16.44	22.05	0.43	0.00	0.05	100.24	91.59
Daxizhang	DXZ-01	50.14	0.56	7.91	0.76	3.80	0.10	16.13	18.24	1.60	0.01	0.03	99.29	88.33
	DXZ-02	51.39	0.06	4.51	1.17	3.09	0.09	18.58	19.94	0.40	0.01	0.02	99.26	91.48
	DXZ-04	51.69	0.17	4.40	0.93	2.66	0.09	17.88	20.95	0.62	0.01	0.03	99.43	92.31
	DXZ-14	52.28	0.11	3.92	1.06	3.37	0.08	17.22	19.77	1.16	0.01	0.02	99.01	90.10
	DXZ-17	52.16	0.10	3.37	1.14	2.74	0.12	18.12	21.24	0.49	0.01	0.03	99.51	92.19
	DXZ-27	52.16	0.20	5.13	0.78	3.19	0.11	16.25	20.22	1.48	0.01	0.02	99.57	90.07
	DXZ-36	51.34	0.21	5.10	0.78	2.68	0.09	16.63	21.18	1.11	0.00	0.02	99.15	91.70
	DXZ-39	52.01	0.06	4.12	0.80	2.74	0.07	18.00	22.11	0.28	0.01	0.01	100.21	92.14
	DXZ-42	51.14	0.17	4.70	1.18	3.27	0.11	18.11	19.97	0.36	0.01	0.03	99.05	90.81
Junan	JN-03	51.00	0.60	7.26	0.69	3.42	0.10	15.62	19.13	1.80	0.01	0.01	99.64	89.06
	JN-08	51.39	0.60	7.35	0.64	3.21	0.10	15.48	19.20	1.88	0.01	0.01	99.86	89.57
	JN-11	51.19	0.58	6.80	0.59	3.04	0.06	15.08	20.46	1.66	0.01	0.01	99.47	89.85
	JN-24	51.08	0.53	7.13	0.81	3.13	0.08	15.80	19.42	1.70	0.01	0.01	99.70	89.99
	JN-26	50.93	0.57	6.94	0.64	3.13	0.09	15.09	20.04	1.64	0.00	0.03	99.09	89.57
	JN-35	50.97	0.57	7.42	0.80	3.02	0.10	15.10	19.41	2.00	0.01	0.02	99.41	89.91
	JN-43	50.72	0.56	7.21	0.66	3.44	0.09	15.70	19.21	1.69	0.01	0.04	99.32	89.05
	JN-44	50.97	0.69	7.63	0.72	3.20	0.11	15.04	19.20	1.94	0.01	0.02	99.52	89.34
	JN-46	50.81	0.65	7.20	0.56	3.05	0.09	15.49	19.57	1.86	0.01	0.02	99.30	90.06
	JN-47	50.83	0.67	7.61	0.63	3.17	0.10	15.24	19.01	1.94	0.01	0.04	99.24	89.54
	JN-53	50.61	0.62	7.37	0.70	2.90	0.09	15.38	19.28	1.91	0.00	0.01	98.86	90.45
	JN-54	51.16	0.57	7.34	0.74	3.04	0.08	15.30	19.29	2.00	0.00	0.03	99.55	89.97
	JN-59	51.03	0.64	7.42	0.59	3.05	0.01	15.12	19.52	1.87	0.01	0.00	99.25	89.85
	JN-65	51.06	0.62	7.42	0.70	3.15	0.09	15.43	19.21	1.79	0.01	0.04	99.52	89.72

Note : Mg # = 100*Mg/(Mg + Fe) (atom ratios)

Table 4-4. Major Element Concentrations of Spl in the Peridotite Xenoliths of this study

Locality	Sample	SiO2	TiO2	Al2O3	Cr2O3	FeO	MnO	MgO	CaO	Na2O	K2O	NiO	TOTAL	Cr#
Penglai	PL-01	0.02	0.07	61.42	5.34	11.58	0.12	20.89	0.00	0.00	0.00	0.27	99.71	5.51
	PL-10	0.03	0.09	59.80	6.12	12.17	0.11	20.64	0.00	0.01	0.00	0.27	99.24	6.42
	PL-17	0.03	0.06	61.43	5.41	12.77	0.12	20.45	0.00	0.01	0.00	0.28	100.56	5.58
	PL-19	0.02	0.08	60.25	6.46	12.85	0.12	20.53	0.01	0.00	0.00	0.28	100.58	6.71
	PL-31	0.03	0.10	58.03	11.15	10.38	0.06	20.56	0.01	0.01	0.01	-	100.34	11.42
	PL-32	0.06	0.83	50.02	16.16	13.92	0.16	18.85	0.04	0.00	0.01	0.22	100.27	17.81
	PL-36	0.01	0.07	58.81	2.95	11.91	0.10	19.89	0.00	0.00	0.00	0.15	93.89	3.26
	PL-42	0.03	0.10	62.07	5.68	11.47	0.10	20.85	0.00	0.01	0.01	0.28	100.59	5.79
	PL-44	0.03	0.07	63.53	4.61	10.54	0.11	20.90	0.01	0.02	0.01	0.29	100.12	4.64
	PL-46	0.01	0.09	32.96	35.78	14.32	0.22	16.64	0.00	0.01	0.00	0.14	100.16	42.14
Qixia	QX-01	0.04	0.06	35.83	34.63	13.67	0.20	16.53	0.00	0.01	0.01	0.12	101.10	39.33
	QX-04	0.00	0.05	47.59	22.56	11.97	0.20	18.12	0.00	0.00	0.00	0.16	100.65	24.13
	QX-15	0.02	0.06	32.57	36.44	14.94	0.22	16.29	0.02	0.00	0.00	0.07	100.63	42.88
	QX-18	0.00	0.07	37.96	31.22	14.38	0.18	16.84	0.00	0.03	0.02	0.15	100.85	35.55
	QX-50	0.02	0.10	33.41	36.54	15.07	0.25	15.94	0.00	0.03	0.00	0.12	101.47	42.32
Hebi	HB-01	0.04	0.06	28.47	41.44	13.58	0.20	16.45	0.01	0.03	0.01	0.15	100.49	49.41
	HB-02	0.02	0.06	24.31	44.52	14.55	0.23	15.74	0.00	0.00	0.01	0.10	99.61	55.12
	HB-06	0.03	0.15	33.77	35.49	12.05	0.24	17.95	0.00	0.00	0.01	0.15	99.89	41.35
	HB-07	0.03	0.14	51.40	16.60	11.72	0.09	19.70	0.00	0.00	0.00	0.19	99.87	17.80
	HB-10	0.03	0.00	18.71	49.65	15.65	0.27	14.96	0.02	0.00	0.01	0.12	99.47	64.03
	HB-12	0.04	0.03	32.09	37.37	12.70	0.23	17.49	0.01	0.00	0.00	0.13	100.09	43.86
	HB-13	0.04	0.01	25.91	44.76	13.08	0.25	16.23	0.00	0.00	0.00	0.12	100.39	53.68
	HB-17	0.04	0.19	34.47	35.89	12.07	0.21	17.95	0.01	0.01	0.00	0.18	101.03	41.12
	HB64	0.04	0.17	34.12	35.95	12.47	0.10	18.27	0.01	0.01	0.01	-	101.15	41.41
Changle	CL-01	0.05	0.05	52.89	15.79	10.54	0.20	19.31	0.02	0.00	0.02	0.18	99.05	16.68
	CL-22	0.03	0.13	54.90	13.39	12.74	0.14	19.24	0.00	0.00	0.01	0.25	100.82	14.06
	CL-31	0.03	0.10	52.55	16.13	11.26	0.15	19.58	0.00	0.01	0.00	0.19	100.02	17.08
	CL-32	0.02	0.03	59.65	9.64	10.63	0.05	20.19	0.01	0.00	0.00	-	100.22	9.78
	CL-35	0.01	0.02	46.51	23.81	10.29	0.17	19.09	0.00	0.01	0.01	0.15	100.07	25.56
	CL-38	0.02	0.05	54.77	14.55	10.57	0.15	19.58	0.00	0.01	0.00	0.21	99.92	15.12
Qingdao	QDPS-16	0.08	0.11	57.09	11.59	10.76	0.10	20.37	0.00	0.01	0.00	0.25	100.37	11.99
Daxizhang	DXZ-01	0.10	0.22	57.70	9.44	12.13	0.08	20.63	0.00	0.00	0.00	0.18	100.49	9.88
	DXZ-02	0.11	0.07	38.75	29.51	13.36	0.16	18.62	0.02	0.01	0.00	0.10	100.69	33.82
	DXZ-04	0.07	0.18	43.74	24.06	12.40	0.14	19.62	0.00	0.04	0.01	0.11	100.38	26.95
	DXZ-17	0.04	0.21	33.60	35.31	13.79	0.20	17.09	0.01	0.02	0.01	0.13	100.40	41.35
	DXZ-27	0.07	0.10	49.98	17.86	13.45	0.16	18.67	0.02	0.01	0.00	0.13	100.45	19.33
	DXZ-36	0.06	0.10	53.42	15.70	12.63	0.18	19.39	0.01	0.01	0.00	0.15	101.66	16.47
	DXZ-39	0.04	0.06	45.27	23.96	12.36	0.15	19.11	0.01	0.00	0.01	0.13	101.09	26.20
	DXZ-42	0.11	0.24	39.53	28.25	13.83	0.18	18.37	0.00	0.01	0.00	0.09	100.62	32.40
Junan	JN-03	0.07	0.15	58.18	9.37	12.18	0.10	20.29	0.00	0.01	0.02	0.15	100.53	9.75
	JN-24	0.05	0.18	57.63	10.55	11.11	0.12	20.98	0.00	0.01	0.01	0.17	100.81	10.94
	JN-35	0.06	0.14	58.45	9.66	11.36	0.16	20.81	0.00	0.00	0.00	0.17	100.81	9.98
	JN-43	0.05	0.18	58.11	9.35	11.81	0.15	20.75	0.01	0.01	0.00	0.16	100.57	9.75
	JN-44	0.05	0.17	59.92	7.86	11.17	0.11	20.79	0.01	0.00	0.00	0.15	100.23	8.09
	JN-47	0.08	0.16	59.33	8.08	11.17	0.10	21.32	0.00	0.02	0.01	0.13	100.41	8.37
	JN-53	0.0437	0.16	58.21	9.32	11.03	0.11	20.82	0.02	0.03	0.01	0.17	99.90	9.70
	JN-54	0.05	0.11	58.26	9.52	11.19	0.12	20.98	0.00	0.02	0.01	0.14	100.39	9.87
	JN-65	0.07	0.17	59.41	8.31	11.27	0.09	21.13	0.04	0.04	0.02	0.17	100.70	8.58

Note: Cr # = 100*Cr/(Cr+ Al) (atom ratios)

4.1.2 Temperature and Pressure estimates

Equilibrium temperatures for peridotite xenoliths are estimated using the Ca in opx geothermometer of Brey and Kohler (1990). Because spinel is the only aluminous phase at absence of garnet or plagioclase in peridotite xenoliths, indicating an equilibration pressure range of 15~18 kbar, the estimates are obtained at pressure of both 15 kbar and 20kbar for comparisons, and are given in Table 4-5. It show that the temperatures estimates under different pressures diverge little, with differences of no more than 30°C, and the estimates at a pressure of 15 kbar are preferred to represent the equilibration temperatures of xenoliths in their mantle source.

These temperatures are mainly between 850 and 1100°C (Fig. 4-3), in the range of those previously reported for the NCC peridotites (Fan and Hooper, 1989; Xu et al., 1995; Zheng et al., 1998, 2001, 2006; Chen et al., 2001; Rudnick et al., 2004; Xu and Bodinier, 2004). Several xenoliths with anomaly high Temperature estimates are likely to reflect the perturbation by recent melt infiltrations rather than the true equilibration state.

In details, xenoliths of Penglai have a narrow temperatures range of 880 to 939°C, so do those of Qixia where temperature estimates vary mainly between 861 and 934°C, except for one higher temperature of 995°C in QX15. The relative low temperature estimates in Qixia here are well consistent with those (most less than 900 °C) reported by Rundnick et al (2004). Changle xenoliths indicate comparable temperatures, ranging from 885 to 986°C. The temperatures for Hebi xenoliths have a large range of 741 to 1034°C, with five out of (totally) eight clustering at 1034, one at 902 and the last two at 714 and 778°C, respectively. Two xenoliths at Qingdao have temperatures of 1005 and 1045°C, respectively. The Daxizhuang xenoliths have the highest temperatures in these studies areas of the NCC, varying from 1028 to 1162°C. At last these temperatures in Junan have a range of 935 to 1039°C.

In a word, these samples from Daxizhuang have the highest equilibration temperatures, followed by those from Qingdao, Hebi and Junan. Changle xenoliths have slight higher temperatures than Penglai and Qixia samples, which have the lowest temperatures here.

Table 4-5. Estimates of equilibrium temperatures for the peridotite xenoliths of this study

based on the Ca-in-opx geothermometerv of Brey and Kohler (1990).

Locality	Sample	15kbar	20kbar
Penglai	PL01	901	924
	PL10	909	932
	PL17	881	903
	PL19	895	918
	PL31	939	963
	PL32	922	945
	PL36	880	903
	PL42	919	942
	PL44	891	914
	PL46	930	953
Qixia	QX01	928	951
	QX04	898	920
	QX14	902	925
	QX15	995	1019
	QX18	922	945
	QX49	866	888
	QX50	934	957
	QX51	861	883
Changle	CL01	941	965
	CL22	986	1010
	CL31	968	992
	CL32	911	934
	CL35	922	945
	CL38	885	907
Hebi	HB01	1034	1059
	HB02	902	925
	HB06	1031	1056
	HB07	778	798
	HB10	741	760
	HB12	1034	1059
	HB17	1032	1057
	HB64	1033	1058
Qingdao	QDPS16	1045	1070
	QDPS24	1005	1030
Daxizhang	DXZ01	1094	1120
	DXZ02	1162	1190
	DXZ04	1079	1105
	DXZ14	1077	1103
	DXZ17	1066	1092
	DXZ27	1037	1062
	DXZ36	1028	1053
	DXZ39	1072	1098
	DXZ42	1150	1177
Junan	JN03	1024	1050
	JN08	1002	1027
	JN11	935	959
	JN24	1018	1043
	JN26	938	961
	JN35	972	996
	JN43	1039	1064
	JN44	1009	1034
	JN46	978	1002
	JN47	992	1016
	JN53	958	982
	JN54	973	997
	JN59	972	997
	JN65	1013	1038

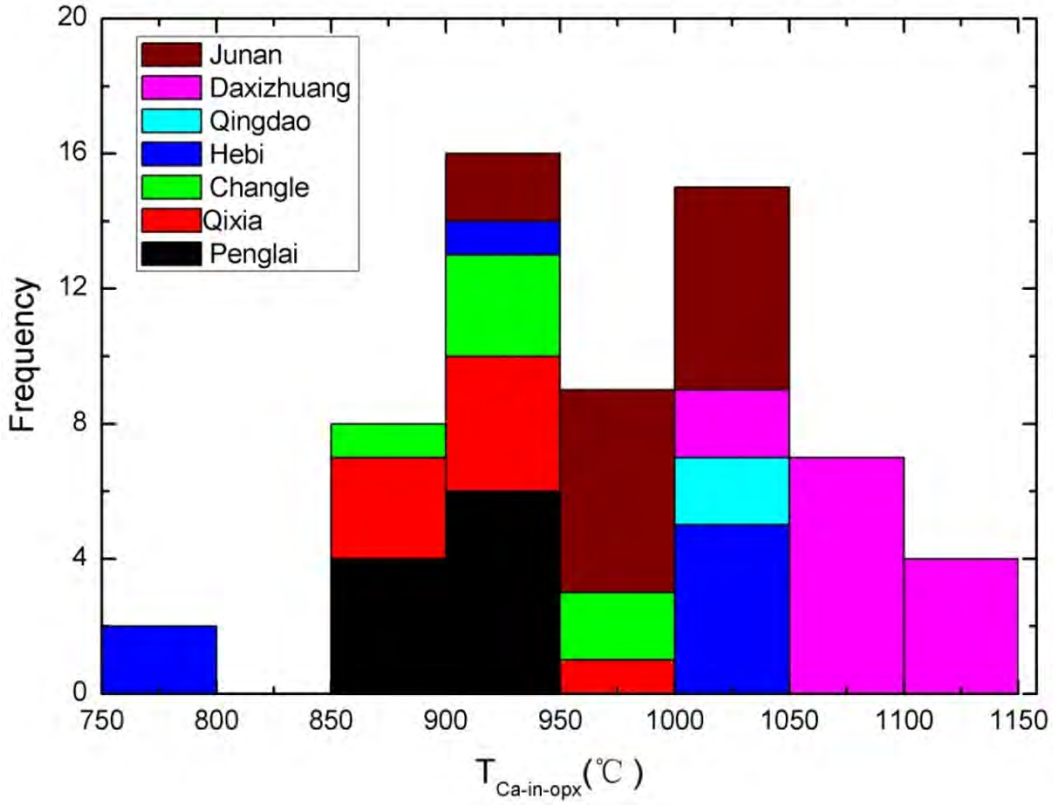

Figure 4-3 The hisgram of the temperature estimates of the NCC peridotites xenoliths in this study.

4.2 LA-ICP-MS results for Trace element

Trace element compositions of cpx in 47 mantle xenoliths from the eastern NCC

were conducted by LA-ICP-MS. Among them 10 xenoliths from Pengali, 7 xenoliths from Qixia, 5 xenoliths from Changle, 2 xenoliths from Hebi, 2 xenoliths from Qingdao, 9 xenoliths from Daxizhuang and 12 xenoliths from Junan. At least four analysis points has been performed within grain or between grains for each xenolith sample. The results show no obvious heterogeneity within sample, so the average compositions are presented in Table 4-6. Trace element is presented here and discussed in the following chapter in two forms: all the trace elements together (all incompatible elements (REEs, LILE, LFSE)) and REEs as a unique group of elements. Because REEs have similar properties that vary as a smooth function of size in geochemical system, making them a very power tool in studying igneous processes and related mantle metasomatism.

The REE patterns of cpx in the peridotite xenoliths from the NCC are quite variable, ranging from LREE-depleted to relatively smooth LREE-enriched patterns to others having convex-upward patterns with a maximum among the LREE and MREE (both $(La/Nd)_N$ and $(Yb/Nd)_N$ ratios of less than unity). Among the peridotite xenoliths five distinct groups can be identified according to their distinct chondrite-normalized REE patterns (both the relative and absolutely abundances).

Group I, with LREE-depleted pattern;

Group II, with convex-upward pattern;

Group III, with flat REE pattern;

Group IV, with LREE-enriched pattern;

Group V, with V or spoon-shaped pattern.

Normally, REEs are subdivided into three groups: LREEs are referred to the elements of La to Nd; MREEs, of Sm to Tb; HREE, of Dy to Lu. We also use several REE abundance ratios as a measure of slopes on a chondrite-normalized REE diagram; e.g., La/Yb reflects fractionation between the typically highly incompatible LREE and relatively more compatible HREE. Yb is used rather than Lu because Yb is more abundant and determined with higher precision; Ce/Yb is also used when La data lacks. Tb/Yb ratios are used because, unlike cpx, spinel and plagioclase, garnet is effective in changing the abundance ratio of these two REEs. So this ratio can be employed to justify the garnet in the melting source or not. Some peridotites are preferentially depleted in the intermediate atomic number REE, Sm to Tb. A measure of this depletion is given by Tb/Yb and La/Sm or Ce/Sm ratios. Sm/Nd ratios are also used because this is the parent/daughter ratio that controls the abundance of ^{143}Nd.

Table 4-6. Trace element Concentrations in cpx of the peridotite xenolith in this study

Samples	Ba	Th	U	Nb	La	Ce	Pb	Pr	Sr	Nd	Sm	Zr	Hf	Eu	Ti	Gd	Tb	Dy	Y	Ho	Er	Tm	Yb	Lu
												ppm												
Penglai																								
PL-01	-	0.01	-	0.10	0.37	1.45	0.02	0.30	34.46	2.19	0.95	13.75	0.51	0.42	1861.58	1.58	0.31	2.16	12.53	0.50	1.35	0.20	1.30	0.19
PL-10	0.01	0.03	0.01	0.24	0.33	1.22	0.02	0.28	28.56	2.06	0.95	11.35	0.44	0.42	1841.72	1.44	0.28	1.92	11.00	0.42	1.20	0.18	1.19	0.17
PL-17	0.00	0.01	0.00	0.09	0.38	1.48	0.03	0.32	35.48	2.21	1.03	14.63	0.54	0.42	1923.73	1.66	0.32	2.22	12.68	0.50	1.40	0.20	1.33	0.19
PL-19	0.01	0.15	0.06	0.06	0.95	2.59	0.09	0.45	50.03	2.76	1.11	20.81	0.64	0.47	2017.51	1.69	0.32	2.17	12.67	0.48	1.37	0.20	1.33	0.19
PL-31	0.01	0.03	0.01	0.23	0.31	1.13	0.02	0.26	26.45	1.88	0.89	10.13	0.40	0.38	1709.57	1.44	0.27	1.80	10.40	0.41	1.13	0.17	1.11	0.17
PL-32	-	-	-	0.25	5.88	17.99	0.19	2.81	106.68	13.94	3.38	114.12	3.00	1.05	1893.79	2.99	0.44	2.49	11.79	0.47	1.19	0.15	0.99	0.14
PL-36	-	0.01	0.00	0.10	0.38	1.41	0.02	0.30	33.89	2.06	0.91	13.70	0.53	0.42	1851.49	1.59	0.31	2.09	12.27	0.47	1.33	0.19	1.29	0.19
PL-42	-	0.01	0.00	0.01	0.24	1.17	0.02	0.29	27.04	2.10	0.99	14.54	0.55	0.47	1958.32	1.77	0.35	2.24	13.39	0.53	1.45	0.20	1.39	0.20
PL-44	-	0.01	0.00	0.04	0.91	3.31	0.05	0.60	61.22	3.68	1.47	29.96	0.93	0.60	2646.74	2.11	0.39	2.63	14.75	0.59	1.62	0.23	1.51	0.22
PL-46	-	0.14	0.03	0.46	2.43	4.70	0.06	0.59	59.58	2.75	0.64	9.62	0.25	0.22	286.19	0.64	0.10	0.57	3.35	0.13	0.37	0.06	0.41	0.07
Qixia																								
QX-01	0.02	0.07	0.02	0.07	1.66	3.20	0.01	0.38	18.33	1.52	0.30	4.71	0.14	0.09	191.30	0.23	0.04	0.27	1.78	0.07	0.23	0.04	0.29	0.04
QX-14	0.00	0.00	0.00	0.01	0.15	0.89	0.02	0.23	22.39	1.80	0.93	12.68	0.55	0.41	1941.76	1.70	0.32	2.23	13.03	0.51	1.44	0.21	1.36	0.20
QX-18	0.03	0.07	0.02	0.11	0.90	1.94	0.02	0.24	12.01	1.02	0.22	1.72	0.04	0.07	162.53	0.21	0.04	0.29	1.93	0.07	0.25	0.04	0.30	0.05
QX-49	1.75	0.04	0.01	0.10	1.33	4.50	0.05	0.77	57.01	4.37	1.27	11.10	0.34	0.53	1575.14	1.66	0.31	2.02	11.31	0.44	1.18	0.17	1.17	0.17
QX-50	0.04	0.20	0.07	0.25	4.00	4.82	0.06	0.37	15.56	1.20	0.17	3.32	0.09	0.06	176.18	0.22	0.04	0.29	1.91	0.07	0.24	0.04	0.25	0.04
QX-51	0.40	0.07	0.02	0.04	2.10	6.62	0.25	1.09	69.79	6.20	1.76	21.45	0.77	0.66	1924.30	2.24	0.37	2.39	12.86	0.50	1.41	0.19	1.23	0.18
QX-57	0.02	0.19	0.03	0.03	12.75	39.43	0.57	5.90	253.02	27.54	5.04	28.00	0.69	1.35	1533.54	3.37	0.40	1.93	8.43	0.32	0.74	0.10	0.58	0.08
Changle																								
CL-01	0.00	-	-	0.58	3.47	5.96	0.16	0.66	82.09	3.04	0.78	9.82	0.26	0.27	991.82	1.03	0.19	1.24	7.45	0.29	0.88	0.12	0.86	0.13
CL-22	0.00	-	-	0.36	9.49	23.00	0.14	2.71	159.66	11.44	2.33	27.66	0.78	0.81	2335.75	2.22	0.36	2.09	11.22	0.46	1.23	0.17	1.10	0.15
CL-31	0.01	0.32	0.08	0.37	5.99	14.21	0.16	1.70	98.74	6.25	1.05	10.19	0.30	0.41	1072.25	1.35	0.25	1.74	9.53	0.39	1.05	0.15	1.00	0.13
CL-38	0.12	-	-	0.00	0.40	1.00	0.17	0.22	22.35	1.57	0.70	14.02	0.49	0.31	1471.13	1.17	0.22	1.54	8.91	0.35	0.97	0.14	0.94	0.14
Hebi																								
HB-01	0.24	0.51	0.16	0.92	12.47	34.47	0.55	4.31	490.15	16.77	2.15	10.48	0.34	0.57	205.32	1.22	0.09	0.26	0.87	0.04	0.08	0.01	0.09	0.01
HB-64	0.07	-	-	0.16	2.12	9.58	0.14	1.76	268.62	9.41	2.05	11.58	0.49	0.63	359.54	1.57	0.20	0.98	4.14	0.17	0.39	0.05	0.32	0.05
Qingdao																								
QDPS-24	0.55	0.45	0.12	0.14	2.18	3.80	0.02	0.28	30.74	0.51	0.18	0.08	0.05	0.09	541.10	0.53	0.12	0.95	6.43	0.25	0.78	0.11	0.76	0.11
QDPS-16	0.43	0.03	0.01	0.17	0.09	0.08	0.00	0.02	23.65	0.36	0.44	1.08	0.18	0.19	1054.68	0.99	0.22	1.61	9.47	0.38	1.05	0.16	1.00	0.15
Daxizhuang																								
DXZ-01	0.11	-	-	0.63	1.07	3.52	0.02	0.65	66.26	4.11	1.61	28.74	0.93	0.65	2867.47	2.25	0.43	2.78	15.48	0.60	1.66	0.23	1.43	0.21
DXZ-02	0.57	-	-	0.24	1.18	1.90	0.01	0.16	18.12	0.45	0.09	0.64	0.03	0.04	282.30	0.23	0.06	0.52	3.55	0.14	0.40	0.07	0.46	0.06
DXZ-04	0.35	-	-	0.57	3.02	7.28	0.09	1.03	81.97	5.81	2.01	30.66	0.69	0.70	865.72	2.17	0.28	1.45	7.34	0.29	0.74	0.10	0.68	0.10
DXZ-14	0.06	-	-	0.35	4.78	11.33	0.06	1.49	119.80	6.76	1.42	11.70	0.18	0.39	409.30	1.05	0.14	0.80	4.30	0.17	0.45	0.06	0.43	0.06
DXZ-17	0.09	-	-	0.32	1.24	1.61	0.02	0.14	11.01	0.55	0.21	2.06	0.12	0.08	416.80	0.38	0.07	0.45	2.43	0.10	0.27	0.04	0.28	0.04
DXZ-27	0.01	-	-	0.39	0.93	1.80	0.09	0.22	19.53	1.00	0.44	3.03	0.17	0.19	782.52	0.85	0.18	1.19	7.37	0.29	0.84	0.12	0.76	0.12
DXZ-36	0.01	-	-	0.34	3.27	7.04	0.15	0.76	68.12	2.98	0.72	3.82	0.14	0.28	779.29	0.93	0.18	1.21	7.33	0.29	0.79	0.12	0.75	0.11
DXZ-39	0.03	-	-	0.14	0.43	0.83	0.02	0.11	9.71	0.68	0.25	2.91	0.09	0.10	297.66	0.39	0.08	0.61	3.63	0.13	0.42	0.06	0.44	0.06
DXZ-42	0.40	-	-	0.18	0.59	1.57	0.01	0.24	18.07	1.33	0.42	4.39	0.14	0.16	633.32	0.56	0.09	0.79	4.09	0.15	0.45	0.07	0.47	0.06
Junan																								
jn-03	0.22	0.33	0.09	0.16	1.32	2.87	0.19	0.52	64.37	3.14	1.27	23.86	0.80	0.53	2307.42	1.84	0.34	2.30	12.63	0.50	1.40	0.20	1.29	0.19
jn-11	0.02	0.01	0.00	0.06	0.62	2.32	0.08	0.46	44.58	2.98	1.25	18.32	0.72	0.48	2201.87	1.82	0.33	2.26	12.74	0.50	1.40	0.21	1.31	0.19
jn-24	0.06	0.03	0.01	0.18	0.87	2.88	0.04	0.51	59.66	3.28	1.22	23.84	0.79	0.50	2300.77	1.94	0.36	2.29	13.11	0.51	1.41	0.21	1.31	0.19
jn-26	0.00	0.03	0.01	0.17	1.09	3.27	0.11	0.51	56.69	2.98	1.20	20.28	0.68	0.51	2347.72	1.76	0.34	2.36	13.35	0.51	1.42	0.21	1.34	0.20
jn-35	0.95	0.22	0.05	0.82	3.87	11.71	0.15	1.81	112.98	9.49	2.57	45.45	1.21	0.90	2408.44	2.78	0.47	2.94	15.80	0.63	1.70	0.24	1.57	0.22
jn-43	0.15	0.03	0.01	0.06	0.76	2.55	0.00	0.47	58.46	3.09	1.28	25.04	0.81	0.57	2593.49	1.96	0.39	2.54	14.34	0.56	1.53	0.23	1.45	0.21
jn-44	0.12	0.01	0.00	0.07	0.99	3.86	0.06	0.69	59.00	4.23	1.62	30.10	0.96	0.66	2838.96	2.35	0.42	2.80	15.64	0.61	1.69	0.24	1.50	0.22
jn-47	0.00	0.00	0.00	0.04	1.01	3.81	0.01	0.69	59.92	4.23	1.62	29.60	0.97	0.66	2821.74	2.21	0.42	2.82	15.74	0.61	1.61	0.23	1.54	0.22
jn-53	0.04	0.18	0.05	0.60	3.51	10.51	0.09	1.67	107.24	8.34	2.27	37.50	0.99	0.81	2380.17	2.52	0.43	2.72	14.71	0.59	1.60	0.23	1.50	0.21
jn-54	0.08	0.18	0.05	0.41	3.37	10.28	0.12	1.60	101.49	8.17	2.15	38.70	1.00	0.78	2265.73	2.47	0.43	2.68	14.99	0.58	1.56	0.23	1.47	0.21
jn-59	0.02	0.01	0.00	0.07	1.10	3.47	0.00	0.59	68.43	3.49	1.30	22.00	0.79	0.58	2643.36	2.05	0.36	2.50	14.35	0.55	1.53	0.22	1.45	0.21
jn-65	0.06	0.02	0.01	0.16	0.83	2.72	0.05	0.48	57.27	3.12	1.28	23.34	0.76	0.52	2315.72	1.84	0.35	2.40	13.41	0.53	1.39	0.20	1.38	0.20

Group I LREE-depleted pattern

This pattern, characteristic of the depleted mantle, is the most common type seen in fertile lherzolite xenoliths worldwide. Cpx of this pattern have varyingly fractionated LREE/HREE ($(La/Yb)_N < 1$) with depleted LREE abundances relative to near chondritic absolute abundances of HREE. There is no obvious fractionation among HREE and MREE, showing a line with flat or slightly positive slope in the REE normalized pattern.

Group II - Upward convex pattern

This pattern is characterized by relative LREE and MREE enrichments with convex upwards in the region of MREE and a maximum at position of element Sm or Nd. Most samples of this group have $(La/Sm)_N$ less than unity and $(Sm/Yb)_N$ greater than unity. This kind of pattern is usually found in the peridotite walls that are close to the anhydrous pyroxenite veins, and these vein in composite xenoliths are believed to high pressure segregations (fractionation) of tholeiitic magmas (the amphibole-bearing pyroxenites as evidence for high pressure fractionation of alkali magmas).

Group III - Flat REE pattern

The cpx of the type has a nearly flat REE normalized patterns with depleted abundances. The ratios of both $(La/Yb)_N$ and $(Tb/Yb)_N$ are near to unity, with low absolute abundances (3~5X chondritic). The xenoliths of the pattern may not represent the fragments of primitive mantle that escaped the ancient melt depletion related to the origin of the continent crust. It is more likely to be a consequence of the combination of melt depletion with the subsequent enrichment processes. This kind of pattern is rare in the xenoliths here, and only one sample from Daxizhuang shares this feature.

Group IV - LREE-enriched pattern

This is a common REE pattern that usually is found in mantle xenoliths, most the refractory harzburgite. They are usually characterized by strong LREE enrichment and varying MREE enrichment, but LREE see the enrichment increasingly grow from Nd to La with strong fractionated (La/Nd). There is no obvious fractionated within HREEs that have relative less absolute abundances.

Group V - Spoon-shaped pattern

This REE pattern was first found by Bodinier et al., (1989) in harzburgite wall rocks that are close to an amphibole pyroxenite vein. In that case, The harzburgites are characterize by strongly LREE-enriched patterns, with "V-shaped" ($(La)_N$~1 and $(Yb)_N$~0.1). In general, the pattern is like the combination of the MREE and HREE part of **Group I,** where the line remains relatively stable from Lu to Dy, with going down mildly from Tb to Sm, and the LREE part of **Group IV**.

Patterns in Penglai xenoliths

In the xenolith here, three types of REE pattern can be identified (Fig. 4-4a). PL46

belongs to Group II; PL32, Group IV and the rest, Group I.

The REE normalized pattern in PL46 cpx displays HREE from Lu to Dy depleted at ~ 2 X chondritic, ane less depleted LREE from Tb to La, with $(Tb)_N$=3.8 and $(La)_N$=14.5. The PL32 cpx, of Group IV, has fractionated LREE/HREE (La_N=35.1; Yb_N =8.5) with enriched LREE flattening from Ce to Nd. In addition, the cpx in PL32 and PL46 have a similar positive slope ($(Nd/Dy)_N$=3) for the Middle region (between Nd and Dy) in the REE patterns. The rest of the samples show a group of lines with relative LREE depleted, with $(La)_N$ ranging from 1.4 to 5.7 and the ratio of $(La/Yb)_N$ from 0.1 to 0.5. HREEs are roughly un fractionated, fixing at 9.5~13.0 for $(Yb)_N$ and ~1.1 for $(Tb/Yb)_N$ and MREE slightly fractionated, varying from 8.5 to 14.0 in $(Sm)_N$, and 0.70 to 0.93 in the ratio of $(Sm/Tb)_N$.

All the samples have more or less the same primitive mantle-normalized incompatible elements plots (Fig. 4-4b), characterized by the depletions in HSFEs with obvious negative anomalies in Ti (Ti*=0.2~0.6) and Nb (Nb/La=0.04~0.73), but not Zr or Hf, and highly depletions in LILEs and soluble elements, such as Pb, U, Th, and Rb whose analyses are always beyond the detect limit and are not presented in the array of elements.

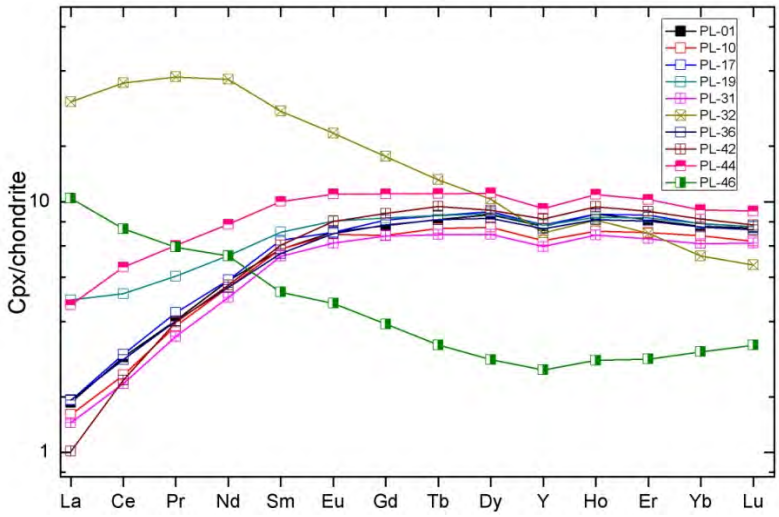

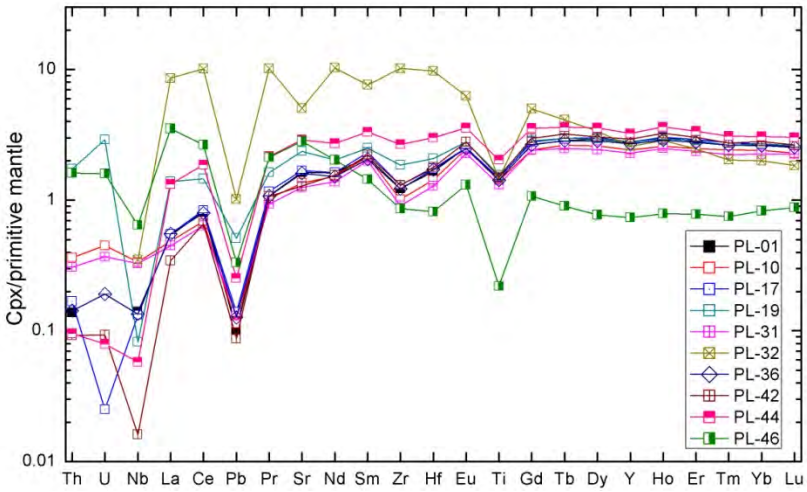

Figure 4-4. Trace element distribution patterns for cpx from Penglai peridotite xenoliths. (a) Chondrite-normalized REE patterns, and (b) Primitive mantle-normalized trace element patterns.

Patterns in Qixia xenoliths

The cpx patterns can be subdivided into three groups at a glance of their HREE stackings (Fig. 4-5a). The QX14 cpx, together with the cpx in QX49 and QX51, have the highest HREE contents of ~11X chondritic and share the same flat-shaped in MREE-HREE region in REE normalized patterns. The Difference is that the cpx in QX49 and QX51 extend this flattening to LREE region with $(La/Yb)_N$ ratio ranging between 0.8 and 1.2, whereas QX14 cpx turn to go down to form a LREE-depleted pattern with $(La/Yb)_N$ ratio as low as 0.07.

The cpx in QX49 and QX51 have roughly flat-shaped REE patterns ($(La/Yb)_N$=0.8~1.2) with slightly upwards convexity ($(La/Nd)_N$=0.59~0.65; $(Sm/Tb)_N$=1.1~1.3) in the MREE region and a maximum at Nd (Nd_N, 13.5 and 19.2). These two samples have the same HREE distribution and absolute abundances.

The cpx in QX01, QX18 and QX50 have the lowest HREE contents at level of ~ 2.5 X chondritic in term of Yb_N. They all belong to the LREE-enriched pattern. These three cpx have similar HREE and MREE contents but different enrichments in LREE, varying from 2.1 in QX18 to 11.0 in QX50 for $(La/Yb)_N$.

In the spider pattern (Fig. 4-5b), that grouping remains, but they share more or less the same features, showing negative anomalies for HSFE, e.g. Ti (Ti*=0.33~0.56), Zr (0.56~0.90), Hf and Nb, and also negative anomalies for Pb (Pb*=0.05~0.35).

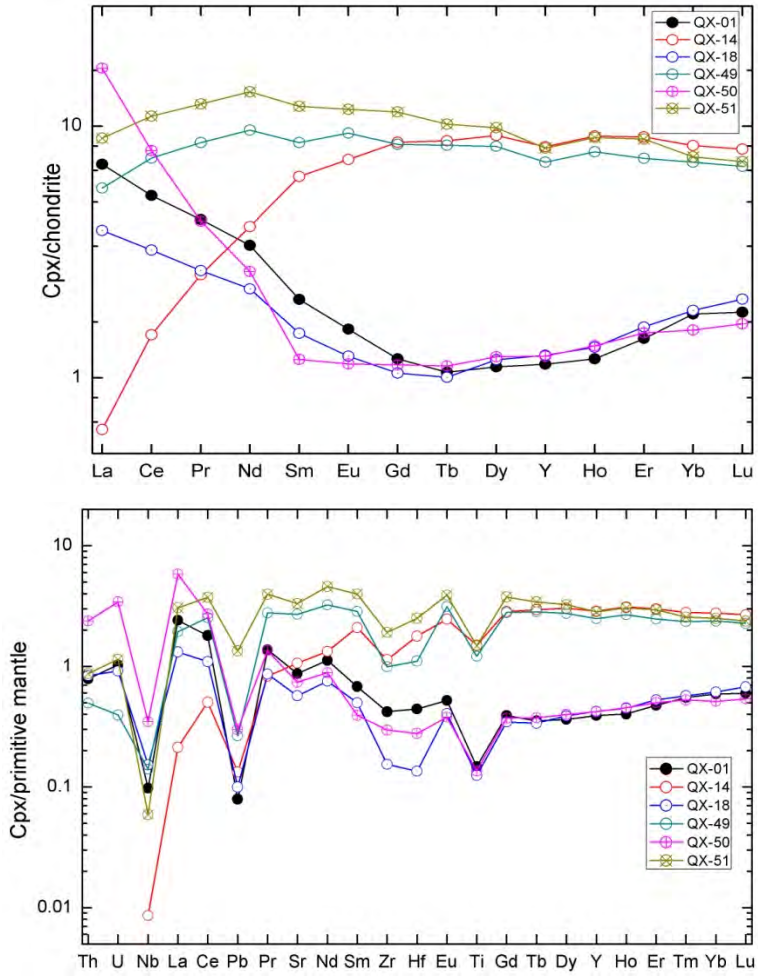

Figure 4-5. Trace element distribution patterns for cpx from Qixia peridotite xenoliths. (a) Chondrite-normalized REE patterns, and (b) Primitive mantle-normalized trace element patterns

Patterns in Changle xenoliths

The cpx in CL38, characteristic of LREE-depleted pattern, has low ratio of (Ce/Yb)N=0.3 with relative enrichment of HREE at the level of ~8 X chondritic. The cpx in CL01, LREE-enriched group, shows a similar both MREE-HREE pattern and contents but LREE enrichment with a $(La/Yb)_N$ ratio of 3.6. The cpx in CL22 and CL31, display relatively strong LREE enrichments, 34 and 57 for $(La)_N$ and 3.6 and 6.0 for $(La/Yb)_N$ ratio. They differ mainly at different patterns for MREE. In a word, these cpx have the similar MREE and HREE abundances and patterns but different LREE absolute abundances and pattern, varying from depleted pattern in CL38 to enriched pattern in CL22 ((Fig. 4-6a)).

The cpx show strong depletion in HFSEs such as Ti, Zr, Hf, Nb, and negative Pb

anomalies on primitive-mantle normalized multi-element plots (Fig. 4-6b).

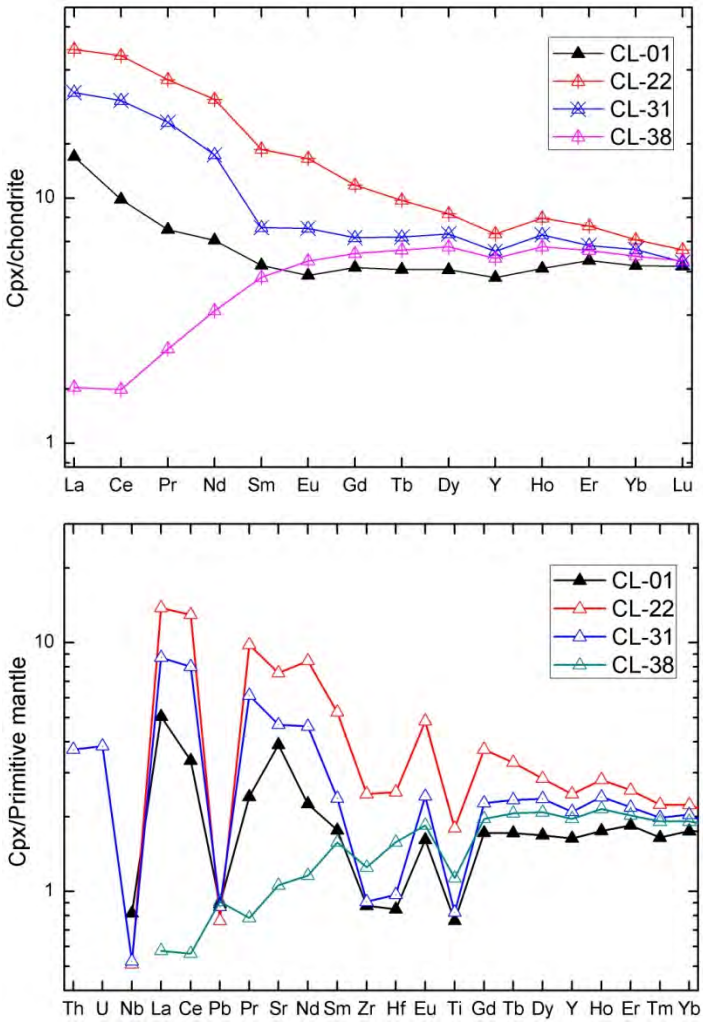

Figure 4-6. Trace element distribution patterns for cpx from CL peridotite xenoliths. (a) Chondrite-normalized REE patterns, and (b) Primitive mantle-normalized trace element patterns.

Patterns in Hebi xenoliths

The HB cpx are highly LREE enriched (La_N=46~74), HREE depleted (Yb_N=0.8~3.4) and MREE fractionated, with the $(Sm/Yb)_N$ ratio ranging between 10 and 26 (Fig. 4-7a). It is noted that the HB01 cpx that displays the lowest HREE contents here and also among all the cpx from the NCC in this thesis, is also the most strongly fractionated in LREE/HREE ($(Ce/Yb)_N$=100.5) and highest in LREE abundances (Ce_N=80).

The cpx show obvious depletion in HFSEs such as Ti, Zr, Hf, Nb, and negative Pb anomalies on primitive-mantle normalized multi-element plots (Fig. 4-7b).

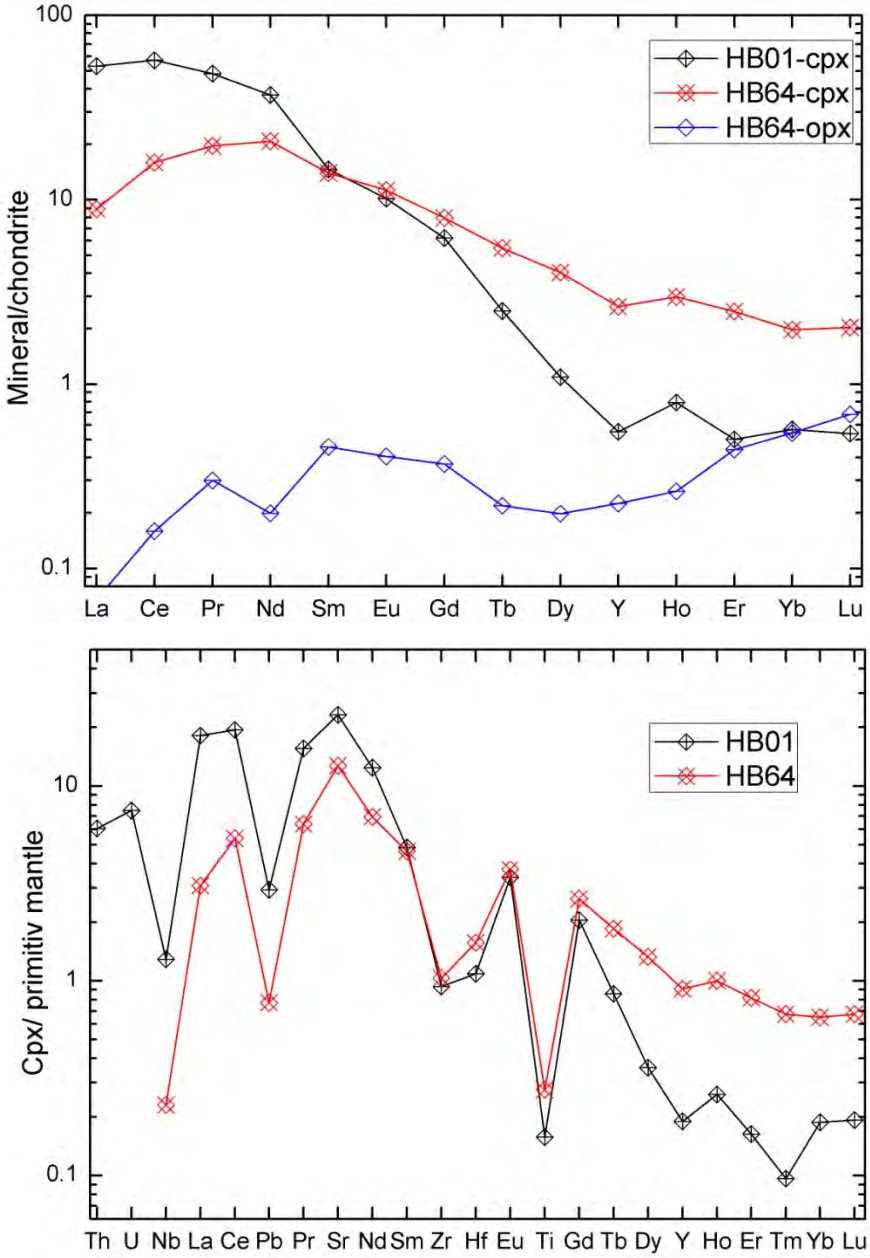

Figure 4-7. Trace element distribution patterns for cpx from Hebi peridotite xenoliths. (a) Chondrite-normalized REE patterns, and (b) Primitive mantle-normalized trace element patterns

Patterns in Junan xenoliths

All lherzolites display the similar HREE features in term of both contents (Yb_N=11~13) and normalized patterns ($(Tb/Yb)_N$=1.1~1.3) (Fig.4-8a), but show different LREE features. The first cpx group, including these in JN43, JN53 and JN54, are characterized by slight LREE enrichments ($(La/Yb)_N$=1.60~1.70) with upwards convex in the MREE region and maximum at position of Nd ($(La/Nd)_N$=0.79~0.81; $(Nd/Yb)_N$=2.0~2.2). Those cpx in the rest of lherzolites show the group of lines with slight different levels (La_N=5.0~7.9 X chondritic) but exactly

the same positive slope in the LREE region ($(Ce/Sm)_N$=0.55~0.66). They are classic LREE-depleted patterns that most seen in fertile lherzolites.

In primitive mantle normalized multi-element plots (Fig. 4-8b), the two groups of cpx display the same trend style (of lines) just with slight differences in absolute abundances for those elements that are more incompatible than Gd (e.g. those element on the left of Gd). All cpx show the pronounced negative anomalies at both Pb (Pb*=<0.03~0.58) and and Nb, and high depletions in Rb and a slight negative Ti anomalies (Ti*=0.37~0.59) without the same anomalies at Zr or Hf.

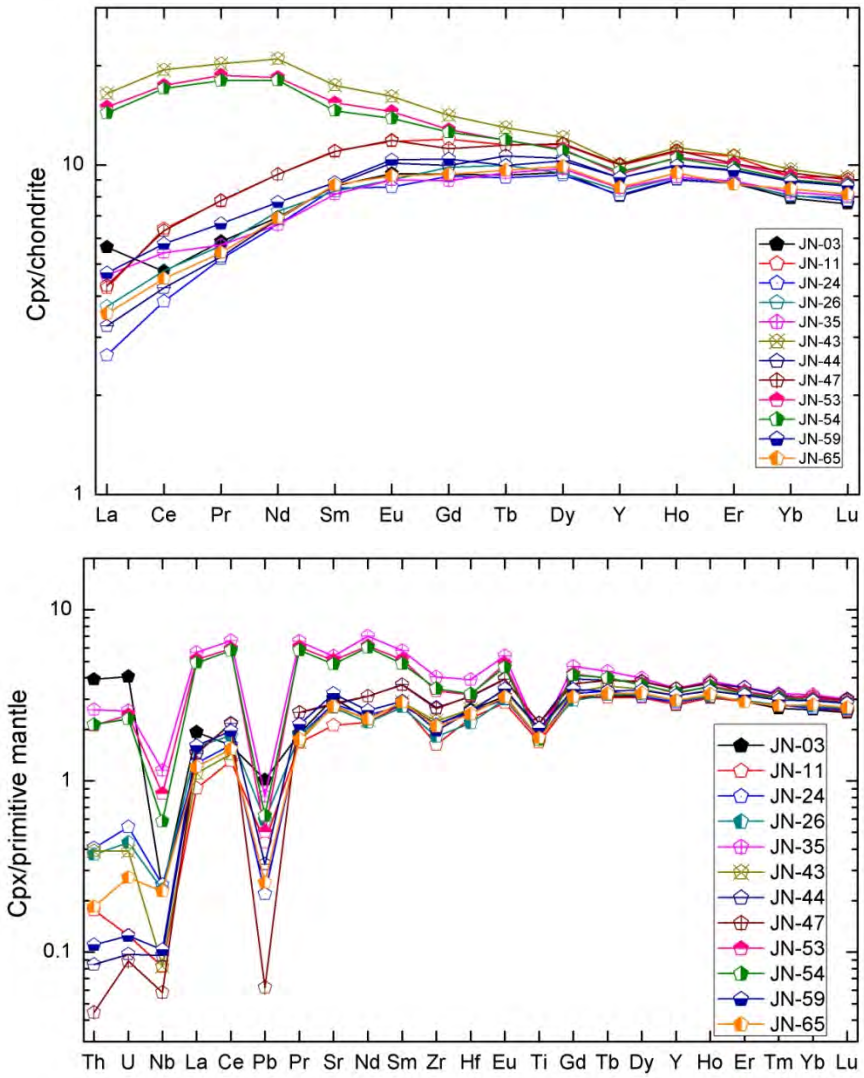

Figure 4-8. Trace element distribution patterns for cpx from Junan peridotite xenoliths. (a) Chondrite-normalized REE patterns, and (b) Primitive mantle-normalized trace element patterns.

Patterns in Qingdao xenoliths

The cpx in both QDPS16 and QDPS24 share the same MREE-HREE pattern that sees two line move in parallel from Lu to Sm, where two line diverge, with the line of QDPS24 turning to subduct deeply to form a LREE-depleted pattern with $(Ce/Yb)_N$

ratio of 0.02 and the other line for QDPS16 rising up to form a "spoon" as a whole (Fig. 4-9a).

In the multi-element plots (Fig. 4-9b), these cpx share the same patterns for the moderately incompatible elements (those on the right of Sm), with significant negative Zr anomalies, especially for QDPS24 (Zr*=0.03), and minor Ti negative anomalies (~0.60). The QDPS24 cpx is characterized by slight LILE enrichments with $(U/La)_N$ ratio of 1.73, with pronounced negative Nb and Pb anomalies, and highly depletion in Rb. The QDPS16 cpx, on the other side, are depleted in LILE with a highly negative Pb anomalies but an elevated $(U/La)_N$ ratio of 2.5, which may record the very initial beginning of a enrichment process.

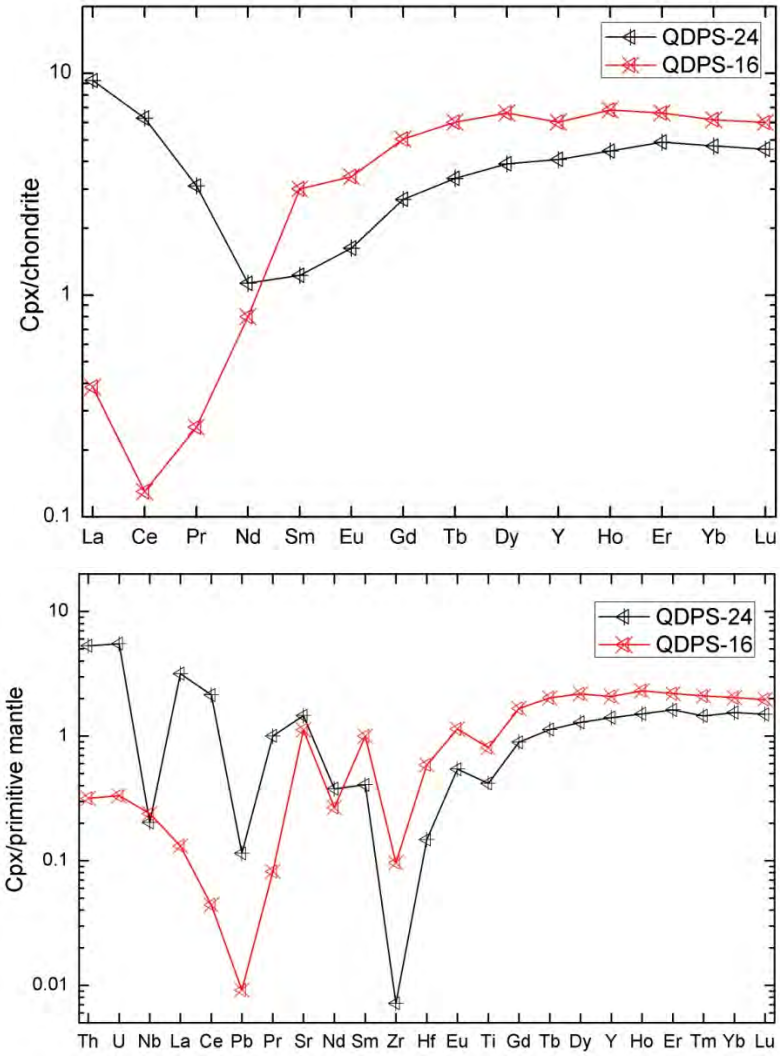

Figure 4-9. Trace element distribution patterns for cpx from Qingdao peridotite xenoliths. (a) Chondrite-normalized REE patterns, and (b) Primitive mantle-normalized trace element patterns

Patterns in Daxizhuang

All the cpx are characterized by the relatively Flat MREE-HREEs distribution in

the normalized REE patterns, but with varying absolute abundance, ranging from 2.4 to 12.4 in $(Yb)_N$ (Fig. 4-10a). The LREE patterns, by contrast, is variable, ranging from the relative depletion in DXZ01 ($(La/Yb)_N$=0.5) to the relative enrichment in DXZ14 ($(La/Yb)_N$=7.8) in the normalized REE patterns. All five types of REE patterns can be found among DXZ samples. The DXZ01 belongs to the LREE-depleted REE pattern; the DXZ17 and DXZ36 the LREE-enriched REE pattern; the DXZ04 and DXZ14 the upward convex REE pattern; the DXZ42 and DXZ39 the flat REE pattern and the DXZ02 and DXZ17 the spoon-shaped REE pattern (Fig. 4-9a).

In the primitive mantle normalized multi-element plot, all the cpx have relative flat pattern with different absolute abundances, and show the obvious depletion in Ti, Zr, and Nb, and negative Pb anomalies that is characteristic of mantle-derived magmas (Fig. 4-10b).

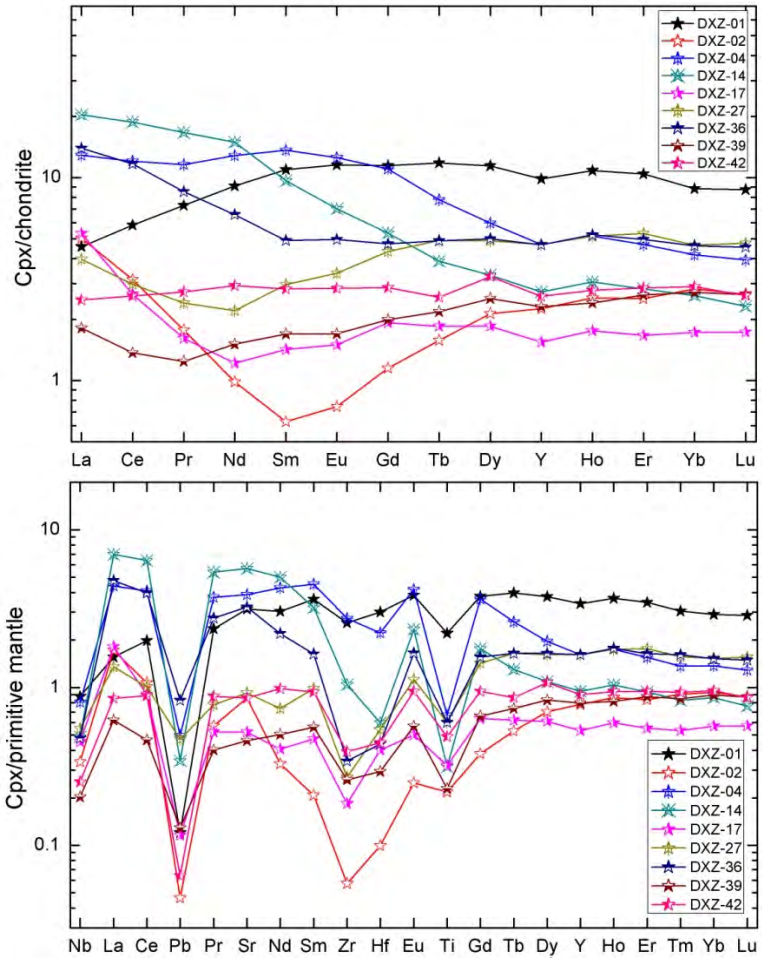

Figure 4-10. Trace element distribution patterns for cpx from Daxizhuang peridotite xenoliths. (a) Chondrite-normalized REE patterns, and (b) Primitive mantle-normalized trace element patterns.

4.3 FTIR results

4.3.1 H-related species in mineral structural

In the typical OH-stretching vibration region (3000–3700 cm^{-1}), all the spectra of analyzed pyroxene, both cpx and opx, in mantle peridotite xenoliths exhibit several distinct absorption bands that are related to the local OH dipole environments. These absorption bands vary in shapes, positions and intensities among different minerals and grains of different orientations within the same mineral phase. The representative infrared spectra are shown in the following figures (from Fig. 4-11 to Fig. 4-18).

Based on the peak positions, the IR absorption bands of pyroxenes can be divided into different groups for each mineral: 1) clinopyroxene: 3620–3655 cm^{-1}, 3510–3550 cm^{-1}, 3445–3470 cm^{-1}; 2) orthopyroxene: 3570–3605 cm^{-1}, 3500–3525 cm^{-1}, 3390–3415 cm^{-1}, 3300–3315 cm^{-1} (rare). The relative absorbances of these bands vary among grains in the same sample due to the pleochroisic absorptions in pyroxene and the variable orientations of grains with respect to the incident IR beam. The positions of these absorption bands are consistent with previous reports (Skogby and Rossman, 1989; Skogby et al., 1990; Peslier et al., 2002), showing that they are produced by the stretching vibration of structural OH as defect in the crystal lattices. The minerals from different localities, however, have slight differences in both shapes and frequencies of the OH absorption bands (from Fig. 4-11 to Fig. 4-18). These differences may be associated with the chemical compositions and crystal structures, both of which influence the vector environment of the structural O-H in the lattice.

Hydrogen profile measurements conducted on pyroxene grains from the core to the rim regions in each suite of samples show no obvious variations among these regions, indicating that diffusion loss of H in clinopyroxene and orthopyroxene during their ascent is insignificant (Peslier et al., 2002; Demouchy et al., 2006) and that the

ascent rate of host magma is fast enough to struggle against hydrogen-related diffusion induced by decompression and to“freeze” the original information concerning the environment where they are derived (Fig. 4-20).

The olivines in peridotite xenoliths from the NCC show no, or in rare case, very weak absorption bands that are peaked at ~3572 cm^{-1} and 3525 cm^{-1}, typical for mantle olivine previously reported in the literatures (Bell and Rossman, 1992a; Berry et al., 2005; Demouchy et al., 2006; Peslier and Luhr, 2006; Grant et al., 2007b). Absorption of coexisting olivine in these samples is too weak to be distinguished from background noise, suggesting the content is beyond the detect limit (2ppm). Only few olivine grains in few samples from Qingdao and Junan, where coexisting pyroxenes are high in water, show visible O-H absorption bands (Fig. 4-18), still amounting to water content less than 5 ppm. The H profile conduct on a large ol-3 grain indicates no heterogeneity.

Besides these intrinsic OH absorption bands in pyroxene, which are our most concerned, absorption bands from hydrous phases included in the pyroxene structures are sometimes encountered. Absorption bands caused by fluid and glass inclusions that introduced by post-volcanisms on the surface are considerably broader around ~3400cm^{-1} (Fig. 4-19), and can normally be detected by the H_2O bending (1630 cm^{-1}) and combination (5200 cm^{-1}) modes, and their isotropic behavior in polarized measurements. In addition, absorption bands that are related to hydrous mineral alterations can also be identified in the absorption spectra. The Amphibole lamellae, frequently occurring in pyroxenes as alterations, normally have sharp and well-defined OH absorption bands at somewhat higher frequencies (>3680 cm^{-1}) (Fig. 4-19) that can be easily distinguished from those intrinsic OH in pyroxene with lower frequencies (<3650 cm^{-1}) for absorption bands.

These aqueous inclusions and hydrous alterations in pyroxenes were later introduced as byproducts of the secondary processes, like melt infiltration during the entrainments and the weathering in the hydrosphere. So their water contents cannot represent the pre-eruption condition for NAMs in the mantle. Apparently, those “exotic” OH absorption bands, if not excluded entirely, will contribute much to the total absorbance that is supposed to be used for calculating the intrinsic water content in pyroxene.

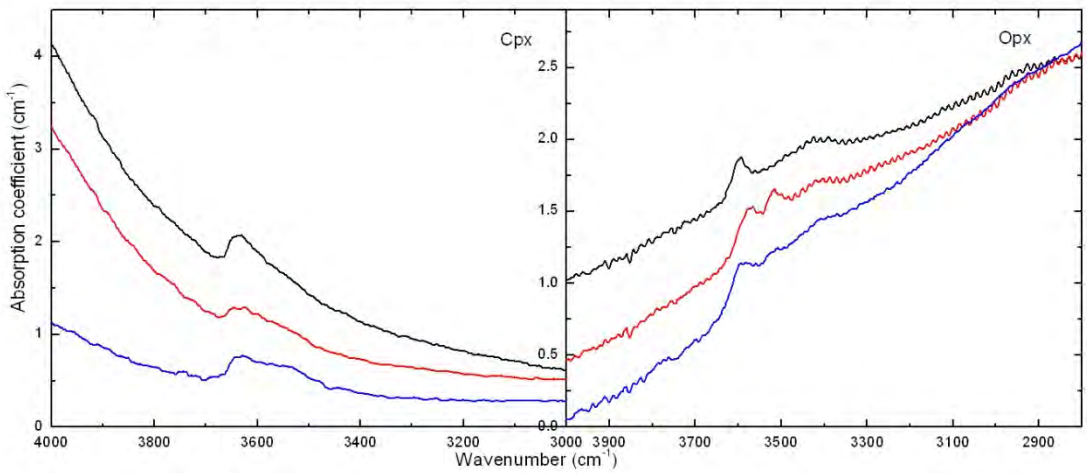

Figure 4-11. Unpolarized IR absorption spectra for Cpx and Opx in the peridotite from Penglai. Normalized to 1 cm thickness and offset for clarity. The spectra are for grains of random orientations in one sample.

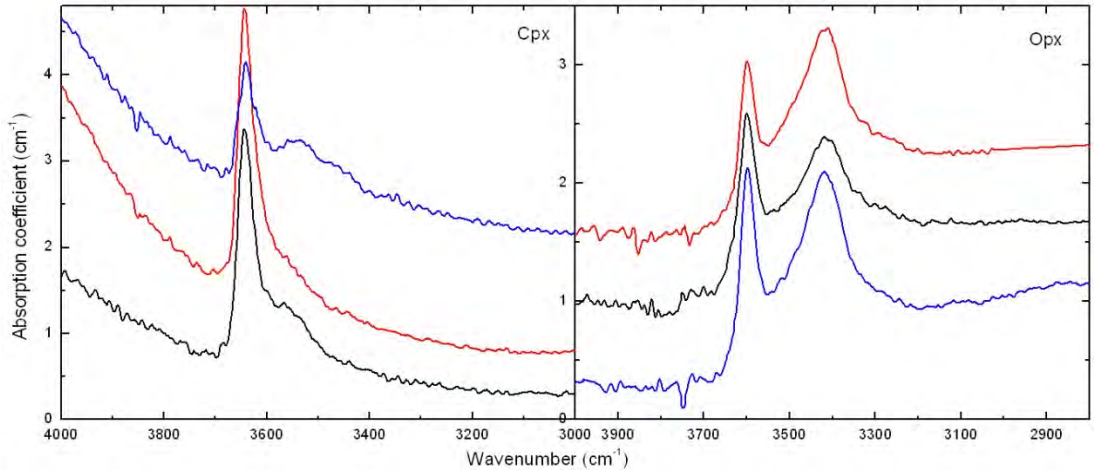

Figure 4-12. Unpolarized IR absorption spectra for Cpx and Opx in the peridotite from Qixia. Normalized to 1 cm thickness and offset for clarity. The spectra are for grains of random orientations in one sample.

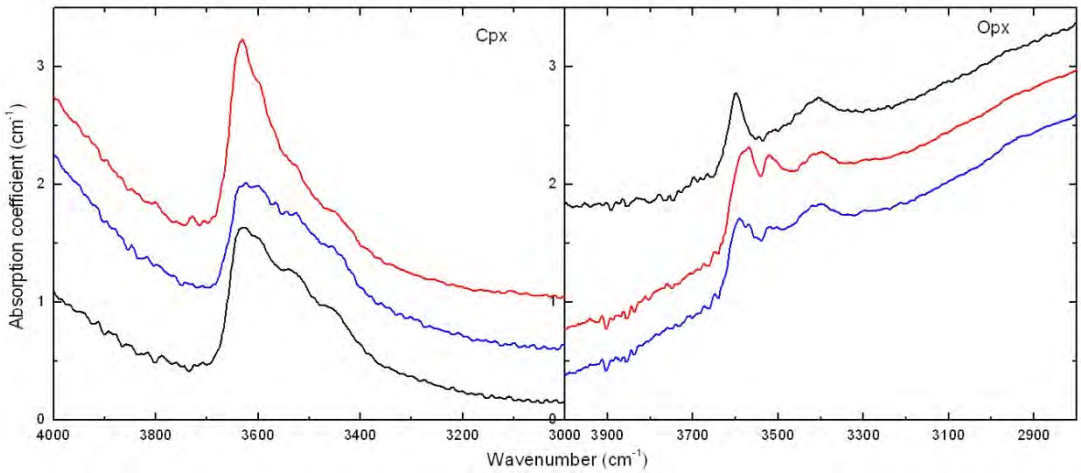

Figure 4-13. Unpolarized IR absorption spectra for Cpx and Opx in the peridotite from Changle. Normalized to 1 cm thickness and offset for clarity. The spectra are for grains of random orientations in one sample.

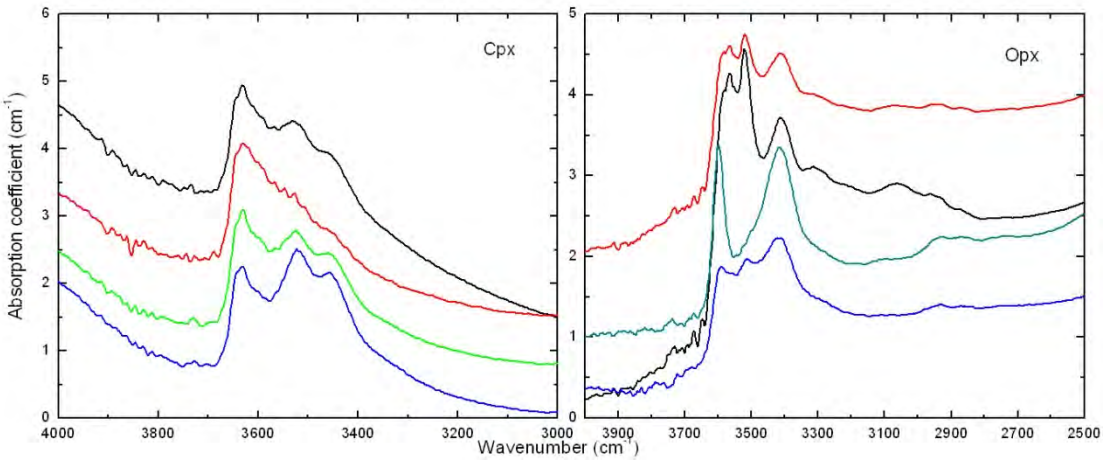

Figure 4-14. Unpolarized IR absorption spectra for Cpx and Opx in the peridotite from Hebi. Normalized to 1 cm thickness and offset for clarity. The spectra are for grains of random orientations in one sample.

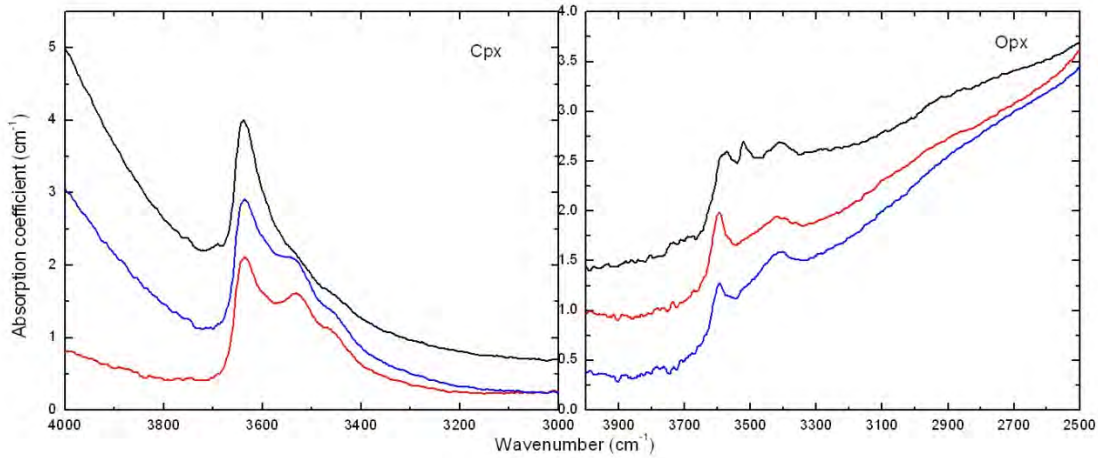

Figure 4-15. Unpolarized IR absorption spectra for Cpx and Opx in the peridotite from Daxizhuang. Normalized to 1 cm thickness and offset for clarity. The spectra are for grains of random orientations in one sample.

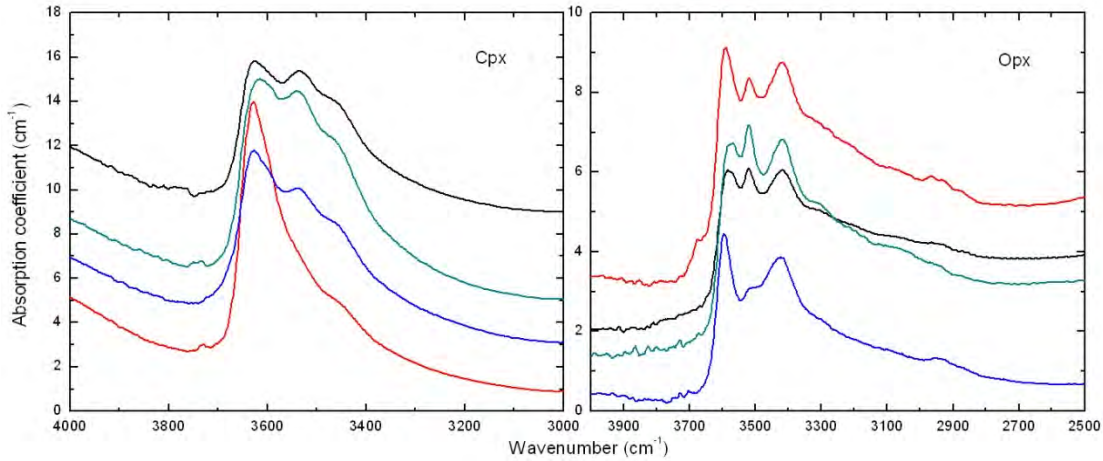

Figure 4-16. Unpolarized IR absorption spectra for Cpx and Opx in the peridotite from Junan. Normalized to 1 cm thickness and offset for clarity. The spectra are for grains of random orientations in one sample.

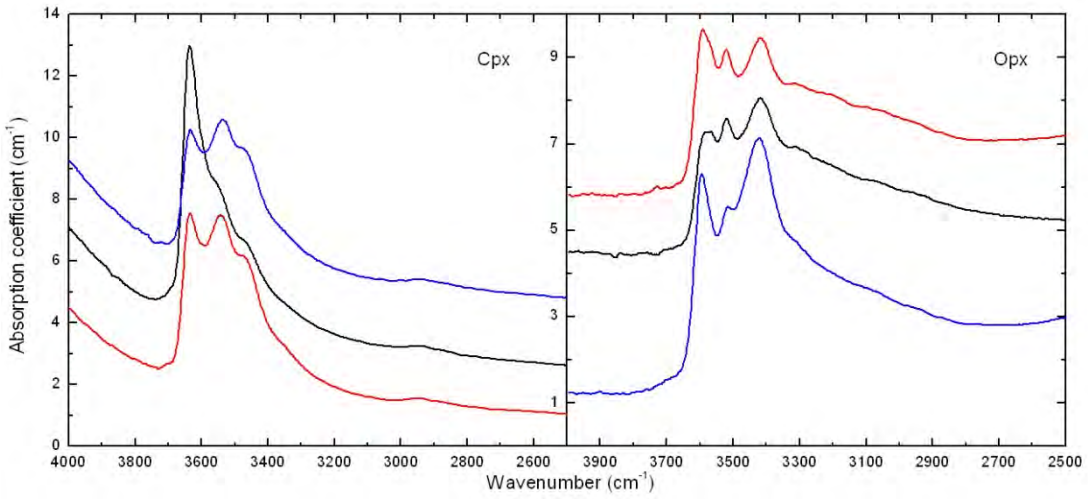

Figure 4-17. Unpolarized IR absorption spectra for Cpx and Opx in the peridotite from Qingdao. Normalized to 1 cm thickness and offset for clarity. The spectra are for grains of random orientations in one sample.

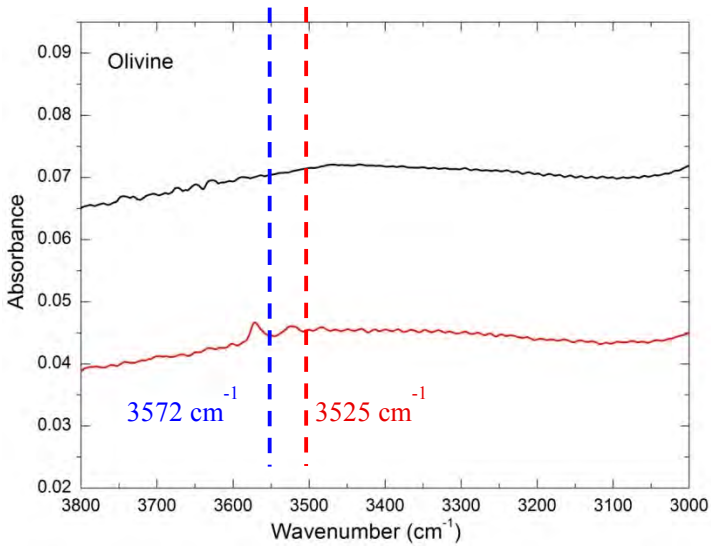

Figure 4-18. Representatives unpolarized IR absorption spectra for olivine in the peridotite from Qingdao. The original spectra remain raw without normalization to 1 cm thickness, and the thickness of grains is about 0.2 mm. Offset was applied for clarity. For most of ol, their spectra do not show any visible OH absorption bands, and the spectra were only and rarely found in few grains from few samples.

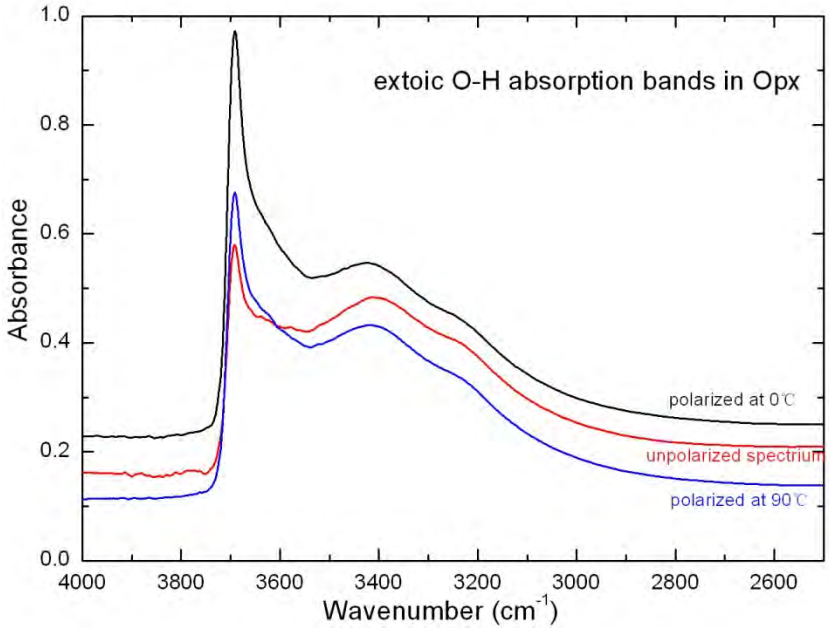

Figure 4-19. Representative of spectra for exotic water (hydrous alteration minerals and fluid inclusions) in mantle pyroxenes. The spectra are not normalized to 1 cm thickness, but offset for clarity.

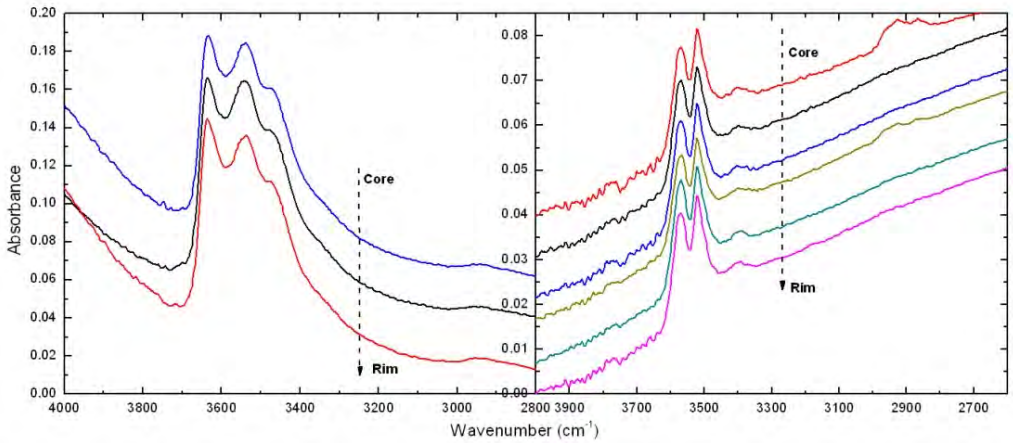

Figure. 4-20 Representative of the H profile conduct on cpx and opx grain. The left pattern is for cpx, and the right pattern for opx.

4.3.2 Water contents in minerals of peridotite

The water contents for cpx and opx in the peridotite xenoliths are given in the Table 4-16. Water contents vary totally from 27 to 746 ppm in cpx and from 8 to 346 ppm in opx. Olivine hardly contains visible OH absorption bands, suggesting the water is too low and the signal/noise ratio is beyond the detect limit (< 2 ppm).

Individually, water contents vary from 27 to 77 ppm for cpx and from 8 to 29 ppm for opx in PengLai xenoliths; from 72 to 175 ppm for cpx and 38 to 72 ppm for opx in Qixia samples; from 71 to 223 ppm for cpx and 25 to 95 ppm for opx in Changle samples; 181 ppm for cpx and 31 to 103 ppm for opx in Hebi samples; from 580 to 728 ppm for cpx and 266 to 346 ppm for opx in Qingdao samples; from 466 to 746 ppm for cpx and 187 to 304 ppm for opx in Junan samples and from 103 to 311 ppm for cpx and 30 to 113 ppm for opx in Daxizhuang samples

It is noted that the pyroxenes in the xenoliths hosted by the Cenozoic basalts generally have much less water contents than those by the Mesozoic basalts. The Daxizhuang xenoliths are not included here, and will be discussed separately. In each locality, the sample with the highest water content in cpx is also the one with the highest water content in opx. This also holds true for the lowest water contents. Moreover, when the water contents of opx and cpx are plotted into the X-Y coordinate system, they correlate well with each other, defining a linear curve with a slope of 2.16 (R^2=0.969, using software OriginPro 8 for linear fit) and meaning that water, if considered a trace element of hydrogen, has approached equilibration partitioning between cpx and opx at the mantle source. Combined with those water contents of pyroxenes from Hannuoba and Nushan (Yang et al., 2008), the other two localities in the NCC, a similar good correlation line with a slope of 2.26 was obtained (Fig. 4-21). These observations are consistent with those reported H-partition coefficients between cpx and opx from both experimental and natural mantle samples (Bell and Rossman, 1992a; Peslier et al., 2002; Koga et al., 2003; Aubaud et al., 2004, 2007; Bell et al., 2004; Grant et al., 2007b; Tenner et al., 2009). In addition, the good preserve of this correlation, in turn, provides the solid evidence that the water contents we measured can well represent the pre-eruptive water contents of these pyroxenes in their mantle sources prior to the transports by the fast ascending magma. The decompression-induced diffusion of hydrogen out of pyroxenes, favored by many others, is not the case for the samples from the NCC here.

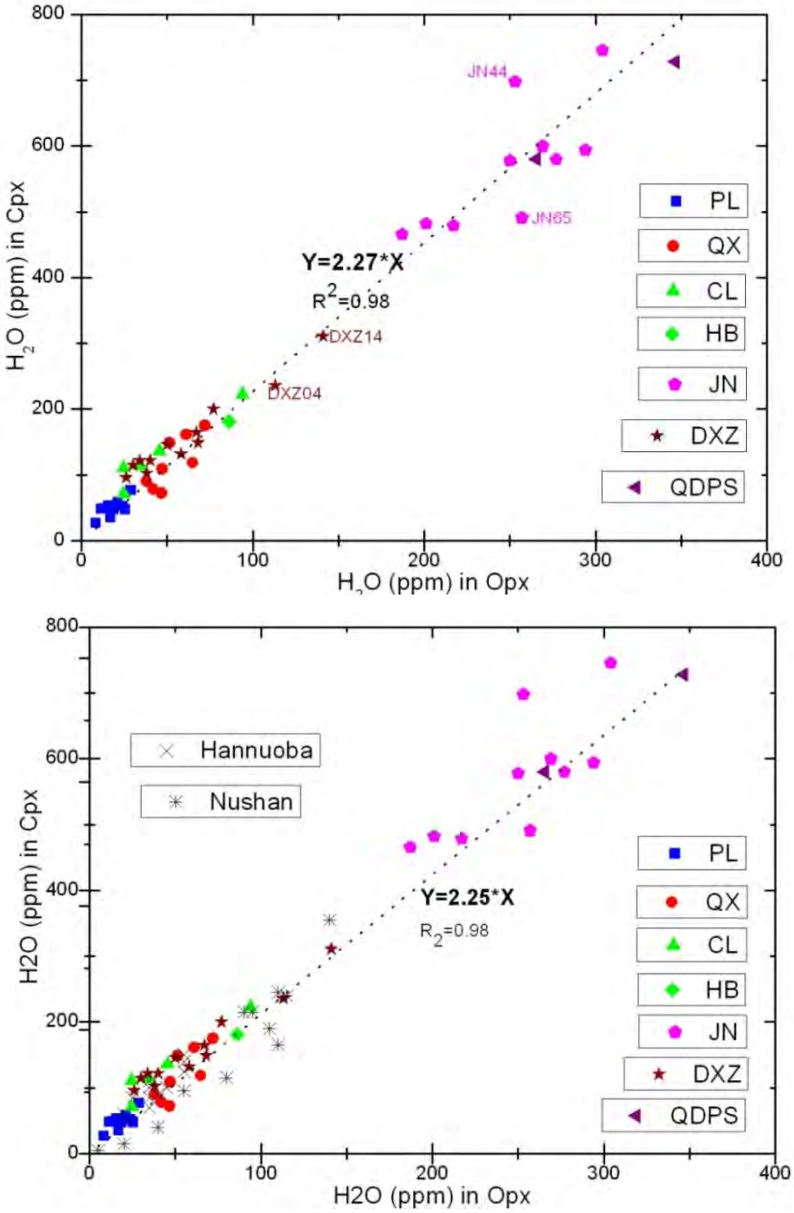

Figure 4-21. Opx H_2O content versus cpx H_2O content for the peridotite xenoliths. (a) (the top) samples from this study, including Penglai, Qixia, Changle, Hebi, Qingdao, Junan, Daxizhuang. (b) (the bottom) samples from this study combined with those from Hannuoba and Nushan (Yang et al., 2008)

4.3.2 Water contents in bulk peridotite

Because olivine is the most abundant mineral phases in mantle peridotite with over 50% vol, it is the water content of olivine that plays a major role in influencing the physical properties of peridotite as a whole. However, the olivines measured here are almost anhydrous, with invisible OH absorption bands in IR spectra, except few grains in few samples from Qingdao and Junan. These observations are in good

agreement with those from Nushan and Hannuoba in the NCC and Daoxian in south China Craton (Yang et al., 2008), and those from three localities at Subei basin in the southeastern NCC (Xia et al., 2010). Now it is generally established that water content of olivine from peridotite xenoliths hosted by alkaline basalts is very low (mostly <10 ppm, Bell and Rossman, 1992a; Peslier and Luhr, 2006; Grant et al., 2007b). Although there are divided arguments over this observed low content in nature samples, it is generally accepted that under the equilibrated partition of water the olivine has much less water content than the coexisting pyroxene in the shallow mantle. In addition to their initial low water contents, this could in part be exacerbated by the loss of H during ascent due to its very fast velocity, as the general favors (e.g. Demouchy et al., 2006; Peslier and Luhr, 2006). By contrast, the coexisting pyroxenes usually preserve their initial H information to a much larger extent (Peslier et al., 2002; Bell et al., 2004; Grant et al., 2007a; Yang et al., 2008; Bonadiman et al., 2009; this study), which are possibly related to their slower H diffusion rates (H may diffuses 1-3 orders of magnitude faster in olivine than in pyroxenes: Wade et al., 2008). The growing evidences, however, from recent experiments claimed that olivine and pyroxene have comparable H diffusion rates and not as different as was once assumed. Then, a peculiar observation is that despite similar diffusivities, pyroxenes appear to retain H even if coexisting olivines show H loss (Grant et al., 2007, Li et al., 2008, Yang et al., 2008)

In our case, the water contents measured in olivines (<2 ppm) are unlikely to represent the original water contents in their mantle source. Instead, we are inclined to consider H loss a main process responsible for the “zero” content during eruption. The initial or pre-eruptive water content in olivine can be retrieved via the assumption of equilibration between olivine and pyroxene for partitioning water. However, the H_2O partition coefficients between pyroxene and olivine determined by experiments are highly variable. The values obtained at low pressure (<3 GPa) are much higher than those at high pressure (>8GPa): At low pressures, Koga et al. (2003) obtained a value of 12±2 for Dopx/ol from a single experiment at P=1.8 GPa; Aubaud et al. (2004) (revised according to the new calibration of Aubaud et al. 2007) determined Dcpx/ol and Dopx/ol of 28±2 (n=2) and 14±2 (n=4) respectively at P=1-1.5 GPa; Hauri et al. (2006) reported Dcpx/ol and Dopx/ol of 15±5 (n=5) and 10±3 (n=8) respectively at P=0.5-1.6 GPa; Grant et al. (2007a) determined Dopx/ol=25±1 (n=2) at 289 P=1.5 GPa; Tenner et al. (2009) obtained Dcpx/ol of 27 (n=1) at P=3 GPa. In

contrast, at higher pressures, Withers and Hirschmann (2007) reported Dopx/ol of 1.3±0.2 (n=4) at P=8.0-12 GPa; Withers and Hirschmann (2008) obtained Dopx/ol of 1.5±0.2 (n=3) at P=8.0 GPa. The difference between low-pressure and high-pressure experiments is probably related to reduced pyroxene Al conte**a** : P>3 GPa, it has been confirmed by experiments that Al could enhance water solubility in pyroxene. Grant et al. (2007a) have shown that ol, opx and cpx from 8 peridotite xenoliths preserved the H2O contents of their mantle source and had Dcpx/ol values of 88±48 and 22±24 for spinel peridotites (P=1.1-2.8 GPa) and garnet peridotites.

Given that the xenoliths from the NCC in this thesis are from relatively shallow layer(< 80 km; Menzies et al. 2007) in the mantle, the partition coefficient determined under low-pressure experiments (i.e. Dcpx/ol>10; Koga et al. 2003; Hauri et al. 2006; Aubaud et al. 2007, 2009; Grant et al. 2007a; Tenner et al.2009) is favored. In the following calculations, we use a $D_{cpx/ol}$ of 10 (Aubaud et al. 2008) to recover the water contents in olivine, and further the contents in bulk rock, using the data for modal mineralogy in xenoliths.

The calculated water contents of bulk rock range from 6 to 19**b** n in Penglai; from 20 to 51 ppm in Qixia; from 7 to 56 ppm in Changle; from 11 to 38 ppm in Hebi; from 24 to 77 ppm in Daxizhuang; from 143 to 203 ppm in Qingdao, and from 122 to 251 ppm in Junan. These rebuilt water contents for the bulk rock make no difference to the water content contrast, observed in cpx and opx.

Table 4-7 Water contents in cpx, opx and rebuilt bulk rock, using the modal mineralogy of samples and a water partitioning coefficient of K_d =10 between cpx and opx, in the peridotite xenoliths from the North China Craton in this study.

Sample	Water content (ppm)			Sample	Water content (ppm)		
	cpx	opx	WR(Kd=10)		cpx	opx	WR(Kd=10)
PL-01	52	24	14	HB-02		57	20
PL-10	53	16	10	HB-06		72	23
PL-17	48	19	10	HB-07		103	37
PL-19	35	17	10	HB-10		72	29
PL-31	77	29	19	HB-12		97	33
PL-32	49	14	10	HB-16		64	20
PL-36	59	21	14	HB-17		31	11
PL-42	48	25	11	HB-64	181	86	38
PL-44	48	11	10				
PL-46	27	8	6	DXZ-01	146	50	46
				DXZ-02	132	58	30
CL-01	71	25	18	DXZ-04	236	113	53
CL-22	223	94	56	DXZ-14	311	141	77
CL-31	136	45	29	DXZ-17	103	38	24
CL-32	111	25	23	DXZ-27	122	34	34
CL-35		32	7	DXZ-36	115	30	27
CL-38	114	35	26	DXZ-39	122	40	34
				DXZ-42	149	68	35
QX-01	72	47	20				
QX-04	109	47	31	JN-03	746	304	251
QX-14	149	51	33	JN-11	482	201	139
QX-15	90	38	23	JN-24	594	294	168
QX-18	118	65	34	JN-26	466	187	156
QX-49	175	72	48	JN-35	600	269	152
QX-50	78	42	21	JN-43	580	277	148
QX-51	161	61	51	JN-44	698	253	166
				JN-47	479	217	172
QDPS-16	728	346	203	JN-53	578	250	122
QDPS-24	580	266	149	JN-65	491	257	122

4.5 SIMS results for Lithium contents and isotopic compositions

The Li contents and isotopic compositions of olivine and pyroxene (both opx and cpx) of mantle peridotite xenoliths from the North China Craton were measured using ion probe. Different analytical conditions were used for lithium content and lithium isotopic ratio. The lithium contents and isotopic compositions were determined in

different sessions so that they do not correspond to the same sputtered spots. But they are close enough to be treated as the same area. For each mineral grain, two (for small grains) to a few tens (for relatively large grains) of points between the rim and the core were analyzed for abundances and isotopic ratios, for which depth profiles were constructed respectively. The following are the details of Li and Li isotopic compositions for peridotite xenoliths from four localities i.e. Penglai, Qixia, Hebi and Junan.

4.5.1 PengLai samples

Seven of ten peridotite xenoliths were measured for Li contents and isotopic ratios. The results are reported in table 4-8. The Li abundances are extremely variable, ranging from 1.7 to 10.6 ppm in olivine, 3.3 to 59.7 ppm in cpx and 2.8 to 43.4 ppm in opx. The δ^7Li are also varibale, ranging from -37.4 to +9.0‰, -44.4 to +22.6‰ and -12.7 to +14.8‰ in olivine, cpx and opx, respectively. These extreme heterogeneities were observed on all levels, from intra-grain to inter-grains.

All the olivine grains but those from PL42 show enriched Li zoning patterns, with enrichment of Li at the rims relative to the cores, to variable extents. The Li contents range from 2.0 to 3.0 ppm at the core and 2.4 to 10.6 ppm at the rims. By contrast, the grains from PL42 show the reverse patterns, with slightly depletion of Li at the rims (2.2 ppm) relative to core (1.7 ppm). Accordingly, the olivine grains can be subdivided into three groups: the highly Li enriched olivines, where the rims with up to 10 ppm Li, about two to four times that of the cores, were found in PL10, PL32 and PL36, the moderately enriched olivine, where the rims show no more than 5 ppm Li, about two times that of the cores, were found in PL01, PL10, PL46, and the relatively depleted olivines, seen in PL42. The relative enrichments or depletion are mainly confined to a narrow area in the rims, with Li content dropping increasingly away from rim.

Li isotope compositions of olivines display a more complex figure. Large Li isotopic variations are evident both inter-grains and intra-grain. The δ^7Li vary broadly from -37.4 to +9.0‰ at the core and from -28.6 to +6.2‰ at the rims. Some grains display the higher δ^7Li at the cores than at the rims, but more grains show the reverse pattern. Few profile analyses even show the obvious Li isotopic troughs between the core and rim. Ol-3 in PL32, for instance, sees δ^7Li, before rebounding to +3.2‰ at

core, drop to -27.3‰ from +3.7‰ at the rim, whereas the other grain (ol-1) almost shares the same situation, seeing δ^7Li decrease from -4.2 at the rim to -14.6‰ at the trough, and then rebound to up to +8.5‰ at the core. Generally, the moderately Li enriched olivines (< 5 ppm) show the overall lower δ^7Li at the rims than the highly enriched olivines.

All the cpx grains show a relatively limited range of high Li contents from 20 to 60 ppm but the those from PL42, which contain much less Li contents of no more than 10 ppm, apparently still much higher than that proposed in the normal mantle and even the those founded in enriched mantle peridotite xenoliths worldwide (Jeffcoate et al., 2007; Rudnick and Ionov, 2007; Ionov et al., 2008; Tang et al., 2007). Most of the cpx grains show the enriched Li zoning pattern, the same as the coexisting olivines, but to a less extent. Cpx-1 in PL10 and cpx-2 in PL32, two of the largest grains in all Penglai peridotites, show the largest Li content contrast across the grain, with Li contents decreasing progressively from more than 50 ppm at the rims to about 20 ppm at the cores, whereas the largest cpx grains (>1500μm) in PL42 share the same Li zoning, seeing Li decreasing from about 10 ppm to 3 ppm. The rest of cpx grains show a more limited Li variation within grains, and the smaller the grain is, the narrower the Li content gap between the core and rim is. The small cpx-1 of PL31, for example, displays a homogenous Li content of ~60 ppm, the highest measured Li content for all Penglai cpx. The individual grains from one sample usually show more or less the same Li range, such those from PL10.

Speaking of Li isotopes, the cpx, to the first order, are characterized by the higher δ^7Li at the rims (up to +20‰) than at the cores (down to -40‰), with the δ^7Li decreasing progressively from the rims to the cores, the same way as their Li contents evolve. The larger the grain is, the deeper the δ^7Li goes down. The δ^7Li in cpx-2 of PL32, for example, drop rapidly from a high value of 9.6‰ at the rim to -42.5‰ at the core. So do the δ^7Li in cpx-1 of PL10, varying from + 14.8 to -41.5‰. The rest show a moderate δ^7Li depletion (no less than -10‰) at the cores. It is noted that the higher δ^7Li are always associated with the higher Li contents within the cpx grains, such as cpx-1 in PL31, which show the highest δ^7Li and Li at the same time.

The opx, although enriched in Li, show the lower contents than the coexisting cpx and do not share the systematic variations as the cpx. The opx usually show the higher Li contents at the cores than the rims, with a factor of less than three times. The opx-2 in PL10, for example, sees Li content decrease to 7.5 ppm at the rim from a maximum

of 18.4 ppm at the core. In some case, the maximum Li content occurs at the mantle. The Li contents in opx-5 of PL36 show a maximum of 32.5 ppm at the mantle, compared to a value of 7.5 ppm and 11.3 ppm at the core and the rim, respectively. Individual grains from one sample usually show more or less the same range of Li variation, except those from PL46 in which Li content ranges from 2.8 to 4.2 ppm in opx-3, compared to a range of 13.1 to 19.3 ppm in opx-4.

The opx show the relatively limited intra-grain and inter-grain variations in δ^7Li, but more scattered variations between samples, compared with those for the cpx. The opx grains from PL31, PL32 and PL36 show relatively high δ^7Li values (>+6‰), which are slightly lower than the coexisting cpx, but are still beyond the proposed range in the normal mantle (+2~+6‰). Within those grains, the higher δ^7Li values are always associated with the higher Li contents. The opx from the rest of samples display low δ^7Li values (-10~0‰), below the proposed range in the normal mantle, with some values down to -20‰.

Table 4-8. The in situ measurements of Li and Li isotopic ratios for the olivines and pyroxenes of the studied Penglai Peridotites.

	spot	Li (ppm)	δ^7Li (‰)	2σ
PL01				
cpx1-1	r	33.1	8.6	0.6
cpx1-2	c	37.5	8.0	0.5
cpx2-1	r	33.0	7.3	0.7
cpx2-2	c	22.6	-8.9	0.4
cpx3-1	r	30.6	12.0	0.4
cpx3-2	c	33.8	20.5	0.5
opx1-1	r	11.1	1.2	0.7
opx1-2	r-m		-9.0	0.5
opx1-3	m	23.9	-20.1	0.5
opx1-4	c	29.7	-22.3	1.2
ol1-1	r	4.5	-14.3	0.4
ol1-2	m		-17.9	0.7
ol1-3	c	2.3	-28.4	0.8
ol2-1	r	4.0	-19.7	0.6
ol2-2	c	2.4	-37.4	1.0
PL10				
cpx1-1	r	49.3	14.8	0.4
cpx1-2		51.3	8.5	0.4
cpx1-3		40.4	1.4	0.5
cpx1-4		32.9	-	-
cpx1-5		26.1	-	-
cpx1-6		22.0	-	-
cpx1-7	c	21.2	-41.5	0.7
cpx2-1	r	55.7	9.5	0.7
cpx2-2		54.0	-	-
cpx2-3		51.6	-	-
cpx2-4		48.2	-	-
cpx2-5	c	46.5	-9.0	0.9
cpx3-1	r	57.2	-	-
cpx3-2		55.3	-	-
cpx3-3		51.9	-	-
cpx3-4		46.3	-	-
cpx3-5	c	42.9	-	-
cpx4-1	r	54.3	-	-
cpx4-2		56.3	-	-
cpx4-3		54.6	-	-
cpx4-4		53.1	-	-
cpx4-5	c	52.3	-	-
cpx5-1	r	56.4	-	-
cpx5-2		54.3	-	-
cpx5-3		51.4	-	-
cpx5-4		50.5	-	-
cpx5-5		46.2	-	-
cpx5-6	c	46.0	-	-
opx2-1	r	7.5	-3.4	1.5
opx2-2		12.3	-	-
opx2-3		17.5	-7.5	2.2
opx2-4	c	18.4	-2.8	1.0
opx3-1	r	6.6	0.4	0.6
opx3-2		6.2	-	-
opx3-3		11.5	-	-
opx3-4		13.0	-	-
opx3-5	c	11.0	12.1	0.7
opx4-1	r	5.8	-	-
opx4-2		6.7	-	-
opx4-3		5.7	-	-
opx4-4		8.1	-	-
opx4-5	c	7.6	-	-
ol1-1	r	2.4	-	-
ol1-2		2.4	-	-
ol1-3		2.4	-	-
ol1-4		2.4	-	-
ol1-5		2.4	-	-
ol1-6	c	2.3	-	-
ol2-1	r	4.2	-28.6	0.7
ol2-2		2.8		
ol2-3	c	2.7	-10.2	1.1
ol4-1	r	10.4	-8.5	1.1
ol4-2		4.3	-27.5	1.0
ol4-3	c	3.0	-28.2	1.0
PL31				
cpx1-1	r	59.7	20.4	0.7
cpx1-2		-	20.8	0.3
cpx1-3	c	57.5	18.9	0.4
cpx4-1	r	49.1	22.6	0.3
cpx4-2		42.9	10.0	0.3
cpx4-3	c	42.9	0.4	0.3
opx1-1	r	13.5	3.7	0.5
opx1-2		21.8	-	-
opx1-3	c	23.8	8.8	0.3
PL32				
cpx1-1	r	51.7	13.9	0.2
cpx1-2		46.6	7.5	0.3
cpx1-3		44.2	0.9	0.4
cpx1-4	c	-	0.4	0.4
cpx2-1	r	53.7	9.6	0.6
cpx2-2		43.4	-0.2	0.2
cpx2-3		38.9	-10.1	0.4
cpx2-4		32.2	-18.2	0.4
cpx2-5		26.7	-27.6	0.6
cpx2-6		23.2	-37.4	0.6
cpx2-7	c	19.3	-44.4	0.5
cpx2-8		21.0	-39.2	0.3
cpx2-9		28.2	-19.8	0.6
cpx2-10		37.2	-10.6	0.6
cpx2-11		40.3	-10.3	0.3
cpx2-12		39.2	-12.9	0.3
cpx2-13		38.4	-14.9	0.5
cpx2-14		39.7	-15.7	0.4
cpx2-15		42.0	-13.7	0.7
cpx2-16	r	43.7	-2.5	0.7
cpx3-1	r	46.2	9.8	0.3
cpx3-2		-	1.6	0.4
cpx3-3		46.9	0.3	0.5
cpx3-4		-	-3.1	0.5
cpx3-5	c	45.8	-4.3	0.7
cpx3-6		-	-0.3	0.7
cpx3-7	r	-	3.2	0.6
opx1-1	r	43.4	11.1	0.9
opx1-2		-	11.4	0.7
opx1-3		36.3	10.8	0.5
opx1-4	c	-	9.4	0.5
opx1-5	r	-	9.6	0.8
opx3-1	r	-	6.6	0.7
opx3-2		-	8.3	0.7
opx3-3		-	9.2	0.7
opx3-4	c	-	11.0	0.6
ol1-1	r	9.8	-4.2	0.8
ol1-2		8.2	-11.3	0.6
ol1-3		3.6	-14.6	0.8
ol1-4	c	2.8	8.5	0.7
ol2-1	r	7.9	-14.2	0.6
ol2-2	c	2.8	8.6	1.3
ol3-1	r	7.8	3.7	0.7
ol3-2		6.4	-24.5	0.7
ol3-3		4.2	-27.3	1.1
ol3-4		3.0	-6.3	1.0
ol3-5		2.9	3.0	1.2
ol3-6	c	2.8	3.2	0.8
PL36				
cpx1-1	r	23.2	7.4	0.4
cpx1-2	c	35.0	6.2	0.5
cpx2-1	r	50.3	15.7	0.8
cpx2-2		41.9	16.0	0.4
cpx2-3	c	39.4	18.8	0.6
cpx3-1	r	44.6	21.6	0.7
cpx3-2		44.1	19.1	0.4
cpx3-3	c	31.0	10.4	0.6
opx1-1	r	-	5.5	0.7
opx1-2		-	7.5	0.9
opx1-3	c	-	11.8	0.6
opx3-1	r	28.8	4.5	0.4
opx3-2		-	3.4	0.2
opx3-3		34.1	9.0	0.4
opx3-4	c	30.0	5.1	0.8
opx5-1	r	11.3	10.9	1.0
opx5-2		20.2	10.6	0.5
opx5-3		27.4	14.8	0.5
opx5-4		32.5	12.7	0.5
opx5-5		24.7	6.8	0.6
opx5-6		12.2	11.6	0.9
opx5-7	c	7.5	12.4	0.9
ol1-1	r	10.1	3.1	0.7
ol1-2		7.1	-1.7	1.1
ol1-3		6.7	-4.5	1.1
ol1-4		6.0	-	-
ol1-5		5.1	-	-
ol1-6		4.4	-	-
ol1-7	c	3.7	-	-
ol2-1	r	10.6	-0.3	0.8
ol2-2		7.3	-	-
ol2-3		2.9	-	-
ol2-4		2.3	-	-
ol2-5	c	2.3	2.0	2.0

To be continued

PL42					cpx2-3	r	33.6	-	-	opx4-1	r	13.1	-4.3	0.8
cpx-1	r	8.8	-9.1	0.6	cpx2-2		36.7	-	-	opx4-2		16.9		
cpx-2		6.6	-	-	cpx2-1	c	43.8	-	-	opx4-3	c	19.3	-3.5	0.6
cpx-3		5.2	-20.6	0.8										
cpx-4	c	3.5	-20.3	1.4	cpx3-1	r	-	25.2	1.2	ol2-1	r	3.8	-20.3	2.2
					cpx3-2		-	13.2	0.7	ol2-2		2.8	-24.2	2.0
cpx2-1	r	8.8	-6.4	0.8	cpx3-3		-	6.1	0.3	ol2-3		2.2	-16.6	1.9
cpx2-2		4.4	-17.1	1.8	cpx3-4	c	-	2.0	0.6	ol2-4	c	2.2	-6.3	1.2
cpx2-3	c	3.3	-12.5	1.5	cpx3-5		-	3.5	0.6					
					cpx3-6	r	-	4.1	0.7	ol3-1	r	5.3	-6.1	0.7
opxl-1	r	9.7	-12.7	0.8						ol3-2		-	-12.5	0.8
opxl-2			-11.1	1	cpx4	c	-	13	0.6	ol3-3	c	2.0	0.5	1.2
opxl-3	c	9.7	-7.4	0.8										
					opxl-1	r	-	6.2	1.2	ol4-1	r	4.5	-10.0	1.0
PL46					opxl-2	c	-	12.8	1.7	ol4-2		2.3		
cpxl-1	r	42.5	8.5	0.2						ol4-3	c	2.0	-0.8	1.3
cpxl-2		37.2	-	-	opx3-1	r	4.2	2.2	1.0					
cpxl-3	c	42.0	-0.2	0.4	opx3-2	c	2.8	6.1	1.4					

4.5.2 Qixia samples

The Li contents and Li isotopic compositions for five representative peridotite xenoliths were compiled and given in Table 4-9.

The olivines show a large Li content range from 1.2 to 10.3 ppm, with 1.2 to 5.4 ppm, and 2.1 to 10.3 ppm at the cores, and the rims, respectively. All the olivines display enriched Li zoning patterns, with enrichment of Li at the rims by a factor of no more than three relative to the cores. The olivines from QX01 display the lowest Li contents (1.2 to 1.6 ppm) at the cores, but with relative high enrichments (more than two times) at their rims, whereas the other samples show relatively variable Li contents between grains, and relatively low enrichments at the rims. The Li contents of ol-2 in QX14, for example, vary from 1.8 to 2.4 ppm, and ol-3, another grain in QX14, displays higher Li content between 5.4 and 10.3 ppm. And the same goes to those in QX50.

The Li abundances of cpx vary from 7.6 to 32.0 ppm in QX01, 3.4 to 27 ppm in QX14, 4.6 to 41.1 ppm in QX18 and 13.1 to 34.0 ppm in QX50. The Li contents variation is evident between grains, and most grains show the reverse Li zoning pattern to variable extents. In detail, the Li contents in QX14 vary significantly among the grains that are slightly depleted in Li at the rims relative to the cores. The average Li content for four cpx grains is 4.4, 5.0, 10.7 and 22.5 ppm, respectively. The cpx grains in QX18 show roughly the same Li contents at their cores, varying from 31.0 to 41.0 ppm, but relatively depleted and variable Li contents at the rim, ranging from 4.6 to 40.3 ppm. The cpx-2 shows the largest relative depletion at the rim with only 4.6 ppm Li, compared with 31.0 ppm Li at the core. The grain cpx-2 in QX01 shares the

same situation, with Li decreasing from 32.0 ppm at the core to 7.6 ppm at the rim, whereas cpx-1 shows slight Li content variation, varying between 28.1 and 19.7 ppm. The two grains in QX50 show roughly homogenous Li distribution.

Opx grains, too, show high Li and variable Li contents, with a total range of 1.1 to 30.3 ppm. Li contents vary from 1.8 to 11.6 ppm in QX01, from 2.5 to 7.5 ppm in QX14, from 1.1 to 30.3 ppm in QX18 and from 1.1 to 17.9 ppm in QX50. All grains display the reverse Li enriched zoning pattern, the same as that for the cpx, but to extreme extents in some cases. The profile analyses for opx-2 of QX18, for example, show Li contents decrease progressively from 32.2ppm Li at the mantle to 13.9 ppm near the rim, and then plunge to only 1.1 ppm at the outermost rim. The opx-4 grain from QX50 shares the same situation. The two opx grains from QX01 have totally different Li ranges, from 1.8 to 3.1 ppm within one grain and from 3.2 to 11.6 ppm within the other grain.

The Li isotopic compositions, the olivines display a very large total δ^7Li range, from -33‰ to +4‰, and mainly between -25‰ and -10‰ if excluding those from QX14. Olivines in other samples are characterized by extremely and extensively low δ^7Li within grains, with much lower values at cores (-16‰ to -33.9‰) than at rims (-3.4 to -19.8‰).

Olivine grains in QX14 can be distinguished from the rest by their relatively high δ^7Li values, varying between -12.9 and +4.0‰ within one grain and -3.6 to +2.1‰ within the other two grains.

Pyroxenes show much higher δ^7Li values and narrower variation than olivines. The δ^7Li values of cpx within and between grains vary from +6.8 to 14.8‰ in QX14, 2.3 to +14.0‰ in QX18 and +8.3 to 11.0‰ in QX50. And the δ^7Li values of opx range from 3.0 to +14.6‰ in QX14, -1.4 to +14.5‰ in QX18, +1.3 to +9.8‰ in QX50 and 0.9 to 12.3‰ in QX51. Two types of isotopic zoning can be observed. For cpx, the grains from QX14 have higher δ^7Li at the cores (+8.6 to +14.8‰) than the corresponding rims (+6.8 to 8.8‰). By contrast, those from QX18 show the opposite, with the heavier rims (+5.9 to +14‰) than the cores (+2.3 to +10.1‰). Of the three cpx grains analyzed in QX50, one grains share the same isotopic pattern as QX18, and the others are roughly homogeneous across the crystals.

Table 4-9. The in situ measurements of Li and Li isotopic ratios for the olivines and pyroxenes of the studied Qixia Peridotites.

	spot	Li (ppm)	δ^7Li (‰)	2σ
QX01				
cpx1-1	r	19.7	-	-
cpx1-2	c	28.1	-	-
cpx2-1	r	7.6	-	-
cpx2-2	m	23.6	-	-
cpx2-3	c	32.0	-	-
ol1-1	r	3.5	-10.1	0.4
ol1-2		2.3	-	-
ol1-3		1.8	-	-
ol1-4	c	1.6	-15.5	0.5
ol2-1	r	2.7	-13.9	0.6
ol2-2	c	1.2	-20.9	0.8
ol3-1	r	5.4	-17.2	0.4
ol3-2	m	1.8		
ol3-3	c	1.5	-7.8	0.8
opx1-1	r	1.8	-	-
opx1-2	c	3.1	-	-
opx2-1	r	3.2	-	-
opx2-2	m-r	8.6	-	-
opx2-3	m-r	10.9	-	-
opx2-4	c	11.6	-	-
QX14				
cpx1-1	r	13.9	8.8	0.9
cpx1-2	c	12.2	9.2	0.6
cpx2-1	r	17.9	8.3	0.6
cpx2-2	c	27.1	14.8	0.4
cpx3-1	r	3.6	6.8	1.0
cpx3-2	c	4.8	8.6	0.7
cpx4-1	r	3.4	7.7	1.2
cpx4-2	c	6.5	12.0	1.0
opx1-1	r	2.5	3.0	1.1
opx1-2	c	7.5	9.9	0.7
opx3-1	r	2.9	14.6	1.3
ol1-1	r	3.7	4.0	0.8
ol1-2	c	3.4	-12.9	0.7
ol2-1	r	2.1	-2.7	1.4
ol2-2	c	1.8	2.1	1.3
ol3-1	r	10.3	-2.5	0.8
ol3-2		4.5	-3.6	1.1
ol3-3	c	5.4	-3.5	0.8
QX18				
cpx1-1	r	17.0	5.9	0.3
cpx1-2		35.9	-	-
cpx1-3	c	38.0	2.3	0.3
cpx3-1	r	4.6	9.3	0.3
cpx3-2		25.1	-	-
cpx3-3	c	31.0	4.2	0.4
cpx6-1	r	40.3	14.0	0.4
cpx6-2		38.1	10.5	0.6
cpx6-3	c	41.1	10.1	0.5
ol1-1	r	3.7	-7.5	2.0
ol1-2	c	2.3	-18.4	1.1
ol2-1	r	6.1	-11.7	0.7
ol2-2		2.9	-17.0	0.9
ol2-3	c	2.7	-21.7	1.0
opx2-1	r	1.1	-1.4	1.1
opx2-2		13.9	14.5	1.0
opx2-3		27.1	12.3	0.6
opx2-4		30.3	-	-
opx2-5		24.2	9.0	0.4
opx2-6	c	24.1	11.1	1.1
QX50				
cpx1-1	r	20.2	9.0	0.3
cpx1-2	c	18	8.7	0.3
cpx2-1	r	24.3	11.0	0.5
cpx2-2	c	28.7	9.6	0.5
cpx3-1	r	13.1	11.0	0.4
cpx3-2	c	34..0	7.6	0.3
opx2-1	r	7.9	8.3	1.8
opx2-3		17.9	9.6	0.5
opx2-3	c	15.4	8.9	1.0
opx4-2		1.1	9.8	1.8
opx4-2		11.4	3.9	0.6
opx4-3		9.5	7.0	0.8
opx4-4		11.1	6.6	0.7
opx4-5		-	6.6	0.5
opx4-6		-	5.2	0.9
opx4-7	r	3.5	1.3	1.3
ol1-1	r	3.1	-26.6	0.9
ol1-2		2.4	-18.3	0.7
ol1-3		2.1	-1.5	1.0
ol1-4		1.9	-13.6	0.7
ol1-5		-	-29.6	0.8
ol1-6		2.3	-33.9	0.9
ol1-7		-	-21.5	0.9
ol1-8		-	-7.6	1.1
ol1-9		-	-9.5	0.8
ol1-10		-	-19.8	0.8
ol1-11		-	-30.3	1.1
ol1-12	r	-	-13.4	0.7
ol3-1	r	4.1	-19.8	0.8
ol3-2		3.1	-30.5	1.1
ol3-3		3.4	-28.1	0.6
ol3-4	r	-	-20.1	0.7
ol4-1	r	7.4	-3.4	1.4
ol4-2	c	5.3	-23.9	1.3
QX51				
ol1-1	r		-18.4	1.1
ol1-2			-26.6	0.9
ol1-3			-24.7	0.8
ol1-4			-23.3	0.9
ol1-5			-21.8	1.0
ol1-6			-20.5	1.0
ol1-7	r		-20.9	0.8
ol2-1	r		-12.4	0.9
ol2-2			-9.9	1.0
ol2-3			-11.3	0.7
ol2-4			-10.1	0.8
ol2-5	c		-16.4	1.1
opx1-1	r		12.3	1.5
opx1-2	c		4.5	0.8

4.5.3 Hebi samples

The Li contents and Li isotopic compositions of the mineral grains in six peridotite xenoliths have been measured, and the results are summarized in Table 4-10.

The olivines contain between 1.3 and 4.4 ppm Li, with only slight enrichment or depletion at the rims relative to the cores. Within a sample, the individual grains

usually have comparable Li contents and distributions, and the Li heterogeneity is more evident between samples. In detail, the Li content within grains vary from 1.9 to 2.4 ppm in HB01, 1.9 to 2.7 ppm in HB06, 2.6 to 3.1 ppm in HB07, 1.5 to 1.8 in HB12 and 1.7 to 4.4 ppm HB64. The cores of olivine grains in HB07 have high Li contents between 2.6 and 3.1 ppm, compared with the range of 1.6 to 2.4 for the rest of Hebi samples. The δ^7Li of the olivines ranges from -13.0 to +5.5‰, with a range of -8.5 to +5.5‰ at the cores and a range of -13.0 to 4.8‰ at the rims. The δ^7Li in the cores are restricted to a narrow range (+0.6 to +5.5‰), when excluding two grains from HB01, which show anomalously low δ^7Li at the cores (-8.5 and -7.5‰).

The Li contents of opx vary broadly from 0.2 to 62.2 ppm with extreme intra-grain and inter-grain heterogeneities. The opx grains are characterized by different Li zoning patterns, from strong Li enriched patterns to the opposite, which usually occur within individual grains from one sample. In HB01, the opx-1 sees the Li contents decrease progressively from 33.8 ppm at the core to 17.3 ppm at the rim, whereas the opx-3 show a totally different figure, with Li contents grow increasingly from 1.6 ppm at the core to more than 50 ppm at the rim. The same goes to HB06, where the Li contents increase outwards from 1.9 to 34.5 ppm in opx-1 and decrease outwards from 37.2 to 4.0 ppm in opx-4. In HB07, the opx-2 shows that Li contents increasingly grow from 2.4 ppm at the core to 31.8 ppm near the rim, and then abruptly drops to 22.8 ppm at the rim. The other grain, opx-1, witnesses the more serious Li loss, dropping down to only 0.5 ppm from the nearby maximum of 23.8 ppm. These indicate that multi-episodes processes were involved: a previous Li diffusive addition was followed by a diffusive Li loss. In HB12, the opx-1 show a homogenous Li content of 1.7 ppm, in contrast to a classic Li enriched zoning in the opx-3, with Li increasing from 1.7 to 31.5 ppm. In HB64, the Li content is up to 62.2 ppm near the rim of the opx-2, whereas the nearby opx-1 displays the lowest content of 0.2 ppm near the rim. The rest (opx-3 and opx-4) show the roughly homogenous Li contents.

The opx show a wide δ^7Li range from -67.7 to +27.2‰, with a dominance of low δ^7Li (<-10‰) within the grains over the high δ^7Li values that are merely observed at a few rims. The opx cores always show the lower δ^7Li than the rims, but they are not always the minimum values within grain. Interestingly, the opx grains that are extremely heterogeneous in δ^7Li usually show the good shaped isotopic profiles, with the δ^7Li going down progressively away from the edge followed by rebounding from

the trough. It is noted, and testified later by Li modeling, that somewhere between the rim and core there always develops a δ^7Li trough, which is produced by the Li diffusion-driven isotope fractionation. Three individual isotopic profiles within the opx-3 of HB01, for example, share the same δ^7Li pattern, seeing the δ^7Li plummet to the minimum values (down to -53.5‰) at the troughs, and then rebound back at the core. It is also noted that the narrower the trough is, the closer to the edge the trough is. The other profiles lack a δ^7Li trough for reasons that will be discussed later, with the δ^7Li decrease continuously from the rim to the core, such the opx-1 in HB01 and the opx-1 in HB06.

Because the peridotite xenoliths are either hazburgites or dunites, only three cpx grains, two from HB64 and one from HB01, are big enough for analyses. The total range is from 1.7 to 44.4 ppm and from -75.3 to 16.0‰ for Li contents and δ^7Li values, respectively. In HB64, cpx-1, a small grain, shows an average Li content of 23.5 ppm and a δ^7Li value of +6.8‰. By contrast, the cpx-2, a large grain, shows a broad spectrum, ranging from 17.4 ppm at the rim to 5.9 ppm at the core for Li content and from -0.8 to -32.6‰ for the corresponding δ^7Li. The Li contents and δ^7Li values within the cpx grain of HB01 are more variable, ranging inward from 44 to 1.7 ppm and +16 to -75.5‰, respectively. They are detailed by four profiles: the Li transect-1, the isotopic transect-2 and the combined transect-3, along different directions across the section. In transect-1, from 44.4 ppm Li at the outermost rim it drops to 24.7, 12.4, 4.5, 2.3, and 1.7 ppm toward the core with an increment of every 100um. The transect-2 sees δ^7Li plummet to the lowest value of -73.7‰ at the core from -13.9‰ near the rim (~50μm away from the rim boundary). The transect-3 shares the same pattern that characterize transect-1 and -2, too, showing a heavy rim of -9.8‰ has enriched Li content of 25.4 ppm, compared with a light core of -66.2‰ with only 2.0 ppm Li.

Table 4-10. The in situ measurements of Li and Li isotopic ratios for the olivines and pyroxenes of the studied Hebi Peridotites.

	spot	Li (ppm)	δ^7Li (‰)	2σ
HB01				
cpx1-1	r	25.4	-3.9	0.4
cpx1-2		5.9	-47.4	1.1
cpx1-3		2.0	-66.2	1.0
cpx1-4	c	5.0	-64.2	0.9
cpx1-5	r	-	-13.4	0.9
cpx1-6		-	-45.9	1.8
cpx1-7		-	-61.0	1.0
cpx1-8		1.6	-73.7	1.3
cpx1-9		-	-75.5	1.7
cpx1-10		-	-67.6	0.7
cpx1-11	r	-	-21.3	0.6
cpx1-12	r	44.4	17.0	0.3
cpx1-13		24.7	-	-
cpx1-14		12.4	-	-
cpx1-15		4.5	-	-
cpx1-16		2.3	-	-
cpx1-17	c	1.6	-73.7	1.3
opx1-1	r	17.3	-1.0	0.7
opx1-2		18.3	-2.9	0.5
opx1-3		21.3	-19.4	0.6
opx1-4	c	33.8	-48.4	0.6
opx3-1	r	52	27.6	0.3
opx3-2		54.9	20.5	0.5
opx3-3		44.1	1.0	0.6
opx3-4		22.4	-28.3	0.5
opx3-5		8	-53.5	0.7
opx3-6		3.9	-43.1	1.9
opx3-7		2.5	-49.1	1.2
opx3-8		-	-39.4	1.0
opx3-9		-	-23.9	1.8
opx3-10	c	1.6	-22.4	1.5
opx3-11	c	-	-27.2	1.2
opx3-12	r	-	21.3	0.7
opx3-13		-	14	0.4
opx3-14		-	9.2	0.6
opx3-15		-	2.1	0.3
opx3-16		-	-15.3	0.2
opx3-17		-	-32.5	0.6
opx3-18		-	-54	0.5
opx3-19	c	-	-48.9	0.9
opx3-20	r	-	20.3	0.8
opx3-21		-	-15.4	1.3
opx3-22		-	-52.4	0.7
opx3-23		-	-49.1	1.4
opx3-24	c	-	-46.9	1.3
ol1-1	r	2.4	-12.7	1.7
ol1-2	c	1.9	-8.5	1.7
ol2-1	r	2.3	-6.5	1.5
ol2-2		2.0	1.6	1.1
ol2-3	c	2.0	0.6	2.0
ol3-1	r	2.3	-13.0	0.9
ol3-2	c	1.9	-7.5	1.3

	spot	Li (ppm)	δ^7Li (‰)	2σ
HB06				
ol1-1	rr	1.3	-	-
ol1-2	r	1.9	4.8	1.2
ol1-3	c	1.9	2.2	1.3
ol4-1	r	2.7	-1.6	1.2
ol4-2	m	-	1.1	1.3
ol4-3	c	2.4	1.4	0.4
opx1-1	r	34.5	8.3	1.3
opx1-2		31.1	-13.2	0.7
opx1-3		28.7	-22.9	0.9
opx1-4	c	1.9	-25.5	1.2
opx1-5		19.4	-34.2	1.2
opx1-6	r	19.4	4.6	4.6
opx4-1	rr	4.0	-	-
opx4-2	r	10.8	0.5	0.7
opx4-3	m	17.0	6.3	0.9
opx4-4	c	37.2	4.8	0.7
HB07				
ol1-1	r	2.8	3.7	0.9
ol1-2		3.0	-	-
ol1-3	c	3.1	0.6	0.9
ol2-1	r	2.1	-	-
ol2-2	c	2.6	-	-
opx1-1	r	0.5	-13.2	1.2
opx1-2		23.8	-11.5	0.3
opx1-3	c	18.0	-43.1	0.8
opx2-1	r	22.8	-0.6	0.6
opx2-2		31.8	-13.8	0.4
opx2-3		21.7	-32.3	0.7
opx2-4		7.9	-53.4	0.4
opx2-5	m	4.2	-49.2	0.6
opx2-6	c	2.4	-13.0	1.4
HB12				
ol1-1	r	1.7	0.5	1.1
ol1-2		1.7	-	-
ol1-3	c	1.8	3.6	1.3
ol2-1	r	1.5	-	-
ol2-2	c	1.6	-	-
opx1-1	r	1.6	-15.7	2.9
opx1-2		1.7	-	-
opx1-3	c	1.7	-15.4	2.6
opx3-1	r	31.5	-26.1	0.4
opx3-2		9.9	-50.6	0.5
opx3-3		3.4	-67.2	0.8
opx3-4	m	2.0	-61.2	1.4
opx3-5		1.9	-	-
opx3-6		1.9	-	-
opx3-7	c	1.7	-32.0	1.3

	spot	Li (ppm)	δ^7Li (‰)	2σ
HB64				
cpx1-1	r	23.3	4.8	0.7
cpx1-2		23.9	-	-
cpx1-3	c	23.5	6.7	1.2
cpx2-1	r	13.4	-3.2	0.7
cpx2-2		-	-25.6	0.7
cpx2-3		-	-33.6	0.8
cpx2-4		-	-34.9	0.7
cpx2-5	c	5.9	-32.6	0.9
cpx2-6		7.5	-23.7	0.5
cpx2-7		-	-17.5	0.6
cpx2-8	r	17.4	-0.8	0.6
ol1-1	r	4.4	-6.6	1.1
ol1-2		2.2	0.3	1.1
ol1-3		2.0	-3.4	1.2
ol1-4		1.8	-2.2	1.2
ol1-5		1.7	-0.5	1.2
ol1-6		1.7	2.4	0.7
ol1-7		1.7	3.3	1.1
ol1-8	c	1.7	3.8	1.9
ol2-1	r	2.7	-3.1	1.5
ol2-2	c	1.9	5.5	1.6
opx1-1	r	0.8	-1.7	1.6
opx1-2		-	-2.3	1.5
opx1-3		-	0.2	2.6
opx1-4		-	-0.2	1.6
opx1-5		1.2	3.4	1.6
opx1-6		-	3.2	1.4
opx1-7		5.3	8.4	1.0
opx1-8	c	5.2	11.8	0.6
opx1-9		-	0.7	2.3
opx1-10		0.2	4.6	3.7
opx1-11	r	0.4	3.2	1.8
opx2-1	r	19.9	4.3	0.7
opx2-2		62.2	15.2	0.7
opx2-3		51.6	4.0	0.5
opx2-4	c	47.6	-15.4	0.8
opx2-5	r	51.6	8.0	0.7
opx3-1	r	13.0	-	-
opx3-2		14.2	-	-
opx3-3	c	11.3	-	-
opx4-1	r	10.5	-	-
opx4-2	c	7.8	-	-

4.5.4 Junan samples

The Li contents and Li isotopic compositions of the mineral grains in three peridotite xenoliths have been measured, and the results were given in Table 4-11.

The Li contents show a relatively narrow range from 2.4 to 2.7 ppm in olivine, from 2.4 to 3.2 ppm in opx and from 1.9 to 2.4 ppm in cpx except the cpx grains from JN53, where the outermost rims show the significantly elevated Li contents (7.1 and 8.8 ppm) relative to the cores (2.1 and 2.4ppm). The Li distribution is roughly homogenous within mineral grains, and the slight Li variation of minerals mainly occurs between samples. If Li contents at rims are excluded in averaging, the relative contents of Li between olivine and coexisting cpx, described as $D^{Li}_{ol/cpx}$ (Li_{ol}/Li_{cpx}), have fixed values of ~1.2, approaching the proposed equilibrium values (1.1~2.0) in mantle peridotite (Rudnick and Ionov, 2007).

The Li isotopic compositions, too, display narrow ranges. The δ^7Li vary from -3.6 to +4.4‰ in olivine, -0.9 to 7.3‰ in cpx and -4.2 to 11.6‰ in opx, with a more limited range of 0 to +3.1‰ for the olivine cores and of -0.5 to 3.3 ‰ for the cpx cores. The offset between δ^7Li in the cores of olivine and cpx, described as $\Delta^7Li_{ol\text{-}cpx}$ (δ^7Li_{ol}-δ^7Li_{cpx}), vary between -1.4 to 1.1‰, within the range for equilibration of Li isotopes at the mantle condition. That δ^7Li offset between olivine and opx is beyond the range for equilibration.

According, we conclude that the Junan peridotites have approached the Li and Li isotopic equilibrium at the mantle source prior to volcanic transports. The slight enrichment of Li relative to the normal mantle values reflect the previous interaction with Li-rich melts in the mantle The slight Li and isotopic variations at the rim, on other side, reflect the late-stage Li diffusive perturbation within the xenoliths during entrainments or post eruption in the host magma.

Table 4-11. The in situ measurements of Li and Li isotopic ratios for the olivines and pyroxenes of the studied Junan Peridotites.

	spot	Li (ppm)	δ^7Li (‰)	2σ
JN24				
cpx3-1	c	2.2	3.3	1.4
cpx3-2		2.2	4.7	1.4
cpx3-3		2.2	4.2	1.0
cpx3-4	r	2.2	0.3	1.1
cpx4-1	r	2.4	-0.9	1.9
cpx4-2		2.1	-	-
cpx4-3	c	2.1	0.5	1.2
opx1-1	c	2.6	3.6	1.0
opx1-2		2.6	7.0	0.9
opx1-3		2.5	2.4	1.1
opx1-4	r	2.6	0.8	1.1
opx5-1	c	2.5	-4.2	1.1
opx5-2		2.5	-0.2	1.8
opx5-3		2.4	3.1	1.2
opx5-4	r	2.9	0.8	1.0
ol3-1	r	2.4	-0.4	0.7
ol3-2	c	2.4	1.9	1.0

	spot	Li (ppm)	δ^7Li (‰)	2σ
JN35				
cpx1-1	r	-	7.3	1.3
cpx1-2	c	-	2.4	1.6
cpx2-1	r	1.9	4.9	1.0
cpx2-2	c	2.2	3.0	1.0
opx1-1	r	2.4	4.9	1.4
opx1-2	m	-	5.4	1.7
opx1-3	c	2.6	11.6	1.3
opx2-1	r	3.2	8.7	1.4
opx2-2	c	3.2	4.7	1.2
ol2-1	r	2.7	4.4	1.2
ol2-2	c	2.7	3.4	1.1
ol3-1	r	2.7	0.9	0.9
ol3-2	c	2.7	2.2	0.6
ol4-1	r	2.6	2.5	1.2
ol4-2		-	-0.7	1.0
ol4-3	c	2.5	0.1	0.7

	spot	Li (ppm)	δ^7Li (‰)	2σ
JN53				
cpx2-1	r	8.8		
cpx2-2	r	2.1	5.5	1.1
cpx2-3	c	2.1	-0.5	1.2
cpx3-1	r	7.1	-0.2	1.4
cpx3-2	c	2.4	2.0	1.2
opx2-1	r	2.5	-0.7	1.1
opx2-2	c	2.5	5.7	2.5
opx4-1	r	2.5	7.3	1.0
opx4-2	c	2.5	6.8	1.0
ol2-1	r	2.6	1.7	0.9
ol2-2	c	2.6	0.0	1.0
ol4-1	r	2.6	-3.6	0.8
ol4-2	m	-	-1.2	1.1
ol4-3	c	2.6	0.6	0.8

5 The melt depletion and enrichment process

Peridotite xenoliths, brought to the surface by continental lava, frequently contain evidence for a multistage history involving depletion in basaltic melt followed by enrichment in incompatible trace elements at some later stages (Menzies and Hawkesworth 1987; Hawkesworth, 1999). So do those from the NCC in this thesis, but with complex histories that will be unfolded into two parts. In this chapter, melt depletion and subsequent enrichment processes (mantle metasomatism) are viewed in term of both major elements and incompatible trace elements but Li. And the enrichment processes will be further detailed in the line of Li isotopes in the following chapter 7.

5.1 Melt depletion

5.1.1 Melt depletion in the mantle sources

Partial melting of mantle peridotite is a very important igneous process in deep earth by which the mantle rock loses a basaltic component, producing the residue more refractory and buoyant, and gives birth to a basaltic melt and start a rock cycle, leading to the formation of the wide diversity of observed igneous rocks and constituting the fundamental process by which earth and planets differentiate.

It is noted that the minerals do not enter the melt in their modal proportions during partial melting of mantle peridotite, with the cpx preferentially entering at first. So the modal proportion of cpx in hand specimen can be used to roughly compare the extents of melting between samples. The modal mineralogy, however, varies strongly depending on equilibration depth, and the sample size would bias the modal minerology, so it is impossible to use that data alone to assess the likely extent of melting. Although the extent of depletion of some chemical components in bulk rock, such as CaO and Al_2O_3, can well correlate with those of melt depletion, the abundances of these elements are also sensitive to the subsequent introduction of secondary cpx and garnet. In fact, the chemical components of olivine, such as Mg number (Mg#=100*Mg/(Mg+Fe), atoms ratio) may be the most robust indicator

guiding the extent of melting. The other useful indicator for the extent melting in minerals is Cr number in spinel, which is defined like Mg# in olivine, as Cr#=100*Cr/(Cr+Al). Both experimental studies (Jaques and Green et al., 1980) and natural samples (Arai et al., 1994) show that Mg# of olivine and Cr# of spinel both progressively increase in peridotite residues with increasing melt extraction. So they are always used combined to constrain the melting extent of their host peridotite.

In a plot of Mg# in ol against Cr# in spl, the data points defines a positive trend, and further pointing to a partial melting process. Broad negative correlation between Mg# of olivine and moderately incompatible elements (e.g. Y, Yb) also suggest these elements behaved similarly in the mantle rocks during partial melting and, therefore, can be used to quantitatively model the degree of partial melting of the xenoliths (Norman, 1998).

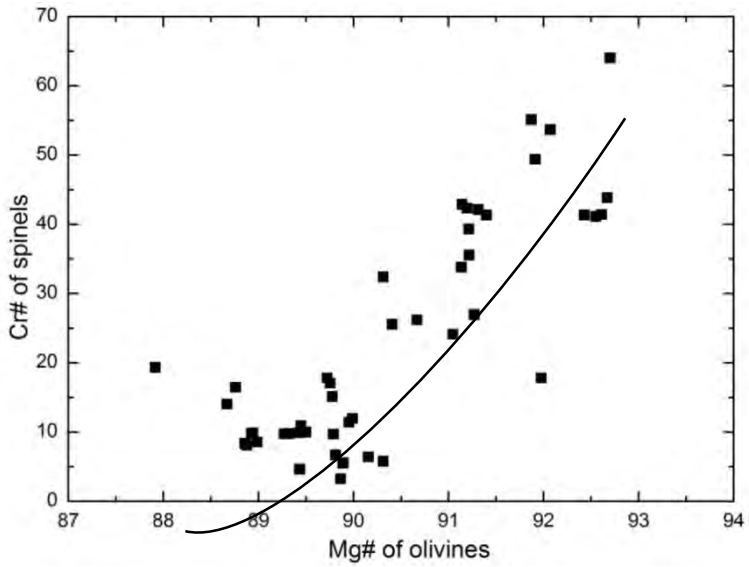

Fig. 5-1. Covariation of Cr# values in spinels and Mg# values in coexisting olivines

5.1.2 The estimate of extents of mantle melting

In spinel-bearing peridotite xenoliths cpx is the major host for most trace elements and its incompatible-element pattern usually mimics that of the peridotite with the exception of Ba, Nb, and Ti (Chalot-Prat and Boullier, 1997; Zangana et al., 1999; Gregoire et al., 2000). The partial melting processes have been modeled using major

element whole rock and mineral geochemistry, as well as REE patterns (e.g. Johnson et al, 1990; Norman, 1998; Gregoire et al., 2000; Wang and Gasparik, 2001; Neumann et al., 2004)

Here, we use the element pair of Y and Yb, two heavy rare earth elements that behave mildly incompatibly during partial melting, to model the partial melting processes. Three main melting models, i.e. batch, fractional and incremental melting equations, have been defined (Johnson et al., 1990; Norman, 1998; Yang, H.J. et al., 1998). In batch melting, solid and liquid fractions remain together throughout the entire melting interval, while in fractional melting infinitesimal increments of melting occur, accompanied by instantaneous segregation of the melt from the solid residue. Incremental melting is intermediate between these two theoretical end-members, and is more likely to approach the real situation of partial melting in the mantle, in which small, but finite, increments of melting and segregation occur, with a new starting composition applied after each segregation event. Equilibrium partitioning of elements is maintained in all models. Given the same extent of partial melting, the fractional melting depletes the residue in the incompatible elements (i.e LREE) far more effectively than the batch melting, and the two processes are easily distinguished in REE and incompatible element diagrams (Johnson et al., 1990; Norman, 1998).

Before the modeling using Y and Yb, we need to confirm that the partial melting took place at stable field of spinel rather than garnet, because garnet is a major host for HREEs and tend to retain them during partial melting, and the modeling is on the ground that cpx is major host in peridotite for REEs. Unlike cpx and feldspar, the occurrence of garnet in melting residues is effective in fractionating the abundances of these two REEs and would produce the low Tb/Yb ratio in the peridotite residues during the partial melting, because Yb is more compatible in garnet than Tb. Then the ratio of Tb/Yb can be used to justify the presence of garnet in the melting source or not.

The Fig. 5-2 shows that most of samples were scattered around at the line of 1 for the Tb/Yb ratio, especially those from Penglai and Junan, suggesting the melt extractions at the absence of garnet. But some samples display the elevated ratios, such as Hebi samples, PL46, and those from Daxizhuang. That reflects slight influences from the subsequent metasomatism.

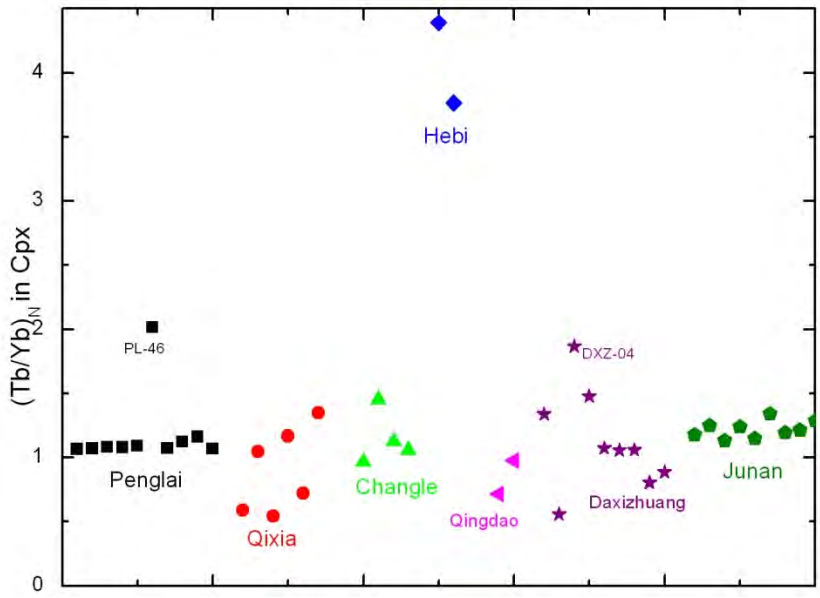

Figure 5-2. The normalized Tb/Yb ratios in cpx from the studied peridotite xenolith from the NCC

The Modeling using Y and Yb contents in the cpx and assuming K_d^Y = 0.42 and K_d^{Yb} = 0.4 (Norman, 1998) and the primitive mantle composition (McDonough and Sun, 1995) indicates that xenoliths have experienced varying extents of melting in their mantles sources, even those from the same localities, no matter the batch or fractional melting is applied (Fig. 5-3). The estimates of the melting extents given by the two melting models will converge when *f* (the partial melting extent) is less than 0.05 and diverge when *f* is greater than 0.05, and the larger the *f* is, the strong the contrast is. The xenolith HB01, for example, is suggested to be the residue after a *f* of 0.23 melt extractions in the fractional melting model, compared with a *f* of more than 0.5 in the batch melting model. Apparently, the fractional melting is more appropriate given that such a large extent of melting is difficult to occur and there was not cpx left. Both the models indicate that the xenoliths from Junan have experienced the extents of melting less than 3%, and some even less than 1%. The xenoliths from Penglai share the similar melting extents, ranging between 3 and 5%, but the exceptional PL46, which requests a higher melting extent, up to 13% in a fractional melting and 30% in a batch melting. The fractional melting model shows scattered melting degrees for the xenoliths from the rest of the localities, from 3 to 15% in Qixia, 2 to 8% in Changle, 8 to 15% in Daxizhuang, and 6 to 15% in Qingdao. The corresponding batch melting model shows a greater melting degree and a larger range. It is noted that not all the sample data are plotted just on the modeled curve, and some

deviate from it, reflecting complex mantle processes, such as subsequent mantle metasomatism.

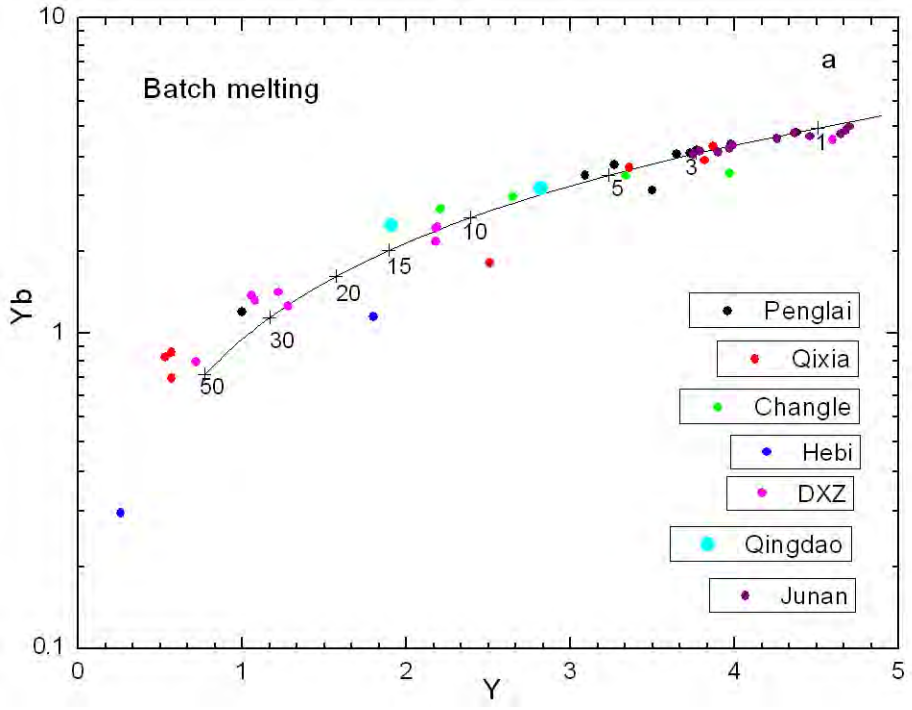

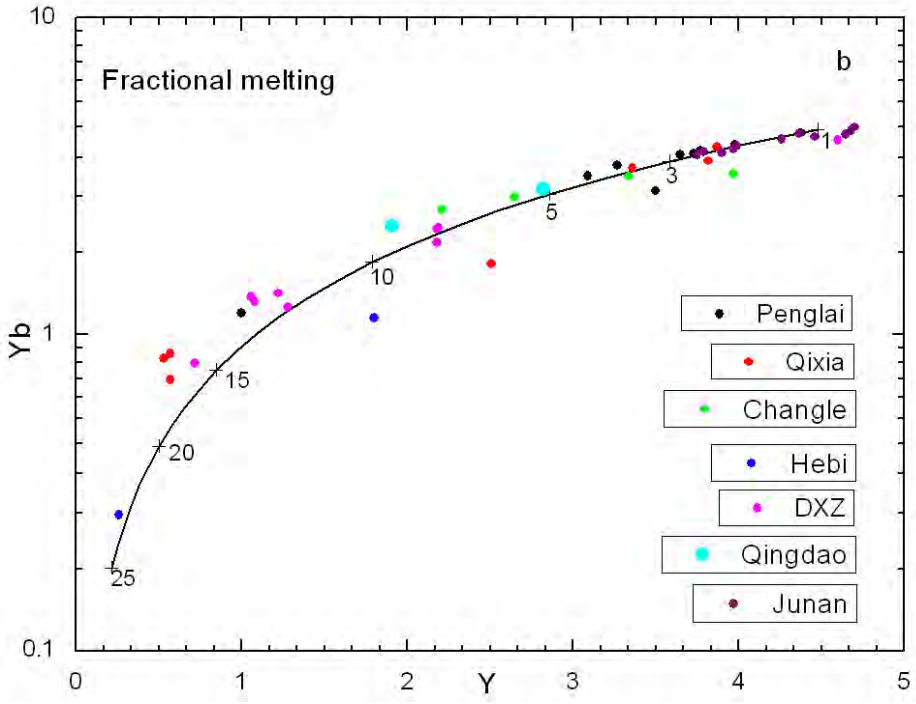

Figure 5-3. Partial melting modeling of cpx in the studied peridotite xenoliths from the North China Craton using primitive mantle-normalized abundances. (a) the batch melting modeling, and (b) the fractional melting modeling.

5.2 The fluids/melts enrichments

The mantle enrichment, like the melt depletion, can also change the nature of lithospheric mantle, but in opposite ways, by fertilizing, weighting, warming and softening the mantle peridotites.

During a single melting of peridotite at free-garnet faces, no matter the batch melting or fractional melting by which it works, all the REEs are expected to be depleted to the variable degrees, which, to a first order, increase from the right to left on the array of elements, producing a line of positive slope with the roughly flattening of HREEs and fractionated LREE/HREE in the REE normalized pattern. Obviously, this is not the case for some peridotites of the NCC, which are characterized by both HREE depletion and LREE enrichment. Moreover, that paradox is a pervasive phenomenon seen in xenoliths worldwide, especially those beneath the continental, implying that the multistage processes involved, including, at least, the primary melt depletion and a later melt/fluid infiltration. While the depleted HREEs abundances

reflect the melt depletion, the variability of LREEs abundances and normalized patterns owe more to the subsequent enrichment processes than the initial melt depletion.

Moreover, the refractory peridotite residues usually show greater overall enrichments than fertile lherzolites for reasons that are not yet entirely clear. The Sample PL46 that has much least HREE abundances is characterized by the most enrichment of LREE relative to HREE in Penglai. In Qixia, the LREE-depleted REE pattern is only found in QX14, which has the highest HREEs contents and the lowest Mg# value of olivine among Qixia samples.

It may reflect the elevated melt permeability of olivine-rich matrices relative to pyroxene dominant matrices, because the dihedral angle in olivine matrices is smaller than that in pyroxene matrices under the same condition. The less the angle, the more efficient the connectivity of fluid or melt system is infiltrating among grain boundaries (Orman et al., 1986; Bargen et al., 1986; Bargen et al., 1988). In other word, it means the longer equilibration time between the two phases.

The enrichment processes can be of multi-episode, and the metasomatic agents can also be of different natures. The metasomatic agents, responsible for enrichment in incompatible trace elements, such as LILEs and LREEs, can be subdivided into carbonatitic melts (Yaxley et al., 1998), volatile-rich silicate melts (Zangana et al., 1999) or H_2O–CO_2 liquids (Stalder et al., 1998) by their different extents and patterns of enrichment of those elements. Experimental studies of trace-element partitioning between cpx and melt in carbonate and silicate systems shows that in the carbonate system cpx-melt partition coefficients for Si, Al, heavy REE, Ti and Zr are higher by factors of 5–200 than those of the silicate system. Conversely, partition coefficients for Nb, LREE, alkali metals and alkaline earths show much less fractionation (<3; Blundy and Dalton, 2000). On the other hand, relative to silicate melt or CO2-rich fluid, carbonatite melts can fractionate HREE and HFSE more effectively and have high contents of LILE, whereas Nb cannot be transported by H_2O-rich fluids (Eggler, 1987).

Like many other pairs of trace elements used for tracing depletion or enrichment processes, Ti/Eu ratio was invented to serve that purpose. From studies of basalt and komatiites, it was well established that Ti/Eu abundance ratios remain nearly constant and chondritic over a wide range of concentrations, suggesting that these two highly incompatible elements have similar partition coefficients during partial melting (Sun

et al., 1989). Ti/Eu ratios in anhydrous peridotite xenoliths vary over a broad range, but the average value of 7850 is close to that of the chondritic ratio, 7700. So the large departure of the Ti/Eu ratio away from the chondritic ratio is usually referred to as a carbonate-related enrichment event, which can fractionate the two elements from each other. By the same token, it holds true for Ti/Eu in cpx when combined with the $(La/Yb)_N$ ratio and HFSE relative abundances (Coltorti et al., 1999).

Low Ti/Eu ratios in cpx of mantle peridotites, combined with high La/Yb ratios and HFSE depletion, have been widely interpreted as the key signatures of carbonatitic metasomatism (Coltorti et al., 1999). Our results for all xenoliths show a large range of the Ti/Eu ratio in cpx, varying from as low as 360 in Hebi, to a high value of 6760, found in DXZ02 (Fig. 5-4).

The cpx in two Hebi xenoliths have extremely both low Ti/Eu ratio (360 and 572) and high $(La/Yb)_N$ (96 and 5), indicating obvious carbonatitic melt metasomatism. This is consistent with those reported by Zheng et al. (2001, 2007). The enriched samples from the rest of localities were influenced mainly by the silicate melts rather than the carbonatitic melts, the combined metasomatism cannot be excluded in samples (those have been plotted in the right corner in Fig. 5-4). It is noted that the cpx that have the LREE-depleted pattern are characterized by a limited range of 4200 to 4700 for the Ti/Eu ratio.

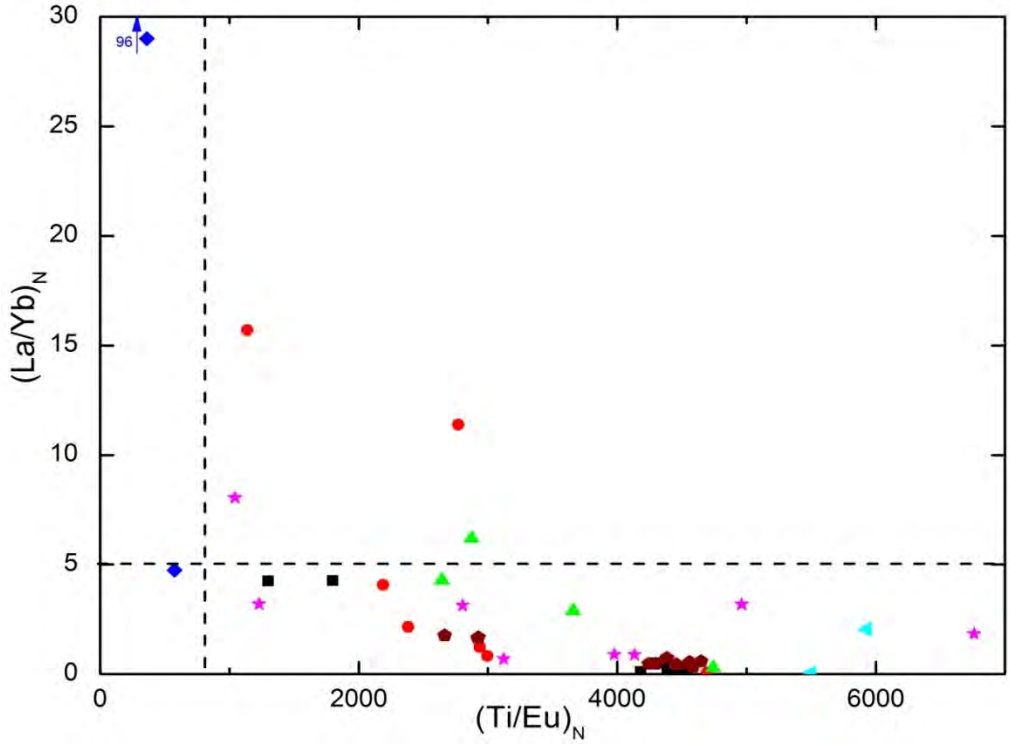

Figure 5-4. Ti/Eu versus $(La/Yb)_N$ in the cpx from anhydrous peridotite xenoliths of this study (Coltorti et al., 1999).

6 Water in the lithospheric mantle

6.1 Preservation of initial water content of mantle pyroxenes

The prerequisite to purposely interpret these water data is that the measured water contents of these minerals in peridotite xenoliths are representatives of the pre-eruption state (Kohlstedt et al. 1998; Lee et al., 2011) at their mantle source, given the high diffusion rate of H and the decompression-induced lowing of solubility of H in these mantle minerals. For P < 3.5 GPa, the solubility of hydrogen in nominally anhydrous minerals (NAMs) increases with increasing pressure (Keppler and Bolfan-Casanova, 2006, and references therein; Mierdel et al., 2007); thus, when peridotite xenoliths are transported to the surface by their host magmas, hydrogen can potentially diffuse out the NAMs due to the sharp pressure fall. Diffusion experiments predict that at 1000°C hydrogen resetting in olivine and pyroxene will be achieved at millimeter scale in a few tens of hours (Kohlstedt and Mackwell, 1998; Hercule and Ingrin, 1999; Carpenter et al., 2000; Stalder and Skogby, 2003). In contrast, studies on natural samples indicate that pyroxenes preserve their mantle-derived OH contents, but olivines do not, despite the similar diffusion rates of H (Bell and Rossman, 1992a; Bell et al., 2004; Peslier et al., 2002; Grant et al., 2007b; Li et al., 2008; Gose et al., 2009a). Possible explanations for the discrepancy may be related to the facts that (1) the loss of hydrogen is influenced by the water and oxygen fugacities of the systems and the H content of coexisting minerals and melt; (2) the incorporation of hydrogen into minerals does not only depend on the diffusion rate of hydrogen, but also on the diffusion rate of point defects associated with hydrogen incorporation, the latter being comparatively slower by at least several orders of magnitude (Kohlstedt and Mackwell, 1998); and (3) experiments are made underwater-saturated conditions, which probably do not prevail in natural systems.

We are convinced that pyroxenes, at least of the NCC peridotite xenoliths here, have largely preserved their initial water content in the mantle source. This claim can be justified by several lines of evidence.

1. All the samples are chemically homogeneous for individual phases, and no major elements or REE zoning were observed for each studied grain (EMPA).

2. The FTIR analyses were performed on the core regions of clean, crack-and inclusion-free pyroxene grains of relatively large size. The core could preserve the initial water as far as it goes, reasoning that the slight diffusive loss of H, if indeed happening, would be magnified at the rims rather at the cores of grain.

3. Water contents are homogeneous within individual pyroxene grains. The core-rim profile analyses for pyroxene grains of the studied peridotites indicate no obvious zoning of water contents within single grains. In addition, the unpolarized absorbances for individual grains of one mineral phase in each sample vary moderately as the theory suggests, neither more volatilely nor more gently. Both of these observations argue against the possibility of the H diffusion out of mineral grains and that induced intra-grain heterogeneity among grains.

4. Water contents are positively correlated between cpx and opx. As shown in Fig. 4-20, water contents of cpx and opx display a good positive correlation. The partition coefficient between cpx and opx ($D_{cpx/opx}$) is 2.27 in considering only the data from this study, and 2.25 when combining those from Nushan and Hannuba. This is in the same range as the literature values reported for natural peridotite xenoliths: $D_{cpx/opx}$ = 2.3 ± 0.5 (n = 38 (Bell and Rossman, 1992a; Peslier et al., 2002; Grant et al., 2007b; Li et al., 2008)), and also close to those determined by experiments using a low−blank SIMS method: Aubaud et al. (2004) reported $D_{cpx/opx}$ = 1.8 ± 0.3 (n = 1, the value is revised according to new calibration of Aubaud et al. 2007); Hauri et al. (2006) obtained $D_{cpx/opx}$ = 0.9–1.4 (n = 6); Tenner et al. (2009) reported Dcpx/opx = 1.2–2.0 (n = 3).

5. The rough correlations between Al_2O_3 (wt%) and water content (ppm) in opx (Fig. 6-1) indicates that the dissolution of hydrogen in these minerals is combined with that of Al^{3+}. The positive correlation between Al_2O_3 (wt%) and H_2O (ppm) evidenced in opx of the studied peridotite xenoliths (Fig. 6-1), are also found in sub-arc mantle wedge samples (Peslier et al., 2002; Grant et al., 2007a), as well as in off-craton intraplate mantle (Grant et al., 2007a; Yang et al., 2008), with different slopes due to the higher values of water contents in the sub-mantle wedge with respect to the intraplate setting. This correlation is also supported by experimental results of Rauch and Keppler (2002) which show that water solubility increases with increasing of Al_2O_3 contents (up to 1 wt%) in synthetic enstatite. This implies that the hydrogen dissolution in these minerals is coupled with that of Al^{3+}, whose diffusion coefficient

is so low that significant loss is unlikely, neither the hydrogen contents.

On the basis of heterogeneous distribution of water within single grains (higher contents in the core and lower contents in the rim), several studies suggested significant loss of hydrogen in olivines by diffusion during xenolith ascent to the surface (Demouchy et al., 2006; Peslier and Luhr, 2006; Peslier et al., 2008). Other studies did not observe any water heterogeneity in their olivines (Bell et al., 2004; Grant et al., 2007b). We cannot address this issue based on the NCC olivines because their water contents are too low to be detected, and only few large grains in few samples from Qingdao and Junan, where the coexisting pyroxene have high water contents, show weak O-H absorption bands, still suggesting a water content of less than 5 ppm.

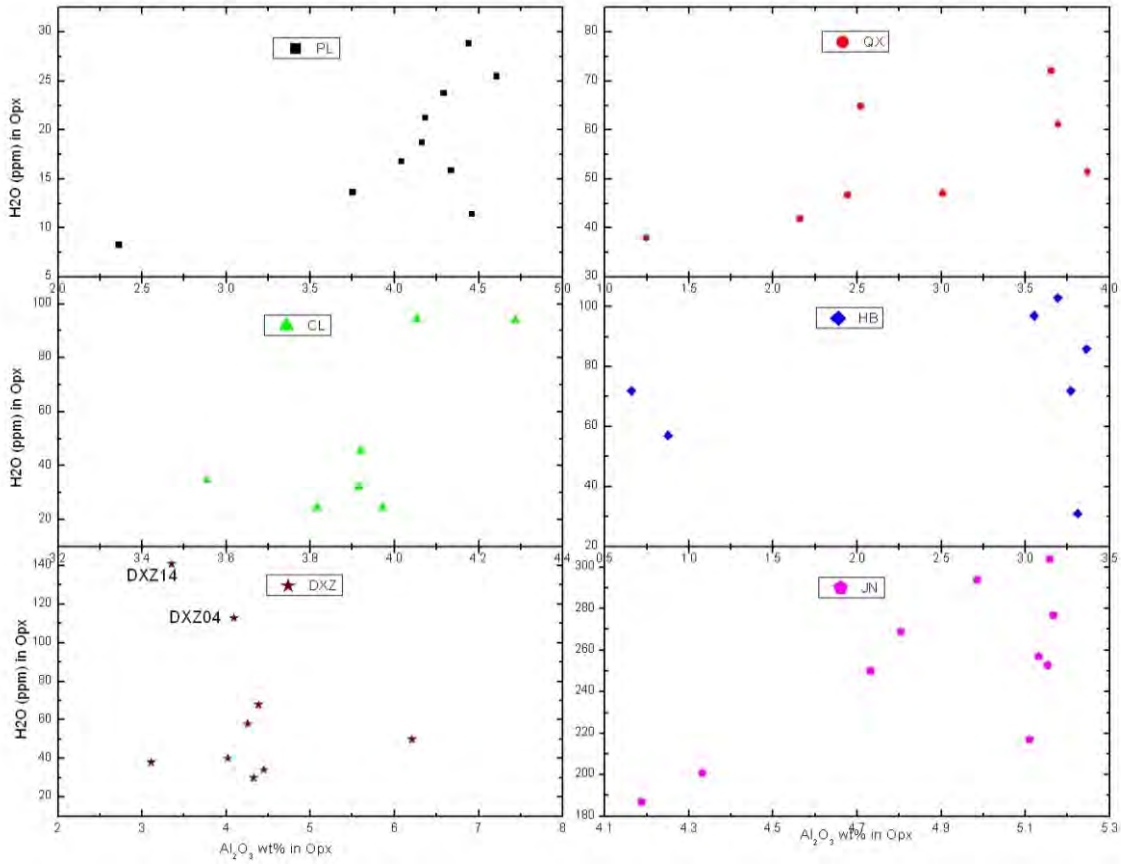

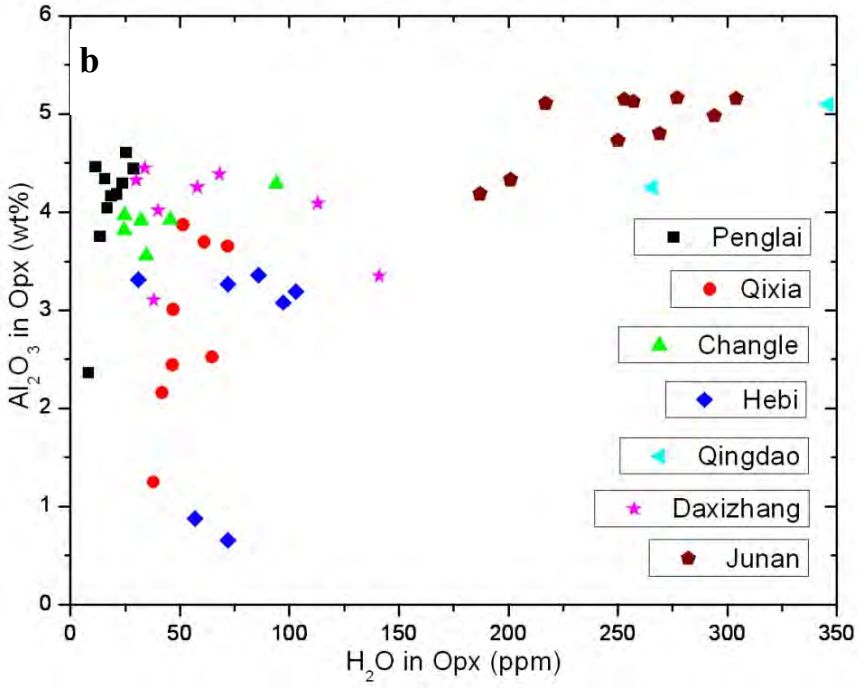

Figure 6-1. Correlation between H_2O (ppm) and Al_2O_3 (%) in opx of peridotite. (a) the covariation between H_2O (ppm) and Al_2O_3 (%) in opx from individual localities, and (b) covariation between H_2O (ppm) and Al_2O_3 (%) in opx from all the localities together.

6.2 Possible factors controlling water contents of pyroxenes

The FTIR results show that water contents of cpx and opx in mantle peridotite xenoliths from the seven localities (Penglai, Qixia, Changle, Hebi, Qingdao, Junan and Daxizhuang) in the NCC vary from 27 to 746 ppm and from 8 to 346 ppm respectively. A large water variation was also observed by Yang et al. (2008) on the xenolith peridotites from Hannuoba and Nushan (also belonging to the NCC). All these H_2O databases in NCC, to the first order, show lateral variation of water contents in the continental lithosphere. Beyond the NCC, these lateral variations were also observed on a larger scale, suggested by the published water data for peridotites from West Kettle River in British Columbia, Lesotho, Namibia, Premier, Kimberley and Jagersfontein in South Africa, Simcoe and New Mexico in USA and Massif Central in France and also several other regions reported by Bell and Rossman (1992b), Peslier et al. (2002) and Grant et al. (2007a) (all these are compiled and illustrated in Figure 6-4).

Xia et al. (2004) attributed the overall high H_2O contents of peridotites in Nushan relative to those in Hannuoba to the metasomatism of subducted oceanic crust in the

Nushan area. At subduction zone or the place that is within reach of subduction processes, the dehydration of the altered oceanic crusts or water-saturated sediments during subduction would have expelled water out of the subducting slab to hydrate the mantle above the down-going plate, hence resulting in the subduction-modified mantle domains that are virtually wetter than in other normal regions (Peacock, 1993; Peslier et al., 2002; Dixon et al., 2004). This explanation, however, cannot extend to the low water contents of peridotites in our case. The eastern China, as part of the active continental margin of East Asia since the Late Mesozoic, has long been influenced by the western subducting of the pacific plates (and also the paleo-Pacific plate) (Wu et al., 2005; Sun, W.D. et al., 2007; Menzies et al., 2007). But the peridotite xenolith from most of those localities did not see the water enrichment, but the high depletion of water instead. The Penglai areas, for instance, is suited the most eastern of the NCC, and those peridotites from there with the lowest water contents among all studied peridotite xenoliths. It is noted that the Cenozoic lithospheric mantle beneath these two localities (Nushan and Hannuoba), even extending to the most of the NCC, are characterized by low water content relative to those from the other domains worldwide.

It is general believed that water, or hydrogen, is highly incompatible during mantle melting, with a K_d similar to the element of Ce (0.007~0.009) (Dixon et al., 1988; Michael, 1995, 1998; Hauri et al., 2006). So, the melt depletion, and the reverse process, i.e. mantle metasomatism in form of fluids or melts infiltrations, can play a significant role in controlling the water contents and their variations in peridotites.

The water contents in either cpx or opx show no indication of the correlation with the indicators, such as Mg# in coexisting olivines that reflect the relative degree of melt depletion to the peridotites (Fig. 6-2), and Ce_N or $(Ce/Yb)_N$ in cpx which are linked to enrichment processes in peridotites (Fig. 6-3).

b

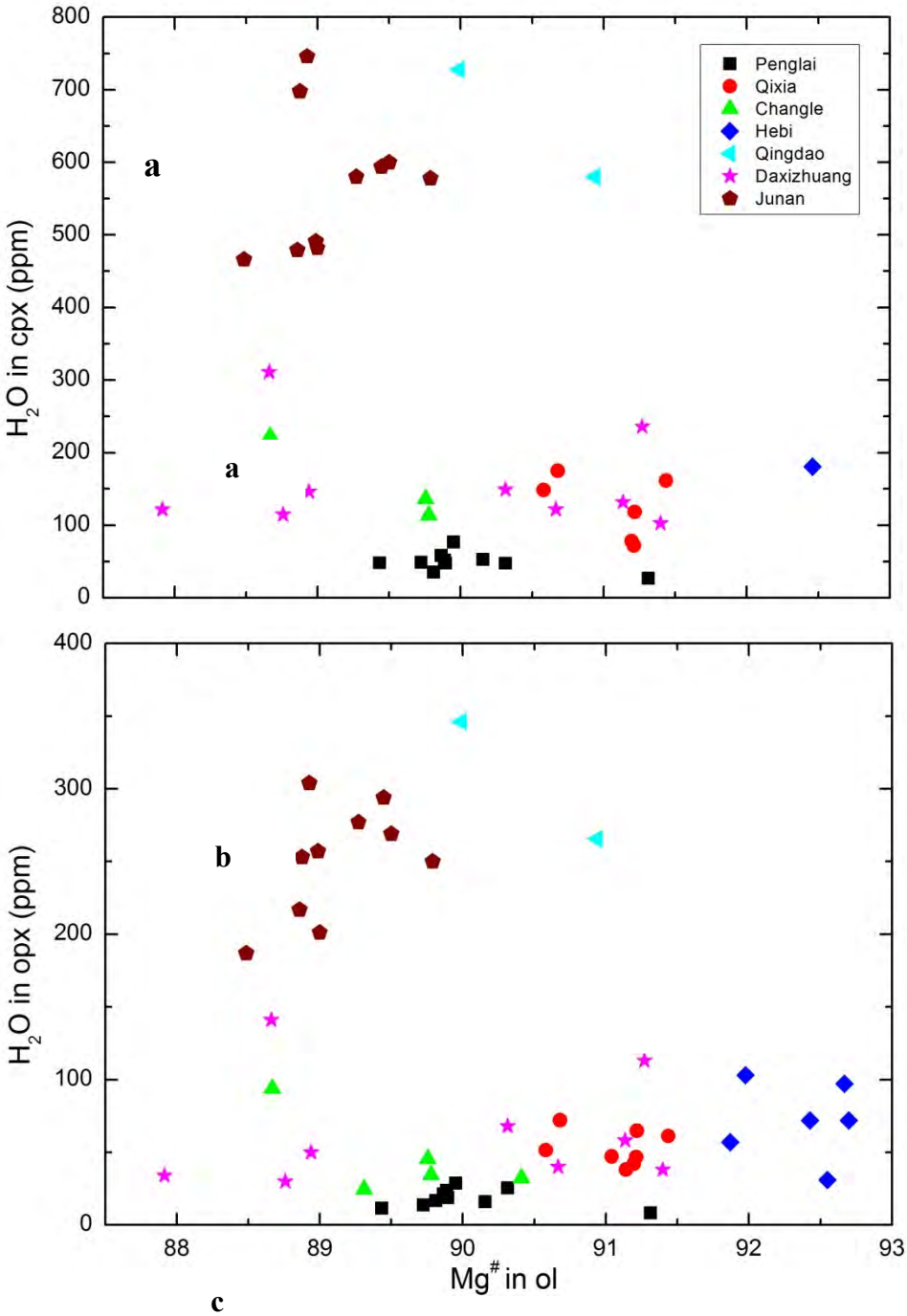

Figure 6-2. Covariat :ween Mg# values in coexisting olivines and cpx H_2O contents in

a, and opx H_2O contents in **b**

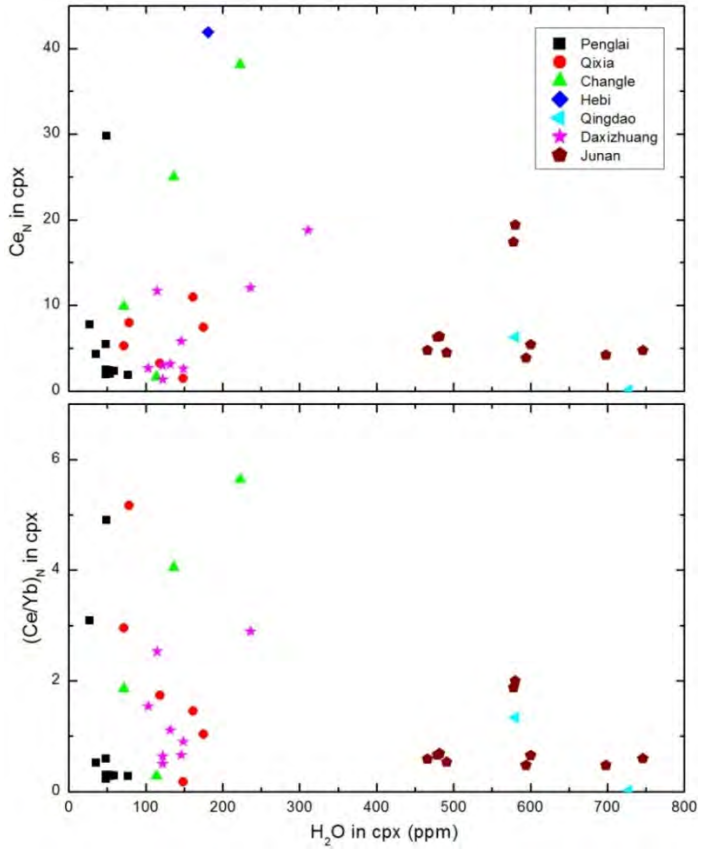

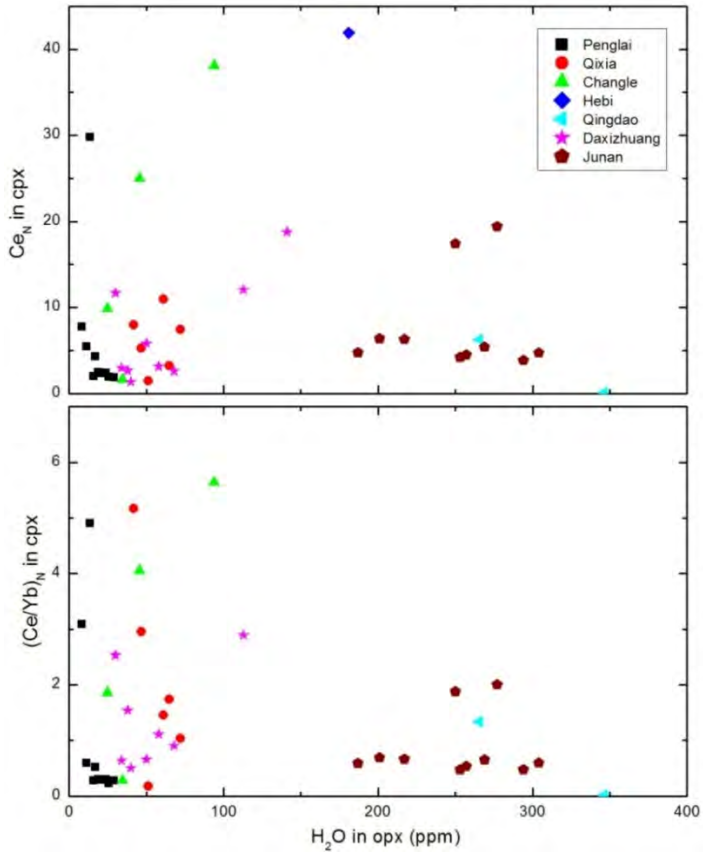

d

Figure 6-3. Covariations between cpx H_2O contents and cpx Ce_N in **a,** and $(Ce/Yb)_N$ in **b**; between opx H_2O contents and cpx Ce_N in **c,** and $(Ce/Yb)_N$ in **d**.

Sample PL46, the most refractory sample with high Mg# of olivines and low HREEs contents in Penglai, have the lowest water contents for both cpx and opx, suggesting the melt depletion a main role in controlling the water content. The rest of samples that shared the same REE pattern and Mg # of olivines show different water contents. The PL31 have two times more water content that PL19 for cpx but without any obvious differences in their chemical compositions. In Qixia, the samples can be subdivided into two groups. The water contents for the samples (QX14, QX49 and QX51) with relatively high HREEs contents have higher water contents of cpx and opx than the rest of sample, which have high LREE/HREE ratios but depleted HREE contents. But when going deeper into group, there is no relation again between water contents and those HREE contents or other indicators. In two samples of Qingdao, the QDPS 16 have higher water contents than the QDPS24, which, although characterized by slightly LREE-enriched, has less HEREE contents and higher Mg# of coexisting olivines. This relation, although exists, still need more samples to justify.

Although the vague correlation was observed locally between water contents and the relative extents of melt depletion (i.e. olivine Mg# values and HREEs abundances) in samples from Penglai, Qixia, Daxizhuang and Qingdao, the relatively refractory samples of Qixia have the higher overall water contents than those of Penglai, arguing against the main role of partial melting in controlling water contents. In a word, the water contents in pyroxenes are likely to a consequence of the combination of a series of mantle processes, such melt depletion, fluids/ melts enrichment, redox state of mantle source, tectonic-thermal history and the like, or of just some combined, rather than one single process.

It is interesting to note that the pyroxenes of peridotite xenoliths host by Mesozoic basalt have much higher water contents than those of xenoliths hosted by Cenozoic basalt. While the water contents of cpx and opx in the xenoliths from Penglai, Qixia, Changle and Hebi vary from 27 to 223 ppm and 8 to 103 ppm, respectively, those in xenolith from Qingdao and Junan range from 466 to 746ppm and 187 to 346 ppm, respectively. The samples from Daxizhuang, although hosted by Mesozoic basalt, have a water affinity to those hosted by Cenozoic basalt, with water contents of cpx and opx ranging from 103 to 311 ppm and 30 to 141 ppm, respectively.

6.3 Low water content of peridotites hosted by Cenozoic basalts

Because the low water content is not only confined to peridotite xenoliths hosted by Cenozoic basalt in our research areas (e.g., Penglai, Qixia, Changle, and Hebi), but also extends to a more broad areas in the NCC. The Nushan and Hannuoba peridotites have been reported to have much lower water contents than peridotites from cratonic and off-cratonic continental areas worldwide (Yang et al., 2008). So do those peridotite xenoliths from Panshishan, Lianshan and Fangshan, three localities at Subei basin (Bonadiman et al., 2009; Xia et al., 2010). Combining all these data (Aubaud et al., 2007; Yang et al., 2008; Bonadiman et al., 2009, Xia et al., 2010), we obtain a total of 105 peridotites hosted by Cenozoic basalts from 9 localities of the eastern part of the NCC, which we use to make the following observations and interpretations. As described below, the Cenozoic lithospheric mantle of the NCC (at least the eastern part) appears to have lower water contents compared to both the continental cratonic and off-cratonic lithospheric mantle worldwide and to the oceanic mantle.

6.3.1 Comparison with the continental craton and off-craton lithospheric mantle

Water contents of peridotites from the NCC (Aubaud et al., 2007; Yang et al., 2008; Bonadiman et al., 2009; this study) and other continental regions worldwide (Bell and Rossman, 1992a; Peslier et al., 2002; Demouchy et al., 2006; Grant et al., 2007b; Li et al., 2008; Bonadiman et al., 2009) are compiled in Fig. 6-4. Tectonically, continental mantle peridotite can be classified as: on craton peridotites, such as samples from South Africa and Colorado Plateau (Bell and Rossman, 1992a; Grant et al., 2007b; Li et al., 2008) and off-craton peridotite, such as samples from Basin and Range (USA), Massif Central (France), Patagonia (Chile) and Antarctic samples (Bell and Rossman, 1992a; Peslier et al., 2002; Demouchy et al., 2006; Grant et al., 2007b; Li et al., 2008;Bonadiman et al., 2009). Water contents of cpx of the NCC peridotites range between 5 and 355 ppm; 85 of the 92 analyzed samples contain less than 200 ppm, and the average value is 108±61 ppm. In contrast, H_2O contents of cpx of the craton peridotites data set range between 370 and 950 ppm with the average value of 577±209 ppm (397±61 ppm if slab-influenced Colorado Plateau samples (Li et al., 2008) are excluded). On the whole, the cpx of the off-craton peridotites range

between 5 and 528 ppm with the average value of 316±151 ppm (Fig. 6-4A). H_2O content of opx of the NCC peridotites range between 5 and 140 ppm, 96 of the 106 analyzed samples contain less than 80 ppm and the average value is 42±27 ppm. Differently, H_2O content of opx of the on-craton peridotites range between 180 and 400 ppm and the average value is 297±94 ppm (244±107 ppm if slab-influenced Colorado Plateau samples (Li et al., 2008) are excluded); that of the off-craton peridotites range between 9 and 300 ppm and the average value is 125±77 ppm (Fig. 6-4B). The estimated whole rock water content (calculated H_2O contents of ol by assuming $D_{cpx/ol}$=10 for all the samples) of the NCC peridotite xenoliths range between 6 and 85 ppm with the average value of 25±18 ppm. In contrast, with that recorded in on-craton peridotites is more than 60 ppm (except one dunite from Colorado with 27 ppm) and the average values is 119±54 ppm (124±62 ppm if slab-influenced Colorado Plateau samples (Li et al., 2008) are excluded); that of off-craton peridotites is between 10 and 154 ppm, and the average value is 78±45 ppm (Fig. 6-4C). The comparison of the water contents in the NCC pyroxenes listed above and those from the two different tectonic setting, show consistent differences. Among the off-craton" peridotites only a few have water contents similar to those of NCC mantle xenoliths (Fig. 6-4C). These are harzburgite and dunite samples which have experienced high degrees of partial melting (Peslier et al., 2006; Li et al., 2008; Bonadiman et al., 2009): as H_2O behaves as a highly incompatible element during partial melting of a mantle source (in solid/liquid system H_2O has the almost the same geochemical behavior of Ce; Hauri et al., 2006; Tenner et al., 2009), the peridotite residues experiencing higher degrees of partial melting are expected to be more depleted in water. Moreover, lherzolites from San Carlos Cenozoic basalts have a similar low water contents (171 to 178 ppm for cpx, 53 to 82 ppm for opx, and 2 to 4 ppm for olivine, Li et al., 2008) to those of the NCC lherzolites. The low water contents of these rocks have been interpreted as the result of water loss during partial melting (Li et al., 2008).

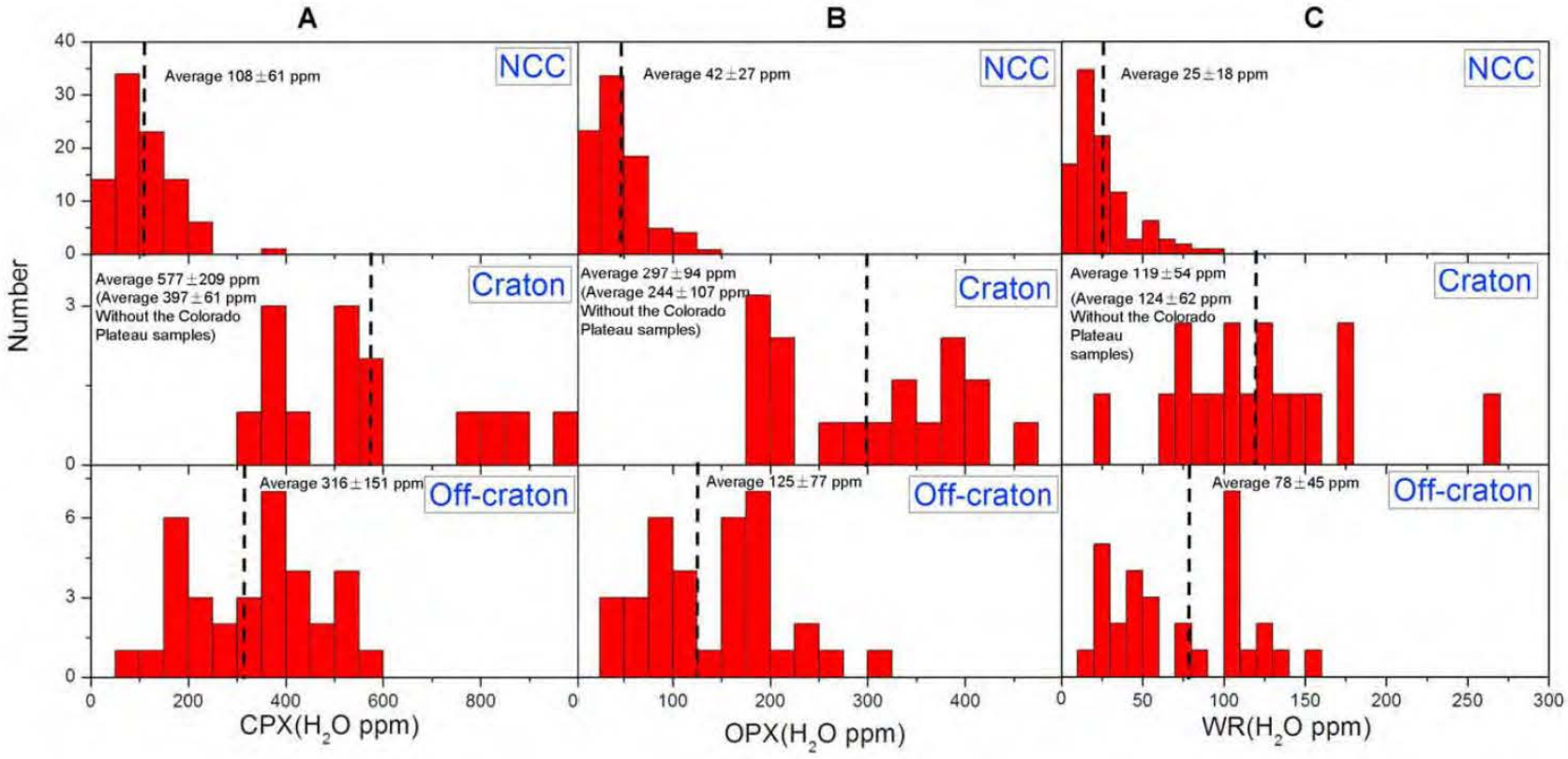

Figure 6-4. Comparison of H_2O contents of cpx, opx, and whole rock (WR) of the NCC peridotite xenoliths with those of cratonic and off-cratonic peridotites. The NCC data are from *Aubaud et al.* [2007] and *Yang et al.* [2008] for Nushan and Hannuoba, *Bonadiman et al.* [2009] for Panshishan and Lianshan, and this study for Fangshan, Penglai, Qixia, Changle, and Hebi. The data for cratonic peridotites (South Africa and Colorado Plateau) are from *Bell and Rossman* [1992a], *Grant et al.* [2007b], and *Li et al.* [2008]; the data for off-cratonic peridotites (Basin and Range area, French Massif Central, Patagonia, Antarctic and West Kettle, British Columbia) are from *Bell and Rossman* [1992a], *Peslier et al.* [2002], *Peslier and Luhr* [2006], *Demouchy et al.* [2006], *Grant et al.* [2007b], *Li et al.* [2008] and *Bonadiman et al.* [2009]. For cratonic samples, two average values are given: with or without the Colorado Plateau samples which were rehydrated by a subduction slab [*Li et al.*, 2008].

6.3.2 Comparison with the oceanic mantle

The available data for oceanic peridotites are very scarce; they are limited to three abyssal peridotites from Gakkel ridge, Arctic Ocean (Peslier et al. (2007)) and Cape Verde mantle xenoliths, Atlantic Ocean (Bonadiman et al., 2009) the H_2O content are <1-5 ppm for ol 25-60 ppm for opx and 130-200 for cpx. The low water content of these samples is likely the consequence of water loss during the slow adiabatic decompression; thus they do not necessarily represent the mid-oceanic basalt (MORB). Gose et al. (2009b) investigated a suit of abyssal peridotites from the Mid-Atlantic Ridge; the measured H_2O contents of opx range between 160 and 270 ppm and was suggested to reflect the original mantle contents. This range is much higher than that of opx of the NCC peridotites (between 5 and 140 ppm, with 96 out of 106 samples being <80 ppm). In contrast to oceanic peridotites and xenoliths, the H_2O content of MORB and OIB have been well constrained from melt inclusion and glass (Dixon et al., 1988, 1997, 2002; Michael, 1988, 1995; Stolper and Newmann, 1994; Sobolev and Chaussidon, 1996; Danyushevsky et al., 2000; Nichols et al., 2002; Saal et al., 2002; Simons et al., 2002; Wallace, 2002; Asimow et al., 2004; Seamon et al., 2004; Workman et al., 2006). Based on these data, the water content of the source of MORB and OIB is calculated to be about between 50 to 250 ppm and between 300 to 1000 ppm respectively. Consequently, the water contents of the NCC peridotites are lower than the oceanic mantle represented by the source of MORB and OIB.

6.3.3 Possible Role of Redox State on Water Content

On the basis of the negative correlation between water content of pyroxenes and oxygen fugacity for Mexican and Simcoe (Washington) spinel peridotite xenoliths, Peslier et al. (2002) suggested that pyroxene water contents are mainly controlled by the redox state of peridotites, i.e. the oxidization of Fe^{2+} is coupled with the reduction of H^+ to $1/2H_2$ that escapes from xenoliths. In order to test this model in the NCC peridotites, we calculated the spinel $Fe^{3+}/\sum Fe$ ratio and the peridotite oxygen fugacity (expressed as variation relative to the fayalite-magnetitequartz oxygen buffer or ΔFMQ) based on EMP data from Yang et al. (2008) and from this study. Fe^{3+} values for spinels were calculated following the equation: $Fe^{3+} = 8 - (4Ti + 3Al + 3Cr + 2Fe$

+ 2Mn + 2Ni + 2Mg) using atomic formula units normalized to three cations and discarding negative values. ΔFMQ values were calculated following the protocol of Woodland et al. (1992). A pressure of 15 kbar was assumed for all the samples. If the temperature estimates from two opx-cpx thermometers (Wells, 1977; Brey and Kohler, 1990) differed by 200°C or more, the samples were discarded for ΔFMQ calculation. The overall uncertainty was empirically estimated to be ±0.5 log units. The spinel $Fe^{3+}/\sum Fe$ ratios and ΔFMQ values are given in Table 6-1. ΔFMQ values for the NCC peridotites vary from −4.2 to +2.2, with most ranging between −2.5 and +0.5. These values fall in the range of continental mantle as represented by peridotite xenoliths and peridotite massifs (Frost and McCammon, 2008, and references therein). Spinel $Fe^{3+}/\sum Fe$ values of the NCC peridotites vary from 0.03 to 0.34, with most values between 0.10 to 0.34, in the range of continental spinel peridotites (most of them range from 0.15 to 0.34 (Frost and McCammon, 2008, and references therein) and the Mexican and Simcoe spinel peridotites (Peslier et al., 2002). Some of the NCC spinels have low $Fe^{3+}/\sum Fe$ values, down to 0.03, and the majority of the NCC peridotites are not characterized by oxidized signatures (ΔFMQ > 0). In addition, no correlation between pyroxene water content and spinel $Fe^{3+}/\sum Fe$ and peridotite ΔFMQ values can be observed (Fig. 6-5). Therefore, the low water content of the NCC samples cannot be related to high oxygen fugacity as has been argued in the case of the Simcoe peridotites (Peslier et al., 2002)

Table 6-1 Water content, mineral mode, temperature, spinel $Fe^{3+}/\Sigma Fe$, and ΔFMQ of peridotite xenoliths hosted by Cenozoic basalts from the North China Craton.

Locality	Sample	Rock Type	Mode(%)				H_2O content (ppm, wt)			T (°C)	ΔFMQ	Spinel $Fe^{3+}/\Sigma Fe$
			cpx	opx	ol	sp	cpx	opx	WR			
Fangshan	FS01	Sp Lher	18	27	53	2	64	25	22	972	-1.0	0.11
	FS03	Sp Lher	13	27	58	2	167	68	50	1191		0.26
	FS06	Sp Lher	10	24	65	1	170	61	43	1044		0.18
	FS07	Sp Lher	12	28	57	3		60		1001	-0.6	0.17
	FS11	Sp Lher	9	21	69	1	109	43	26	998	2.2	0.29
	FS12	Sp Lher	7	30	61	2	158	54	37	1139		0.14
	FS13	Sp Lher	8	28	61	3	108	41	27	1092		0.17
	FS14	Sp Lher	11	20	66	3	120	53	32	1063		0.17
	FS16	Sp Lher	6	17	76	1	90	33	18	1023	-0.4	0.16
	FS17	Sp Lher	16	26	56	2	53	28	19	972	-1.5	0.09
	FS18	Sp Lher	9	20	70	1		63		1172	0.2	0.32
	FS19	Sp Lher	14	25	58	3		74		1113		0.22
	FS21	Sp Lher	10	20	68	2	177	69	44	1017		0.16
	FS23	Sp Lher	12	14	71	2	101	39	25	1094	0.6	0.25
	FS24	Sp Lher	16	34	48	1	41	21	16	928	0.3	0.22
	FS26	Sp Lher	9	20	70	1	67	28	16	967	-2.1	0.07
Penglai	PL01	Sp Lher	9	27	62	2	52	24	14	924	0.5	0.20
	PL10	Sp Lher	6	20	72	2	53	16	10	932	0.9	0.24
	PL17	Sp Lher	7	19	72	2	48	19	10	903	0.9	0.20
	PL19	Sp Lher	12	18	67	3	35	17	10	918	0.9	0.22
	PL32	Sp Lher	10	13	76	1	49	14	10	945	0.3	0.20
	PL36	Sp Lher	10	22	65	3	59	21	14	903	1.4	0.26
	PL42	Sp Lher	8	16	75	1	48	25	11	942	0.0	0.16
	PL44	Sp Lher	11	15	72	2	48	11	10	914	-1.7	0.10
	PL46	Sp Lher	9	14	78	1	27	8	6	953	0.4	0.19
Qixia	QX01	Sp Lher	6	23	68	3	70	32	16	951	-1.0	0.10
	QX04	Sp Lher	12	25	60	3	104	48	31	920	-4.2	0.02
	QX14	Sp Lher	8	20	70	2	158	52	34	925		
	QX18	Sp Lher	9	23	67	2	115	54	30	945	0.2	0.16
	QX50	Sp Lher	9	20	70	1	78	42	21	957	-0.1	0.14
	QX51	Sp Lher	18	20	61	1	158	59	50	883		
Changle	CL01	Sp Lher	11	25	61	3	71	25	18	965		0.06
	CL22	Sp Lher	9	22	68	1	223	94	56	1010	-0.7	0.12
	CL31	Sp Lher	9	16	72	3	136	45	29	992	-1.2	0.11
	CL32	Sp Lher	10	16	73	1	111	25	23	934		
	CL35	Sp Harz	2	22	74	2		32		945		0.05
	CL38	Sp Lher	11	15	72	2	114	35	26	907		0.03
Hebi	HB02	Sp Harz	<0.5	15	82	3		57	9	925	0.5	0.22
	HB06	Sp Harz	0	15	83	2		72	11	1056	0.2	0.21
	HB07	Sp Harz	0	20	78	2		52	10	798	0.6	0.17
	HB10	Sp Harz	0	25	73	2		72	18	760	1.2	0.27
	HB12	Sp Harz	0	18	80	2		96	17			0.22
	HB16	Sp Harz	0	15	84	1		64	10			0.16
	HB17	Sp Harz	<0.5	20	78	2		31	6	1057		0.18
	HB64	Sp Lher	10	10	77	3	181	86	41	1043	0.3	0.25
Panshishan	PSS01	Sp Lher	10	18	71	1	95	26	21	960	-3.9	0.16
	PSS02	Sp Lher	15	20	65	1	129	30	34	956	-1.5	0.16
	PSS05	Sp Lher	12	20	62	2	161	34	36	964	-3.6	0.03
	PSS07	Sp Lher	15	31	52	2	147	30	39	971		0.08
	PSS10	Sp Lher	7	17	73	3		16		967		0.03
	PSS11	Sp Lher	12	29	57	2	103	26	26	888	0.0	0.32
	PSS12	Sp Lher	15	24	58	1	183	56	52	957	-4.1	0.09
	PSS13	Sp Lher	13	20	65	2	112	25	27	966		0.03
	PSS15	Sp Lher	10	26	62	3	64	17	15	902	0.3	0.25
	PSS16	Sp Lher	16	33	50	1	181	61	58	961		0.11
	PSS17	Sp Lher	5	18	75	2	177	50	31	953	-1.0	0.20
	PSS18	Sp Lher	15	22	60	3	121	23	31	861	-2.3	0.02
	PSS19	Sp Lher	13	16	70	1	145	23	33	959		
	PSS20	Sp Lher	12	27	59	2	150	23	33	902		

Locality	Sample	Rock Type	Mode(%)				H_2O content (ppm, wt)			T (°C)	ΔFMQ	Spinel $Fe^{3+}/\Sigma Fe$
			cpx	opx	ol	sp	cpx	opx	WR			
Lianshan	LS01	Sp Lher	10	21	67	2	55	18	11	924	0.0	0.08
	LS02	Sp Lher	23	26	49	2	41	13	14	907	-1.0	0.04
	LS03	Sp Lher	8	20	70	2	41	17	8	949	0.4	0.29
	LS04	Sp Lher	24	39	37		56	28	25	977	0.0	0.22
	LS05	Sp Lher	10	28	60	2	90	34	20	904		0.23
	LS06	Sp Lher	10	23	66	1	73	32	16	972	-0.6	0.08
	LS07	Sp Lher	12	27	60	1	96	30	21	967		0.20
	LS08	Sp Lher	14	27	57	2	42	15	11	931	-0.1	0.09
	LS12	Sp Lher	9	16	72	3	78	32	14	954	0.6	0.28
	LS17	Sp Lher	7	17	73	3	37	17	7	972	0.2	0.23
	LS19	Sp Lher	11	21	67	1	89	45	21	904	-0.4	0.07
	LS20	Sp Lher	10	10	78	2	84	34	13	966	-1.6	0.20
	LS21	Sp Lher	9	9	76	1		16	3		-2.5	0.05
	LS22	Sp Lher	12	22	64	2	102	41	23	914	-0.5	0.06
	LS23	Sp Lher	15	20	63	2	73	32	19	949	-1.1	0.11
	LS24	Sp Lher	15	28	56	1	80	34	23	950	-0.1	0.08
	LS26	Sp Lher	7	20	70	3	57	19	9	946	0.0	0.13
	LS30	Sp Lher	13	34	52	1	92	29	23	983	-0.7	0.10
	LS31	Sp Lher	16	15	68	1	55	16	13	893		0.06
Hannuoba	P1	Sp Lher	9	18	71	2	85	25	14	866	-0.2	
	P2	Sp Lher	10	25	63	2	90	40	20	887	-1.3	0.16
	P3	Sp Lher	10	24	65	1	60	20	12	858	1.1	0.09
	P4	Sp Lher	5	18	74	3	50	20	8	1027	-0.1	0.34
	P6	Sp Lher	7	20	72	1	150	55	23	988	-0.3	0.18
	P8	Sp Lher	7	20	71	2	85	35	14	1006	-0.2	0.17
	P11	Sp Lher	9	15	75	1	70	35	13	992	-1.3	0.17
	P12	Sp Lher	13	20	65	2	110	35	23	969	-0.6	0.08
	P13	Sp Lher	15	27	55	3	100	45	28	915	-0.9	0.13
	P14	Sp Lher	9	25	65	1	140	55	28	857	-0.9	0.10
	P15	Sp Lher	7	23	68	2	125	55	23	947	0.1	0.11
	P17	Sp Lher	8	15	74	3	100	35	15	965		0.21
Nushan	NS01	Sp Lher	9	25	64	1	190	105	45	913		
	NS03	Sp Lher	10	27	61	2	95	55	26	1099	-0.7	0.24
	NS06	Sp Lher	5	24	70	1	40	40	13	1084	-0.3	0.29
	NS07	Sp Lher	10	25	62	3	115	80	33	1107	-0.7	0.21
	NS08	Sp Harz	0	25	72	1		15	5	912	-0.4	0.29
	NS12	Sp Lher	7	28	63	2	165	110	44	1073		0.16
	NS13	Sp Lher	12	25	61	2	15	20	8	931	-1.4	0.12
	NS14	Sp Lher	18	30	51	1	215	95	68	1089		0.27
	NS16	Sp Lher	9	20	70	1	240	115	46	1090		0.09
	NS21	Sp Lher	9	22	65	2	215	90	40	937	-1.6	0.08
	NS22	Sp Lher	15	27	56	1	5	5	3	945	-3.4	0.09
	NS24	Sp Lher	18	25	55	2	245	110	73	1101	-1.7	0.14
	NS25	Sp Lher	7	18	73	2	355	140	52	1090		0.03
	NS29	Sp Lher	13	20	64	1	240	105	53	973		
	NS30	Sp Lher	5	16	75	1	55	40	11	899	-0.6	0.19

Note: The compiled data for the NCC peridotite xenoliths include those from Nushan and Hannuoba (Yang et al., 2008), those from Panshishan and Lianshan in Subei Basin (Bonadiman et al., 2009) and those from Fangshan (Xia et al., 2010). The whole rock (WR) H_2O contents here were calculated by assuming 2 ppm H_2O to olivine for all samples. Some samples have not calculated ΔFMQ values because T-estimates on the basis of different two-pyroxene geothermometers differed by 200 ºC or more.

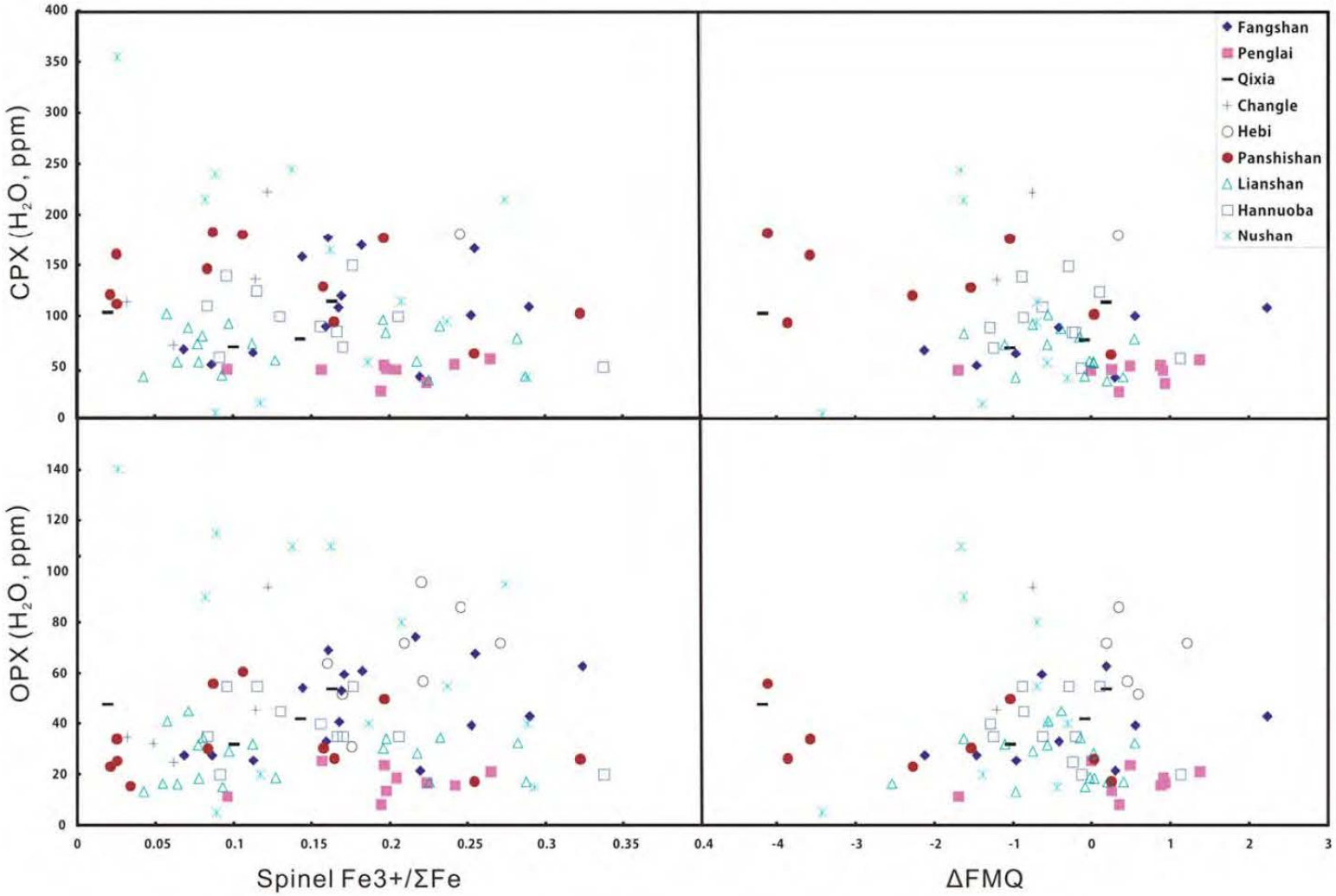

Figure 6-5 .H_2O content of cpx and opx versus $Fe^{3+}/\Sigma Fe$ of spinel and ΔFMQ of peridotite from the NCC.

6.3.4 Implications of the Low Water Content

The mechanisms responsible for lithospheric thinning of the NCC have been extensively debated (Menzies and Xu, 1998; Griffin et al., 1998; Zheng et al., 1998, 2001, 2006; Xu, et al., 2001, 2008; Gao et al., 2002, 2004, 2008; Zhang et al., 2002, 2008, 2009a; Wu et al., 2003a, 2006; Niu, 2005; Menzies et al., 2007). Several models have been proposed, which can be grouped into two end-members: "top-down" rapid (<10 Ma) delamination models versus "bottom-up" protracted (possibly up to 100 Ma) thermomechanical-chemical erosion models. Delamination would have produced the removal of the entire lithospheric mantle and probably part of the lower crust (Wu et al., 2003a, 2006; Gao et al., 2004, 2008). Thus the resulting (present) lithospheric mantle beneath the NCC would be asthenospheric mantle, newly accreted and cooled during the late Mesozoic-early Cenozoic thinning. On the other hand, thermal erosion models predict that most of the present lithospheric mantle is composed of thinned, relict Archean-Proterozoic mantle (Griffin et al., 1998; Menzies and Xu, 1998; Xu, 2001). According to the delamination model, the newly formed lithospheric mantle should be composed of essentially unmodified, cooled asthenosphere because there was no significant asthenosphere-derived basaltic magmatism associated with the NCC lithospheric thinning (Menzies et al., 2007, and references therein). If the delamination model is accepted, the water contents of the present lithospheric mantle should be similar to that of the source of MORB (50–250 ppm), which is not the case for the majority of the eastern NCC peridotites. Moreover, the fact that the NCC peridotites display water contents much lower than those of oceanic peridotites from the Mid-Atlantic Ridge Gose et al., 2009b) also argues against an asthenospheric source.

Therefore, we suggest that the low water contents of the eastern NCC samples result from the reheating of the lithosphere from below by an upwelling asthenospheric flow that occurred in concert with lithospheric thinning. If so, most of the Cenozoic lithospheric mantle of the eastern NCC should be considered as relict ancient mantle after lithospheric thinning during the late Mesozoic-early Cenozoic. A few peridotite xenoliths from Nushan and Changle that have water content greater than 50 ppm (up to 85 ppm) may actually represent the newly accreted and cooled asthenospheric materials. This scenario is in agreement with the available age constraints from Re-Os isotopic data on peridotite xenoliths hosted by Cenozoic

basalts from the eastern NCC (including whole rock and sulfides) (Meisel et al., 2001; Gao et al., 2002; Xia et al., 2004; Reisberg et al., 2005; Wu et al., 2006; Zhi et al., 2007; Xu et al., 2008; Xu, X.S. et al., 2008; Zhang et al., 2009a). Using the Os proxy isochron ($^{187}Os/^{188}Os$ versus Al_2O_3 or Yb, etc.), the melting age of the eastern NCC lithospheric mantle is early Proterozoic to Mesoproterozoic. Taking into consideration the Re depletion model ages (TRD) of the most depleted samples of each area, we also obtain a Proterozoic age, which represents a minimum age for melt extraction.

6.3 High water contents in the Mesozoic lithospheric mantle

In contrasting to these low water contents recorded by peridotite xenoliths hosted in Cenozoic basalts, the xenoliths from Qingdao and Junan, two Mesozoic volcanic basalt outcrops, display much higher water contents in pyroxens, hinting at the totally different natures of lithospheric mantle in term of water during those two periods.

The high water content of cpx, opx and rebuilt bulk rock ranges from 482 to 746 ppm, 187 to 304 ppm and 122 to 251 ppm, respectively for Junan samples, and varies between 580 and 728 ppm, 266 and 348 ppm and 149 to 203 ppm, respectively for Qingdao samples. These high water contents here would correspond to the bulk rock water content equal to or slightly higher than the MORB source (50-250 ppm), and are also similar to those reported for pyroxenes of peridotite xenoliths from Colorado Plateau (Lee et al., 2009), where water contents of cpx and opx vary from 439 to 957 ppm and 274 to 402 ppm, respectively (Fig. 6-6).

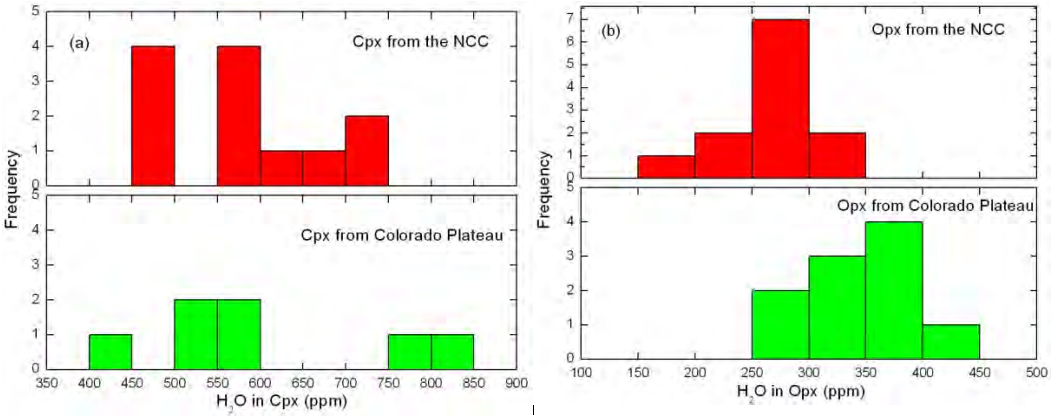

Fig 6-6 The comparison of water contents of cpx and opx from the NCC (Junan and Qingdao) with those from the Colorado Plateau. a) the comparison of water contents in cpx, and b) the comparison of water contents in opx.

Those high water contents in peridotite xenoliths from Colorado Plateau seem be

to be inconsistent with their melt depleted nature that are documented by the high Mg# of their olivines (between 90 and 92), and the most depleted samples (Mg# of olivine, 91~92) from the central the Plateau appear to be the wettest, indicated by high water in olivines (~45 ppm). Lee et al. (2009) attributed the wet lithospheric mantle to a consequence of a dry archetypal lithospheric mantle rehydrated recently by fluids released from a shallowly subducting Farallon plate.

In our case, however, all the peridotites of Junan are characterized by the low and narrow olivine Mg# range (~89) and high HREEs abundances (> 10 times chondritic value) in their cpx with the normalized LREE-depleted pattern (characteristic of the depleted MORB source), implying limited melt depletion or enrichment processes. Although few samples (JN43,JN53 and JN54) are slightly enriched in LREE relative to HREE, they do not show the relevant enrichment of water in cpx or opx to the rest of the samples. In addition, there is no indication of a correlation between the olivine Mg# and water contents in both cpx and opx, in part due to a narrow range of Mg# and of water content. All these evidences seem to point to the newly accreted lithospheric mantle beneath the Junan areas. In Qingdao, the relatively refractory sample with Mg# of 90.9 in olivine has lower water contents in both cpx and opx than the fertile sample (Mg# of 89.9 in olivine). More samples from Qingdao are needed to test this partial melting-controlled water content in samples. If that negative trend did exist, it would hint at the existence of a relatively young lithospheric mantle that has experienced a simple evolution history, such as the melt depletion but the mantle metasomatism that would blur the previous correlation between the Mg# and water content.

Whether these high water contents in Junan and Qingdao reflect the nature of the newly accreted, cooled asthenosphere that upwelled to fill the gap created by lithospheric thinning or the relatively ancient lithosphere, which was probably hydrated by fluids/melts from ancient subduction, like what happened in the case of the Colorado Plateau Craton, is not clear yet and need further more work to testify. Either scenario has its deeper meanings.

If the first possibility is favored, it means that the lithospheric thinning has ceased to proceed beneath the Qingdao and Junan areas before the emplacement of Pishikou mafic dike (78-86 Ma), and the accretion of new fertile lithospheric mantle commenced due to conductive cooling of upwelling asthenosphere much earlier than previously assumed, i.e. at the Late Cretaceous era (Ying et al., 2006). So it is natural

to assume that beneath the eastern NCC dominated the newly accreted lithospheric mantle that should have the similar high water contents to that of the N-MORB source. It, however, strongly contrasts with what we observed in the samples of the Cenozoic lithospheric mantle that was believed to be relatively ancient relicts. It seems difficult to resort to the lateral heterogeneity of lithospheric thinning beneath the research areas, given close geographic locations.

In addition, the modeling in section 5.1.2 (Fig. 5-3) suggests QDPS-16 is the melting residue that have experienced a ~8% melt extraction in the normal mantle. If we take a partition coefficient $D^{H}_{rock/melt}$ of 0.01, we can estimate that QDPS-16 retained only one tenth of the origin water after partial melting (1/((0.08/0.01+1))). Then the protolith mantle rock should have much higher water than those for the normal mantle (50-200 ppm) or the melting residue have experienced the subsequent water enrichment in the lithosphere.

So we are more inclined to accept that the Late Mesozoic lithospheric mantle represents the thinned, relict Archean-Proterozoic lithospheric mantle, so does its Cenozoic counterpart, and it has been previously rehydrated. The water contrast reflects the decrease of water content in the relict lithosphere, resulting from the reheating by upwelling asthenosphere flow that replenished the vacuum due to the thinning. Then the peridotite xenoliths of different times are a snapshot of the evolution of water content in in the lithospheric mantle, and the xenolith from Daxizhuang, which have intermediate water content, may be the missing part of the evolution story. We can speculate further that the water content of the lithospheric mantle should be much more higher before the emplacement of these Junan and Qingdao samples, and probably peaked at the early Cretaceous (~120Ma), when destruction of NCC, as well as the thinning of the lithospheric mantle, was generally believed to culminate. It has been shown that the NCC was within reach of active Pacific plate subduction for at least 200 Ma (Mezies et. al., 2007, and the references therein), which could hydrate the overlying NCC lithosphere. The continued addition of water can weak the rheological strength of lithospheric mantle which, until to a point, was not robust enough to resist the lateral flow from the underlying asthenosphere, initiating the lithospheric thinning at early Cretaceous (~120 Ma). As the thinning continued, the relict mantle was being comprehensively devolatilized due to the reheating from bottom until it became dry and strong enough to cease to thin itself at the Cenozoic.

7 Lithium isotopic systematics of the lithospheric mantle

In the chapter 4.4, we have report the Li contents and Li isotopic compositions of the peridotite xenoliths from four localities, including Penglai, Qixia, Hebi, and Junan. According to their different Li enrichment patterns and Li isotopic signatures, the peridotite samples, to the first order, can be subdivided into two groups: those hosted by Cenozoic basalts from Penglai, Qixa and Hebi showing extreme Li enrichments, combined with extreme Li isotopic fractionation and disequilibria, and those hosted by Mesozoic basalts from Junan displaying the rough Li and Li isotopic equilibrium with slightly Li enrichment. Because the mantle peridotites from Junan have approached Li re-equilibrium in the mantle, we cannot derive more valuable information about melt-rock interaction from their Li isotopic systematics, and the chapter will focus on studying the first group of samples.

7.1 Lithium infiltration and disequilibria in peridotites

The in-situ measurements by ion probe presented in chapter 4.4 demonstrate the extremely high and variable Li contents for the mineral phases in most of studied peridotite xenoliths, and the representatives of the profile measurements were present in Fig. 7-1.

The Li abundances range from 3.3 to 59.7 ppm in cpx, 2.8 to 43.4 ppm in opx and 1.7 to 10.6 ppm in ol for Penglai peridotites; from 3.4 to 41.1 ppm, 1.1 to 30.3 ppm and 1.2 to 10.3ppm in cpx, opx, and ol respectively for Qixia peridotites; and 1.6 to 44.0 ppm, 0.2 to 62.2 ppm and 1.5 to 4.3 ppm in cpx, opx, and ol respectively for Hebi peridotites. The high Li content in pyroxene is up to 60 ppm, greatly exceeding a range of 0.8 to 1.3 ppm inferred for the pyroxene of the normal mantle or moderately depleted mantle (Seitz et al. 2004; Woodland et al. 2004; Jeffcoate et al.2007), and those have ever been reported for metasomatised mantle xenoliths worldwide (Tang et al., 2010, and the referenced therein), including up to 24 ppm Li cpx in mantle xenoliths from Southwest Japan (Nishio et al., 2004), up to 15.5 ppm for cpx phenocrysts in mantle-derived magmas from New Georgia Group in the Solomon Islands (Parkinson et al., 2007). The similarly high Li contents have been newly

reported for the enriched peridotite xenoliths from the North China Craton, such as up to 24 ppm Li measured by MC-ICP-MS in the cpx from Fanshi, Trans-North China Orogen (Tang et al., 2010), and the much higher Li contents of up to 75 ppm in the cpx and 16 ppm in the olivine measured by ion microprobe from western Qinling (Su et al., 2011). The in situ measurements of Li contents of the olivines (up to 10 ppm at rim) in our samples, although lower compared with the coexisting pyroxenes, still dwarf the proposed Li range of the olivine (1-1.8 ppm) in the upper mantle or moderately depleted mantle (Seitz et al. 2004; Woodland et al. 2004; Jeffcoate et al.2007).

According, the great enrichment of Li contents in the ol, opx and cpx of the peridotites in this study, coupled with the heterogeneous Li at all levels (within and between mineral grains) and increased Li contents at the mineral rims, unambiguously point to a Li addition into these xenoliths from the Li-rich melts/fluids. The Li enrichments should also be recent metasomatic events that occurred just prior to or during entertainment of xenoliths (Rudnick and Ionov, 2007). This is because Li is one of the fastest diffusion elements in melts (Richter et al., 2003) and mantle minerals, especially cpx, in which Li diffusion is several orders of magnitude higher than for the other incompatible trace elements at the mantle temperature (Coogan et al., 2005; Van Orman et al., 2001). Then any Li isotopic heterogeneity in the mantle will be erased in a relatively short time (Parkinson et al., 2007; Halama et al., 2008; Gallagher and Elliott, 2009). Rudnick et al. (2007) estimated that the Li zoning of a 1 mm wide cpx would disappear in only a few ten thousands of years under a temperature in the mantle xenoliths of 900 to 1000 ℃ (corresponding to a Li diffusion coefficient between 10^{-13} and 10^{-12} $m^{-2}s^{-1}$). The details over the Li diffusion will be unfolded by profile measurements in the following sections.

Although the Li zoning and grain-to-grain variations abound, it is still evident that Li enrichments were not shared equally among individual mineral phases, with much higher Li in the pyroxenes, especially the cpx, than the coexisting olivines. If the maximum in-situ measurements of Li content of cpx and olivine (always at the rims) in each sample are chosen to represent its bulk Li content respectively, the Li partition coefficient (e.g., $^{ol/cpx}D_{Li}$) ranges from 0.1 to 0.2 for Penglai samples, from 0.2 to 0.3 for Qixia samples and from 0.05 to 0.2 for Hebi samples. Apparently, the Li partitioning strongly deviates from the equilibrium trend that follows the order of

ol>cpx>opx with the partition coefficient between 1.1 and 2.0 for $^{ol/cpx}D_{Li}$ in the equilibrated mantle (Brenan et al., 1998; Eggins et al., 1998; Seitz and Woodland, 2000; Domen et al., 2010; Yakob et., 2012). This preferential enrichment of Li in pyroxene relative to olivine in peridotite xenoliths was similarly observed worldwide, such those from Finero, Italy (Seitz and Woodland 2000), Tok, far-east Russia (Rudnick and Ionov 2007), French Massif Central (Wagner and Deloule 2007), Tanzanian Labait volcano (Aulbach et al. 2008) and the North China (Tang et al., 2007, 2010; Zhang et al., 2010, 2011; Su et al., 2011; Li, P. et al., 2012). These observations might be explained if the distribution of Li content between the olivine and cpx is strongly temperature dependent at mantle conditions such that a change in temperature, i.e. cooling upon exhumation, which initiates diffusive re-equilibration of Li between phases in the xenolith (Ionov et al., 2008; Gallagher and Elliott., 2009; Gao et al., 2011). The recent experiments conducted at 1.5 GPa and over a broad temperature range of 700 to 1100 by Yakob et al. (2012), however, have confirmed a fixed equilibrium partition coefficient of Li between olivine and diopside at 2.0±0.2, independent of temperature.

This preferential enrichment of Li in pyroxene relative to olivine in peridotite xenoliths was interpreted to have been infiltrated by the recent mafic silicate melts (Seitz et al., 2000; Ottolini et al., 2004; Woodland et al., 2004), or probably fluids (Brenan et al. 1998). By contrast, The peridotite samples from Victoria, Australia and a few refractory peridotites and wehrlites from Tok, Far-east Russia show the reverse partitioning pattern with $^{ol/cpx}D_{Li}>2$, previously attributed to the metasomatism by carbonatitic melts (Seitz and Woodland, 2000; Woodland et al., 2004; Rudnick and Ionov, 2007). Although the preferential enrichment of Li in pyroxene relative to olivine is obvious in our case, the extremely high Li contents in cpx (up to 60 ppm) are more likely to reflect the interaction with highly differentiated metasomatic agents, such as carbonatitic melts observed in Oldoinyo Lengai (Halama et al., 2007) and inferred from western Qinling (Su et al., 2011), rather than a silicate melt. It is generally accepted that Li diffuse much faster in cpx than in olivine by order of magnitude (Parkinson et al., 2007; Rudnick and Ionov, 2007; Jeffcoate et al., 2007; Ionov et al., 2008). Then, we are more inclined to believe that the extreme Li disequilibrium, observed between pyroxene and olivine, mainly reflects the differential potential of Li addition into the mineral phases, depending more on the diffusion rate than the equilibrium partition coefficient of Li for the mineral at an

inception of the Li influx. The shorter the duration is, the stronger the inter-mineral Li disequilibrium and the Li within grain zoned.

The minimum partition coefficient between olivine and pyroxene is 0.05, 0.1 and 0.2 for the peridotites from Hebi, Qixa, and Penglai, respectively (see the above calculation). This is consistent with the relative difference of duration of Li addition inferred from the Li zonation in the pyroxenes. The shorter the duration is, the more extreme the Li zonation. In Hebi samples, most of the pyroxenes are extremely Li zoned, such as opx-3 of HB01, where Li content dramatically increase from 1.7 ppm at the core to 52 ppm at the rim (Li diffusion simulation in the following section suggests a much higher initial value of 120 ppm at the rim, followed by the serious Li diffusion loss). The extreme Li zoning, resulting from a very short duration of Li addition, contributes much to the total variability of Li within a sample, and can be further used to estimate duration as a geospeedometer (seen Fig. 7-5 in the following section 7.3.3.3). By contrast, the pyroxenes from Qixia usually display the reverse sense of zonation, with the relative enrichment of Li at core to at rim. The decrease of elevated Li contents from core to rim indicates that the recent Li addition into pyroxene grains, probably at equilibrium due to a long duration, was followed by Li diffusion loss at the rim. The Li loss is relatively protracted and believed to have been extended deep to the cores for most of grains, compared with diffusive loss profiles only limited to narrow rims in Penglai cpx. In Penglai samples, the cpx grains show a Li zoning of lesser magnitude (with a Li variability across grain no more than two times), except a few large grains, reflecting a relatively long duration of Li influx intermediate to that of Li addition in Hebi and that of Li addition in Qixia. Cpx-1 of PL10 and cpx-2 of PL32, the relatively large gain, have a rim that is enriched in Li by three times that of the grain interior (~20 ppm), The larger the grain size is, the wider the Li gap is between the core and rim, confirming the duration-dependent Li diffusion within grain. The small cpx-1 of PL31, for example, displays the homogenous Li content of 60 ppm, the highest measured Li content for all Penglai cpx, indicative of approaching equilibrium with the Li-rich melts/fluids.

The inter-grain Li heterogeneity, on the other side, is more likely to reflect low connectivity of spatially restricted fluid/melts operating along the grain-boundary at the scale of thin section. The inter-grain Li heterogeneity becomes more extreme, when combined with a short duration of Li addition that characterized the samples from Hebi. Two opx from HB12, for example, are the showcase for seeing the

juxtaposing of a homogenous Li content of 1.7 ppm in opx-1 with the extremely variable Li content of 1.7 to 32 ppm in opx-3.

In addition, the differentiated Li diffusive loss is another factor contributing much to the inter-grain Li heterogeneity. The cpx grains from QX14, for example, display a Li variation by up to 6 times (from 4.8 to 27.1 ppm at the cores). Because cpx is relatively susceptible to Li addition due to fast diffusion rate of Li in it, individual grains in a sample infiltrated recently and transiently by Li addition, to the first order, are supposed to show the similar Li content range on the rims and variable Li contents inside grains (depending on duration of diffusive addition and radius of grain), as that observed in the Penglai samples. The smaller the grain is, the easier to approach Li intra-grain equilibrium during addition and also to suffer from post Li loss. Then, the large inter-grain variation, seen by low Li contents in small grains and high Li contents in large grains, is more likely to reflect a consequence of Li diffusion loss that varies significantly among individual grains rather than the Li disequilibria caused by the prior Li addition, and the large grains have potential to retain Li influx.

Figure 7-1. The representatives of the measured Li contents and isotopic compositions in this study (the whole data were presented in from Table 4-8 to Table 4-10). The profile measurements of Li content for: **a**, the ol; **c**, the opx; **e**, the cpx. The combined measurements of δ^7Li for: **b**, the ol; **d**, the opx; **f**, the cpx. The offset is applied to the distance across traverses for individual profiles. **a-e**, the data for the Pengai, Qixia and Hebi are in black, red and blue, respectively. Different symbol types are different samples: the Square, Circle,

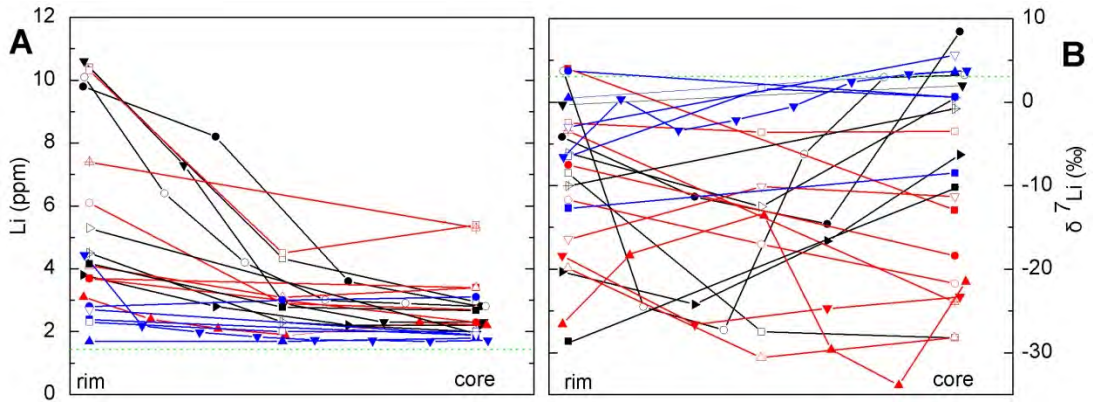

UpTriangle, DownTriangle, LeftTriangle, and RightTriangle in black are from PL10, PL31, PL32, PL36, PL42 and PL46, respectively; the Square, Circle, UpTriangle and DownTriangle in red are from QX14, QX18, QX50 and QX51, respectively; the Square, Circle, UpTriangle and DownTriangle in blue are from HB01, HB07, HB12 and HB64, respectively. The different

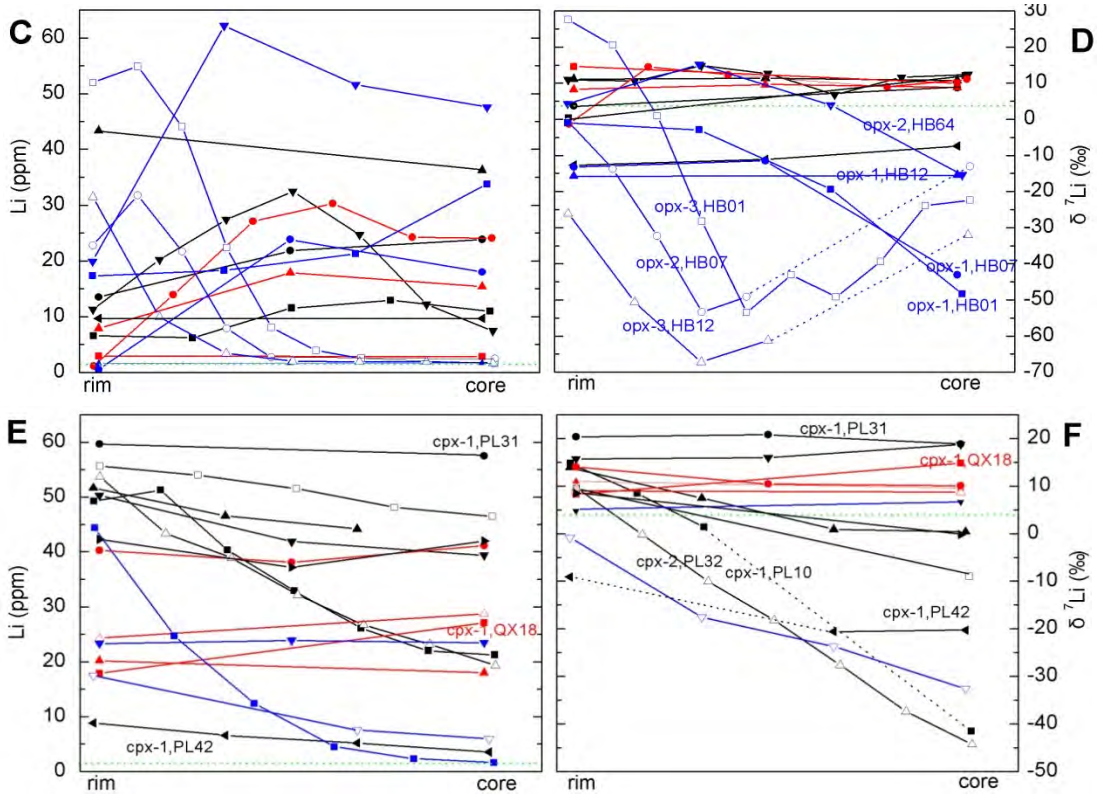

symbol interiors represent individual grains in one sample. The green dots represent the proposed Li contents and δ^7Li values for the normal.

7.2 The Li enrichments and mantle metasomatism

The Preferential enrichment of incompatible trace elements in peridotite xenoliths, especially refractory hazburgites, is a common worldwide phenomenon (Frey and Green, 1974), and is generally attributed to mantle metasomatism that brings in fluxes of incompatible trace elements, as well as Li, through infiltration or exchange with a highly enriched melt or fluid (McDonough et al., 1989, and the references therein). The REE concentrations data presented in chapter 4.2 and the corresponding REE patterns compiled in Fig. 7-2 show that the cpx in the peridotite samples were enriched in incompatible elements to the varying extents. However, we further find that the mantle metasomatism defined by the degree of enrichments in LREEs for cpx is not the one that invited the Li enrichments.

For the peridotites from Penglai, the PL46, the most refractory sample, sees strong enrichment of LREEs relative to HREEs only secondary to PL32. But there is no indication of obvious enrichment of Li abundances in either PL46 or PL32 relative to the rest of samples, which show no signs of mantle metasomatism by their similar and LREE-depleted pattern (N-MORB source-like). Even among those LREE-depleted samples, the extent of Li enrichment also varies, and sometimes violently irrespective of enrichment of LREEs. The cpx of PL31, which obtains the highest Li contents (up

to 60 ppm), is undistinguished from that of PL42, which shows the lowest Li contents (3 ppm at the cores), in term of both REE pattern and absolute abundances. There is no reason to specially request that Li enrichment is decoupled from enrichment of other incompatible trace elements for the metasomatic fluids/melts that infiltrated our xenoliths. The same reasoning goes to PL32 and PL10, which show the similar Li content range and zoning pattern for olivine and cpx, but totally different REE patterns and abundances. These observations above demonstrate that Li was added to Penglai peridotites in the events that were distinct from the metasomatic events responsible for enrichments of the incompatible elements e.g., the signatures of metasomatism in PL32 and PL46, indicated by enriched-LREE patterns. It is not surprising to come to the claim, because the observed Li zoning and disequilibria, on one side, requires that the Li enrichment was a recent process given high diffusion rate of Li at high temperature, and also a transient process based on the following numerical modelling and reproducing. On the other side, the diffusivities of other incompatible trace elements (e.g., REE, Hf, Sr) in cpx are several orders of magnitude slower than Li, requiring a protracted process to account for the homogenous REEs abundances within cpx grains. Accordingly, the most likely and simple interpretation is that the Penglai samples just simply did not have enough time to intake those incompatible elements which, as well as Li, were carried by the same enriched fluids or melts. And the enrichments of highly incompatible trace elements observed in PL32 and PL46 reflect ancient events that predated those responsible for Li enrichments.

However, the vague correlations between δ^7Li value of olivine and Sr isotopes or Nd isotopes in cpx are reported in some case of enriched peridotite xenoliths by others (Tang et al., 2010; Zhang et al., 2009b; Rudnick and Ionov, 2007), and was interpreted to be caused by the same mantle metasomatism. The interpretation is probably needed to re-examine. Instead, this fortuitous correction may simply reflects the general incompatible trace elements enriched characteristics and greater Li isotopic equilibrium of the refractory harzburgites relative to the fertile lherzolites (Rudnick and Ionov, 2007).

The distinction of the recent Li enrichment event from the metasomatism responsible for LREE enrichments is also evident in the samples from Hebi. Cpx-1 of HB01 is the showcase for distinguishing the two enrichment processes. The extreme Li zoning, combined with the profile reproducing for the coexisting opx grain (see the

following Fig. 7-6), suggest that the recent Li addition was a transient event, no more than years. During such short interaction with Li-rich melts/fluids, the cpx grain apparently was not granted enough time to uptake these incompatible trace elements, such as LREEs, from the melts/fluids. On the other side, the cpx grain is enriched the LREEs, showing a high LREE-enriched pattern, and the profile analyses show no element zoning for the REEs, within the grain. So, this metasomatism should be a protracted event that predated the Li enrichment event.

For the peridotite samples from Qixia, all the measured cpx but those from QX14 are enriched in LREEs. The LREE-depleted pattern of QX14 cpx indicates that Li enrichment was a recent event that was too short to take in other incompatible trace elements that the metasomatic agent may have been carrying. Although the cpx in the rest of samples show the similar LREE-enriched pattern and enrichment of Li, we are inclined to assume that the vague correlation simply reflects the general incompatible trace elements enriched characteristics of the refractory peridotites relative to the fertile lherzolites (Rudnick and Ionov, 2007). The narrow Li zoned rims of olivine suggest a recent Li addition and the immune cores from diffusion. The high and variable Li contents of the cores in each sample and the lack of correction between Mg# of olivine and Li content among samples result from the ancient Li enrichments rather than melt depletions of xenoliths.

While Li disequilibria abound on different scales, there is not inter-grain or intra-grain variation of REEs abundances for cpx in sample. The Li enrichments observed in peridotites are not added in the events that the highest average Li contents in all mineral phases suggest that QX18 have experienced the most enrichment of Li, its REE pattern, however, show that QX18 is the less LREE enrichment among three LREE-enriched samples. The QX14, the only LREE-depleted sample, has the highest Li content of 10.3 ppm for olivines at the rim of one grain, although it have few Li contents than the rest of samples in average Li content for pyroxene. This relative depletion of Li contents in the pyroxenes and extreme grain-to-grain variability is more likely to be a consequence of spatially restricted, non-penetrative metasomatism or the subsequent Li diffusive loss within small grains rather than of a short duration of the metasomatic agents. Because the observation of slight Li enrichment at cores relative to at rims for enriched cpx grains indicates a longer equilibration duration that would allow Li to be absorbed equally by the whole grain rather than preferentially by the rims. Moreover, it is note that the zoned cpx of this type or unzoned cpx with also

high Li contents were pervasive among all Qixia samples, reflecting longer equilibration times for peridotites of Qixia than for those Penglai. That reasoning can be supported in part by the observation that Qixia samples are more refractory than Penglai samples in term of Mg# values in olivines. However, the equilibration duration was still not long enough to smooth the Li zoning across olivine grains, and of course is much less than that needed to take in REEs-like trace elements. In addition, the longer equilibration duration, probably assisted by enhanced melt permeability of refractory matrices, does not mean greater Li contents in minerals. The relative Li enrichments of both pyroxenes and olivines in Penglai peridotites to Qixia samples are more likely to reflect slight differences in nature of metasomatic fluids/melts, with more Li content for that metasomatism in Penglai samples.

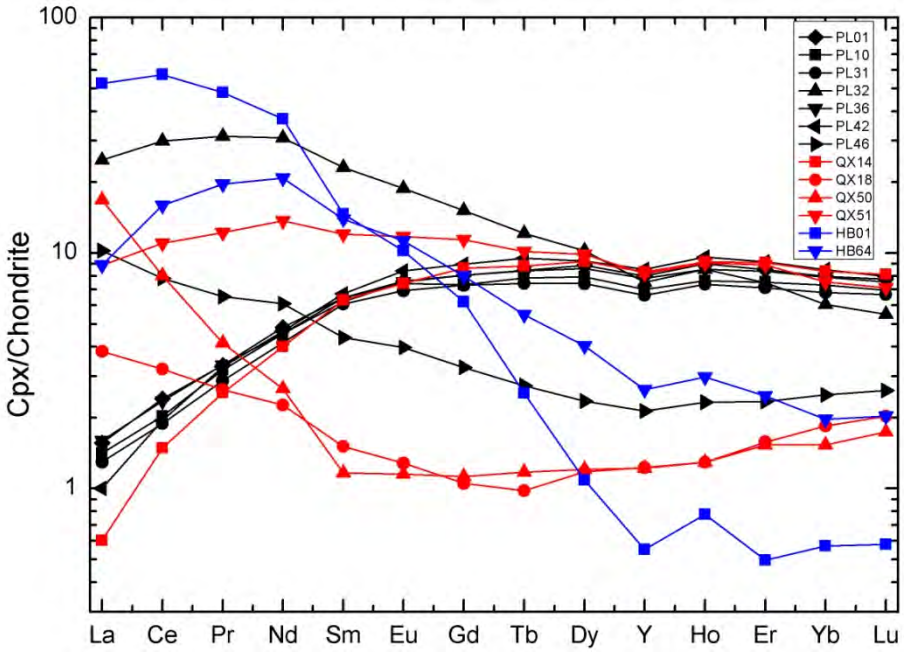

Figure 7-2. Chondrite-normalized REE concentration diagram for cpx from the studied peridotite xeonoliths. The measurements show no inter- and intra-grain heterogeneities for individual cpx grains in each peridotite samples based on the core and rim analyses. The trace elements concentrations of chondrite are taken from Anders et al. (1989).

7.3 Lithium isotopic fractionation in peridotites

The recent Li addition into the peridotite xenoliths is companied by the strong Li

isotopic differences between the coexisting olivine and pyroxene, including the inter-grain and intra-grain heterogeneities (Fig. 7-1). In Penglai, the minerals show extremely variable δ^7Li values, varying from -37 to +9‰ in ol, from -44 to +23‰ in cpx and from -13 to +15‰ in opx. The dominant δ^7Li values of ol are below the proposed range of values for the normal mantle (+2~+6‰) (Tomascak et al., 2008), although a few grain cores and highly enriched rims (up to 10 ppm) show relatively high δ^7Li value. In cpx the δ^7Li values decrease progressively from rim to core for the large grains, such as cpx-1 of PL10 and cpx-2 of PL32, the same way as their Li contents evolve. In Qixia, the ol show a large range from -34 to +4‰ in δ^7Li, mainly between -20 and -10‰. The pyroxenes, on contrast, display the overall high δ^7Li values, varying from +2 to +15‰ in cpx and -1 to +15‰ in opx. In Hebi, the δ^7Li values of olivines range from -13 to +6‰, with a narrow δ^7Li range between +1 and +6‰ at the cores, overlapping the proposed range for the normal mantle range (Tomascak et al., 2008). In contrast, the δ^7Li values vary broadly from -76 to +17‰ in cpx and from -67 to +28‰ in opx, with extreme intra-grain heterogeneity.

7.3.1 The isotopic fractionation at high temperature

Because peridotite xenoliths are fragments of the lithospheric mantle that usually have experienced partial melting and subsequent silicate melt enrichment to varying extents, the possibility of Li isotope fractionation during these processes need to be considered first. At magmatic temperature, Li isotopes do not show per mil-level mass fractionation between olivine and pyroxene in the peridotite (Tomascak et al., 1999), or between mantle minerals and Li-rich melts/fluids in the mantle (Wunder et al., 2006), suggesting that such high temperature cannot promise a significant thermodynamic equilibrium fractionation. Although isotopic fractionation at high temperature has been suggested by Seitz et al. (2004), the difference is relatively small (<2‰), and just beyond analytical uncertainty. The equilibrium fractionation factors for temperatures of 950–1160°C also indicate little or no fractionation and this has been confirmed by the study of igneous systems equilibrated at the same temperatures (Tomascak et al., 1999; Chan and Frey, 2003; Bryant et al., 2004; Teng et al., 2006b). Experimental results indicate that Li isotopic fractionation between mantle minerals and fluid at temperatures >900 °C is <1.0‰ (Wunder et al., 2006), much smaller than the differences in isotopic composition in our samples. The lower

limit of temperature is put to extreme by Halama et al. (2007) on reporting the lack of per mil level differences in δ^7Li between primitive lava (olivine melilitites) and highly differentiated lava (nephelinite, carbonatites), indicating that there is no or very little Li isotope fractionation during magmatic differentiation with the temperature down to 500°C. Thus, igneous processes, such partial melting, fractional crystallization and melt infiltration and metasomatism, are unlikely to produce per mil level Li isotopic thermodynamic fractionation, let alone the extreme Li isotopic compositions in our case. So, for the pristine mantle or the "equilibrated" mantle, the δ^7Li difference between olivine and cpx, described as $\Delta^7Li_{ol\text{-}cpx}$ ($=\delta^7Li_{ol}-\delta^7Li_{cpx}$), should approach zero (Tomascak et al., 1999; Rudnick et al., 2008).

7.3.2 The diffusion-driven isotopic fractionation

Apparently, the Li isotopic partitioning for olivine and pyroxene in our xenoliths strongly deviates from the equilibrium trend, with heavier Li isotopic compositions in pyroxene than in olivine, although the inter-grain heterogeneity and isotopic zoning abounds. These isotopic equilibria are not only limited to our studied mantle peridotite xenoliths. The inter-mineral disequilibria and mineral zoning, combined with higher and lighter Li in pyroxenes, were pervasively observed in enriched mantle xenoliths worldwide (Tang et al., 2010; and the references therein), and were generally believed to be a consequence of the diffusion-driven kinetic isotopic fractionation due to a large diffusion rate difference of Li isotopes at high temperature (^{6}Li migrates faster by up to 3% than ^{7}Li) (Richter et al., 1999, 2003; Lundstrom et al., 2005; Beck et al., 2006; Jeffcoate et al., 2007; Parkinson et al., 2007; Rudnick and Ionov, 2007; Magna et al., 2008; Zhang et al., 2009b, 2010; Tang et al., 2007, 2010, 2011).

When Li diffuses into the mineral from Li-rich source, ^{6}Li will preferentially enter into the mineral interiors, producing the isotopically lighter minerals relative to the Li-rich source at an inception of Li addition (Lundstrom et al., 2005; Jeffcoate et al., 2007). As more Li diffuse into the mineral, the mineral start to recover from the lightest Li composition towards isotopically equilibrating with the contacting Li-rich source. The late-stage Li diffusion-induced Li isotopic fractionation is generally attributed to two processes: (1) an infiltration of Li-rich melts/fluids into the xenoliths short prior to the eruption or Li addition from the host magma during transport to the

surface (Jeffcoate et al., 2007; Rudnick and Ionov, 2007); these processes can be justified by studies of mantle xenoliths containing interstitial glass or "melt pocket" (Ionov et al., 1994); (2) the Li isotope disequilibria as a consequence of post-eruption inter-mineral re-distribution of Li in the xenoliths during slow cooling in magma flows (Ionov et al., 2008). Then these highly anomalous Li isotope compositions reflected the artifact resulting from Li kinetic diffusion rather than the nature of the metasomatism that fed them or further the existences of those anomalous Li sources in the mantle.

However, the coupling of high δ^7Li in pyroxenes with low δ^7Li in olivines in this study, in contrast to the conventional paradigm above, seems unlikely to result from Li diffusion alone. It needs additional processes or metasomatism, evidenced by the following observations and reasoning.

The high δ^7Li values, combined with increased Li contents, at the pyroxene reflect a latest Li enrichment and its Li specific isotopic signature. Apparently, the Li addition into the pyroxenes cannot produce a diffusion-induced high-δ^7Li signature. Rather it could instead produce the low δ^7Li signature in the mineral interiors, which is evident in the large pyroxene interiors from Penglai and Hebi samples. Accordingly, the high-δ^7Li signature is either inherited from the metasomatic agent itself or a consequence of Li diffusion loss, as ^{6}Li will preferentially leave out of the minerals. Evidently, the latter possibility is not the cause in the case of the pyroxenes from Qixia, given their pervasive high δ^7Li values within the large grains. On the other side, although most of the pyroxenes from Penglai and Hebi samples have experienced a subsequent Li loss at the rims, the Li diffusion simulations (section 7.3.3) show that the measured Li isotopic profiles near the rims evolve as the modellings suggest, implying the limited influence on δ^7Li the by diffusion loss. Further, the small Li equilibrate cpx grains, such as cpx-1 and cpx-2 of PL31, and the intact Li zoned cpx, such as cpx-1 of HB01, both confirm that the high δ^7Li signature reflect the nature of the infiltrating Li-rich melt/fluids.

These high δ^7Li values, mostly observed on the rims, are not shared equally between cpx and opx, and even individual grains. That probably reflects spatially restricted fluid/melts interactions along grain-boundary with a short duration, (Rundnick and Ionov, 2007), noting that higher δ^7Li are usually associated with higher Li among the rims in each locality. That argues against the likelihood that the high δ^7Li signature was inherited from the relict fluids/melts that have experienced a

preferential diffusion ^{6}Li loss during previous interaction with wall-rock (Rundnick and Ionov, 2007). Further, the pyroxene grains that experienced the greatest Li influx approached maximum equilibrium with Li-rich sources. The δ^{7}Li value of +20.4‰ in cpx-1 from PL31, +20‰ in opx-3 from HB01 and +14‰ in cpx-2 from QX18, could be used to reflect the δ^{7}Li signatures of the metasomatic fluids/melts at Penglai, Hebi and Qixia, respectively (Fig. 7-1).

The absence of the high δ^{7}Li in the retarded olivines implies a limited influence by this event, and the abundance of low δ^{7}Li values, on the other side, seems to record a previous ^{7}Li depletion by an ancient Li enrichment event (Table 4-8 to 4-10 and Fig. 7-1). Among these samples the olivine grains from Qixia are showcases for preserving the extensively low δ^{7}Li values (around -20‰) which, combined with slight Li zoning (less than a factor two), excludes the main cause by kinetic diffusion. This ancient "memory" was also remembered in the Penglai olivines that show moderately high (<5 ppm) and zoned Li contents (about a factor of two), such as those from PL01, PL10 and PL46, and the similar low δ^{7}Li values (-20~-10‰). The olivines with high Li rims (up to 10 ppm), by contrast, are probably affected by recent Li addition to some extents, noting that the higher δ7Li are associated with the higher Li contents on a few rims. The coarse Hebi olivines, with δ^{7}Li values from -13 to +6‰, are among those least affected by both the recent Li flux and the previous δ7Li depletion in all three localities. Only two grains from HB01 bear that low δ7Li signature, and the others are in the normal mantle range at the cores. That may reflect a combination of a limited duration of Li addition and of a large grain size.

Generally, the mantle olivines is mostly within the narrow δ^{7}Li of range proposed for the normal or equilibrated mantle, and is almost never lighter (Aulbach et al., 2009), compared with an abundance of the low-δ^{7}Li signature in coexisting pyroxenes. And it is generally interpreted to be a consequence of a limited Li addition into olivine during a short late-stage Li influx due to a much lower Li diffusion rate in olivine than in pyroxene (Jeffcoate et al., 2007; Rudnick and Ionov, 2007). However, the recently published Li systematic data from the North China, including Penglai and Qixia in this study, show that the olivine in peridotite xenoliths can be δ^{7}Li depleted, just as what evidently observed in the coexisting pyroxene. The origin of that low δ^{7}Li in olivine remains unclear.

Using MC-ICP-MS mineral separates, Tang et al. (2010) reported two exceptional peridotite xenoliths from Fanshi that contain olivines with low δ^{7}Li (-3.0 and -7.9%),

and argued for the existence of low δ^7Li domain in the mantle that was perhaps generated by meter-scale diffusion of Li during melt/fluid-peridotite interaction.

Further, Su et al. (2011) investigated Li isotopic systematics of the peridotite xenoliths from Western Qinling by ion microprobe, showing the extremely low δ^7Li values (down to -40‰) in the highly Li zoned olivines. This low δ^7Li signature was ascribed either to the fractionation of Li isotopes that strongly depends on the metasomatic medium and tends to effectively transfer ^{6}Li into olivine and ^{7}Li into pyroxene from a Na-rich carbonatitic melts (high Li enrichment ~200 ppm, but with a normal mantle level of 3–6‰ in δ^7Li), or to the existence of a reservoir with a high Li content but low δ^7Li in the mantle (Su et al., 2011).

If the olivine has been affected by low δ^7Li melts/fluids in our samples, we can expect the same of the coexisting pyroxene. The low-δ^7Li memory in the pyroxenes, however, is always difficult to trace, because the pyroxene is easily susceptible to a late-stage diffusive fractionation (Rudnick and Ionov, 2007). For the most of pyroxenes from Qixia and from Penglai, the measured Li and Li isotopic profiles show that the mineral interiors have been overwhelmingly diffused by the recent Li infux, and the observed isotopic profiles are composites that combined the initial compositions with the influx of fractionated Li isotopes. Hence the initial Li isotopic signature has been erased, and there is no way to recover them. On the other side, most of the pyroxenes from Hebi and a few large ones from Penglai are characterized by the extremely zoned Li and Li isotopic profiles that seem far from re-equilibrium with the recent infiltrating melts/fluids, and then these composite profiles may partially reserve the ancient “memory”, leaving a chance of recovering the initial Li and Li isotopic signatures prior to the Li influx. Apparently, the prerequisite is to better understand how Li and Li isotopic profiles evolve within grain when Li diffuses.

In the following, we develop a numerical model for Li diffusion within mineral grains, allowing the initial conditions to vary, to serve two main purposes: (1) to figure out what are the factors that determine the kinetic Li isotopic fractionation, (2) to understand the form of the Li and Li isotope profiles that we have observed in our mineral grains, and (3) to test if the Li isotopic fractionation observed in our samples can be reproduced by the diffusion-driven Li isotopic diffusion alone, and if not, what is the cause and how to produce them.

7.3.3 The quantitative simulation of Li diffusion

Although Li isotopic zoning, inter-grain heterogeneity and inter-mineral disequilibria abound in the peridotite xenoliths, some measured profiles, both for Li and Li isotopes, are evolving in a good shape, either decreasing. There seems the reasoning behind. In order to figure out the rules and factors that govern the formations of the good-shaped profiles and unveil the story inside, we undertake the numerical modeling to learn how do Li isotopes diffuse in a mineral.

7.3.3.1 The diffusion theory

Diffusion, the second transport phenomenon, is the movement of individual atoms or molecules through a group of atoms and driven by a concentration gradient, or a chemical potential gradient, more strictly. Two routes of diffusion are possible in an aggregate of mineral grains: grain-boundary diffusion, also called inter-granular diffusion, and volume diffusion. Grain-boundary diffusion occurs along mutual boundaries between contacting mineral grains. Atoms on surfaces are underbonded, and the atomic structure is also deformed with more defects. Both lead to more available jumping sites and lower activation energies for diffusion, and a very thin film of fluid along grain boundaries may facilitate diffusion. Volume diffusion, on contrast, occurs within any single homogenous phase, such as a crystal or a melt body. Volume diffusion through solid is generally the slowest, commonly by many orders of magnitude, of the two types of diffusion (Nagy et al., 1986; Farver et al., 2000). Nagy et al. (1986) concluded that grain-boundary diffusion of oxygen is at least four orders of magnitude faster than volume diffusion. Farver et al. (2000) also showed that grain-boundary diffusion of ^{30}Si dominates Si transfer through fine-grained forsterite aggregates and concluded that grain-boundary diffusivity is 10^9 times greater than volume diffusivity of Si. Hence, mass transport across a rock may be facilitated by grain boundary diffusion, especially for a fine-grained rock with abundant grain boundaries. If our interest is to understand the bulk effect of mass transfer, such as how rapidly mass may be transferred from one location to another in a rock, and if the space scale of our interest is much larger than grain sizes in the rock, these diffusion problems may be treated mathematically the same as volume diffusion, but the diffusivity would not be volume diffusivities in single grains, but

some effective diffusivity due to the multiple grain-boundary diffusion paths. It is noted that the grain-boundary diffusion, although able to transfer masses across a rock medium at a large scale, cannot modify the composition of the grain interiors

In geological cases, the most common diffusion issues, such as Li diffusion into mineral grain from Li-rich melt, are treated as the simplest one-dimensional diffusion equation (i.e., Fick's general mass-conservation equation) in isotropic medium for a binary system with a constant diffusivity as the following:

(7-1)

From this Fick's equation, the concentration of the diffusion element of interest within grain is both duration (t) and position (x) dependent, and the rate of change of the concentration at a given position is proportional to the curvature (the second derivative) of the concentration curve as a function of x.

Before this equation can be solved analytically, we need to specify the boundary conditions, which can be distinguished in the following three cases for one-dimensional diffusion: (1) there are two ends. If both ends participate in diffusion, the diffusion medium is called a finite medium with two boundaries. The two boundaries may be defined differently; (2) if diffusion starts in the interior and has not reached either of the two ends yet, the diffusion medium is called an infinite medium, and (3) if diffusion starts from one end (surface) and has not reached the other end yet in one-dimensional diffusion, the diffusion medium is called a semi-infinite medium. It is noted that an ‘‘infinite’’ or a ‘‘semi-infinite’’ reservoir merely means that the medium at the two ends or at one end is not affected by diffusion. Combined with the initial conditions (i.e., the concentration distribution is given at t=0, and the simplest initial condition is that the concentration is constant within mineral at t=0), the equation can be easily solved using the Boltzmann transformation for infinite and semi-infinite media, and be solved by the separation of variables using Fourier series for a finite medium.

In the more generalized case of three-dimensional diffusion, the boundary conditions are complicated. The most common approach to solving this equation is to approximate the geometry of the object of interest by a simple shape such sphere, cube, or long-cylinder in which diffusion is assumed to be symmetric. If there is spherical symmetry (i.e., concentration depends only on radius within an anisotropic medium), for example, the diffusion equation can be transformed to a one-dimensional type by redefining the concentration variable w=r*C. This transformation

would work for a solid finite sphere, and the diffusion equation is given by the following equation (7-2).

7.3.3.2 Diffusion approach and results

For the case of this study, assuming that Li diffuse into mineral grains from the grain-boundary Li-rich fluids/melts with constant Li surface concentration, the diffusion process can be more precisely described using a version of Fick's second law for radial diffusion within a solid finite sphere rather than for one-dimension diffusion in infinite or semi-infinite space. It matters for the natural minerals that usually have the limited size and round shape. The diffusion equation is as the following:

(7-2)

In this equation, is either ^{6}Li or ^{7}Li, is the concentration of a lithium isotope (at t and r) insider the grain, is the diffusion rate of a lithium isotope, r is the radial distance from the centre of the grain (r=0 is the center of the mineral and $r=r_{max}$ is the surface of the mineral) and t is time (or duration). This equation has analytical solutions for simplified boundary conditions, but it can also be solved numerically by various finite-difference methods. Here, we use an explicit the Crank–Nicolson method, similar to that used by Parkinson et al. (2007) and Gallagher and Elliott (2009). For this diffusion equation, this method is unconditionally stable. It can develop composition oscillations with exponentially expanding errors if the time step (Δt) is too large; The solutions are only stable when s, a measure of the solution stability, is less than 0.5. s is defined by:

(7-3)

where Δr is the distance step. We use a combination of the Δt of 10000s and the Δr of 10 or 5 μm (depending on the r_{max}) to model the profiles with a around $1.0\times10^{-15} m^{-2}s^{-1}$.

In order to solve the equation, we need to define the boundary conditions as below:

(7-4a)

(7-4b)

The equations (7-4a) define the initial concentration of a Lithium isotope for the mineral surface (i.e. in equilibrium with the Li-rich fluids/melts) and the mineral

interior, respectively, while the equation (7-4b) is a symmetry condition at the center of the diffusion domain. It has been generally accepted that Li diffuses fast in the silicate minerals, although the experimental measurements were only available for the silicate melts. In this modeling, we adopt a diffusion rate of $1.0\times10^{-15}m^{-2}s^{-1}$ for ^{7}Li, and that of $1.03351\times10^{-15}m^{-2}s^{-1}$ is derived for ^{6}Li from a coefficient β of 0.215, which was borrowed from the experimental determination for Li diffusion in silicate melts (Richter et al., 2003). As ^{6}Li and ^{7}Li have different diffusion rates, the two isotopes are treated as two elements and each diffusion curve is modeled separately. So the $^{7}Li/^{6}Li$ ratio and the Li mass balance can be calculated by combining the concentrations at different distance. The $\delta^{7}Li$ values are calculated relative to a $^{7}Li/^{6}Li$ ratio of 12.0191(Flesh et al., 1973).

The modelling predicts that Li diffusion, driven by the Li contrast between the mineral surface and the interior, will produce the low $\delta^{7}Li$ values in the mineral at the form of an isotopic trough. This is a natural consequence of the differential diffusion rates of the two isotopes of lithium, reflecting the relative extent of the ^{7}Li lagging behind ^{6}Li during competitive running within crystals. Normally, the larger the C_r/C_o ratio is, the stronger the diffusion-driven isotopic fractionation is or the deeper the $\delta^{7}Li$ trough is (Fig. 7-3). So does the coefficient β, which defines the difference in the diffusion rates of ^{6}Li and ^{7}Li.

The minimum value of the isotopic trough, however, is also a non-steady state feature that will evolve with time and matters much for the later fitting of the measured profiles. The $\delta^{7}Li$ trough will migrate and broaden away from the rim with time and the minimum $\delta^{7}Li$ value of the trough will also decrease (Fig. 7-4). By the time when the trough reaches the core of the mineral, the $\delta^{7}Li$ will fall deep to the minimum value at the core in absence of an isotopic trough, of-52‰ (in this example). After that, the profile will relax and the grain will recover its initial Li isotopic composition, as more Li diffuse into the core.

The corresponding Li content diffusion pattern is relatively simple. It is easy to conclude that variations of Li isotopic compositions ($\delta^{7}Li$ vary as far as it goes for either the mineral interior or the mineral surface) make no sense to the significant change of a $^{7}Li/^{6}Li$ ratio, then the change of Li diffusion pattern. A 50‰ variation of $\delta^{7}Li$ values, such as, can merely result in a responding change of $^{7}Li/^{6}Li$ ratio by 0.6, which is apparently insignificant. Accordingly, the relative shape of Li profile across grain is only duration (t) and grain size (r_{max}) dependent, regardless of neither the

initial C_r/C_o ratio nor the isotopic compositions (Fig. 7-5). The longer the duration is or the smaller the crystal is, the flatter the profile is. When the initial Li contents for both the surface and interior of the mineral are known, we can estimate the duration by projecting the measured Li profile onto the standard plot (the modeled curves with different duration in a fixed radius grain) that looks like those in Fig. 7-5, where the maximum and minimum at the y axis corresponds to the C_r and C_o respectively. Then, Li content profile can be used as a geospeedometer alone, or to derive more Li isotopic details when combined with the corresponding isotopic profiles. It is also found that the Li content of the mineral core usually exceed twice the initial value when the isotopic trough is there, meaning that Li has extensively diffused the core (seen in Fig. 7-4).

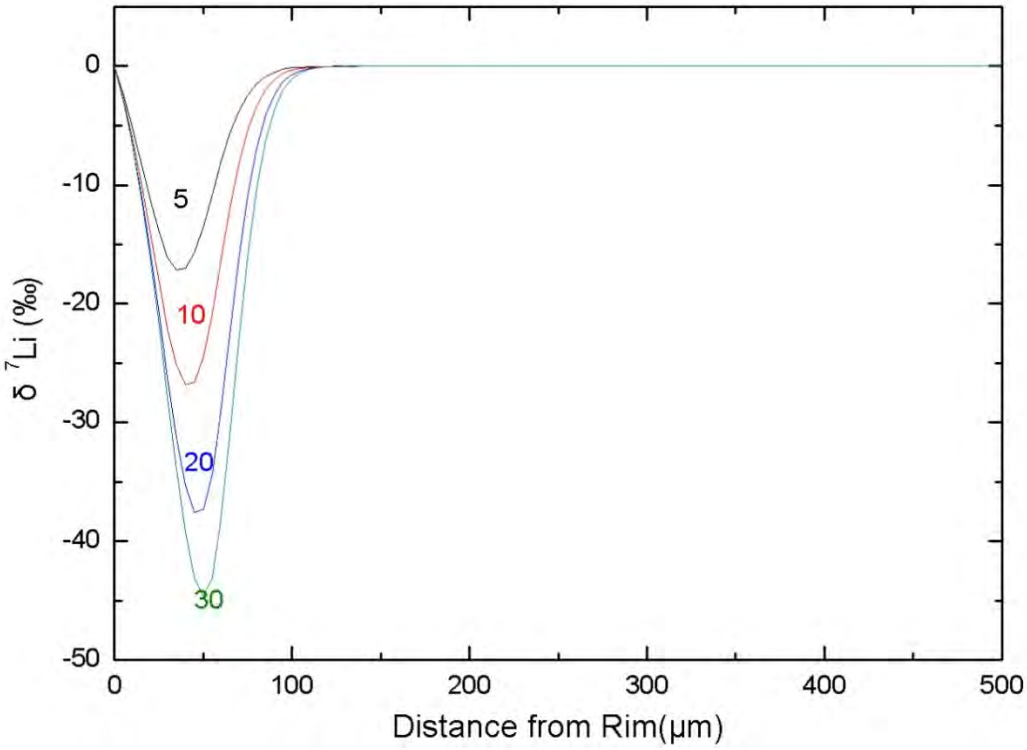

Figure 7-3. The dependence of the magnitude of an isotopic trough on the initial C_r/C_o ratio. These curves represent the "instantaneous" diffusion-driven Li isotopic fractionation with the duration of 0.01 year. The "instantaneously" generated δ^7Li troughs are minimum estimates for a given initial Li contrast, as they will evolve with time. The numbers on the curves are the C_r/C_o ratios. The diffusion rates of Li isotopes are assumed the same as those in the text.

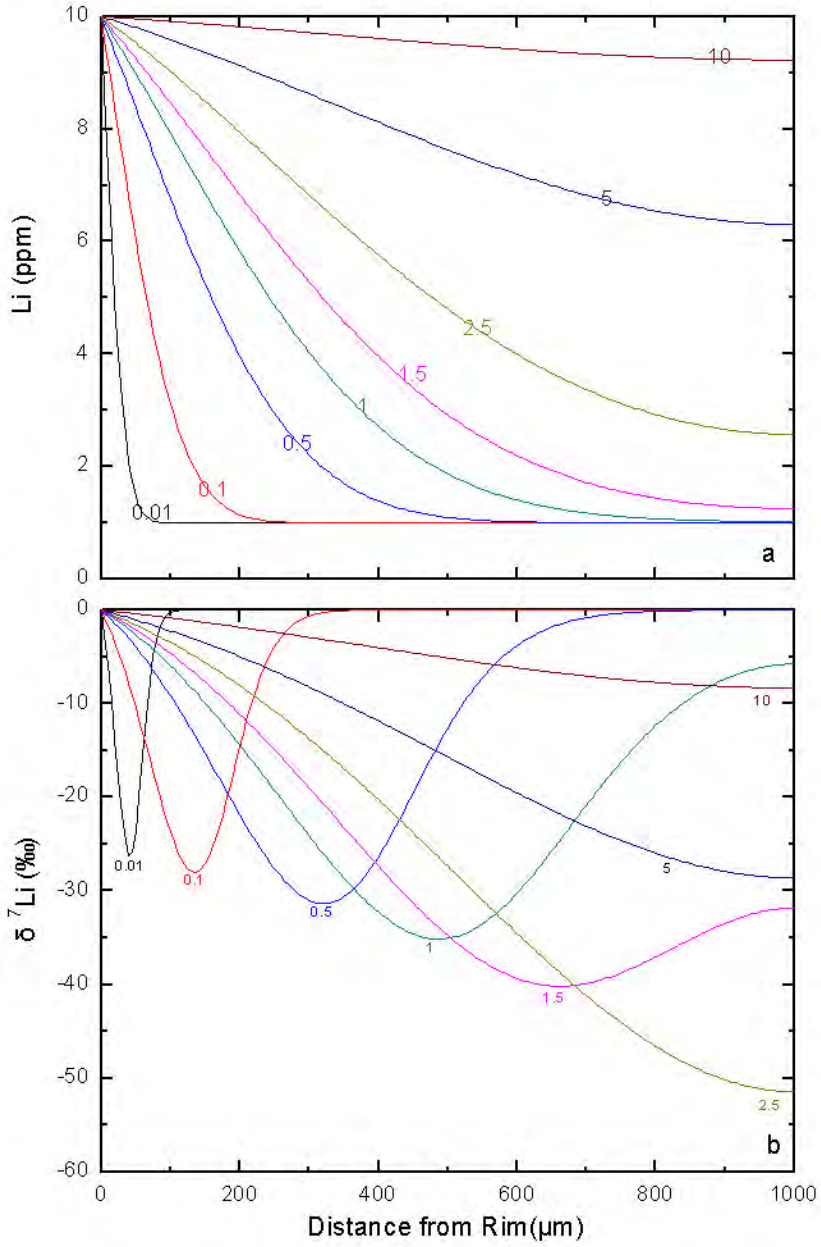

Figure 7-4 The Li content and isotopic profiles within the mineral with time. (a) the evolution of Li content with time; (b)the evolution of δ^7Li with time. The numbers on the curves are duration in years. The Li content at the mineral surface is ten times that of the initial mineral interior, and the δ^7Li value for both the mineral surface and interior are set to zero for clarity.

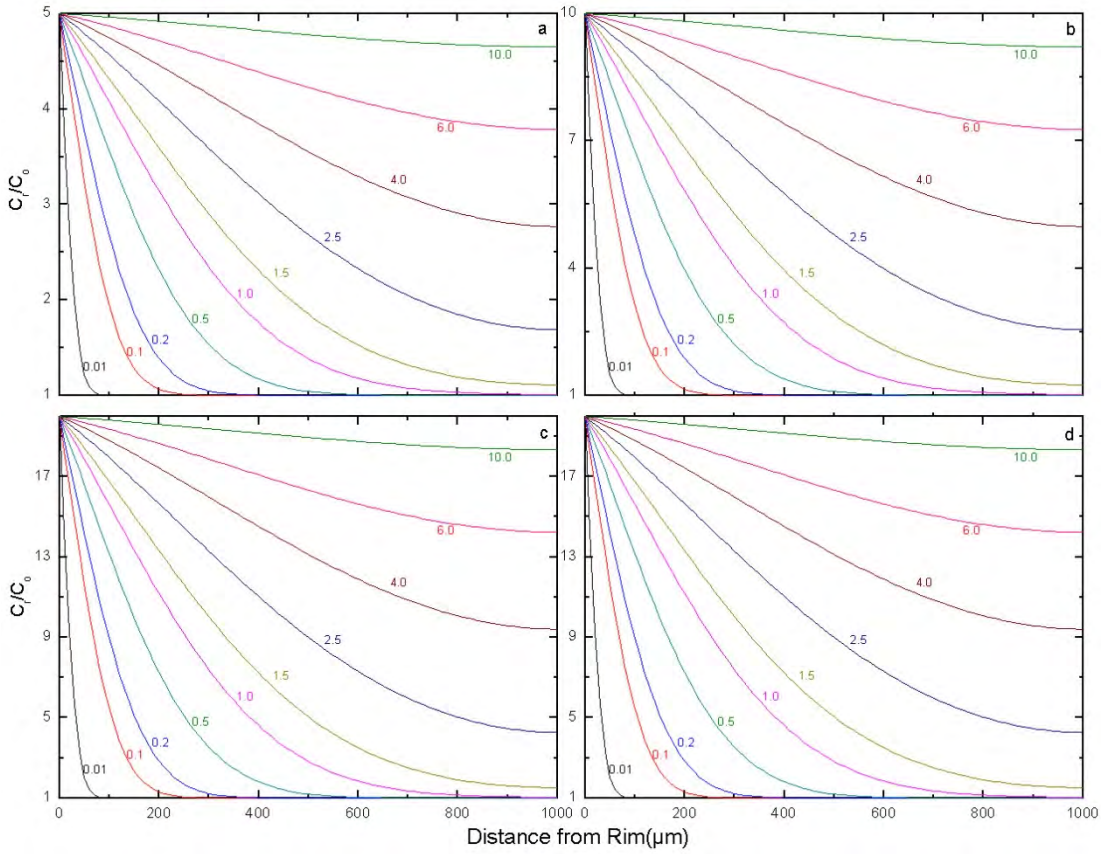

Fig. 7-5 The Li content profile within the mineral as a geospeedometer. The Li profiles evolve with time at an initial C_r/C_o ratio of 5 in a, of 10 in b and of 20 in c and d, respectively. The profiles are modeled in d assuming the different Li isotopic compositions from those in a-c. It is notable that the relative shape of Li profile is only decided by the duration in a fixed room, irrespective of the initial Li contrasts or the isotopic compositions.

7.3.3.3 The reproduction of measured profiles in our samples

According to the above numerical simulations and general results, we tempt to decompose the representative Li and Li isotopic profiles that were far from re-equilibrating with the recent Li enrichment.

The presence of a δ^7Li trough within the profiles of Hebi opx reflects a relatively narrow diffusion profile, thereby protecting mineral cores from Li diffusion. Accordingly, the measured Li and δ^7Li values at the cores for opx-3 (1.6 ppm Li with a δ^7Li of -22.4‰) in HB01, the opx-2 (2.4 ppm Li with a δ^7Li of -13.0‰) in HB07 and the opx-3 (1.7 ppm Li with a δ^7Li of -32.0‰) in HB12 reflect their initial signatures. Here, these measured Li content profiles can serve as a geospeedometer (Fig. 7-5). The modeling, for example, suggests a duration of 0.16 year for Li diffusion in opx-3 of HB01 (Fig.7-6a). The same goes to the profile of opx-2 in HB07

(~1.0 years) and of opx-3 in HB12 (~0.20 year). Opx-1 of HB12, characterized by the depleted and homogenous Li content (1.7 ppm) and δ^7Li value (-15‰), seems to have escaped that transient Li enrichment, emphasizing the restricted melt/fluid infiltration with a short duration. Moreover, this transient Li enrichment was usually followed by a serious Li diffusion loss at the mineral rims. The simulations in Fig.7-7 show that the outermost rim of Opx-3 has suffered a Li decrease from 120 to 53 ppm and a δ^7Li lift from +27 to +20‰. The rough estimate of duration is about 0.005 year for the Li diffusion loss, which was most likely to occur during or following the eruption in the host magmas (Fig.7-7).

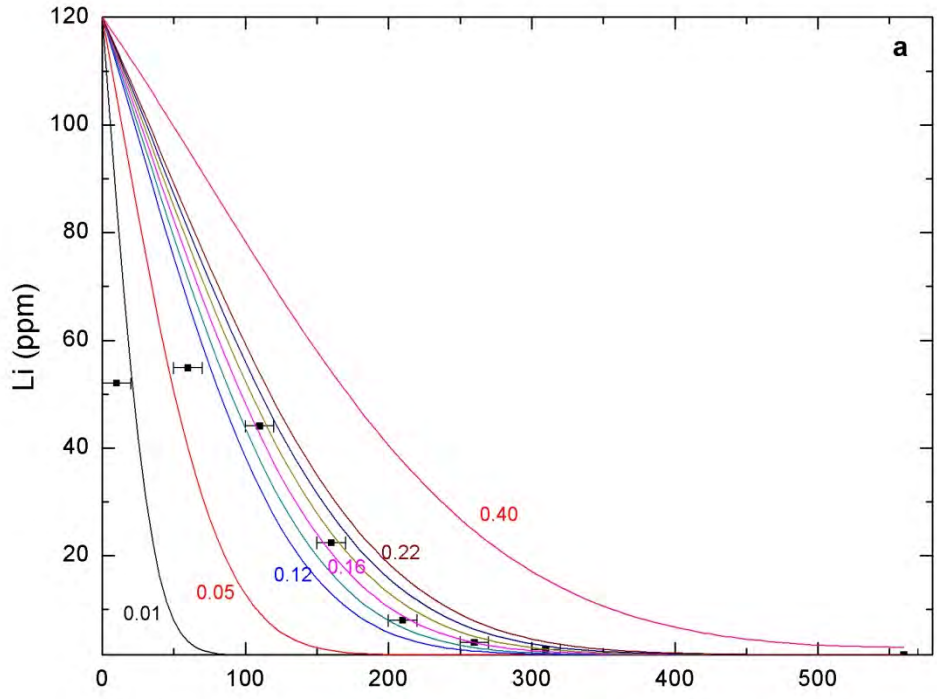

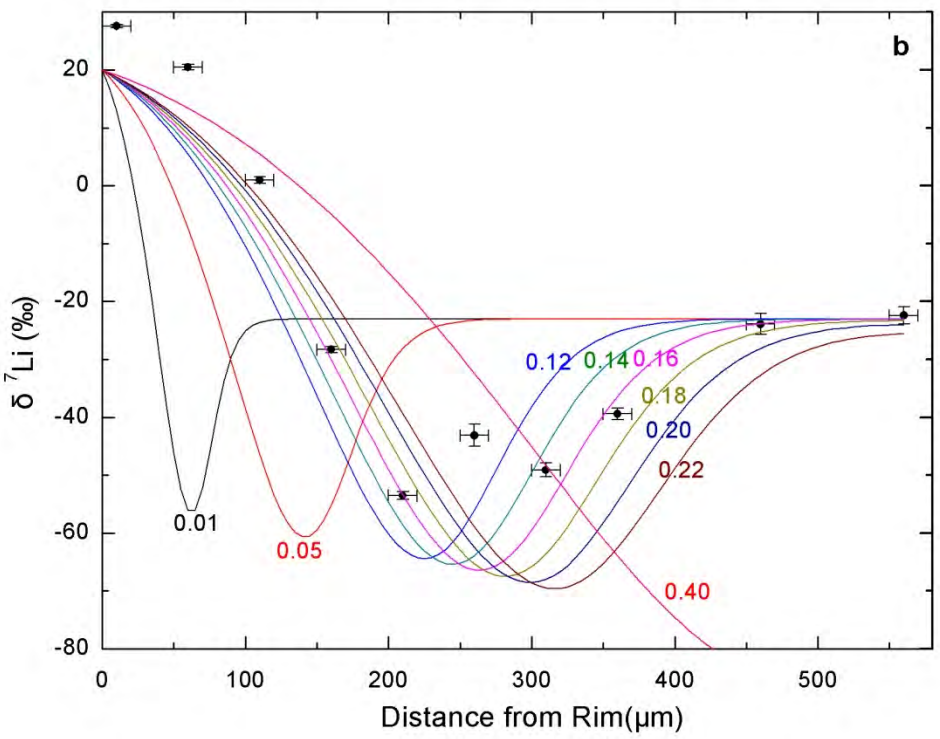

Fig. 7-6 The numerical modelling of the measured Li and Li isotopic profiles in opx-3 of HB01. a-b, measured Li and δ^7Li (the uncertainties are the 2 s.e. internal measurement errors), combined with the modeled curves, are plotted against distance across traverses (with an errors set as 10 μm) for: **a**, the Li contents; **b**, the Li isotopic compositions. Because of the presence of an intact isotopic trough, the measured values (1.6 ppm; -24‰) at the core can represent initial compositions of the mineral.. The modelling in **a** shows that the rim has experienced the latest Li diffusion loss, and is required to have a minimum Li content of 120 ppm to fit the high Li contents and Li gradients (dc/dx) inside the grain. The measured Li isotopic profile (except the rim within 100 μm affected by Li diffusion loss) can be further reproduced in **b** with a δ^7Li_{Cr} of +20‰, given the C_r of 120 and t of 1.6 from **a**. The diffusion rate for ^{7}Li and ^{6}Li is $10^{-15}m^2s^{-1}$ and $1.0335*10^{-15}m^2s^{-1}$, respectively, as assumed before. The radium of opx-3 is 560 μm. The numbers on the modeled curves are durations in years.

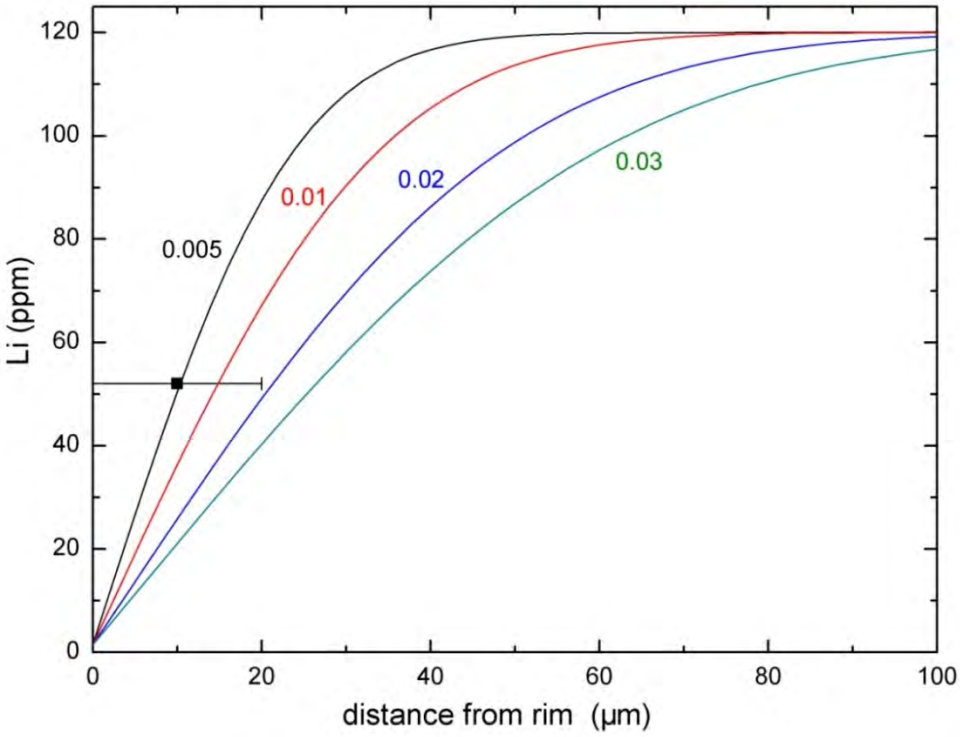

Fig. 7-7 The estimate of duration of the latest Li diffusive loss at the outermost rim of opx3 in HB01. Because the opx grain displayed an extreme intra-heterogeneity of Li caused by the previous Li addition (Fig. 7-6), it is complicated to numerically model the evolution of Li profile with time during the latest Li diffusion loss. However, it is noted that the Li diffusive loss was just limited to the outermost rim (no more than 100 um), so we can simplify the diffusion process, only considering the influence of Li diffusion on the rim (the outermost sputtered point) that dropped to 53 ppm from an initial 120 ppm. To assume that the mineral with a Li content of 120 ppm (C_o) was exposing to the host magma with the normal Li content, and the contacting rim remains a constant Li content of 1.5 ppm (C_r). Using the same Li diffusion equation and boundary conditions in chapter 7.1.1.2, we find that it has taken 0.005 year to decrease their Li content to the value that we observed at the mineral rim.

Additionally, this δ^7Li depletion of the Hebi pyroxene is confirmed by the Neptune MC-ICP-MS data reported by Tang et al. (2010) on the collected harzburgite xenoliths from the same locality. The reported Li contents vary from 0.98 to 2.29 ppm in olivine, from 4.48 to 7.96 ppm in opx and from 7.0 to 13.1 ppm in cpx. And the δ7Li range from 0.21 to 2.91‰ in olivine, from -20.19 to -25.98‰ in opx and from -11.4 to -21.41‰ in cpx. The low δ^7Li in pyroxenes cannot be produced only by Li diffusion, because the integral calculation indicates a maximum depletion of only 17‰ to the mineral (Fig. 7-8) (Parkinson et al., 2007). Thereby, we need a δ^7Li of the

mineral, which should be lower than -10‰ or even be much depleted if given the late high δ^7Li addition.

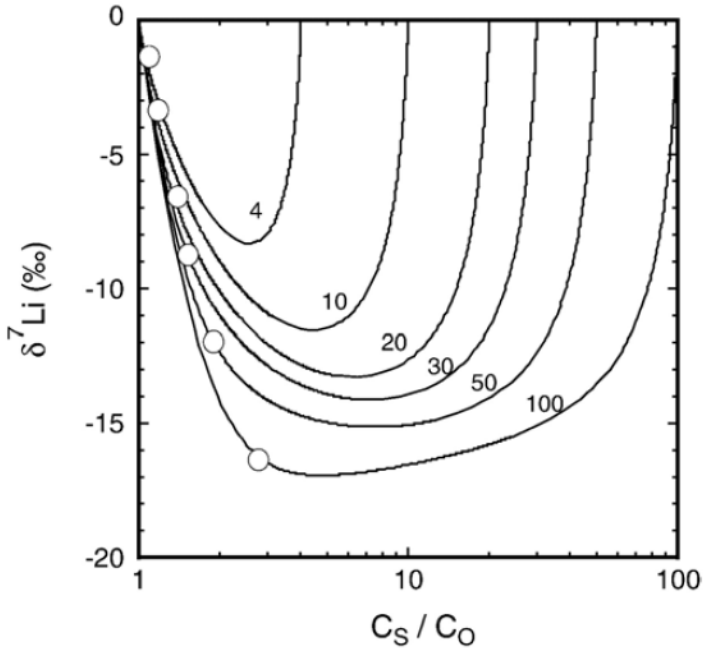

Figure 7-8. Evolution of the Li concentration (expressed as a function of C_S/C_0) and δ^7Li in a whole grain. The parabolic trajectories define the evolution of the whole grain until it recovers back to δ^7Li =0. Form Parkinson et al. (2007)

The other isotopic profiles show the minimum δ^7Li at the cores without a δ^7Li trough, implying that Li diffusion has already reached the cores and that the initial signatures have been erased. Cpx-1 in PL10, in contrast to those having too much Li taken up by the cores, shows the profiles far from relaxing, leaving a chance of recovering the initial compositions. The numerical simulations (Fig.7-9) suggest an initial Li of 2~5 ppm and δ^7Li around -20‰ for the mineral infiltrated by a late Li addition lasting 1.2 years. That is in good agreement with what observed directly in PL42, where the cores of two large cpx (>1500μm in radius) display the homogenous Li content (3.3 ppm) and δ^7Li value (~ -20‰).

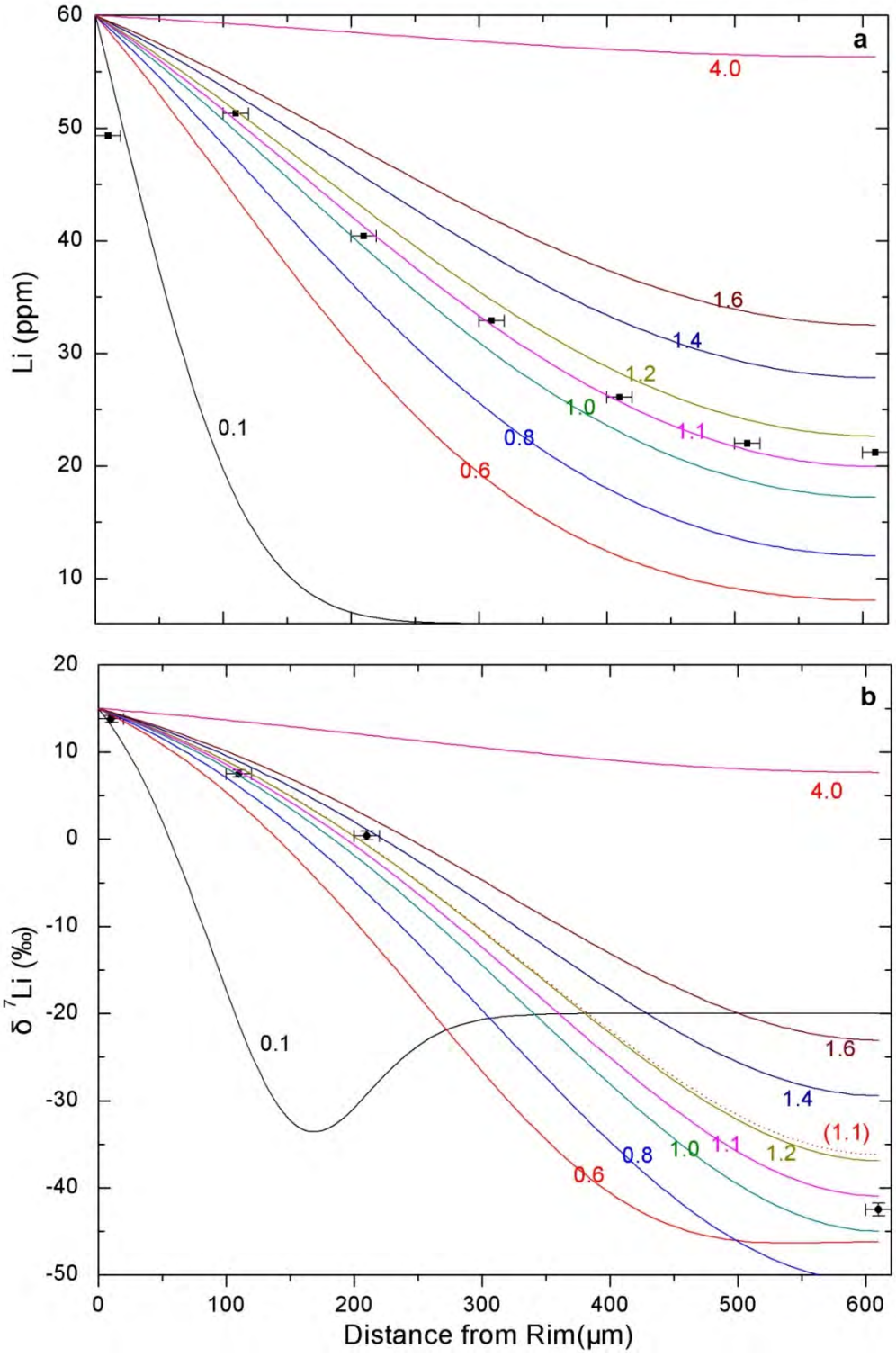

Figure 7-9. The numerical modelling of the measured Li and Li isotopic profiles in opx-3 of HB01. **a-b**, measured Li and δ^7Li (the uncertainties are the 2 s.e. internal measurement errors), combined with the modeled curves, are plotted against distance across traverses (with an errors set as 10 μm) for: **a**, the Li contents; **b**, the Li isotopic compositions. The lack of an isotopic trough implies the Li have diffused into the core with time, so the measured compositions of the core cannot reflect the initial values. We can estimate the boundary conditions (60 ppm and +15‰) for the rim given the stable Li and Li isotopic gradients near

the rim. We allow C_o to vary below 10 ppm (half of the observed values) for obtaining the duration, and find that the measured Li profile is well fitted with the modeled curved in **a** when C_o is between 2 and 5 ppm. With the combination of t and C_o, the δ^7Li_{Co} varies as far as it goes to match the observed isotopic profile. We find that for any given C_o between 2 and 5 ppm, a low δ^7Li_{Co} (around -20‰) is required to reproduce the measured isotopic profile. That is because the low δ^7Li value at core, produced by a lower C_o value, hence higher C_r/C_o ratio, will be offset by a longer duration (to fit the observed Li content at the core) that will result in a relaxing isotopic profile. The curves in **b** are modeled with a δ^7Li_{Co} of -20‰ and a C_o of 5 ppm. The dash in **b** is modeled with the same initial conditions but a δ^7Li_{Co} of +4‰ and t of 1.1 for comparison.

In summary, the above profile reproductions demonstrated that the low δ^7Li observed in the pyroxenes is a composite signature: an initial depleted δ^7Li of mineral was superimposed by the subsequent δ^7Li depletion by diffusive fractionation. Then, we may extend this initial low δ^7Li signature to the rest of pyroxenes that have been overwhelmingly diffused by the recent Li influx, and conclude that the low δ^7Li signature of the pyroxenes in Penglai and Hebi peridotites reflect a δ^7Li depletion event by interaction with low δ^7Li melts/fluids. The pyroxenes from Qixia, however, were assumed to have once equilibrated with the recent Li-rich melts, and there is no way to trace that ancient memory.

The above Li diffusion simulations and subsequent reproducing determine that the Li isotopic profiles, such as those having an isotopic trough, observed in the pyroxenes are a consequence of Li diffusion into the mineral grains. However, this type of Li isotopic zoning is rarely seen and once regarded as a puzzle in minerals of the metasomatised peridotites worldwide (Jeffcoate et al., 2007; Tang et al., 2007), and the most commonly observed Li isotopic zoning in which the isotopically light rims have more Li contents than the heavy cores, on the other side, is instead considered the classic zoning pattern for diffusive addition of Li into mineral (Jeffcoate et al., 2007; Tang et al., 2007). The ostensible contradiction can be reconciled as the following reasoning.

The Li isotopic trough is blurred in most of mantle pyroxenes by the pining of a δ^7Li trough to the rim that is difficult to be mapped as a whole. According to the Li diffusion simulation in the above, an isotopic trough is becoming increasingly narrow and short when moving towards the rim due to short duration of Li addition in the host magmas. The figure becomes even worse when a low Li concentrate ratio was initially established between the rim and the interior, which would expect a much

slimmer and shorter trough. Then, the attempt to probe this narrow and short isotopic trough near the rim with a high spatial resolution raises a technical challenge. In addition, the outermost part of the rim that encompasses this isotopic trough is easily to be got rid of during the pre-experiment prepare. Accordingly, this biased profile, losing its down-going limb part of trough, will see δ^7Li progressively increase from the low value near the rim inwards the grain and flatten around the core with the high δ^7Li, as what we observe mostly in Li enriched pyroxenes.

On the other side, the Li isotopic trough is intensified by several factors in our samples. First, the mineral rims are highly enriched in Li content (up to 120 ppm), and the hence high Li content contrast between rim and core will promise a deeper isotopic trough, making it easier to be identified. Second, an appropriate duration of Li addition, not too short or too long, will push the increasingly broad and deep trough away from rims, making it easier to be identified. Otherwise, a too short duration will pin an increasingly narrow trough too close to rim, and a too long duration will depress a trough formation, such as cpx-1 of HB01, where the grain see its δ^7Li decrease all the way from +16 at rim to -75‰ at core without a trough. Third, the high δ^7Li of the Li addition will significantly lift the down-going limb of the δ^7Li trough, such as opx-3 of HB01. In a word, all these combined factors help in generating a Li isotopic trough that always lacks worldwide.

7.4 The Li-rich influx with anomalous isotopic compositions

According to the above observations and reasoning, we conclude that the peridotite samples from these three localities share more or less the similar Li and Li isotopic signatures that suggest two superimposed Li enrichment events: a limited Li enrichment (< 5 ppm) and the δ^7Li depletion (-20~-10‰) of the domains of these xenoliths, followed by a recent and transient infiltration of high Li and δ^7Li (up to +20‰) melts/fluids.

7.4.1 The low δ^7Li influx

The large δ^7Li depletion should be inherited from the low δ^7Li melts/fluids that infiltrated with peridotite. However, whether the low δ^7Li signature reflect the true

nature of the melts/fluids itself or the Li isotopic fractionation on large scale, i.e. diffusive fractionation of Li isotopes in the melts/fluids that then equilibrated with the surrounding rocks, need to be resolved.

The diffusion-driven Li isotope fractionation has been broadly recognized in natural samples. It can operate on a small scale to cause the mineral zoning and inter-grain heterogeneity observed in the thin section (Jeffcoate et al., 2007; Parkinson et al., 2007, 2009; Tang et al., 2007). In this case, Li isotopes fractionate as they diffuse into the minerals from the grain-boundary Li-rich melt/fluid that is unnecessarily δ^7Li depleted. This diffusion mechanism has been dismissed by above observation and reasoning.

The diffusion-driven Li isotope fractionation can also operate on a large scale to invite a low δ^7Li domain of meters (Lundstrom et al., 2005; Teng et al., 2006; Marschall et al., 2007). In this case, when Li diffuses from melt within a volcanic conduit into the pre-existent intergranular melts in the surrounding peridotites at depth, Li isotopes will fractionate in melts at a large scale of meters. These isotopic shifts will be recorded by the surrounding peridotite minerals if equilibration between the melts and the minerals is reached through the volume diffusion or dissolution and re-precipitation (Lundstrom et al., 2005). Then, the Li contents and Li isotope ratios between the mineral phases on a scale of thin section (a few centimeters) should approach equilibria, i.e. the coexisting pyroxene olivine should share the similar Li content and δ^7Li value (Rudnick and Ionov, 2007). The diffusive influx of Li on a large scale was first put forward by Lundstrom et al. (2005) to interpret the large variations in δ^7Li (up to 10‰) occurring in a consistent pattern across three transects (up to 3 meters) from dunite to plagioclase lherzolite within the Trinity peridotite, an ultramafic body interpreted to represent an ophiolite reflecting a former spreading center within a back arc or marginal basin setting (Quick et al., 1981). Teng et al. (2006) reported another more extreme case occurring in the crustal environment at relatively low temperature. In this case, Li diffuses from the intrusion of the Tin Mountain pegmatite having high Li content (471 ppm) and high δ^7Li (+7.6‰) value into the country rocks, including the amphibolite with an initial Li content of 20 ppm and δ^7Li value of +7.6‰ over a range of about than 10 meters, and the Quartz mica schists with an initial Li content of 70 ppm and δ^7Li value of +2.5‰ over a range of more than 300 meters. The Li and Li isotope profiles in both country rocks can be well predicted by the diffusion model.

The diffusive influx of Li from melts channels into the adjacent wallrocks has been invoked to interpret the pervasive δ^7Li depletion in the peridotite xenoliths, especially the low δ^7Li in olivines that are rarely seen before. Tang et al. (2010) has reported the Li isotopic systematics of the peridotite xenoliths from the North China Craton, showing that the pyroxenes with elevated Li content (up to 24 ppm in cpx) are highly depleted in δ^7Li (-3.3 to -23%), whereas the δ^7Li in most olivine (+0.7 to +5.4%) are similar to the range of the normal mantle. Among them two exceptional samples (FS5 and FS13) show the low δ^7Li (-3.0 and -7.9%) in the olivine, which was interpreted as evidence for the existence of low δ^7Li domain in the lithospheric mantle, perhaps generated by meter-scale diffusion of Li during melt/fluid-peridotite interaction (Tang et al., 2010). However, this kind of diffusive fractionation seem unlikely the main cause, in that the olivines in these two exceptional samples are far from Li enriched or light enough to equilibrate with the coexisting pyroxenes, if the infiltrating melts acquire the low δ^7Li by diffuse.

In our peridotite samples, we can assume that the pyroxene and olivine share the similar Li contents and low δ^7Li in Penglai samples, probably at equilibrium, prior to the late high-δ^7Li enrichment. However, this large δ^7Li depletion should be most inherited from the low δ^7Li melts/fluids itself but least from the diffusive fractionation of Li isotopes occurring in the pre-existent interconnected melts/fluids that interacted with the mineral grains (Lundstrom et al., 2005; Teng et a., 2006). This claim is justified as following.

As discussed above, this diffusive influx of Li on a large scale will require the protracted interaction of the pre-interconnected melts with the peridotites, which would result in an extra enrichment of incompatible trace elements, such as the LREE enriched cpx. That, however, contrasts with the observed LREE-depleted pattern in the Penglai cpx (Fig. 7.2), implying a lack of that pre-existent interaction. The coupling of low δ^7L in olivine and pyroxene may reflect a relatively long interaction of the new-coming low δ^7Li melts which, however, seems not long enough to invite the corresponding enrichment of other incompatible trace elements. On the other side, the olivine cores of HB samples show a normal mantle-like δ^7Li range that strongly contrasts with the inferred low δ^7Li for the initial pyroxene, also excluding the main cause of δ^7Li depletion by that diffusive fractionation at large scale. Otherwise, the Li isotopic re-equilibrium between the coexisting olivine and pyroxene would be expected (Rudnick and Ionov, 2007). Then, the decoupling of the low δ^7Li in

pyroxene from olivine reflects a short interaction with the low δ^7Li melts.

7.4.2 The recent high δ^7Li influx

The high Li contents of the pyroxenes require much more for the infiltrating melts/fluids that fed them. The mineral of 120 ppm Li at the initial rim of opx-3 of HB01 (Fig. 7-6), for example, will require the equilibrating melt with 600 ppm Li when assuming the $^{opx/melt}D_{Li}$ value of 0.2. This argue for the late Li addition was a short melt-rock interaction event occurring at the sources of xenoliths rather than in the host magmas during eruption, because there is no report of such high Li contents in xenolith-bearing alkali-basalts worldwide, including those from the North China. The Cenozoic alkali-basalts from Shangdong province, including Penglai and Qixia, where the peridotite xenoliths were analyzed in this study, show a Li content of around 10 ppm (Zeng et ., 2010), in the range for relative primitive magmas from mantle (Halama et al., 2007). Given moderately incompatibility of Li in partial melting, the undifferentiated mantle-derived melts typically show the enrichment of Li over their mantle sources by a factor of ~ 5 (Halama et al., 2007, 2008). The upper mantle, for example, is estimated to contain ~1.5 ppm Li (Ottolini et al., 2004), and their derivations, the unaltered MORBs, have the Li contents of ~5 ppm. Accordingly, the mere Li enrichment of the melting source is far from enough to produce such extremely high Li content no matter how tiny the fraction of partial melting is, because the maximum Li content in melt can be easily constrain by no more than $1/D_{melt/rock}$ times the initial value (when the fraction of partial melts approaches zero). The subsequent differentiation of melts is expected, such as the highly differentiated carbonatitic melts/fluids from Oldoinyo Lengai, where the high degree of differentiation, combined with a possible preference of Li for the carbonatitic melt during immiscible liquid separation, was proposed to produce the high Li content up to 300 ppm in natro-carbonatites (Halama et al., 2007). The may hold true in our case, too. The carbonated upper mantle source has been invoked to explain the geochemical signatures of the Cenozoic alkali-basalts from eastern North China (Zeng et al., 2010, 2011), so there is a possibility that a small fraction of partial melting of these carbonated mantle pieces give rise to the Li-rich carbonatitic melts from which the late metasomatic agents featured by the high Li and δ^7Li were derived. The absence of these carbonatitic melts on the surface may reflect their small volumes that have

been mostly exhausted at grain-boundaries, so that they may not survive the way up to surface.

In addition, the recent Li enrichment occurring at the mantle source of these xenoliths is not only a short event that has been estimated by the profile reproducing to last no more than few years. The intact preservation of the Li and Li isotopic diffusion profiles will require this melt-rock interaction took place very short prior to the volcanic transport of these xenoliths, probably in one or two years. Otherwise the diffusion profiles will be erased. Moreover, the fragmentation of the relatively large xenoliths near the surface is probably invoked to avoid the direct contact with the host magmas of low Li content (Aulbach et al., 2009).

The lack of per mil level differences in δ^7Li between primitive lavas (olivine melilitites) and highly differentiated lavas (nephelinite, carbonatites) from Oldoinyo Lengai suggests that there is no or very little Li isotope fractionation during magmatic differentiation with temperatures down to 500 °C (Halama et al., 2007). So if the high Li metasomatism inferred in our samples is carbonatitic melts in nature as that from Oldoinyo Lengai, the differentiated processes that were involved in concentrating Li content would not fractionate Li isotope at the same time, i.e. preferentially enrich ^{7}Li in the remaining melts. The extremely high δ^7Li signature in our samples is also unlikely to result from the increase of δ^7Li by diffusion-induced isotopic fractionation, which usually happens to erupted magmas as a result of effective melt-peridotite interaction during volcanism (Lundstrom et al., 2005; Elliott et al., 2006). Rather, it reflects the nature of the mantle metasomatism itself.

7.5 The anomalous Li isotopic domains in the mantle and their origins

It is generally accepted that Li isotopes do not show per mil-level mass fractionation during magmatic processes in the mantle (Tomascak et al., 1999; Bryant et al., 2004; Wunder et al., 2006; Teng et al., 2006b; Halama et al., 2007). Hence, these inferred anomalous Li isotopic signatures (both heavy and light) of the Li-rich melts/fluids that infiltrated our samples will acquire the same of their mantle sources.

7.5.1. The heavy Li domains in the mantle

The heavy Li components in the mantle are inevitably linked to the materials that have been once isotopically fractionated by the low temperature processes on the surface. The large mass difference (~16%) between its two isotopes, ^{6}Li and ^{7}Li, can generate a large isotopic fractionation at low temperatures, vary from -10 to +40‰ in nature samples (Seitz et al., 2000; Rudnick et al., 2004). This fractionation of Li isotopes is dominated by partitioning of Li between clays and water in the hydrological cycle. Minerals are enriched in ^{6}Li relative to co-existing aqueous fluid during the weathering of the continents, which both releases Li and isotopically fractionates it. These isotopically heavy river water with the average δ^{7}Li of +23‰ then feeds the oceans, where partitioning of Li between sea water and clays produces major isotopic fractionation again. The more weathering the oceanic crust suffers, the more Li and the heavier Li taken up by the alteration mineral in oceanic crust. The altered oceanic crust can approach as high as +14‰ in δ^{7}Li, and up to 75 ppm in Li content. These Li are mainly stored in secondary mineral phases, such as chlorite and smectite, in the uppermost crust (Chan et al., 1992). The subducted sediment veneer is another possible source for Li input, varying between -2.5 to +15‰ in δ^{7}Li, but most of those components have δ^{7}Li <+6‰, due to their continental origins. However, the creations of heavy Li component alone constitute only part of the story, and the mechanism by which they are transferred to the mantle matters much.

The subduction zones are where crustal materials sink back into the mantle. It has been predicted that during subduction the metamorphic dehydration of the slab will release heavier Li into fluids and isotopically fractionate it, resulting in the hydrated

overlying mantle wedges with heavy Li, ultimately to be sampled again in island arc lavas (Tomascak et al., 2002; Elliott et al., 2004). Since the Mesozoic, eastern China has long been influenced by the western subduction of the Pacific plate beneath East Asia continent (Wu et al., 2005), and the successive subduction could have generated a big mantle wedge (BMW) above the subducted slab and invoked the compositional heterogeneity in the upper mantle beneath the eastern China (Zhao et al., 2007).

Although the studied localities, such as Penglai and Qixia, are both more than a thousand kilometers from the trench, where the Pacific plate was sinking at the Neogene eruptions of the host magmas, let alone a more inland Hebi, we can expect a closer distance from the Mesozoic trench, given that the paleo-Pacific plate rolled back during subduction (Hall et al., 2002; Wu et al., 2005; Schellart et al., 2006). In addition, it has been suggested that the heavy Li carried in upward slab-derived fluids were captured and isotopically re-equilibrated by the overlying mantle wedge viscously coupled to the down-going plate during residency in the subduction zone, because of the weak incompatibility of lithium the rapid diffusion of lithium into mantle minerals. Then the slab-derived heavy Li fluids can hardly survive the way to the melting source in the mantle wedge, and ultimately to be sample by arc lavas, unless the transport facilitated by fractures in mantle wedge. This is also one of main reasons why Li is decoupled from the other fluid-mobile elements such B and Ba in studies of island arcs, and most island arcs have Li isotopic compositions that are indistinguishable from those of MORB (Tomascak et al 2002; Elliott et al., 2004). As this fluids-modified mantle warms up, it will peel away from the denser basaltic slab, and naturally re-mix back into the upper mantle to form the heavy-Li mantle domains that are far from subduction zone and beyond, and to be sampled during melting beneath the mid-ocean ridges (Elliot et al., 2004, 2006). The cartoon in Fig. 7-10 from Widom (2006) is based on the model suggest by Elliot et al. (2006).

According, we are inclined to believe that the subduction-modified mantle wedge produced at subduction zone, probably derived from western subduction of the paleo-Pacific plate, were delivered and dissipated in the upper mantle beneath the eastern NCC. The partial melting of these enriched mantle pieces will produce the parent melts from which the late metasomatism featured by high Li and δ^7Li was derived. However, the δ^7Li values up to +20‰ seem still too high in relative to those produced and found at subduction zone (Tomascak et al., 2002; Chan et al., 2002), although diverse subducted inputs, including Subducted sediments, metamorphosed basaltic

rocks, and serpentinized peridotites, display diverse Li isotopic compositions (-19 to +21%) (Bouman et al., 2004; Chan et al., 2002; Chan et al., 2006; Decitre et al., 2002).

Caciagli et al. (2012) tests a chromatographic exchange mechanism by which the slab-derived Li enriched fluids achieve instantaneous equilibrium with the coexisting solid minerals when passing through the mantle wedge column and hint that the slab-derived fluids would become increasingly enriched in in ^{7}Li by a simple Rayleigh distillation. In this model, the slab-derived fluids will percolate at near the slab-wedge interface, where the temperature (as low as 700-800) there could promise a relative large isotopically fractionation (still no more than 2 per mil), and the last fraction of the remanding fluid should be very small (at least less than 0.03, i.e. the less the Li content in the fluids is, the heavy Li isotopic composition is). This Rayleigh distillation scenario seems unlikely to account for the high δ^{7}Li melts in our case. The 600 ppm Li with a δ^{7}Li of +20, for example, will need an initial slab-derived fluid with a Li content of 20000 ppm with a δ^{7}Li of +10. We have no reason to call on such an unreasonably high Li content for slab-derived fluids.

The creation of these anomalous Li isotopic domains alone constitutes part of the story. Growing evidences, on the other side, show that these domains can survive and remain isotopically distinguished in the upper mantle for billion years, despite of the fast diffusion rates of Li isotopes. The Li diffusion simulation adopted by Vlastelic et al. (2009) shows that the long-term preservation of the isotopic disequilibrium of the domain partly results from very early, large isotopic fractionation, which raises the mean composition of the domain up to nearly two times the initial value (Fig. 7-11). This may be part of the mechanism responsible for producing the artifact of the high δ^{7}Li signature (up to +20‰), but it just serve to slightly amend but fundamentally change the “story”, because even the δ^{7}Li value of +10‰, half of the observed high values, is still high enough to hint at recycled components. Accordingly, the extremely high δ^{7}Li signature of the infiltrating melts recorded in our xenoliths most likely reflect a combination of a larger portion of relatively “pure” recycles components in melting regions and the diffusive disequilibrium of these recycled components preserved in the upper mantle.

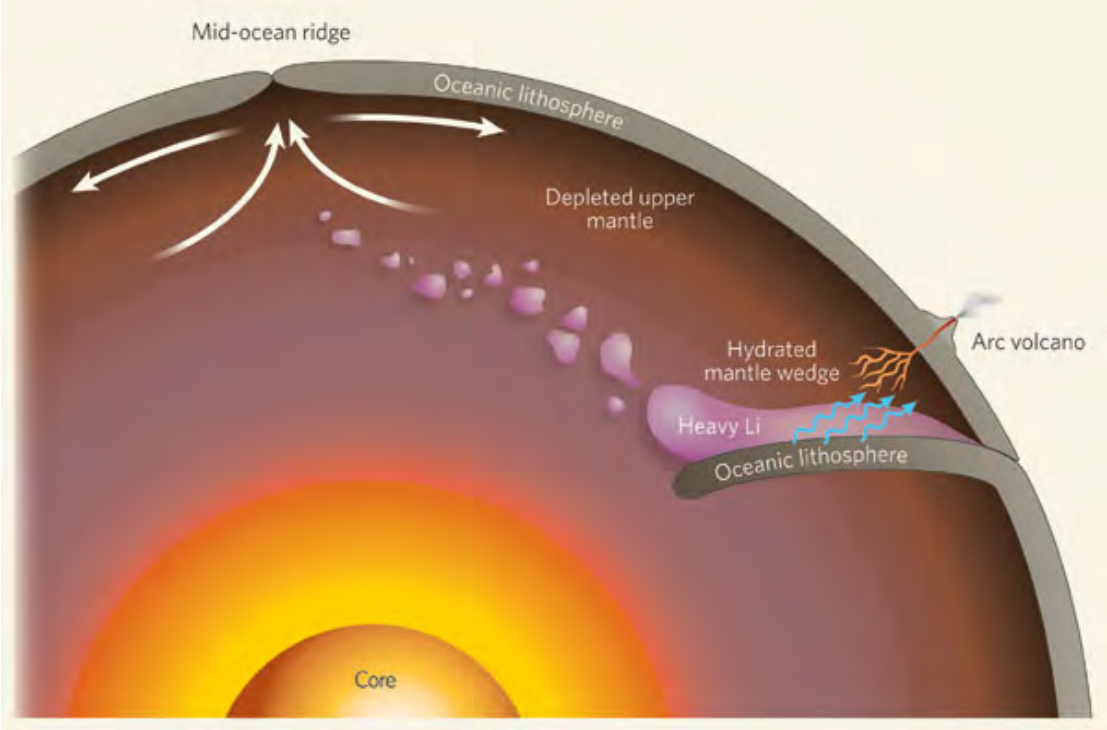

Figure 7-10. The cartoon is from Widom (2006) based on the model proposed by Eillot et al. (2006), showing how the enriched mantle domains produced at subduction zones are sampled during melting beneath the mid-ocean ridges in term of Li isotopes. At a subduction zone, one plate of oceanic lithosphere dives under another plate. This is associated with the release of fluid (blue arrows) into the overlying mantle wedge, as well as melting that produces arc volcanism at the surface. It is part of the hydrated mantle wedge above the subducting lithosphere, which is initially viscously coupled to the descending slab, and eventually frees itself and mixes back into surrounding depleted mantle.

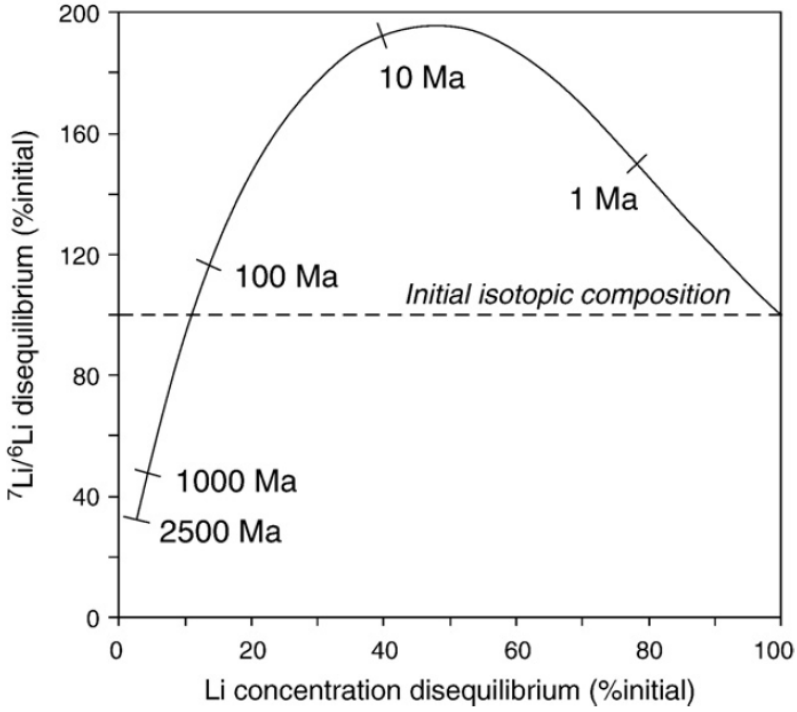

Figure 7-11. The figure is from Vlastelic et al., (2009). The extent of isotopic disequilibrium between mean anomalous Li domain and mantle plotted versus chemical disequilibrium. References for chemical and isotopic disequilibria are 100% for the initial condition and 0% for complete homogenization. The curve is shown for a domain thickness of 700 m and $D_{Li}=5\times10^{-10}$ m^2/s. Time (in Ma) is indicated. Slower diffusivity and thicker domain would give older age at the indicated tick marks, while following the same trajectory. Varying domain thickness by a factor of five contributes less than 1% variation to the maximum isotopic composition; the shape of the curve remains essentially unchanged

7.5.2. The light Li domains in the mantle

According to the paradigm, recycled components characteristic of heavy and light Li isotopic composition are derived from slab-derived fluids at subduction zone and from dehydrated residues of deeply subducted slab, respectively (Tomascak et al., 2002; Zack et al., 2003; Elliott et a., 2004, 2006). The Li isotopic composition of slab residues, however, is recently under debate (Marschall et al., 2007; Rudnick and Ionov, 2007; Vlastelic et al., 2009; Chan et al., 2009), and the origin of the light Li domains in the mantle remains under debate.

Zack et al. (2003) presented a novel study on the alpine orogenic eclogites from Trescolmen (Switzerland) which provided the first Li isotope data on high pressure metamorphic rocks. The authors reported the extremely δ^7Li values (as low as -11‰)

in these eclogites, rocks thought to be fragments of previously subducted oceanic crust, and argued that these low δ^7Li values are a consequence of Li isotopic fractionation during subduction dehydration, and the isotopic fractionation processes can be modeled using a simple Rayleigh distillation formulation (Fig. 7-3). These findings have important implications for Li geochemical cycling in the mantle and identifying deeply subducted slab in term of Li isotopes.

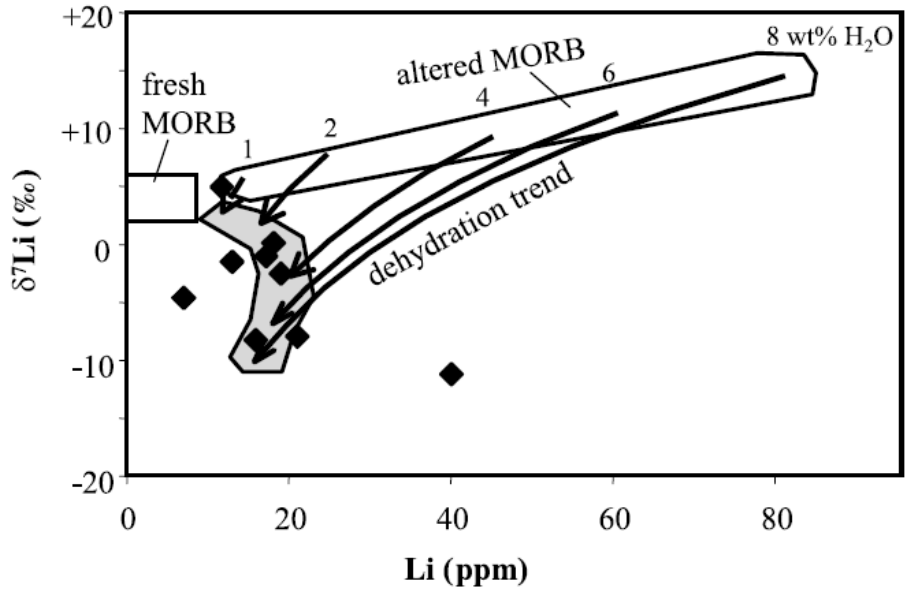

Figure 7-12. Whole rock Li concentration and δ^7Li of Trescolmen eclogites (black diamonds). Also shown is field for fresh MORB and MORB altered at low temperatures. Numbers next to altered MORB field are approximate wt% H_2O bound at interlayer sites of clays at corresponding Li concentration. Rayleigh distillation was modeled with α =1.015 (α defined as Li isotopic fractionation factor between fluid and whole rock) and D=0.05 (D defined as Li partition coefficient between whole rock and fluid). Shaded field surrounds calculated compositions of altered MORB after Rayleigh distillation. The details can be seen in Zack et al (2003).

However, mounting evidences, including experimental works and natural observations, suggest that the dehydrated slab residues may be characteristic of heavy Li (Marschall et al., 2007; Vlastelic et al., 2009; Chan et al., 2009) rather than light Li as previously accepted (Zack et a., 2003), because of the limited removal of Li from the slab during dehydration at low temperature Marschall et al., 2007; Penniston-Dorland et al., 2012).

The recent findings revealed that metamorphic dehydration has had little discernible effect on δ^7Li, even in the presence of lithium depletion (Marschall et al., 2007b; Qiu et al., 2009; Teng et al., 2007). Marschall et al. (2007) based on the study of 41 orogenic HPM rocks from 11 localities, combined with the modelling, showed that metamorphic dehydration processes cannot shift significantly Li isotopic composition (less than 3‰ in δ^7Li) of subducted crust because of the limited Li removal at relatively low temperature, and the extremely light Li observed in orogenic eclogites is a consequence of Li isotopic fractionation driven by Li redistribution between the eclogites and the surrounding Li-rich wall-rock during exhumation in the crust.

More recently, Penniston-Dorland et al. (2012) has conduct a more comprehensive investigation on the Catalina Schist, a suite of 63 samples representing a range of metamorphic grades and diverse lithologies, to evaluate the extent of Li mobility in slab derived fluids and the degree to which Li isotopes can trace metamorphic fluid-rock interactions. The study demonstrates a local-scale re-distribution of Li but a robust retention of Li (a lock of an appreciable across-grade bulk shift in δ^7Li) in a sedimentary-mafic-ultramafic lithological package subducted to depths of at least 40 km, despite the extensive devolatilization at the higher metamorphic grades that led to the removal of the fluids-mobile trace elements.

If the above observations and reasoning are correct, and subduction zone metamorphism imposes a limited Li isotope shift in the subducting slab, the robust transfer of the seafloor Li inventories in deeply subducted rocks has direct implications for modern and long-term Li isotope mass-balance among the deep Earth and surface reservoirs (Elliott et al., 2004). There are no mantle components characterized by Li isotopic depletion, reflecting contaminations by recycled materials, and the growing findings of isotopically heavy rather than light Li in some OIBs with strong HIMU affinity may just reflect involvement of these heavy Li subducted slab in the melting regions (Vlastelic et al., 2009; Chan et al., 2009).

However, the inferred low δ^7Li melts in our samples, and the low δ^7Li melts reported by Agostini et al. (2008) acquire such low δ^7Li domains in the mantle. Instead, the local Li isotopic disequilibrium zones, caused by kinetic fractionation adjacent to melts or volcanic conduits, are usually proposed as that light Li domains in the mantle (Lundstrom et al., 2005; Marschall et al., 2007). The detail over the how to produce these diffusive zones have been discussed in the section 7.4.1.

The zones of diffusive Li disequilibrium, however, seem unlikely to be the melting sources of the low δ^7Li melts, because they are too small volumetrically to dominate in anomalies melting that will yield a δ^7Li signature averaging a large source region (at least a few km^3) (Agostini et al., 2008). In addition, these small zones of diffusive disequilibrium, unlike the large anomalous Li domain, can hardly survive the rapid Li diffusion that will facilitate a fast isotopic homogenization at high temperature in the convecting mantle. Thus the low δ^7Li melts have to call upon "pure" recycled materials in melting sources that have experienced extensive removal of Li under low temperature during dehydration at the shallow depths, such as the scenario proposed by Agostini et al. (2008), in which the ongoing solid-fluid exchange could lower the δ^7Li of the slab more extensively at the shallow depths where the nearly stagnant slab is being comprehensively devolatilized than is observed in normal arc setting.

Recent high-resolution tomographic images reveal that the subducted Pacific slab became stagnant within the mantle transition zone beneath eastern China, and its western edge under the NCC has reached to approximately Bohai bay area but not Hebi area yet (Huang and Zhao, 2006). In east China, the surface topography changes suddenly from east to west, and the boundary, located to the west of Hebi area and generally parallel with the western edge of the stagnant slab, may indicate that the subduction of the Pacific slab and its stagnancy in the mantle transition zone have a great influence on the structure and tectonics of the crust and upper mantle beneath the east China (Huang and Zhao, 2006). The real western edge of the stagnant slab may become tomographically invisible due to the thermal equilibrium with the surrounding mantle, and have already reached beyond Hebi and to the topographic boundary. The observed low-velocity anomaly under the central NCC, which extends to more than 500 km depth within the transition zone, may provide a conduit for the fast ascent of the warm materials that include the subducted slab pieces, probably at the form of the mantle upwellings or mantle plume (Zhao et al., 2009; Zeng et al., 2011). When the deep materials migrate upward into the shallow mantle, they will continue to flow laterally and east under the base of the lithosphere to serve as the melting source of low δ7Li melts, because the central NCC is much thicker than that of the eastern NCC (Zeng et al., 2011).

7. 6 The melt-rock interactions beneath the NCC

7.6.1 The melt-rock interactions and the re-fertilization

The Li isotopic systematics of the peridotite xenoliths demonstrate that the lithospheric mantle beneath these three localities (Penglai, Qixia and Hebi) have experienced recent melt-rock interactions. The kind of melt-rock interactions are not only limited to the above three localities, but were also extensively recognized across whole North China by recent Li isotopic studies on peridotite xenoliths from Hannuoba, central NCC (Tang et al., 2007), Hebi (the same locality as this in our study) and Fanshi, central NCC (Tang et al., 2010), Qingdao, eastern NCC (Zhang et al., 2009b), Longgang, northeastern NCC (Tang et al., 2011) and the Western Qinling in the western Qinling- Sulu-Dabie suture zone in central China (Su et al., 2011). These peridotite xenoliths, especially those from Fanshi, Hebi, and Western Qinling, show extremely high Li enrichment and Li isotopic fractionation among mineral phase, similar to those observed in our samples, reflecting the very recent melt/fluids-rock interactions in the lithospheric mantle.

Combined with the Sr-Nd isotopic evidences, the authors suggested that the lithospheric mantle beneath the NCC has experienced multistage melt/ fluid-peridotite interactions, which have transformed the Archean refractory lithospheric mantle into

the lithospheric mantle that was less refractory and incompatible element and Sr–Nd isotopically enriched at the Mesozoic time (Zhang et al.,2009b; Tang et al., 2010).

However, it is noted that Li isotopic system can hardly record or hint at a relatively ancient melt-rock interaction event, given that Li isotopes diffuse fast at high temperature. The Li zoning in mineral grain can be used to determine the duration of Li addition, such as the reproduction of the measured Li profiles in our pyroxenes. In addition, Li addition must be also a recent event, otherwise the Li zoning or Li heterogeneity in the samples would be erased, the numerical calculation shows, for example, that it would take only a few ten thousand years (depending on the chosen diffusion rates of Li isotopes) for the Li zoning to disappear in a 1 mm wide cpx. Thus, the melt/fluids-interaction that recorded by the Li enrichment in peridotite xenoliths must have been a very recent event, occurring within tens of thousands of years before volcanic transport and cooling of the host magmas.

7.6.2 The Li enrichments and the water depletion

According above discussions in previous chapters, we find an interesting phenomenon that the water contents, to the first order, are negatively correlated with the Li content in the pyroxenes among these localities. Those peridotite samples from the Cenozoic Penglai, Qixia and Hebi show the low water contents but extremely high Li enrichments, compared with those Mesozoic samples from Junan and Qingdao (only one sample, QDPS-16, was measured for lithium content. The Li elemental profiles indicate no zoning within mineral grains or variation between grains. The average Li content is 2.1ppm in olivine, 1.3 ppm in cpx and 2.2 ppm in olivine, respectively, in the range of those reported by Zhang et al., (2009b)).

Although the inter- and intra Li heterogeneities abound within these Li highly enriched samples and hence we cannot derive the Li content for the bulk minerals or peridotites from the in-situ measurements, it is still evident that the degree of Li enrichment in individual locality follows the order: Penglai > Qixia > Hebi (Table 4-8 to 4-9. Although the in-situ measurements show extremely high Li content up to 120 ppm at mineral rim, the enrich rims are too narrow due to a very short duration of Li addition. Tang et al. (2010) reported the Li contents of no more than 8 ppm in bulk pyroxenes for three Hebi peridotites using MC-ICP-MS). On the other side, the water contents apparently follow the reverse order (Table 4-7).

Given that hydrogen and lithium are two fast diffusion elements, we may attribute that negative correlation to their coupled substitutions in pyroxene by which Li diffusion into mineral is coupled to H loss. We need to review their incorporation mechanisms in the pyroxene first.

Pyroxenes, both cpx and opx, have two cation sites, M_1 and M_2; M_1 has six-fold coordination with respect to oxygen and M_2 has eight-fold coordination. Given that the M_1 (optimal site radius ~ 0.7 Å) site is slightly smaller than M_2 (~ 1.1 Å) and has lower defect energies for univalent cations, it is likely that the primary site for lithium in the cpx structure is M_1 where it can substitute for Mg^{2+} (Shannon and Prewitt, 1969; Purton et al., 1997). The substitution should be charge-balanced by a trivalent cation, such as Al^{3+}, Fe^{3+}, Cr^{3+}, Sc^{3+} and REE^{3+} (Brenan et al., 1998a; Seitz and Woodland, 2002). The increased concentrations of the trivalent cations should enhance the uptake of lithium in the mineral, and the addition of divalent cations such as Na would have the opposite effect as lithium would not be charge balanced when coupling with a divalent cation. One important crystal chemical aspect for the incorporation of Li in mantle minerals, such as ol, opx and cpx, is that a coupled substitution is required to maintain electrostatic neutrality. There are many different possibilities that can be considered, including coupled substitution with defects or the redox of variant valence cations.

For the Li enriched pyroxenes in this study, the diffusion simulations show Li diffused into the pyroxenes as a form of Li^+ with high concentrations (up to 120 ppm at rim) in a few years. According to the rule of electrostatic neutrality, one kind of divalent cation should leave the mineral, or the redox reaction that involves the reduction of variant valence cations is required during Li addition, such as . Because Li is a fast diffusion element that no other cations but hydrogen can equal in pyroxenes and previous works show that hydrogen is located in M_1, the same as Li^+ in the lattice, we may assume that Li diffusion into the xenoliths is coupled to H loss from nominally anhydrous minerals following the Li enrichments, defined by the substitution mechanism: . Pogge von Strandmann et al. (2011) have proposed the similar scenario that degassing of magmas both drives diffusion of Mg (and Li) into entrained xenoliths, to charge balance hydrogen loss from the minerals.

However, the above scenario is just a rough hypothesis that attempt to the possible link the unique low water content with the Li enrichments found in Cenozoic mantle pyroxene from NCC, and the problems still remain to be resolved.

First, the Li recent diffusion into mineral with a maximum 60 ppm, if coupled with H loss, would only lead to a water loss of ~ 80 ppm, which is still far from accounting for the low water contents in xenoliths, such as ~ 50 ppm in Penglai cpx. The multi-stage Li enrichments were probably involved, and the Li-rich peridotites will re-equilibrate with sorroudning mantle through Li diffusion loss in the intervals. An additional oxidation of Fe^{2+} to Fe^{3+} rather the H addition is more likely to charge-balance this kind of Li loss. Second, the low water content, so far, seems a common signature for the Cenozoic lithospheric mantle beneath the NCC, suggested by the mantle xenoliths studies (Yang et al., 2008; Bonadiman et al., 2009; Xia et al., 2010, 2012). If we assume that the low water contents of peridotite xenoliths result from that melt-peridotites interactions short before eruption, the Cenozoic lithospheric mantle as a whole should not be so depleted in water content as previously suggested, and the low water signature of xenoliths just reflects a local phenomenon within lithospheric mantle columns that have been recently infiltrated by Li-rich melts.

In summary, combined with the discussion in chapter 6 the observed low water signature may result from the combined processes in the lithospheric mantle, and the above observations and reasoning just hint at a possibility that the interactions or infiltrations of Li-rich melts contribute much to or just add to the low water of the Cenozoic lithospheric mantle beneath the NCC. The further and detailed works are needed to figure out the causes.

8 Conclusions

In this thesis, we have examined the lithospheric mantle beneath the eastern NCC in term of both "water" and Li isotopes. The combined investigations of these metasomatism-sensitive "elements" provide a new view to better understand the water distribution and the melt-rock interactions in the deep lithospheric mantle. The main conclusions drawn from this thesis are summed up as:

1. The peridotite xenoliths studied in this thesis are fragments of the lithospheric mantle transported fast to surface by volcanisms, and their chemical compositions are consistent with those reported by others on the similar samples from these localities in the eastern North China Craton. These peridotite xenoliths are further testified to be partial melting residues that have experienced variable degrees of basaltic melt extractions, usually followed by mantle metasomatism to varying extents that invited the relative enrichment of the incompatible trace elements.
2. Nominally anhydrous minerals, such as cpx and opx in peridotite xenoliths, generally contain some amounts of structural OH, known as water, with their contents (ppm H_2O by wt%) varying from 27 to 746 ppm for cpx and 8 to 346 ppm for opx in all studied xenoliths. The homogenous H_2O distribution within grains and the equilibrium partitioning of H_2O between cpx and opx both determine that the water in pyroxenes largely preserve their initial H_2O contents and truly record the pre-eruptive water information in their mantle sources. The ol are almost anhydrous, generally considered as a consequence of H loss during decompression ascent.
3. The correlation, although exits vaguely and locally in some cases, lacks generally between the water content in either cpx or opx and the extents of partial melting, the enrichment of incompatible trace elements or the oxidation state, implying the complex and combined processes controlling the water contents and their variations.
4. A significant contrast in water content is observed in peridotite xenoliths hosted by the Mesozoic and Cenozoic basalts, implying a temporal evolution of water content in the lithospheric mantle beneath the eastern NCC. The H_2O contents in cpx and opx of the Cenozoic samples (Penglai, Qixia, Changle, and Hebi) are

from 27 to 223 ppm and from 8 to 94 ppm, respectively, and are generally lower than their counterparts worldwide and those proposed for pyroxene in the MORB source. By contrast, the H_2O contents in cpx and opx of the Mesozoic samples (Qingdao and Junan) are from 470 to 746 ppm and from 190 to 346 ppm, respectively. The water contents in Daxizhuang xenoliths display the Cenozoic affinity, with the H_2O contents vary from 103 to 311 ppm in cpx and from 30 to 141 ppm in opx.

5. The low water signature of the Cenozoic lithospheric mantle probably reflects the nature of the relatively ancient lithosphere that predated and survived the late Mesozoic to early Cenozoic lithospheric thinning event. The reheating from upwelling asthenospheric flow, accompanying that lithospheric thinning, would devolatilize the overlying lithospheric mantle and account for the water depletion. By contrast, the relatively high water signature of the late Mesozoic lithospheric mantle is likely to represent the intermediate between the Cenozoic water depletion and the early Cretaceous water enrichment due to the paleo-Pacific subduction. The devolatilization, facilitated by thinning of the hydrated and weak lithospheric mantle, reflects the way by which the lithospheric mantle strengthens itself to survive in the convecting mantle.
6. The in-situ Li contents vary from 1.5 to 10.6 ppm in ol, from 0.2 to 62.2 ppm in opx and from 1.6 to 59.7 ppm in cpx for the Cenozoic peridotites from Penglai, Qixia and Hebi. These extreme Li inter-mineral and intra-mineral equilibria, combined with the numerical simulations, demonstrate a strong and transient Li enrichment event that occurred at the mantle source shot prior to the volcanic transports. The melt-rock interaction was too short-lived to be recorded by the others trace systems rather than Li isotopes, and then the mantle metasomatism defined by the degree of enrichment in LREEs for cpx in our samples is not the one that invited the recent Li enrichment. The inferred Li content of up to 600 ppm would call on differentiated carbonatitic melts to infiltrate the peridotites and the high Li enrichment of their mantle sources from which the melts were derived. The kind of melt-rock interaction is unlikely to transform the refractory ancient lithospheric mantle into the fertile “juvenile” mantle.
7. The peridotite samples from Penglai, Qixia and Hebi share more or less the similar Li and Li isotopic signature that suggests two superimposed Li enrichment events: a limited Li enrichment (< 5 ppm) and large δ^7Li depletion (-20~-10‰) of

the domains of these xenoliths, followed by a recent and transient infiltration of high Li and δ^7Li (up to +20‰) melts/fluids. The inferred low δ^7Li melts call upon anomalies melting in the mantle source that contains Li isotopic anomalous components, so does the inferred high δ^7Li melts.

8. From the line of Li isotopic evidence, we conclude that there are recycled components, both Li isotopically heavy and light, in the mantle beneath the eastern North China, and they are most likely derived from the western subduction of the paleo-Pacific plate, i.e. the subduction-modified mantle wedges and the highly dehydrated slab, respectively.
9. The decoupling of high water contents from Li enrichments, i.e. high Li contents and low Li contents in Cenozoic samples; and low Li contents and high water contents in late Mesozoic samples, may hint at an incorporation mechanism by which Li diffusion into mineral is coupled with H loss out of mineral (defined by the substitution), during recent melt-peridotite interactions. This may contribute much or just add to the low water contents of the Cenozoic lithospheric mantle beneath the eastern NCC.

References

Ackermann, L., Cemic, L., and Langer, K., 1983. Hydrogarnet substitution in pyrope: a possible location for water in the mantle. Earth Planet. Sci. Lett., 62, 208–214.

Adam, J., and Green, T.H., 1994. The effects of pressure and temperature on the partitioning of Ti, Sr and REE between amphibole, clinopyroxene and basanitic melts. Chem. Geol., 117, 219-233. doi: 10.1016/0009-2541(94)90129-5.

Agostini, S., Ryan, J.G., Tonarini, S., and Innocenti, F. 2008. Drying and dying of a subducted slab: coupled Li and B isotope variations in Western Anatolia Cenozoic Volcanism. Earth Planet. Sci. Lett. 272, 139–147.

Anders, E., and Grevesse, N., 1989, Abundances of the elements: meteoritic and solar. Geochim. Cosmochim. Acta, 53, 197–214.

Andrut, M., Brandstatter, F., Beran, A., 2003. Trace hydrogen zoning in diopside. Miner. Petrol., 78, 231-241.

Arai, S., 1994. Characterization of spinel peridotites by olivine-spinel compositional relationships: review and interpretation. Chem. Geol.,, 113, 191-204

Arndt, N.T., Ginibre, C., Chauvel, C., Albarede, F., Cheadle, M., and et al., 1998. Were komatiites wet? Geology, 26, 739-742.

Asimow, P.D., Stein, L.C., Mosenfelder, J.L., and Rossman, G.R. 2006. Quantitative polarized infrared analysis of trace OH in populations of randomly oriented mineral grains. Am. Mineral., 91, 278–284.

Aubaud, C., Hauri, E.H., and Hirschmann, M.M., 2004. Hydrogen partition coefficients between nominally anhydrous minerals and basaltic melts. Geophys. Res. Lett., 31(20), L20611

Aubaud, C., Withers, A.C., Hirschmann, M.M., Guan, Y., Leshin, L.A., Mackwell, S., and Bell, D.R. 2007. Intercalibration of FTIR and SIMS for hydrogen measurements in glasses and nominally anhydrous minerals. Am. Mineral., 92, 811–828.

Aulbach, S., Rudnick, R.L., McDonough, W.F., 2008. Li–Sr–Nd isotope signatures of the plume and cratonic lithospheric mantle beneath the margin of the rifted Tanzanian craton (Labait). Contrib. Mineral. Petrol., 155, 79–92.

Bai, J., and Dai, F.-Y., 1998. Archaean crust of China. In: MA, X. Y. & BAI, J. (eds) Precambrian Crustal Evolution of China. Geological Publishing House, Beijing, 15–86.

Basu, A., Wang, J.W., Huang, W.K., Xie, G.H., Tatsumoto, M., 1991. Major element, REE and Pb, Nd and Sr isotopic geochemistry of Cenozoic volcanic rocks of eastern china: implications for origin from suboceanic-tyoe mantle reservoirs. Earth Planet. Sci. Lett., 105, 149–169.

Beck, P., Barrat, J.A., Chaussidon, M., Gillet, Ph., and Bohn, M., 2004, Li isotopic variations in single pyroxene from the Northwest Africa 480 (NWA 480) shergottite: a record of degassing of martian magmas: Geochim. Cosmochim. Acta, 68, 2925–2933.

Becker, A. 1903. Kristalloptik, 362 p. Ferdinand Lieke, Stuttgart.

Bell, D.R., Ihinger, P.D., Rossman, G.R., 1995. Quantitative analysis of trace OH in garnet and pyroxenes. Am. Mineral., 80(5-6), 465-474.

Bell, D.R., Rossman, G.R, Maldener, J., Endisch, D., and Rauch, F. (2003) Hydroxide in olivine: A quantitative determination of the absolute amount and calibration of the IR spectrum. J. Geophys. Res., 108(B2), 2105, DOI: 10.1029/2001JB000679.

Bell, D.R., Rossman, G.R., 1992a. The distribution of hydroxyl in garnets from the subcontinental mantle of Southern Africa. Contrib. Mineral. Petrol., 111, 161-178.

Bell, D.R., Rossman, G.R., 1992b. Water in Earth's mantle: The role of nominally anhydrous minerals. Science, 255, 1391-1397.

Bell, D.R., Rossman, G.R., and Moore, R.O. (2004) Abundance and partitioning of OH in a high-pressure magmatic system: Megacrysts from the Monastery kimberlite, South Africa. J. Petrol., 45, 1539–1564.

Bell, D.R., Rossman, G.R., Maldener, J., Endisch, D., Rauch, F., 2003. Hydroxide in olivine: A quantitative determination of the absolute amount and calibration of the IR spectrum. J. Geophys. Res.,-Solid Earth, 108(B2), 2105, doi:10.1029/2001JB000679

Bell, D.R., Rossman, G.R., Moore, R.O., 2004. Abundance and partitioning of OH in a high-pressure magmatic system: Megacrysts from the Monastery kimberlite, South Africa. J. Petrol., 45(8), 1539-1564.

Benton, L.D., Ryan, J.G. & Savov, I.P., 2004. Lithium abundance and isotope systematics of forearc serpentinites, Conical Seamount, Mariana forearc: Insights into the mechanics of slab-mantle exchange during subduction: Geochemistry Geophysics Geosystems, 5(8):Q08J12, doi:10.1029/2004GC000708.

Berry, A.J., Hermann, J., O'Neill, H.S.C., and Foran, G.J. 2005. Fingerprinting the water site in mantle olivine. 33(11), 869-872. doi: 10.1130/G21759.1.

Beyer, E.E., Griffin, W.L., O'Reilly, S.Y., 2006. Transformation of Archaean lithospheric mantle by refertilization: evidence from exposed peridotites in the Western Gneiss Region, Norway. J. Petrol., 47, 1611–1636.

Blundy, J.D., Falloon, T.J., Wood, B.J., Dalton, J.A., 1995. Sodium partitioning between clinopyroxene and silicate melts. J. Geophy. Res., 100(B8), 15,501–15,515.

Bodinier, J.L., Vasseur, G., Vernieres, J., Dupuy, C., and Fabries, J. 1989. Mechanisms of mantle metasomatisum: geochemical evidence from the Lherz orogenic peridotite. J. Petrol.,

Bolfan-Casanova, N., 2005. Water in the Earth's mantle. Mineral. Mag., 69, 229-257.

Bolfan-Casanova, N., Keppler, H., Rubie, D.C., 2003. Water partitioning at 660 km depth and evidence for very low water solubility in magnesium silicate perovskite. Geophys. Res. Lett., 30(17) 1905, doi:10.1029/2003GL017182

Bonadiman, C., Hao, Y.T., Coltorti, M., Dallai, L., Faccini, B., Huang, Y., Xia, Q.K., 2009, Water content of pyroxenes in intraplate lithospheric mantle. European Journal of Mineralogy, 21, 637-647

Born, M. and Wolf, E. 1980. Principles of Optics, 6th edition, 952 p. Pergamon Press New York.

Bouman, C., Elliott, T., Vroon, P.Z., 2004. Lithium inputs to subduction zones. Chem. Geol., 212, 59–79.

Boyd, F.R., and McAllister, R.H., 1976. Densities of fertile and sterile garnet peridotites. Geophysical Research Letters, 3, 509–512.

Brenan, J.M., Neroda, E., Lundstrom, C.C., Shaw, H.F., Ryerson, F.J., Phinney, D.L., 1998a. Behaviour of boron, beryllium and Lithium during melting and crystallization: constraints from mineral–melt partitioning experiments. Geochim. Cosmochim. Acta, 62, 2129–2141.

Brenan, J.M., Ryerson, F.J., Shaw, H.F., 1998b. The role of aqueous fluids in the slab-tomantle transfer of boron, beryllium, and lithium during subduction: experiments and models. Geochim. Cosmochim. Acta, 62, 3337–3347.

Brey, G., Kohler, T., Nickel, K.G., 1990. Geothermobarometry in four phase lherzolites I Experimental results from 10–60 kb. J. Petrol.31, 1313–1352.

Carlson, R.W., Pearson, D.G., and James, D.E., 2005. Physical, chemical, and chronological characteristics of continental mantle. Rev. Geophys., 43: 2004RG000156.

Chan, L.-H., Alt, J.C., Teagle, D.A.H., 2002. Lithium and lithium isotope profiles through the upper oceanic crust: a study of seawater–basalt exchange at ODP Sites 504B and 896A. Earth Planet. Sci. Lett. 201, 187–201.

Chan, L.-H., Edmond, J.M., Thompson, G., and Gillis, K., 1992. Lithium isotopic composition of submarine basalts: implications for lithium cycle in the oceans. Earth Planet. Sci. Lett. 108, 151–160.

Chan, L.H., Lassiter, J.C., Hauri, E.H., Hart, S.R., and Blusztajn, J., 2009, Lithium isotope systematics of lavas from the Cook-Austral Islands: Constrains on the origin of HIMU mantle: Earth Planet. Sci. Lett., 277, 433-442, doi:10.1016/j.epsl.2008.11.009.

Chan, L.-H., Leeman, W.P., Plank, T., 2006. Lithium isotopic composition of marine sediments. Geochem. Geophys. Geosys., 7, Q06005. doi:10.1029/2005GC001202.

Chaussidon, M., and Robert, F., 1998, $^{7}Li/^{6}Li$ and $^{11}B/^{10}B$ variations in chondrules from the Semarkona unequilibrated chondrite: Earth Planet Sci Lett., 164, 577–589.

Choi, S.H., Kwon, S.-T., Mukasa, S.B., Sagong, H., 2005. Sr–Nd–Pb isotope and trace element systematics of mantle xenoliths from late Cenozoic alkaline lavas, South Korea. Chem. Geol. 221, 40–64.

Chu, Z.Y., Wu, F.Y., Walker, R.J., Rudnick, R.L., Pitcher, L., Puchtel, I.S., Yang, Y.H., and Wilde, S.A. 2009. Temporal evolution of the lithospheric mantle beneath the eastern North China Craton. J. Petrol., 50, 1857–1898.

Chung, S.L. 1999. Trace element and isotope characteristics of Cenozoic basalts around theTanlu fault with implication for the eastern plate boundary between North and South China, J. Geol. 107, 301–312.

Chung, S.L., 1999. Trace Element and Isotope Characteristics of Cenozoic Basalts around the Tanlu Fault with Implications for the Eastern Plate Boundary between North and South China. Geology, 107, 301-312

Crank, J., 1976, The Mathematics of Diffusion, Oxford University Press.

Davis, G., 1994. Thermomechanical erosion of the lithosphere by mantle plume. J. Geophys. Res., 99, 15709-15722.

Decitre, S. et al., 2002, Behavior of Li and its isotopes during serpentinization of oceanic peridotites: Geochem. Geophys. Geosyst., 3, 1007, doi:10.1029/2001GC000178.

Deloule, E., Albarède, F., and Sheppard, S. M. F., 1991. Hydrogen isotope heterogeneities in the mantle from ion probe analysis of amphiboles from ultramafic rocks: Earth Planet. Sci. Lett., 105, 543–553.

Demouchy, S., Jacobsen, S.D., Gaillard, F., Stern, C.R., 2006. Rapid magma ascent recorded by water diffusion profiles in mantle olivine. Geology, 34(6), 429-432.

Dohmen, R., Kasemann, S.A., Coogan, L., Chakraborty, S., 2010. Diffusion of Li in olivine. Part I: Experimental observations and a multi species diffusion model. Geochim. Cosmochim. Acta, 74, 274–292.

Elliott, T., Jeffcoate, A. B., and Bouman, C., 2004. The terrestrial Li isotope cycle: light-weight constraints on mantle convection: Earth Planet. Sci. Lett., 220, 231–

245.

Elliott, T., Thomas, A., Jeffcoate, A., and Niu Y. L., 2006, Lithium isotope evidence for subduction-enriched mantle in the source of mid-ocean-ridge basalts: Nature, 443, 565-568.

Elphick, S.C., Graham, C.M., Dennis, P., 1988. An ion-microprobe study of anhydrous O diffusion in anorthite: a comparison with hydrothermal data and some geological implications. Contrib. Mineral. Petrol., 76, 440-454.

Fan, Q.C., Hooper, P.R., 1989, The mineral chemistry of ultramafic xenoliths of Eastern China: implications for upper mantle composition and the paleogeoterms. J. Petrol., 30, 1117-1158

Fan, Q.C., Liu, R.X., Li, H.M., Li, N., Sui, J.L., et al., 1998. Zircon chronology and REE geochemistry of granulite xenoliths from Hannuoba. Chin. Sci. Bull., 43(2), 133-137.

Fan, Q.C., Sui, J.L., Liu, R.X.,Wei, H., Li, N., 2000a. Petrology and geochemistry of Jinlongdingzi active volcano—themost recent basaltic explosive volcano at Longgang. Chinese Journal of Geochemistry 19, 312–317.

Fan, W.M., Guo, F., Wang, Y.J., Lin, G., and Zhang, M. 2001. Post-orogenic bimodal volcanism along the Sulu orogenic belt in eastern China. Physics and Chemistry of the Earth (A) 26, 733–46.

Fan, W.M., Menzies, M.A., 1992. Destruction of aged lower lithosphere and accretion of asthenosphere mantle beneath eastern China. Geotectonica et Metallogenia 16(3-4), 171–180.

Fan, W.M., Zhang, H.F., Baker, J., Jarvis, K.E., Mason, P.R.D., Menzies, M.A., 2000b. On and off the North China Craton: where is the Archaean keel? J. Petrol., 41, 933–950.

Faure, M., Lin, W., and Breton, N. Le. 2001. Where is the North China-South China block boundary in eastern China. Geology 29,119–122.

Flesch, G.D., Anderson, A.R., and Svec H.J., 1973, A secondary isotopic standard for $^{6}Li/^{7}Li$ determinations: Int J Mass Spect Ion Proc, 12, 265-272.

Frey, F.A., and Green, D.H., 1974. The mineralogy, geochemistry and origin of lherzolite inclusions in Victorian basanites, Geochim. Cosmochim. Acta 38 (1974) 1023–1059.

Fyfe, W.S.,1970. Lattice energies, phase transformations and volatiles in the Earth's mantle. Phys. Earth Planet. Inter., 3, 196–200.

Gallagher, K., Elliott, T., 2009. Fractionation of lithium isotopes in magmatic systems as a natural consequence of cooling. Earth Planet. Sci. Lett. 278, 286–296.

Gao, S., Rudnick, R.L., Carlson, R.W., McDonough, W.F., Liu, Y.S., 2002. Re–Os evidence for replacement of ancient mantle lithosphere beneath the North China craton. Earth Planet. Sci. Lett., 198, 307–322.

Gao, S., Rudnick, R.L., Yuan, H.L., Liu, X.M., Liu, Y.S., Xu, W.L., Ling, W.L., Ayers, J., Wang, X.C., Wang, Q.H., 2004. Recycling lower continental crust in the North China craton. Nature 432, 892–897.

Gao, S, Rudnick, R.L., Xu,W.L., Yuan, H.L., Liu, Y.S., Puchtel, I., Liu, X., Huang, H., Wang, X.R., 2008. Recycling deep cratonic lithosphere and generation of intraplate magmatism. Earth Planet. Sci. Lett., 270(1-2), 41-53.

Gao, Y., Snow, J.E., Casey, J.F., Yu, J., 2011. Cooling-induced fractionation of mantle Li isotopes from the ultraslow-spreading Gakkel Ridge. Earth Planet. Sci. Lett., 301, 231–240.

Geng, Y.S., 1998. Archaean granite pluton events of Qianan area, East Hebei province and its evolution. In: CHEN, Y. Q. (ed.) Corpus on Early Precambrian Research of the North China Craton. Geological Publishing House, Beijing, 105–121.

Goldsmith, J.R., 1987. Al/Si interdiffusion in albite: effect of pressure and the role of hydrogen. Contrib. Mineral. Petrol., 95, 311-321.

Gose, J., Reichart, P., Dollinger, G., Schmadicke, E., 2009a. Water in natural olivine— determined by proton-proton scattering analysis, Am. Mineral., 93, 1613-1619.

Gose, J., Schmädicke, E., Beran, A., 2009b. Water in enstatite from Mid-Atlantic Ridge peridotite: Evidence for the water content of suboceanic mantle? Geology, 37, 543-546.

Grant, K.J., Ingrin, J., Lorand, J.P., Dumas, P., 2007a. Water partitioning between mantle minerals from peridotite xenoliths. Contrib. Mineral. Petrol., doi: 10.1007/s00410-006-0177-1.

Grant, K.J., Kohn, S.C., Brooker, R.A., 2007b. The partitioning of water between olivine, orthopyroxene and melt synthesised in the system albite-forsterite-H_2O. Earth Planet. Sci. Lett., 260, 227-241.

Griffin, W.L., O'Reilly, S.Y., and Ryan, C.G., 1999. The composition and origin of sub-continental lithospheric mantle. In: Fei, Y., Bertka, C.M. & Mysen, B.O. (eds) Mantle Petrology: Field Observations and High Pressure Experimentation: A Tribute to Francis R. (Joe) Boyd. Geochemical Society, Special Publications, 6, 13–45.

Griffin, W.L., Zhang, A.D., O'Reilly, S.Y., Ryan, C.G., 1998. Phanerozoic evolution of the lithosphere beneath the Sino-Korean craton. In: Flower, M., Chung, S.L., Lo, C.H., Lee, T.Y. (Ed.), Mantle Dynamics and Plate Interactions in East Asia. American Geophysical Union, Washington, DC, 107-126.

Griggs, D.T., 1967. Hydrolytic weakening of quartz and other silicates. Geophys. J. Int., 14, 19-31.

Griggs, D.T., Blacic, J.D., 1965. Quartz: anomalous weakness of synthetic crystals. Science, 147, 292-295.

Hacker, B.R., Ratschbacher, L., Webb, L., Ireland, T., Walker, D., et al., 1998. U/Pb zircon ages constrain the architecture of the ultrahigh-pressure Qinling-Dabie Orogen, China. Earth Planet. Sci. Lett., 161, 215-230.

Halama, R., McDonough, W.F., Rudnick, R.L., Bell, K., 2008. Tracking the lithium isotopic evolution of the mantle using carbonatites. Earth Planet. Sci. Lett. 265, 726–742.

Hauri, E.H., Gaetani, G.A., Green, T.H., 2006. Partitioning of water during melting of the Earth's upper mantle at H_2O-undersaturated conditions. Earth Planet. Sci. Lett., 248, 715-734.

Hawkesworth, C. J., Pearson, D.G., and Tuner, S.P., 1999. Chemical and temporal variations in the Earth's lithosphere. Phil. Trans. R. Soc. Lond. A, 357, 647-669.

Hercule, S., Ingrin, J., 1999. Hydrogen in diopside: diffusion, kinetics of extraction incorporation, and solubility. Am. Mineral., 84, 1577-1587.

Hirth, G., Kohlstedt, D.L., 1996. Water in the oceanic upper mantle: implications for rheology, melt extraction and the evolution of the lithosphere. Earth Planet. Sci. Lett., 144, 93-108.

Hirth, G., Kohlstedt, D.L., 2003. Rheology of the upper mantle and the mantle wedge: A view from the experimentalists. In: Eiler, J. (Ed.), Inside the Subduction Factory. Geophysical Monograph, American Geophysical Union, 83-105.

Hofmann, A.W., 1997. Mantle geochemistry: the message from oceanic volcanism. Nature 385, 219–229.

Hu, S., He, L., Wang, J., 2000. Heat flow in the continental area of China: a new data set. Earth Planet. Sci. Lett., 179, 407-419.

Huang, J.L., Zhao, D.P., 2006. High-resolution mantle tomography of China and surrounding regions. J. Geophys. Res., 111, doi: 2005JB004066.

Ingrin, J., Blanchard, M., 2006. Diffusion of hydrogen in minerals. In: Keppler, H., Smyth, J.R. (Ed.), Water in nominally anhydrous minerals. Mineralogical Society of America, Washington D C, pp. 291-320.

Ingrin, J., Hercule, S., Charton, T., 1995. Difffusion of hydrogen in diopside: results of dehydration experiments. J. Geophys. Res., 100, 15489-15499.

Ingrin, J., Skogby, H., 2000. Hydrogen in nominally anhydrous upper-mantle minerals: concentration levels and implications. Eur. J. Mineral., 12(3), 543-570.

Jeffcoate, A.B., Elliott, T., Kasemann, S.A., Ionov, D.A., and Cooper, K.M., 2007, Li isotope fractionation in peridotites and mafic melts: Geochim. Cosmochim. Acta, 71, 202–218.

Johnson, K.T.M., Dick, H.J.B., Shimizu, N., 1990. Melting in the oceanic upper mantle: an ion microprobe study of diopsides in abyssal peridotites. J. Geophys. Res., 95, 2661–2678.

Karato, S., 1986. Does partial melting reduce the creep strength of the upper mantle? Nature 319, 309-310

Karato, S., 1990. The role of hydrogen in the electrical conductivity of the upper mantle. Nature, 347, 272-273.

Keppler, H., and Bolfan-Casanova, N., 2006. Thermodynamics of water solubility and partitioning. In: Keppler, H., Smyth, J.R. (Ed.), Water in Nominally Anhydrous Minerals. Mineralogical Society of America, Washington D C, pp. 193-230.

Keppler, H., and Smyth, J.R., 2006. Water in Nominally Anhydrous Minerals. Washington D C, Mineralogical Society of America.

Koga, K., Hauri, E., Hirschmann, M., Bell, D., 2003. Hydrogen concentration analyses using SIMS and FTIR: Comparison and calibration for nominally anhydrous minerals. Geoch. Geophy. Geosys., 4(2), 1019.

Kohlstedt, D.L., Mackwell, S.J., 1998. Diffusion of hydrogen and intrinsic point defects in olivine. Z. Phys. Chem., 207, 147-162.

Kovács, I., Hermann, J., O'Neill, H.S.C., Gerald, J.F., Sambeidge, M., and Horváth, G. 2008. Quantitative absorbance spectroscopy with unpolarized light: Part II. Experimental evaluation and development of a protocol for quantitative analysis of mineral IR spectra. Am. Mineral., 93, 765-778.

Kronenberg, A.K., 1994. Hydrogen speciation and chemical weakening of quartz. In: Heaney, P.J., Prewitt, C.T., Gibbs, G.V. (Ed.), Silica: physical behavior, geochemistry and materials applications. Mineralogical Society of American, Washington D C, pp. 123-176.

Kronenberg, A.K., Kirby, S.H., Aines, R.D., Rossman, G.R., 1986. Solubility and diffusional uptake of hydrogen in quartz at high water pressures: implications for hydrolytic weakending. J. Geophys. Res., 91, 12723-12744.

Kushiro, I., 1972. Effect of water on the composition of magmas formed at high pressures. J. Petrol., 13, 311-334

Kusky, T.M., and LI, J.H., 2003. Paleoproterozoic tectonic evolution of the North China Craton. Journal of Asian Earth Sciences, 22, 383–397.

Kusky, T.M., Li, J.H., and Santosh, M. 2006. The Paleoproterozoic North Hebei Orogen: North China Craton's Collisional Suture with Columbia Supercontinent. In: Zhai, M.G., Xiao, W.J., Kusky, T.M., Santosh, M. (eds) Tectonic Evolution of China and Adjacent Crustal Fragments, Special Issue of Gondwana Research, doi: 10.1016/j.gr.2006.11.012.

Kusky, T.M., Li, J.H., Tucker, R.D., 2001. The Archean Dongwanzi opiolite complex, North China Craton 2.505-billion-year-old oceanic crust and mantle. Science, 292, 1142-1145.

Kusky, T.M., Li, Z.H., Glass, A., and Huang, H.A., 2004. Archaean ophiolites and ophiolite fragments of the North China craton. In: Kusky, T.M., (ed.) Precambrian Ophiolites and Related Rocks. Developments in Precambrian Geology, 13, 223–274.

Lee, C.-T., 2003. Compositional variation of density and seismic velocities in natural peridotites at STP conditions: implications for seismic imaging of compositional heterogeneities in the upper mantle. Journal of Geophysical Research, 108, 2441–2451.

Lee, C.-T., Luffi, P., Plank, T., Dalton, H.A., Leeman, W.P., 2009. Constraints on the depths and temperatures of basaltic magma generation on Earth and other terrestrial planets using new thermobarometers for mafic magmas. Earth Planet. Sci. Lett. 279, 20–33.

Lee, C.-T., Luffi, P., and Chin, E.J., 2011. Building and Destroying Continental Mantle. Annu. Rev. Earth Planet. Sci., 39, 59–90.

Li, J.H., Qian, X.L., Zhai, M.G., and Guo, J.H. 1996. Tectonic division of a high-grade metamorphic terrain and late Archaean tectonic evolution in north–central part of the North China Craton. Acta Petrologica Sinica, 12, 179–192 [in Chinese with English abstract].

Li, P., Xia, Q.-K., Deloule, E., 2012. Anomalous lithium isotopic compositions of the Cenozic lithospheric mantle beneath Penglai, Shangdong Province: the ion probe analyses of peridotite xenoliths. Geol. J. Chi.Uni., 18(1), 62-73.

Li, T,S., 1999. Taipingzhai–Zunhua Neoarchaean island arc terrain and continental growth in eastern Hebei, North China. PhD thesis, Chinese Academy of Sciences, Beijing.

Li, Z.X., Lee, C.T., Peslier, A.H., and Lenardic, A. 2008. Water contents in mantle xenoliths from the Colorado Plateau and vicinity: implications for the mantle rheology and hydration-induced thinning of continental lithosphere. J. Geophys. Res., 113, B09210. doi:10.1029/2007JB005540.

Libowitzky, E. and Rossman, G. (1996) Principles of quantitative absorbance measurements in anisotropic crystals. Physics and Chemistry of Minerals, 23, 319–327.

Liu, R.W., Chen, J. Sun, and D. Li (1990), The K-Ar age and tectonic environment of Cenozoic volcanic rock in China, in The Age and Geochemistry of Cenozoic Volcanic Rocks in China, edited by R. Liu, pp. 1–43, Seismol. Publ. House, Beijing.

Liu, D.Y., Nutman, A.P., Compston, W., Wu, J.S., Shen, Q.H., 1992. Remnants of ≥3800Ma crust in the Chinese part of the Sino–Korean craton. Geology 20, 339–342.

Liu S.W., Pan, Y. M., Xie, Q. L., Zhang, J. and LI, Q. G. 2004. Archean geodynamics in the Central Zone, North China Craton: constraints from geochemistry of two contrasting series of granitoids in the Fuping and Wutaishan complexes. Precambrian Research, 130, 229–249.

Liu, S.W., Zhao, G.C., Shu, G.M., and ea al. 2006. Th–U–Pb monazite geochronology of the Luliang and Wutai Complexes: constraints on the tectonothermal evolution of the Trans-North China Orogen. Precambrian Research, 148, 205–224.

Liu, S., Zou, H.B., Hu, R.Z., Zhao, J.H., and Feng, C.X. 2006. Mesozoic mafic dikes from the Shandong Peninsula, North China Craton: Petrogenesis and tectonic implications. Geochemical Journal 40, 181–95.

Lundstrom, C.C., Chaussidon,M.,Hsui, A.T., Kelemen, P., Zimmerman,M., 2005.Observations of Li isotopic variations in the Trinity Ophiolite: evidence for isotopic fractionation by diffusion during mantle melting. Geochim. Cosmochim. Acta, 69, 735–751.

Magna, T., Wiechert, U., Halliday, A.N., 2006. New constraints on the lithium isotope compositions of theMoon and terrestrial planets. Earth Planet. Sci. Lett., 243, 336–353.

Marschall, H.R., Pogge von Strandmann, P.A.E., Seitz, H.M., Elliott, T., Niu, Y., 2007. The lithium isotopic composition of orogenic eclogites and deep subducted slabs. Earth Planet. Sci. Lett., 262, 563–580.

Martin, R.F., Donnay, G., 1972. Hydroxyl in the mantle. Am. Mineral., 57, 554-570.

McDonough, W.F. and Sun, S.S., 1995. The composition of Earth.Chem. Geol., 120, 223–253.

McDonough, W.F., and Frey, F.A. 1989. Rare earth elements in upper mantle rocks, in: B.R. Lipin, G.A. McKay (Eds.), Geochemistry and Mineralogy of Rare Earth Elements, vol. 21, Mineralogical Society of America, 99–145.

Meade, C., Jeanloz, R., 1991. Deep-focus earthquakes and recycling of water into the Earth. Science, 252, 68-72.

Menzies, M. A., 1990. Petrology and geochemistry of the continental mantle, pp. 1-

184. Oxford: Clarendon.

Menzies, M. A., and Hawkesworth, C. J., (eds) 1987. Mantle metasomatism. Academic.

Menzies, M., Xu, Y.G., Zhang, H.F., Fan, W.M., 2007. Integration of geology, geophysics and geochemistry: a key to understanding the North China Craton. Lithos 96, 1–21.

Menzies, M.A., Weiming, F., Zhang, M., 1993. Palaeozoic and Cenozoic lithoprobes and the loss of N120 km of Archaean lithosphere, Sino-Korean craton, China. Geol. Soc. Spec. Publ., 76, pp. 71–81.

Menzies, M.A., Xu, Y., 1998. Geodynamics of the North China Craton. In: Flower, M., Chung, S.-L., Lo, C.-H., Lee, T.-Y. (Eds.), Mantle Dynamics and plate interactions in East Asia. American Geophysical Union Monograph, vol. 27, pp. 155–165.

Nishio, Y., Shun'ichi, N., Yamamoto, J., Sumino, H., Matsumoto, T., Prikhod'ko, V.S., Arai, S., 2004. Lithium isotopic systematics of the mantle-derived ultramafic xenoliths: implications for EM1 origin. Earth Planet. Sci. Lett., 217, 245–261.

Niu, Y.L., 2005. Generation and evolution of basaltic magmas: some basic concepts and a new view on the origin of Mesozoic-Cenozoic basaltic volcanism in eastern China. Geol. J. Chi.Uni., 11, 9-46.

Nyblade, A.A., Pollack, H.N., Jones, D.L., Pdomore, F., Mushayandebvu, M., 1990. Terrestrial heat flow in East and Southern Africa. J. Geophys. Res., 95, 17371-17384.

Oh, C.W., and Kusky, T.M., 2007. Review of the Late-Permian to Triassic Hongseong–Odesan collision belt in South Korea and its tectonic correlation with Korea, China and Japan. International Geology Reviews, Special Liu volume, 49.

Okay, A.I., and Sengor, A.M.C. 1992. Evidence for continental thrust related exhumation of the ultra-high-pressure rocks in China, Geology 20 (1992) 411–414.

Okay, A.I., Xu, S.T., Sengor, A.M.C., 1989. Coesite from the Dabie Shan eclogites, central China. Eur. J. Mineral., 1, 595-598.

O'Reilly, S.Y., Griffin, W.L., Poudjom, Y.H., Morgan, P., 2001. Are lithosphere forever? Tracking changes in subcontinental lithospheric mantle through time. GSA Today 11, 4–10.

Pancharatnam, S. 1955. The propagation of light in absorbing biaxial crystals—I.

Parkinson, I.J., Hammond, S.J., James, R.H., and Rogers, N.W., 2007, High-temperature lithium isotope fractionation: Insights from lithium isotope diffusion in magmatic systems: Earth Planet. Sci. Lett., 257, 609-621.

Parsons, B., and Sclater, J.G., 1977. An analysis of the variation of ocean floor bathymetry and heat flow with age. J. Geophys. Res., 82(5), 803–827.

Penniston-Dorland, S.C., Bebout, G.E., Pogge von Strandmann, P.A.E., Elliott, T., and Sorensen, S.S., 2012, Lithium and its isotopes as tracers of subduction zone fluids and metasomatic processes: Evidence from the Catalina Schist, California, USA: Geochim. Cosmochim. Acta, 77, 530–545, doi:10.1016/j.gca.2011.10.038

Peslier, A. H., J. E. Snow, E. Hellebrand, and A. Von Der Handt (2007), Low water contents in minerals from Gakkel ridge abyssal peridotites, Arctic Ocean, paper presented at 17th V. M. Goldschmidt Conference, Geochem. Soc., Cologne, Germany.

Peslier, A. H., Woodland, A. B., and Wolff, J. A. 2008. Fast kimberlite ascent rates estimated from hydrogen diffusion profiles in xenolithc olivines from South Africa, Geochim. Cosmochim. Acta, 72, 2711–2722.

Peslier, A.H., Luhr, J.F., 2006. Hydrogen loss from olivines in mantle xenoliths from Simcoe (USA) and Mexico: mafic alkalic magma ascent rates and water budget of the sub-continental lithosphere. Earth Planet. Sci. Lett., 242, 302-319.

Peslier, A.H., Luhr, J.F., Post, J., 2002. Low water contents in pyroxenes from spinel-periditites of the oxidized, sub-arc mantle wedge. Earth Planet. Sci. Lett., 201, 69-86.

Pogge von Strandmann, P.A.E., Elliott, T., Marschall, H.R., Coath, C., Lai, Y.J., Jeffcoate, A.B., Ionov, D.A., 2011. Variations of Li and Mg isotope ratios in bulk chondrites and mantle xenoliths. Geochim. Cosmochim. Acta, 75, 5247–5268.

Pollack, H.N. 1986. Cratonization and thermal evolution of the mantle. Earth Planet. Sci. Lett., 80(1-2), 175–182.

Priestley, K., Debayle, E., McKenzie, D., Pilidou, S., 2006. Upper mantle structure of eastern Asia from multimode surface waveform tomography. J. Geophys. Res., 111, doi: 2005JB004082.

Rauch, M. and Keppler, H., 2002. Water solubility in orthopyroxene. Contrib. Mineral. Petrol., 143, 525-536.

Reisberg, L., Zhi, X.C., Lorand, J-P., Wagner, C., Peng, Z.C., Zimmermann, C., 2005. Re-Os and S systematics of spinel peridotite xenoliths from east central China: evidence for contrastiong effects of melt percolation. Earth and Planet. Sci. Lett., 239, 286-308

Richter, F.M., Davis, A.M., Depaolo, D.J., Watson, E.B., 2003. Isotope fractionation by chemical diffusion between molten basalts and rhyolite. Geochim. Cosmochim. Acta, 67, 3905–3923.

Rudnick, R.L., and Ionov, D.A., 2007, Lithium elemental and isotopic disequilibrium in minerals from peridotitic xenoliths from far-east Russia: product of recent melt-

fluid/rock reaction: Earth Planet. Sci. Lett., 256, 278–293, doi:10.1016/j.epsl.2007.01.035.

Rudnick, R.L., Gao, S., Ling, W.L., Liu, Y.S., and McDonough, W.F., 2004. Petrology and geochemistry of spinel peridotite xenoliths from Hannuoba and Qixia, North China craton. Lithos, 77, 609-637.

Rudnick, R.L., McDonough, W.F., and O'Connell, R.J., 1998. Thermal structure, thickness and composition of continental lithosphere. Chem. Geol., 145, 395–411.

Sambridge, M., Gerald, J.F., Kovács, I., O'Neill, H.S.C., and Hermann, J. 2008. Quantitative absorbance spectroscopy with unpolarized light: Part I. Physical and mathematical development. Am. Mineral., 93, 751–764.

Seitz, H.M., Brey, G.P., Lahaye, Y., Durali, S.,Weyer, S., 2004. Lithium isotopic signatures of peridotite xenoliths and isotopic fractionation at high temperature between olivine and pyroxenes. Chem. Geol., 212, 163–177.

Seitz, H.M., Woodland, A.B., 2000. The distribution of lithium in peridotitic and pyroxenitic mantle lithologies-an indicator of magmatic and metasomatic processes. Chem. Geol., 166, 47–64.

Shannon, R.D., and Prewitt C. T. 1969, Effective ionic radii in oxides and fluorides, Acta Crystallogr. B25, 925–946.

Skogby, H., Bell, D.R., and Rossman, G.R., 1990. Hydroxide in pyroxene - variations in the natural environment. Am. Mineral., 75(7-8), 764-774.

Skogby, H., Rossman, G.R., 1989. OH- in pyroxene: an experimental study of incorporation mechanisms and stability. Am. Mineral., 74, 1059-1069.

Song, Y., Frey, F.A., 1989. Geochemistry of peridotite xenoliths in basalt from Hannuoba, eastern China: implications for subcontinental mantle heterogeneity. Geochim. Cosmochim. Acta, 53, 97–113.

Stalder, R., Foley, S.F., Brey, G.P., and Horn, I., 1998. Mineralaqueous fluid partitioning of trace elements at 900-1200 ℃ and 3.0-5.7 GPa: new experimental data for garnet, clinopyroxene, and rutile, and implications for mantle

Stalder, R., and Skogby, H., 2003. Hydrogen diffusion in natural and synthetic orthopyroxene, Phy. Chem. Mineral., 30, 12-19.

Stiefenhofer, J., Viljoen, K.S., Marsh, J.S., 1997. Petrology and geochemistry of peridotite xenoliths from the Letlhakane kimberlites, Botswana. Contrib. Mineral. Petrol., 127, 147–158.

Strens, R.G.J., Mao, H.K., Bell, P.M. 1982. Quantitative spectra and optics of some meteoritic and terrestrial titanian clinopyroxenes. In: Saxena SK (ed.) Advances in physical geochemistry, vol. 2, Springer, New York, Heidelberg, Berlin, pp. 327-346.

Su, B.X., Zhang, H.F.,Deloule, E., Sakyi, P.A., Xiao, Y., Tang, Y.J., and Hu, Y., 2012, Extremely high Li and low δ^7Li signatures in the lithospheric mantle: Chem. Geol.,, 292-293, 149-157.

Sun, S.S., and McDonough, W.F., 1989. Chemical and isotopic systematics of oceanic basalts: implications for mantle composition and processes. In: A.D. Saunders, and M.J. Norry Eds., Magmatism in the ocen basins, Geol. Soc. Lond. Spec. Pub., 313-345.

Sun, W., Ding, X., Hu, Y.H., and Li, X.H., 2007. The golden transformation of the Cretaceous plate subduction in the west Pacific. Earth Planet. Sci. Lett., 262, 533–542.

Tang, Y.J., Zhang, H.F., Nakamura, E., Moriguti, T., Kobayashi, K., Ying, J.F., 2007. Lithium isotopic systematics of peridotite xenoliths from Hannuoba, North China Craton: implications for melt–rock interaction in the considerably thinned lithospheric mantle. Geochim. Cosmochim. Acta, 71, 4327–4341.

Tang, Y.J., Zhang, H.F., Nakamura, E., Ying, J.F., 2010. Multistage melt/fluid–peridotite interactions in the refertilized lithospheric mantle beneath the North China Craton: constraints fromthe Li–Sr–Nd isotopic disequilibrium between minerals of peridotite xenoliths. Contrib. Mineral. Petrol., 161, 845–861.

Tang, Y.J., Zhang, H.F., Ying, J.F., Zhang, J., Liu, X.M., 2008. Refertilization of ancient lithospheric mantle beneath the central North China Craton: evidence from petrology and geochemistry of peridotite xenoliths. Lithos 101, 435–452.

Teng, F.Z., McDonough, W.F., Rudnick, R.L., Walker, R.J., 2006. Diffusion-driven extreme lithium i sotopic fractionation in country rocks of the Tin Mountain pegmatite. Earth Planet. Sci. Lett., 243, 701–710.

Tenner, T. J., Hirschmann, M. M., Withers, A. C., Hervig, R. L., 2009. Hydrogen partitioning between nominally anhydrous mantle minerals and melt between 3 and 5 GPa and applications to hydrous peridotite partial melting, Chem. Geol., 262, 42-56.

Tomascak, P. B., Tera, F., Helz, R. T., and Walker, R. J., 1999. The absence of lithium isotope fractionation during basalt differentiation: new measurements by multicollector sector ICP-MS: Geochim. Cosmochim. Acta, 63, 907–910.

Tomascak, P. B., Widom, E., Benton, L. D., Goldstein, S. L., and Ryan, J. G., 2002. The control of lithium budgets in island arcs: Earth Planet. Sci. Lett., 196, 227–238.

Tomascak, P.B., Langmuir, C.H., le Roux, P.J., and Shirey, S.B., 2008. Lithium isotopes in global mid-ocean ridge basalts: Geochim. Cosmochim. Acta, 1626–1637.

Vlastelic, I., Koga, K., Chauvel, C., Jacques, G., and Telouk, P., 2009, Survival of lithium isotopic heterogeneities in the mantle supported by HIMU-lavas from

Rurutu island, Austral Chain: Earth Planet. Sci. Lett., 286, 456-466, doi:10.1016/j.epsl.2009.07.013.

Wade, J., Plank, T., Hauri, E.H., Kelley, K.A., Roggensack, K., Zimmer, M., 2008, Prediction of magmatic water contents via measurement of H_2O in clinopyroxene phenocrysts. Geology, 36, 799–802.

Wagner, C., and Deloule, E., 2007. Behaviour of Li and its isotopes during metasomatism of FrenchMassif Central lherzolites. Geochim. Cosmochim. Acta, 71, 4279–4296.

Wang, S.Y., Liu, M.W., and Liang, B.Q. 2003. New discovery of Cenozoic volcanic craters and its significance of tourism and geology in Changle County, Shandong Province, Land and Resource of Shandong Province 8, 48–50 (in Chinese with English abstract).

Wang, X.M., Liou, J.G., Mao, H.K., 1989. Coesite-bearing eclogites from the Dabie Mountains in central China. Geology, 17, 1085-1088.

Wells, P.R.A., 1977. Pyroxene thermometry in simple and complex systems. Contrib. Mineral. Petrol., 62, 129-139.

Williams, Q., Hemley, R.J., 2001. Hydrogen in the deep earth. Annu. Rev. Earth Planet. Sci., 29, 365-418.

Woodland, A.B., Seitz, H.M., Yaxley, G.M., 2004. Varying behaviour of Li in metasomatised spinel peridotite xenoliths from western Victoria, Australia. Lithos 75, 55–66.

Workman, R. K., Hauri, E.H., Hart, S.R., Wang, J.H., Blusztajn, J., 2006. Volatile and trace element in basaltic glasses from Samoa: implications for water distribution in the mantle, Earth Planet. Sci. Lett., 241, 932-951.

Wu, F.Y., Ge, W.C., Sun, D.Y., Guo, C.L., 2003a. Discussions on the lithospheric thinning in eastern China. Earth Science Frontiers, 10(3): 51-60.

Wu, F.Y., Walker, R.J., Ren, X.W., Sun, D.Y., Zhou, X.H., 2003b. Osmium isotopic constraints on the age of lithospheric mantle beneath northeastern China. Chem. Geol., 196, 107–129.

Wu, F.Y., Lin, J.Q., Wilde, S.A., Zhang, X.O., Yang, J.H., 2005. Nature and significance of the Early Cretaceous giant igneous event in eastern China. Earth Planet. Sci. Lett., 233, 103–119.

Wu, F.Y., Walker, R.J., Yang, Y.H., Yuan, H.L., Yang, J.H., 2006. The chemical–temporal evolution of lithospheric mantle underlying the North China Craton. Geochim. Cosmochim. Acta, 70, 5013–5034.

Wu, F.Y., Zhang, Y.B., Yang, J.H., Xie, L.W., Yang, Y.H., 2008. Zircon U-Pb and Hf isotopic constraints on the Early Archean crustal evolution of the North China

Craton. Precambrian Res., 167(3–4), 339–362.

Wu, J.S., Geng, Y.S., Shen, Q.H., Wan, Y.S., Liu, D.Y., and Song, B. 1998. Archean Geology and Tectonic Evolution of the North China Craton (in Chinese), Geological Publishing House, Beijing, 212 pp.

Wunder, B., Meixner, A., Romer, R.L., Heinrich, W., 2006. Temperature-dependent isotopic fractionation of lithium between clinopyroxene and high-pressure hydrous fluids. Contrib. Mineral. Petrol., 151, 112–120.

Xiao, Y., Zhang, H.F., Fan, W.M., Ying, J.F., Zhang, J., Zhao, X.M., and Su, B.X. 2010. Evolution of lithospheric mantle beneath the Tan-Lu fault zone, eastern North China Craton: Evidence from petrology and geochemistry of peridotite xenoliths. Lithos 117, 229-246.

Xu, J.W., Zhu, G., Tong, W., and et al., 1987. Formation and evolution of the Tangcheng-Lujiang wrench fault system: a major shear system to the northeast of the Pacific Ocean, Tectonophysics, 134, 273-310.

Xu, S.T., Okay, A.I., Ji, S.Y., Sengor, A.M.C., Su, W., et al., 1992. Diamond from the Dabie Shan metamorphic rocks and its implication for tectonic setting. Science, 256, 80-82.

Xu, X. S., O'Reilly, S. Y., Griffin, W. L., Zhou, X. M., and Huang, X. L., 1998. The nature of the Cenozoic lithosphere at Nushan, eastern China, in Mantle Dynamics and Plate Interactions in East China, Geodyn. Ser., vol. 27, edited by M. F. J. Flower et al., pp. 167–196, AGU, Washington, D. C.

Xu, X.S., Griffin, W. L., O'Reilly, S.Y., Pearson, N. J., Geng, H.Y. and Zheng, J.P. 2008. Re-Os isotopes of sulfides in mantle xenoliths from eastern China: Progressive modification of lithospheric mantle. Lithos. 102, 43-64

Xu, Y. G., Lin, C.Y., Shi, L.B., Mercier, J.C.C., and Ross, J. V., 1995. Upper mantle geotherm for eastern China and its geological implications, Sci. China B, 38, 1482-1492.

Xu, Y.G., 2002. Evidence for crustal components in the mantle and constraints on crustal recycling mechanisms: pyroxenite xenoliths from Hannuoba, North China. Chem. Geol., 182, 301-322.

Xu, Y.G., Chung, S.L., Ma, J., Shi, L., 2004. Contrasting Cenozoic lithospheric evolution and architecture in the Western and Eastern Sino-Korean Craton: constraints from geochemistry of basalts and mantle xenoliths. J. Geol., 112, 593-605.

Xu, Y. G., Blusztajn, J., Ma, J.L., Suzuki, K., Liu, J. F., and Hart, S.R., 2008. Late Archean to Early Proterozoic lithospheric mantle beneath the western North China craton: Sr-Nd-Os isotopes of peridotite xenoliths from Yangyan and Fansi, Lithos, 102, 25−42.

Yan, J., Chen, J.F., and Xie, Z. 2003. Mantle xenoliths from Late Cretaceous basalt in eastern Shandong Province: New constraint on the timing of lithospheric thinning in eastern China. Chinese Science Bulletin 48 (19), 2139–44.

Yang. H.J., Sen, G., Shimizu, N., 1998. Mid-ocean ridge melting: constraints from lithospheric xenoliths at Oahu, Hawaii. J. Pertol. 39(2), 277-295.

Yang, J.H., Chung S.L., Zhai M.-G., and Zhou, X.H. 2004. Geochemical and Sr-Nd-Pb isotopic compositions of mafic dikes from the Jiaodong Peninsula, China: Evidence for vein-plus-peridotite melting in the lithospheric mantle. Lithos, 73, 145–60.

Yang, J.H., Wu, F.Y., Wilde, S.A., 2003. A review of the geodynamic setting of large-scale late Mesozoic gold mineralization in the North China Craton: an association with lithospheric thinning. Ore Geol. Rev., 23, 125-152.

Yang, X. Z., Xia, Q.K., Deloule, E., Dallai, L., Fan, Q.C., Feng, M., 2008. Water in minerals of the continental lithospheric mantle and overlying lower crust: A comparative study of peridotite and granulite xenoliths from the North China Craton, Chem. Geol., 256, 33-45.

Ye, K., Cong, B.L., Ye, D., 2000. The possible subduction of continental material to depths greater than 200 km. Nature, 407, 734-736.

Yin, A., and Nie, S.Y. 1993. An indentation model for the North and South China collision and the development of the Tan-Lu and Honam fault systems, eastern Asia, Tectonics 12, 801–813.

Ying, J. F., Zhang, H. F., Kita, N., Morishita, Y. and Shimoda, G., 2006. Nature and evolution of Late Cretaceous lithospheric mantle beneath the eastern North China Craton: constraints from petrology and geochemistry of peridotitic xenoliths from Junan, Shandong province, China. Earth Planet. Sci. Lett., 244, 622-638.

Ying, J.F., Zhang, H.F., Tang, Y.J., 2010. Lower crustal xenoliths from Junan, Shandong province and theri bearing on the nature of the lower crust beneath the North China Craton. Lithos, 119(3-4),363-376.

Yu, H.M., Xia, Q.K., Wang, R.C. and Chen, X.M., 2005. Oxygen isotope and trace element compositions of peridotite xenoliths from Panshishan volcano, SE China. Acta Petrologica Sinica, 21, 1609-1616 (in Chinese with English abstract).

Yui, T.F., Rumble, D., Lo, C.H., 1995. Unusually low $d^{18}O$ ultrahigh-pressure metamorphic rocks from the Sulu terrain, eastern China. Geochim. Cosmochim. Acta, 59, 2859-2864.

Zack, T., Tomascak, P. B., Rudnick, R. L., Dalpé, C., and McDonough, W. F., 2003, Extremely light Li in orogenic eclogites: the role of isotope fractionation during dehydration in subducted oceanic crust: Earth Planet. Sci. Lett., 208, 279–290.

Zeng, G., Chen, L.H., Xu, X.S., Jiang, S.Y., and Hofmann, A.W., Carbonated mantle

osurces for Cenozoic intra-plate alkaline basalts in Shangdong, North China: Chemcal Geology, 273, 35-45.

Zeng, G., Chen, L.H., Hofmann, A.W., Jiang, X.S., and Xu, X.S., 2011. Crust recycling in the sources of two parallel volcanic chains in Shandong, North China. Earth Planet. Sci. Lett., 208, 279–290. 302, 359-368.

Zhai M.-G., Cong B.L., Guo, J.H., Liu, W.J., Li, Y.G. and Wang Q. C. 2000. Sm-Nd geochronology and petrography of garnet pyroxene granulites in the northern Sulu region of China and their geotectonic implication. Lithos 52, 23–33.

Zhai, M.-G., 2004. Precambrian geological events in the North China Craton. In: MALPAS, J., FLETCHER, C. J. N., ALI, J. R. & AITCHISON, J. C. (eds) Aspects of Tectonic Evolution of China. Geol. Soc. Spec. Publ., 226, 57–72.

Zhang, H. F., 2005. Transformation of lithospheric mantle through peridotite–melt reaction: A case of Sino‐Korean craton, Earth Planet. Sci. Lett., 237, 768–780.

Zhang, H.F., Sun, M., Zhou, X.H., Fan, W.M., Zhai, M.-G., and Yin, J.F., 2002. Mesozoic lithosphere destruction beneath the North China Craton: Evidence from major–, trace–element and Sr–Nd–Pb isotope studies of Fangcheng basalts. Contrib. Mineral. Petrol., 144, 241–253.

Zhang, H. F., Goldstein, S.L., Zhou, X.H., Sun, M., Zheng, J.P., and Cai, Y., 2008. Evolution of subcontinental lithospheric mantle beneath eastern China: Re‐Os isotopic evidence from mantle xenoliths in Paleozoic kimberlites and Mesozoic basalts. Contrib. Mineral. Petrol., 155, 271–293.

Zhang, H.F., Goldstein, S.L., Zhou, X.H., Sun, M., and Cai, Y., 2009a. Comprehensive refertilization of lithospheric mantle beneath the North China Craton: Further Os–Sr–Nd isotopic constraints. J. Geol. Soc., 166, 249–259.

Zhang, J., Zhang, H.F., Kita, N., and et al. 2009. Secular evolution of the lithospheric mantle beneath the eastern North China craton: evidence from peridotitic xenoliths from Late Cretaceous mafic rocks in the Jiaodong region, east-central China. International Geology Review.

Zhang, J., Zhang, H.F., Ying, J.-F., and et al. 2008. Contribution of subducted Pacific slab to Late Cretaceous mafic magmatism in Qingdao region, China: A petrological record, Island Arc 17, 231–241.

Zhang, K.J. 2000. Trace element and isotope characteristics of Cenozoic basalts around the Tanlu Fault with implications for the Eastern Plate Boundary between North and South China: An extended discussion, J. Geol. 108, 739–743.

Zhang, Z.Q., Liu, M.W. 1996. The Academy of Geological Survey of Shandong Province, 1:50000 Field Geological Survey Report (in Chinese), 46-57.

Zhao, D.P., Maruyama, S., and Omori, S., 2007, Mantle dynamics of Western Pacific and East Asia: Insight from seismic tomography and mineral physics. Gondwana Research, 11, 120-131, doi:10.1016/j.gr.2006.06.006.

Zhao, G.C., Wilde, S.A., Cawood, P.A., Sun, M., 2001. Archean blocks and their boundaries in the North China Craton: lithological, geochemical, structural and P-T path constraints and tectonic evolution. Precambrian Res., 107, 45-73.

Zhao, G.C., Sun, M., Wilde, S., and Li, S.Z., Liu, S.W., and Zhang, J. 2006. Composite nature of the North China Granulite-Facies Belt: tectonothermal and geochronological constraints. Gondwana Research, 9, 337–348.

Zhao, G.T., Han, Z., Luan, G., Xing, G., and Chen, Z.L. 2001. Geochemistry of basaltic rocks in the Laoshan Mountain area. Geological Journal of China Universities 7, 432–43 (in Chinese).

Zhao, G.T., Wang, D.Z., Cao, Q.C., and Yu L. 1998. Thermal evolution and signification of I-A type granite: The example of Laoshan granite. Science in China (D) 28, 296–302.

Zheng, J. P., O'Reilly, S. Y., Griffin, W. L., Lu, F. X., and Zhang, M., 1998. Nature and evolution of Cenozoic lithospheric mantle beneath Shandong Peninsula, Sino-Korea craton, eastern China, Int. Geol. Rev., 40, 471-499.

Zheng, J.P., 1999. Mesozoic-Cenozoic Mantle Replacement and Lithospheric Thinning Beneath the Eastern China. Wuhan, Publishing House of China University of Geosciences.

Zheng, J.P., O'Reilly, S.Y., Griffin, W.L., Lu, F.X.., Zhang, M., and Pearson, N.J., 2001. Relics of refractory mantle beneath the eastern North China block: significance for lithosphere evolution. Lithos 57, 43-66.

Zheng, J.P., Griffin, W.L., O'Reilly, S.Y., Yang, J.S., Li, T.F., et al., 2006. Mineral chemistry of peridotites from Paleozoic, Mesozoic and Cenozoic lithosphere: constraints on mantle evolution beneath Eastern China. J. Petrol., 47, 2233-2256.

Zheng, J.P., Griffin, W.L., O'Reilly, S.Y., Yu, C.M., Zhang, H.F., Pearson, N., and Zhang, M., 2007, Mechanism and timing of lithospheric modification and replacement beneath the eastern North China Craton: peridotitic xenoliths from the 100 Ma Fuxin basalts and a regional synthesis: Geochim. Cosmochim. Acta, 71, 5203–5225.

Zheng, Y.F., Fu, B., Gong, B., Li, L., 2003. Stable isotope geochemistry of ultrahigh pressure metamorphic rocks from the Dabie-Sulu orogen in China: implications for geodynamics and fluid regime. Earth-Sci. Rev., 62, 105-161.

Zhi, X.C., Reisberg, L., and Xu, X.S., 2007. Re-Os geochemistry of mantle peridotite xenoliths from Nushan (in Chinese). J. Univ. Sci. Tech. China, 37, 945–952.

Zou, H.P., 2001. Continental marginal rifting along the northern South China Sea: the crustal response to the lower lithospheric delamination. Marine Geol. Quaternary Geol., 21, 39-44.

Water contents and lithium isotope compositions of the Mesozoic-Cenozoic lithospheric mantle of eastern North China Craton: constraints from peridotite xenoliths

Thesis by **Pei LI**

Related publications and manuscripts

Li Pei, Xia Qunke and Deloule Etienne, 2012, Anomalous lithium isotopic compositions of the Cenozoic lithospheric mantle beneath Penglai, Shangdong province: the ion probe analyses of peridotite xenoliths. Geol. J. Chi.Uni., 18(1), 62-73 (in Chinese with English abstract).

Xia, Q.-K., Y. Hao, **P. Li**, E. Deloule, M. Coltorti, L. Dallai, X. Yang, and M. Feng, 2010, Low water content of the Cenozoic lithospheric mantle beneath the eastern part of the North China Craton, J. Geophys. Res., 115, B07207, doi:10.1029/2009JB006694.

P.Li, Q.-K. Xia and E. Deloule, Anomalous lithium isotopic components in the mantle beneath the eastern North China. Submited to J. Geophys. Res., 2012.